JYU DISSERTATIONS 578

Ville Korpelin

Computational Studies of Catalytic Active Site Properties and Reactions at the Metal–Oxide Interface

UNIVERSITY OF JYVÄSKYLÄ
FACULTY OF MATHEMATICS
AND SCIENCE

JYU DISSERTATIONS 578

Ville Korpelin

Computational Studies of Catalytic Active Site Properties and Reactions at the Metal–Oxide Interface

Esitetään Jyväskylän yliopiston matemaattis-luonnontieteellisen tiedekunnan suostumuksella
julkisesti tarkastettavaksi Ylistönrinne-rakennuksen auditoriossa Kem1
joulukuun 9. päivänä 2022 kello 12.

Academic dissertation to be publicly discussed, by permission of
the Faculty of Mathematics and Science of the University of Jyväskylä,
in building Ylistönrinne, auditorium Kem1, on December 9, 2022, at 12 o'clock.

JYVÄSKYLÄN YLIOPISTO
UNIVERSITY OF JYVÄSKYLÄ

JYVÄSKYLÄ 2022

Editors
Karoliina Honkala
Department of Chemistry, University of Jyväskylä
Päivi Vuorio
Open Science Centre, University of Jyväskylä

ISBN 978-951-39-9236-1 (PDF)
URN:ISBN:978-951-39-9236-1
ISSN 2489-9003

Permanent link to this publication: http://urn.fi/URN:ISBN:978-951-39-9236-1

There are secrets within secrets, though—always.
—David Foster Wallace, *The Pale King*

ABSTRACT

Korpelin, Ville
Computational Studies of Catalytic Active Site Properties and Reactions at the Metal–Oxide Interface
Jyväskylä: University of Jyväskylä, 2022, 78 p. (+included articles)
(JYU Dissertations
ISSN 2489-9003; 578)
ISBN 978-951-39-9236-1 (PDF)

In this thesis work, the geometric and electronic structures of metal–oxide catalysts were studied using density functional theory. The studied systems were zirconia-supported metal atoms and clusters, and ReO_x-modified rhodium. Various aspects of these metal–oxide systems were investigated, including the metal–oxide interaction and interfacial properties, the structural variation and dynamics of the supported clusters, and the reducibility and acidity of the oxide components. The dissociation of water over the metal–oxide interface and the hydrodeoxygenation of glycerol on ReO_x-modified Rh were used as model reactions.

It was shown that small Pt and Rh clusters on zirconia exhibit unique interfacial reaction sites, producing non-scaling behavior in the interfacial water splitting reaction. Less stable cluster isomers were found to dissociate water more exothermically due to the stronger binding of the dissociated fragments. The challenges of simulating the dynamics of such clusters using constant-temperature DFT-MD were investigated, highlighting the necessity of tight SCF convergence and proper thermostatting to avoid anomalies such as temperature gradients. The metal-enhanced reducibility of monoclinic zirconia was studied using a variety of adsorbed single transition metal atoms, with Ir and Pt providing the strongest enhancement. To account for the origin of the enhancement, the metal–oxide and metal–vacancy binding were investigated in detail, with a focus on the charge transfer and covalent interactions. Finally, the metal-acid bifunctional ReO_x–Rh catalyst was found to acid-catalyze the dehydroxylation of glycerol, with a competitive metal-catalyzed pathway possibly explaining the experimentally observed poor selectivity. The same catalyst was found unable to acid-catalyze the ring opening of glycidol, pointing toward a ring-size effect in solid acid catalysis.

Keywords: density functional theory, metal–oxide interface, supported clusters, reducibility, molecular dynamics, acid catalysis

TIIVISTELMÄ (ABSTRACT IN FINNISH)

Korpelin, Ville
Laskennallisia tutkimuksia katalyyttisten aktiivisten paikkojen ominaisuuksista ja reaktioista metalli–oksidi-rajapinnalla
Jyväskylä: University of Jyväskylä, 2022, 78 s. (+artikkelit)
(JYU Dissertations
ISSN 2489-9003; 578)
ISBN 978-951-39-9236-1 (PDF)

Tässä väitöskirjatyössä tutkittiin tiheysfunktionaaliteorian avulla metalli–oksidi-katalyyttien geometrisia ja elektronisia rakenteita. Tutkittuina systeemeinä olivat zirkoniatuetut metalliatomit ja -klusterit, ja ReO_x-muokattu rodium. Työssä tarkasteltiin näiden metalli–oksidi-systeemien useita piirteitä, kuten metalli–oksidi-vuorovaikutusta ja rajapinnan ominaisuuksia, tuettujen klustereiden rakenteellista vaihtelua ja dynamiikkaa, sekä oksidikomponentin pelkistyvyys- ja happamuusominaisuuksia. Mallireaktioina käytettiin veden dissosiaatiota metalli–oksidi-rajapinnalla ja glyserolin hydrodeoksygenaatiota ReO_x-muokatulla rodiumilla.

Työssä osoitettiin, että pienten Pt- ja Rh-klusterien rajapinnat zirkonialla sisältävät ainutlaatuisia reaktiopaikkoja, mikä johtaa veden halkeamisreaktiossa skaalautumattomaan käytökseen. Epästabiilimpien klusteri-isomeerien osoitettiin dissosioivan vettä eksotermisemmin, johtuen dissosioituneiden fragmenttien voimakkaammasta sitoutumisesta niille. Tällaisten klustereiden vakiolämpötiladynamiikan DFT-MD-simuloinnin haasteita tarkasteltiin, ja tuloksissa korostuivat tiukan SCF-konvergenssin ja oikein valitun termostaatin merkitys anomalioiden kuten lämpötilagradienttien välttämiseksi. Monokliinisen zirkonian metalliavusteista pelkistymistä tutkittiin useiden adsorboituneiden yksittäisten siirtymämetalliatomien tapauksessa, joista Ir ja Pt avustivat pelkistymistä voimakkaimmin. Ilmiön alkuperän selvittämiseksi metalli–oksidi- ja metalli–vakanssi-vuorovaikutuksia tarkasteltiin yksityiskohtaisesti keskittyen varauksensiirtoon ja kovalenttisiin vuorovaikutuksiin. Bifunktionaalisen metalli-happokatalyytin, ReO_x–Rh:n, todettiin happokatalysoivan glyserolin dehydroksylaatiota, joskin kilpaileva metallikatalysoitu reaktiopolku on läsnä ja saattaa selittää kokeellisesti havaitun heikon selektiivisyyden. Sama katalyytti todettiin kyvyttömäksi happokatalysoimaan glysidolin renkaanaukeamisreaktiota, mikä viittaa renkaankokoefektiin kiinteähappokatalyysissä.

Avainsanat: tiheysfunktionaaliteoria, metalli–oksidi-rajapinta, tuetut klusterit, pelkistyvyys, molekyylidynamiikka, happokatalyysi

Author

Ville Korpelin
Department of Chemistry
Nanoscience Center
University of Jyväskylä
P.O. Box 35
FI-40014 University of Jyväskylä
Finland

Supervisor

Professor Karoliina Honkala
Department of Chemistry
Nanoscience Center
University of Jyväskylä
P.O. Box 35
FI-40014 University of Jyväskylä
Finland

Reviewers

Professor Anastassia N. Alexandrova
Department of Chemistry and Biochemistry
University of California Los Angeles
Los Angeles, USA

Associate Professor Peter Broqvist
Department of Chemistry - Ångström Laboratory
Uppsala Universitet
Uppsala, Sweden

Opponent

Professor Hannes Jónsson
Faculty of Physical Sciences
University of Iceland
Reykjavík, Iceland

ACKNOWLEDGEMENTS

The studies included in this thesis were carried out between 2018 and 2022 in the Nanoscience Center at the University of Jyväskylä. The research was funded by the Academy of Finland and the University of Jyväskylä, and the computational resources were provided by CSC – IT Center for Science.

Thank you to my supervisor, Professor Karoliina Honkala, for the relentless encouragement and unwavering support over the years. Thank you also for the opportunity to explore a wide variety of chemical concepts and methodological details; this diversity of experience has allowed me to become a well-rounded computational scientist.

Many thanks in advance to my opponent Professor Hannes Jónsson for what I anticipate will be a stimulating defense, and to the reviewers Professor Anastassia N. Alexandrova and Associate Professor Peter Broqvist for their invaluable contribution to the thesis.

Thank you to my past and present colleagues in the Honkala group, which has grown quite a bit since I joined almost five years ago; it has been a joy to troubleshoot together. In particular, thanks to Dr. Toni Kiljunen for first introducing me to computational chemistry as a fledgling student, and to Dr. Marko Melander for showing me how deep the rabbit hole goes. Marko's astute comments and suggestions on the thesis are also greatly appreciated.

Finally, my deepest thanks to my friends and family for always being there for me. A special thank you to the MTG-BFF collective for keeping me (mostly) sane for the past 11 years – you're all honorary co-authors as far as I'm concerned.

Ville Korpelin
Jyväskylä 30.9.2022

LIST OF ACRONYMS

AIMD	ab initio molecular dynamics
AOOM	atomic orbital occupation matrix
APW	augmented plane wave (method)
ASE	Atomic Simulation Environment
BEP	Brønsted–Evans–Polanyi
CI	climbing image
CN	coordination number
COM	center of mass
DFT	density functional theory
FNV	Freysoldt–Neugebauer–van der Walle
KE	kinetic energy
KS	Kohn–Sham
LDA	local density approximation
GCN	generalized coordination number
GGA	generalized gradient approximation
GM	global minimum
GPAW	grid projector augmented wave
MD	molecular dynamics
MEP	minimum energy path
MvK	Mars–van Krevelen
NEB	nudged elastic band
NGM	near-global minimum
PAW	projector augmented wave
PBE	Perdew–Burke–Ernzerhof
PDO	propanediol
PES	potential energy surface
SCF	self-consistent field
SGCN	strain-adjusted generalized coordination number
SMSI	strong metal–support interaction
SOAP	smooth overlap of atomic positions
TDDFT	time-dependent density functional theory
THFA	tetrahydrofurfuryl alcohol
TM	transition metal
TMO	transition metal oxide
TS	transition state
vdW	van der Waals

CONTENTS

LIST OF INCLUDED ARTICLES

I Minttu M. Kauppinen, Ville Korpelin, Anand Mohan Verma, Marko M. Melander, and Karoliina Honkala. Escaping scaling relationships for water dissociation at interfacial sites of zirconia-supported Rh and Pt clusters. *The Journal of Chemical Physics* **2019**, *151*, 164302.

II Ville Korpelin, Toni Kiljunen, Marko M. Melander, Miguel A. Caro, Henrik H. Kristoffersen, Nisha Mammen, Vesa Apaja, and Karoliina Honkala. Addressing Dynamics at Catalytic Heterogeneous Interfaces with DFT-MD: Anomalous Temperature Distributions from Commonly Used Thermostats. *The Journal of Physical Chemistry Letters* **2022**, *13*, 2644–2652.

III Ville Korpelin, Marko M. Melander, and Karoliina Honkala. Reducing the Irreducible: Dispersed Metal Atoms Facilitate Reduction of Irreducible Oxides. *The Journal of Physical Chemistry C* **2022**, *126*, 933–945.

IV Ville Korpelin, Gokarneswar Sahoo, Rasmus Ikonen, and Karoliina Honkala. ReO_x as a Brønsted acidic modifier in glycerol hydrodeoxygenation: computational insight into the balance between acid and metal catalysis. *Submitted,* **2022**.

The author performed the Pt_{13}/ZrO_2 DFT calculations and analyses for Paper I and co-wrote the manuscript, contributing equally with M. M. Kauppinen. The author performed the N_2 and Pt_{13}/ZrO_2 DFT calculations and analyses for paper II and co-wrote the manuscript. The author is the primary author of paper III and carried out all DFT calculations and analyses. The author performed most vdW-corrected DFT calculations for paper IV and co-wrote the manuscript, contributing equally with G. Sahoo.

1 INTRODUCTION

1.1 Computation and catalysis

Chemical processes are ubiquitous in nature, industry and everyday life. It is therefore no surprise that catalysis, a method to accelerate and facilitate chemical reactions, is likewise omnipresent in both nature and society. On an individual level, living organisms rely on the ability of enzymes to catalyze the reactions required for life to exist. Catalysis also supports life on a wider scale: by one estimate, half of the world's population is supported by nitrogen fertilizers obtained via the Haber process.[1] In the chemical industry, catalysis is utilized in making 85–90 % of all products comprising fuels, materials, pharmaceuticals, consumer chemicals and more.[2]

For industrial purposes, accelerating chemical reactions has the obvious benefit of improving production rates; often, a catalyst is necessary to make the desired process run on a reasonable timescale.[2] Lowering the activation barrier can also allow the use of milder reaction conditions, such as lower temperatures and pressures, decreasing the required energy investment and increasing safety. Furthermore, a suitably chosen catalyst can improve the product distribution, minimizing undesired waste products by inhibiting side reactions. To the extent that waste is unavoidable, it can ideally be collected and used as a feedstock in other catalytic processes. Catalysis is therefore crucial for the development of affordable, green chemistry by improving both the energy and atom economies.

In order to develop new and improved catalysts, an understanding of their properties and behavior is necessary.[3] Both experimental and computational methods play an important role in the process. Experiments can provide very direct and practical information on the performance of catalysts and the effects of reaction conditions, but the atomic-level details of the reaction, including the mechanism and the nature of the active sites and species, are challenging to determine from experiments alone. Quantum chemical calculations, on the other hand, are well suited to such atomic-level investigations. Computational work can help explain experimental results and direct new efforts based on the gained understanding. Of course, the merit of any potential catalyst must ultimately be settled by real-world experiment.

The computational study of catalysis takes many forms.[4] On the reactor scale, the heat and mass transport properties, flow dynamics and diffusion in the reaction mixture can be modeled using computational fluid dynamics.[5] On the atomic scale, quantum chemical simulations of the catalyst structures, reactant adsorption geometries and reaction mechanisms can provide a detailed understanding of the underlying chemistry. Between these extremes, the catalytic reaction network can be described using various methods, such as microkinetic modeling and kinetic Monte Carlo simulations.[6–9] Increasingly popular multiscale methods linking the above approaches help attain a more complete picture of the catalytic process.[4,10]

In addition to elucidating the details of individual systems, computational work can discover or confirm broader catalytic trends, leading to important conceptual advances. One key area is the development of activity descriptors: efficiently computable atomic-scale properties that can predict catalytic activity at the macroscale.[3] For instance, the d band model[11] and BEP relations[12] have been highly successful in rationalizing and predicting the catalytic properties of transition metal surfaces using data that can be readily obtained with DFT. Such general insights enable the rational design of improved catalysts and help direct further studies in fruitful directions.

In order to acquire computational results in a reasonable timeframe, approximations are typically required. These, too, come in many forms. In quantum chemical calculations, the description of the electronic structure must necessarily be simplified in some way for the equations to become tractable. The geometry of the catalyst is also typically simplified for computational purposes, and often greatly so: for instance, the active sites on metal catalysts may be described by only their most stable facets, excluding defects and other small-scale structures.[13] The reaction conditions, such as temperature, pressure and solvent, and the dynamics of the catalytic system can be modeled by simple approximations or excluded entirely. In spite of these sometimes relatively drastic simplifications, useful results can be obtained as long as the approximations are well justified.

There are, however, many situations in which approximate descriptions fail to capture some crucial feature of the system, necessitating more realistic simulations.[14] One of the main goals of modern computational catalysis is to bridge the gaps between simulation and experiment.[4,9] As there are many such gaps, it is important to identify the most significant ones for a given simulation in order to target the improvements rationally and effectively. In this thesis, the electronic and geometric properties of the active sites on various metal–oxide catalyst models are investigated to shed light on their structure and activity, and to guide future efforts toward more realistic simulations. Papers I and II explore the geometric variety and structural dynamics of the active sites, while papers III and IV focus on the metal–oxide interaction and the catalytic properties of the oxide at the reaction site.

1.2 Active sites on metal–oxide catalysts

Oxide-supported metal catalysts have been used for decades in the chemical industry.[15] Traditionally, the support was mainly considered to provide a high surface area for the dispersion of the active metal particles. In modern times, the role of the support and the metal–support interaction have been recognized as crucial elements in heterogeneous catalysis.[16] Even if the active reaction sites are on the metal particle, its characteristics can be modulated by the chemical and physical interactions with the oxide support. The physical structure of the oxide affects the size and shape of the supported metal particles, while the chemical nature of the oxide can alter, e.g., the redox properties of the metal clusters.

Even on conventional, idealized oxide-supported metal catalysts, there exists a wide array of possible active sites (Figure 1). A well defined, ideal metal nanoparticle features various sites consisting of differently coordinated metal atoms: while terrace sites are most common, edges and corners can produce higher activities due to the higher coordinative unsaturation and possibly more favorable local geometry. A particle can feature many different terrace sites corresponding to different facets, and the same goes for edges and corners. In real systems, the metal particles are not ideal, and can exhibit features such as step defects, vacancies and adatom islands, adding further complexity to the metal sites. In the small-particle limit, the metallic nature of the particle gives way to a more molecular character, the relative significance of the metal–oxide interaction increases and the particle no longer exhibits clear facets.[15,17–19] On such small clusters, each metal site can be considered unique. In addition to the metal, the oxide support can also be catalytically active and exhibit a variety of active sites, ranging from well-defined facets to more complicated nanostructures.[20–22]

Some reactions that are not effectively catalyzed by the metal or the oxide alone can instead occur on the metal–oxide interface, where both components may simultaneously participate in the catalytic reaction.[15,23,24] The characteristics of such interfacial reaction sites are determined by the geometric and electronic

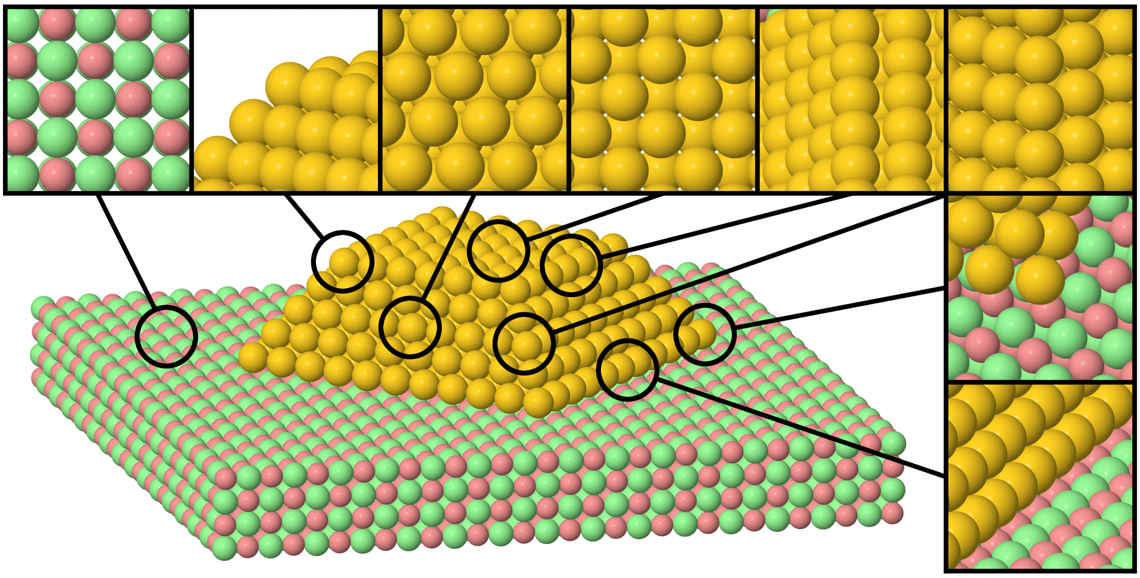

FIGURE 1 Various possible reaction sites on a model Au/MgO cluster system.

properties of both components and their interaction with each other, potentially resulting in very rich catalytic chemistry. The oxidation of CO on Au/TiO_2 perimeter sites is a typical example of an interfacial reaction.[25,26] While the details of the mechanism are still debated, interfacial oxygen vacancy formation and oxide-mediated gold–oxygen charge transfer have been noted as relevant interfacial phenomena.[26]

The nature of the active site can be markedly different depending on the type of metal–oxide catalyst, and the details of the atomic configuration are often unknown. The matter is further complicated by the dynamics of the catalyst under operating conditions, as high temperatures and chemical substrates can induce structural changes that alter the site assembly and distribution. It is therefore important to characterize the catalyst in various stages of the catalytic process, ideally using *in situ* or *operando* measurements.[27]

In the following subsections, some key properties of the metal and oxide components are introduced.

1.2.1 Oxide properties

If the role of the oxide is limited to supporting the metal particles, as in the traditional view, its most important properties are high surface area, thermal stability and chemical inertness.[2] These enable the oxide to disperse the metal effectively and maintain the structure of the catalyst. While these features are often desirable for practical reasons, the oxide can play additional catalytic roles via its other chemical properties, such as reducibility and acidity.

The oxide supports are often divided into nonreducible (e.g., MgO, SiO_2, ZrO_2) and reducible (e.g., TiO_2, CeO_2) oxides, with distinct catalytic properties; ZrO_2, the oxide studied in papers I–III, has also occasionally been placed into an "intermediate" or "scarcely reducible" category.[28,29] The reducibility of the oxide can play a direct role in the catalytic reaction in the case of the Mars–van Krevelen (MvK) mechanism, where the reactant is directly oxidized by the addition of a surface oxide anion.[28] The oxide vacancy left behind by the reaction can be repaired by molecular oxygen, regenerating the catalyst, or even actively assist the reaction: the vacancy can, e.g., produce reactive atomic hydrogen by accepting the oxygen atom from a H_2O molecule, or convert O_2 into strongly oxidizing (su)peroxo species.[30] Clearly, such mechanisms are only feasible when the oxide is sufficiently reducible to exchange O atoms with the reactant mixture.

The reducibility of the oxide support can be modified by the adsorbed metal particles, which can provide favorable gap states for the vacancy electrons.[28] This metal-enhanced reducibility has been proposed to play a role in interfacial reactions such as CO oxidation over Au/TiO_2.[28] In some cases, the strong metal support interaction (SMSI) between a metal and a reducible oxide has been found to result in (partial or complete) metal encapsulation by the oxide, producing a dramatically altered interfacial structure.[31–33] Reducibility can therefore affect the geometric as well as the electronic structure of the catalyst.

In addition to reducibility, the acid-base properties of the oxide can also be catalytically relevant.[34] In fact, the two concepts are related. The removal of an oxygen atom from an oxide leaves two electrons inside the vacancy, producing an electron-rich surface site. This electron surplus can act as a Lewis base and enhance the binding of Lewis acidic reactants such as O_2 or atomic Au.[34] Reducible oxides feature cations that are able to accept electrons, i.e., are Lewis acidic. Thus, the oxygen vacancy formation in reducible oxides can be considered an acid-base reaction, with the Lewis basic vacancy electrons (at least partially) neutralizing the Lewis acidic surface cations. The Lewis acidity of the oxide can also directly influence the catalytic reaction by modulating the binding strength of the adsorbates and their charge transfer with the surface. Also, while pure transition metal oxides have no protons to donate, catalytically active Brønsted acid sites may still be formed by, e.g., (partial) hydration of the surface or by accepting H from a reactant.[35,36]

The structure of the oxide is another consideration. Many oxides exhibit multiple polymorphs with different properties, and the surface structure may vary depending on the catalyst preparation.[37,38] While oxide surfaces are often modeled using the most stable facets, less stable geometries or defect sites are present in some concentration and may have a considerable impact on the catalytic properties.[39] Such "imperfections" often feature undercoordinated atoms, which may be particularly reactive and effective even in low concentrations.[39] Nanostructured oxides have attracted considerable interest for their wide variety of local structural environments and properties distinct from the bulk or well-defined surfaces.[40,41]

1.2.2 Metal nanoparticle size

The metal particles deposited on the oxide support can also exhibit varying properties, the most obvious ones being the chemical identity and particle size. Precious metals such as Pt, Au and Rh are often utilized for their high activities, though cheaper alternatives with comparable properties are under constant investigation. Typically, a small particle size is considered preferable, as it produces a high surface–volume ratio and thus a high activity for the amount of metal used.[2] Small particles also feature more interfacial metal–oxide sites, which may be relevant for some reactions.[15] Catalyst preparation methods therefore often aim toward maximal dispersion of the metal component.

In the "scalable regime" of roughly 100-atom and larger particles, the properties of the metal are more or less bulk-like and the number of surface sites may be considered the most important size-related feature.[13,15] Only a relatively small part of the particle is in direct contact with the support, diminishing the effect of the metal–oxide interaction. Large nanoparticles typically exhibit well defined crystal facets, which are structurally simple and can be modeled using periodic surface models.[13] However, defects and coordinatively unsaturated reaction sites can be crucial for catalytic activity, as has been shown in the case of ammonia synthesis.[42]

For smaller particles, the properties start to diverge from those of the bulk metal, as the particle becomes increasingly molecular in character.[17,18] The significance of the metal–oxide interaction and charge transfer also increases for such small particles.[19] While large nanoparticles likely present similar, well ordered facets at the metal–oxide interface, small clusters instead feature a broad variety of interfacial sites, as the bulklike structure is no longer retained.[15] Of particular note are the increasingly studied single atom catalysts, representing the far end of the particle size spectrum, for which every reaction site is interfacial in nature.[43] Various particle sizes are illustrated in Figure 2, in which the geometric aspect of scalability is highlighted: the Pt_{13} cluster is irregular in shape and exhibits various interfacial sites, while the larger Pt_{43} cluster is starting to exhibit some regular facets.

For small supported clusters such as Pt_{13}/ZrO_2, many structural isomers can be available at typical reaction temperatures.[44,45] As their catalytic properties are sensitive to the cluster geometry, the total activity is a function of the cluster ensemble.[45] To further complicate matters, the clusters are not static, and can undergo temperature- or adsorbate-induced transformations; this susceptibility

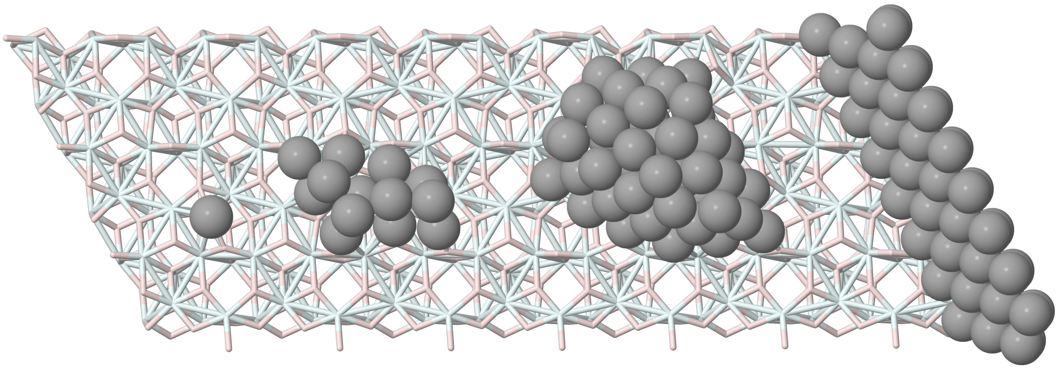

FIGURE 2 Examples of Pt/ZrO_2 catalyst models. From left to right: single Pt atom, Pt_{13} cluster, Pt_{43} cluster, Pt(111) facet representing the edge of a large nanoparticle. The small clusters are global minimum structures,[44] while the (111) facet is a schematic representation.

to isomerization is known as fluxionality.[46] Although large nanoparticles also exhibit structural variation and dynamics, their more bulklike character makes these phenomena less impactful.

In real catalysts, many nanoparticles of different sizes can be present depending on the catalyst preparation and reaction conditions. The size distribution is not static, as small metal particles tend to form larger ones by coalescence or Ostwald ripening.[24,47] This sintering is usually an undesirable process, as it decreases the number of active metal or metal–oxide interface sites. The separation of particles can be improved by, e.g., improving the uniformity of the particle size distribution or altering the support such that it strongly anchors the particles.[47,48] The latter can be achieved by choosing a support material that strongly interacts with the metal and/or structuring the support by, e.g., introducing oxide vacancies that can anchor the metal particles.[49]

1.2.3 Acidic modifiers

An alternative avenue to introduce oxide functionality to metal catalysts is to add oxophilic metal modifiers, which can form various catalytically active MO_x species depending on the materials and conditions.[50] Typical examples include MoO_x-, WO_x- and ReO_x-modified Rh, Pt and Ir catalysts, which exhibit C–O hydrogenolysis activity and have been studied for biomass valorization.[50,51] The noble metal provides the necessary ability for hydrogen activation, while the MO_x species assists in the C–O bond cleavage.[23,50] Two possible roles have been proposed for the MO_x components: they can bind the reactants in a manner that favors deoxygenation, or form Brønsted acidic MO_xH_y sites that can remove oxygen by acid-catalyzed dehydration.[23] The Brønsted acidity has been computationally found to be modulated by the identity of the noble metal and the geometry of the acid site.[51]

A typical reaction catalyzed by such materials is the hydrodeoxygenation of glycerol.[50] Glycerol is produced in large quantities as a byproduct of biodiesel synthesis, and is therefore available as a cheap feedstock for valorization processes.[52,53] Some of the main targets are the 1,2- and 1,3-propanediols (PDOs) that are used, for instance, as building blocks in the polymer industry.[52,53] Selectivity is a major issue, especially toward the more desirable 1,3-diol, but including acidic functionality in the catalyst has been found to increase the production of 1,3-PDO.[50,53,54] A Brønsted acid catalyst could favor removal of the secondary OH over the primary one due to the higher stability of the resulting secondary carbocation, although the secondary OH is more sterically hindered and its removal is thermodynamically less favorable.[52,53]

In addition to the oxophilic metals discussed above, sulfated zirconia, heteropolyacids and zeolites have also been studied as 1,3-PDO selectivity promoters.[54] On SO_4/ZrO_2, the adsorbed sulfate has been proposed to enhance the Lewis acidity of existing Zr^{4+} cation sites and provide some Brønsted acid functionality, but the nature of the active acid site(s) is generally not fully understood.[55,56] Heteropolyacids such as phosphotungstic acid are stable, nontoxic and very strong Brønsted acids, and can therefore provide highly acidic functionality while being environmentally friendly.[57] Finally, zeolites are porous aluminosilicates that are extensively utilized in catalysis for their acidic and structural properties.[2] Zeolites can exhibit both Lewis and Brønsted acidic sites, and the acid properties are also utilized in, e.g., the catalytic cracking of hydrocarbons.[58] The pores can act as molecular sieves, allowing only certain sizes of molecules to pass through the structure, potentially excluding undesirable substrates from the active sites.[2] Zeolites can be combined with metal nanoparticles, forming another type of metal–oxide catalyst.[59] The porous zeolite can encapsulate the nanoparticles, reducing sintering and leaching, and possibly creating metal–acid bifunctionality via the close contact between the metal and zeolite acid sites.[59,60]

2 THEORY, METHODS AND MODELS

2.1 Density functional theory

2.1.1 Brief theoretical background

In the traditional Hartree–Fock approach, electrons are considered in terms of their wavefunctions. While useful, this approach has the issue of requiring 3 coordinates for every electron. In density functional theory (DFT), the problem is simplified by disregarding the wavefunctions and instead considering electron density as the central variable of interest. In this way, it is possible to describe all of the electrons using only three coordinates in total. This approach is well justified by the famous Hohenberg–Kohn theorems,[61] which state that (1.) a ground-state density uniquely determines an external potential, and (2.) the ground-state density obeys the variational principle, meaning that the energy of any candidate density is always greater than equal to the correct ground state energy.

The DFT energy expression is

$$E = T[\rho] + V[\rho] + E_{\mathrm{xc}}[\rho], \tag{1}$$

where T is the kinetic energy functional of the non-interacting electrons, V includes the classical contributions to the potential energy, and E_{xc} (the exchange–correlation functional) contains corrections to the kinetic energy due to electron–electron interaction and all nonclassical components of the potential energy. The T and V terms can be computed exactly, and make up most ($\sim$ 95 %) of the total energy. However, the remaining 5 % is large enough to encompass the chemically relevant energy scale, meaning that E_{xc} must also be determined with good accuracy. Unfortunately, the exact form of E_{xc} is unknown, and approximations must be applied.

Typical approximations include the local density approximation (LDA),[62] which relies on the properties of homogeneous electron gas, the generalized gradient approximation (GGA),[63] which incorporates the gradient of the density, and hybrid functionals,[64] which include some fraction of exact exchange. Under the LDA, the xc energy is computed as

$$E_{\mathrm{xc}}^{\mathrm{LDA}}[\rho] = \int \rho(\vec{r})\epsilon_{\mathrm{xc}}(\rho(\vec{r}))\mathrm{d}^3\vec{r}, \tag{2}$$

where $\epsilon_{\mathrm{xc}}(\rho(\vec{r}))$ is the xc energy of a homogeneous electron gas of density ρ. The local nature of the approximation is apparent from Eq. (2), as the value of the integrand at a given $\vec{r}$ only depends on $\rho(\vec{r})$, i.e., the local density. The general form of a GGA functional is

$$E_{\mathrm{xc}}^{\mathrm{GGA}}[\rho] = \int \rho(\vec{r})\epsilon_{\mathrm{xc}}(\rho(\vec{r}), \nabla\rho(\vec{r}))\mathrm{d}^3\vec{r}, \tag{3}$$

where the gradient of the density has been introduced. Unlike in the LDA, where ϵ_{xc} is generally taken from the homogeneous electron gas, various approximations are used for the GGA ϵ_{xc}; commonly used ones include PBE,[65,66] PW91[67] and BLYP.[68,69] Both the LDA and GGA can be generalized to treat spins by replacing the total density ρ with the spin densities $\rho_\uparrow$ and $\rho_\downarrow$. Finally,

$$E_{\mathrm{xc}}^{\mathrm{hyb}} = aE_{\mathrm{x}}^{\mathrm{exact}} + (1-a)E_{\mathrm{x}}^{\mathrm{GGA}} + E_{\mathrm{c}}^{\mathrm{GGA}} \tag{4}$$

is a simple example of a hybrid functional, in which a fraction a of exact exchange is mixed into a GGA functional.[70]

While LDA and GGA have been successfully applied for a broad range of systems, they have their limitations: for instance, they fail to describe dispersion forces and predict band gaps that are too narrow (or nonexistent).[70] Various correction schemes have been developed to improve the results, some of which will be discussed in the following sections.

Once a suitable approximation for E_{xc} has been chosen, the density can be found through an iterative self-consistent field (SCF) method. In this method, after an initial density guess has been constructed, the Kohn–Sham secular equation

$$\left[-\frac{\nabla^2}{2} + v_{\mathrm{KS}}[\rho](\vec{r})\right]\phi_i(\vec{r}) = \epsilon_i\phi_i(\vec{r}) \tag{5}$$

is constructed and solved for it.[62,70] A new density matrix is built from the solutions, and the process continues iteratively until the density no longer changes in the process, i.e., becomes self-consistent.

All surface systems studied in this thesis are periodic in at least two dimensions. When studying such systems, Bloch's theorem can be applied to reduce the problem into the primitive cell of the reciprocal lattice, i.e., the first Brillouin zone.[71] As the lattice-periodic part of the wavefunctions typically only weakly depends on the crystal momentum $\vec{k}$, the calculation may be simplified by only sampling the first Brillouin zone at some, often fairly small set of k points. For small real-space cells, the reciprocal cell is large, requiring many k points to describe accurately; likewise, metallic systems require more k points than semiconducting or insulating ones, due to the presence of partially occupied bands. In papers I–III, the studied M/ZrO$_2$ models are large and semiconducting, only needing 1 k point to describe; in paper IV, a $2 \times 2 \times 1$ Monkhorst–Pack mesh[72] was utilized for the metallic Rh systems.

In this work, all DFT calculations were carried out within the PAW formalism[73] introduced in the next section, using the GPAW[74,75] code with the ASE[76] interface. The PBE exchange-correlation functional[65,66] was used throughout the work, supplemented by the Hubbard correction (discussed in Section 2.1.3) in paper III and the Tkatchenko–Scheffler correction (Section 2.1.4) in papers II and IV. For further computational details, see the included publications.

2.1.2 The projector augmented-wave method

Treating the full KS wavefunctions computationally is challenging, as they exhibit large oscillations near the atomic cores due to the orthogonality condition. Describing this behavior accurately requires a cumbersome representation for the wavefunctions, such as a large plane-wave basis set or a dense real-space grid. To facilitate the practical treatment of larger systems, the wave functions of the core electrons are typically simplified in some way. One possibility is to describe the nuclei and core electrons of each atom with smooth, tabulated pseudopotentials, solving the KS equations only for the valence wavefunctions.[77,78] Another avenue is to partition space into near-nucleus regions (augmentation spheres) and a bonding region, using different wavefunctions in each region. This is the idea behind the augmented plane wave method (APW)[79,80] and the projector augmented-wave method (PAW).[73,81] The calculations discussed in this dissertation were carried out in the PAW formalism, which this section will introduce.

Instead of dealing with the true KS wavefunctions $|\psi\rangle$, let us consider pseudo wavefunctions $|\tilde{\psi}\rangle$ related to the KS wavefunctions via a linear transformation $\hat{T}$:

$$|\psi_n\rangle = \hat{T} |\tilde{\psi}_n\rangle . \tag{6}$$

Using this transformation, the KS equations

$$\hat{H} |\psi_n\rangle = \epsilon_n |\psi_n\rangle \tag{7}$$

become

$$\hat{T}^\dagger \hat{H} \hat{T} |\psi_n\rangle = \epsilon_n \hat{T}^\dagger \hat{T} |\psi_n\rangle . \tag{8}$$

In order for this transformation to be useful, the pseudo wavefunctions $|\tilde{\psi}_n\rangle$ should be smooth. As the KS wavefunctions $|\psi_n\rangle$ are already smooth in the bonding region, it is sufficient to only modify the wavefunctions in the regions near the nuclei. This can be accomplished by writing

$$\hat{T} = 1 + \sum_a \hat{T}^a, \tag{9}$$

where $\hat{T}^a$ are atom-centered transformations that only have an effect within a certain distance of the corresponding nuclei a, i.e., inside the (non-overlapping) augmentation spheres. Within the spheres, the wavefunctions can now be expanded in partial waves ϕ_i^a, for which corresponding smooth pseudo partial waves $\tilde{\phi}_i^a$ are chosen. The transformation $\hat{T}$ can now be defined by requiring

$$\phi_i^a = \hat{T}\tilde{\phi}_i^a = (1 + \hat{T}^a)\tilde{\phi}_i^a \quad \forall i, a. \tag{10}$$

If the pseudo partial waves $\tilde{\phi}_i^a$ form a complete basis, the pseudo wavefunctions can be expanded within the augmentation spheres as

$$|\tilde{\psi}_n\rangle = \sum_i P_{ni}^a \, |\tilde{\phi}_i^a\rangle, \tag{11}$$

where P_{ni} are unknown expansion coefficients. The same coefficients describe the expansion of the KS wavefunctions, as

$$|\psi_n\rangle = \hat{T}\,|\tilde{\psi}_n\rangle = \hat{T}\sum_i P_{ni}^a \,|\tilde{\phi}_i^a\rangle = \sum_i P_{ni}^a \hat{T}\,|\tilde{\phi}_i^a\rangle = \sum_i P_{ni}^a \,|\phi_i^a\rangle \tag{12}$$

by the linearity of $\hat{T}$ and Eq. (10). The linearity of $\hat{T}$ further implies that the expansion coefficients

$$P_{ni}^a = \langle \tilde{p}_i^a | \tilde{\psi}_n \rangle\,, \tag{13}$$

where $|\tilde{p}_i^a\rangle$ are a set of *smooth projector functions*. As the augmentation spheres do not overlap, the pseudo wavefunction $|\tilde{\psi}_n\rangle$ and its one center expansion around nucleus a, $|\tilde{\psi}_n^a\rangle$, should be equal inside each augmentation sphere defined by a:

$$|\tilde{\psi}_n^a\rangle = \sum_i |\tilde{\phi}_i^a\rangle\,\langle \tilde{p}_i^a | \tilde{\psi}_n\rangle = |\tilde{\psi}_n\rangle \implies \sum_i |\tilde{\phi}_i^a\rangle\,\langle \tilde{p}_i^a| = 1. \tag{14}$$

Outside the augmentation spheres, the projectors can be set to 0.

From the previous result, it follows that

$$\hat{T}^a = \sum_i \hat{T}^a\,|\tilde{\phi}_i^a\rangle\,\langle \tilde{p}_i^a| = \sum_i \left(|\phi_i^a\rangle - |\tilde{\phi}_i^a\rangle\right)\langle \tilde{p}_i^a|, \tag{15}$$

which can be inserted into Eq. (9):

$$\hat{T} = 1 + \sum_a \sum_i \left(|\phi_i^a\rangle - |\tilde{\phi}_i^a\rangle\right)\langle \tilde{p}_i^a|. \tag{16}$$

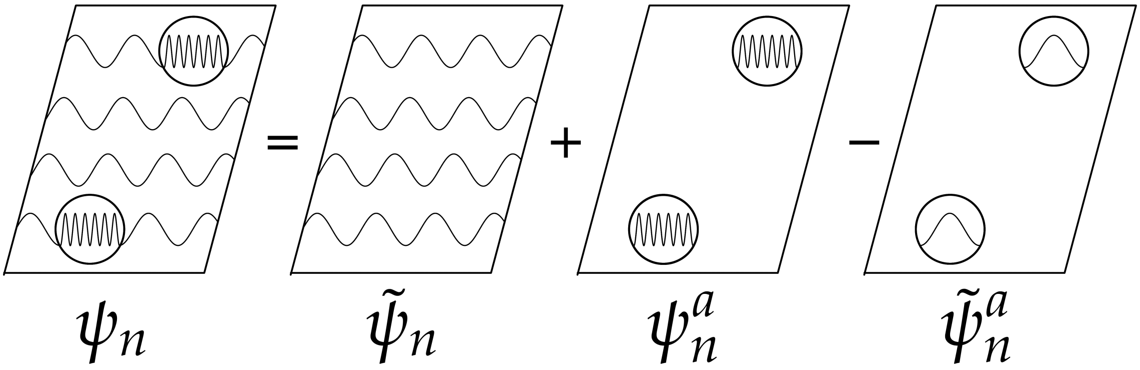

FIGURE 3 Schematic representation of the PAW decomposition of the true KS wavefunction ψ_n into the smooth pseudo wavefunction $\tilde{\psi}_n$ and the one-center expansions ψ_n^a and $\tilde{\psi}_n^a$. The two circles correspond to augmentation spheres.

Finally, the true KS wavefunction can be written as

$$|\psi_n\rangle = |\tilde{\psi}_n\rangle + \sum_a \sum_i \left(|\phi_i^a\rangle - |\tilde{\phi}_i^a\rangle\right) \langle \tilde{p}_i^a | \tilde{\psi}_n \rangle \tag{17}$$

$$= \tilde{\psi}_n(\vec{r}) + \sum_a \left(\psi_n^a(\vec{r} - \vec{R}^a) - \tilde{\psi}_n^a(\vec{r} - \vec{R}^a) \right), \tag{18}$$

where

$$\psi_n^a(\vec{r}) = \sum_i \phi_i^a(\vec{r}) \langle \tilde{p}_i^a | \tilde{\psi}_n \rangle \tag{19}$$

$$\tilde{\psi}_n^a(\vec{r}) = \sum_i \tilde{\phi}_i^a(\vec{r}) \langle \tilde{p}_i^a | \tilde{\psi}_n \rangle. \tag{20}$$

Now, the troublesome oscillations have been separated into the partial wave components ψ_n^a, which can be handled separately from the otherwise smooth (auxiliary) wavefunctions (Figure 3).

2.1.3 The Hubbard correction

Typical exchange-correlation functionals in the LDA and GGA families have a tendency to overdelocalize electrons.[82] This tendency arises from an inaccurate description of electron correlation, along with self-interaction error, which causes electrons to interact with themselves.[83] This spurious delocalization is particularly troublesome for the d and f orbitals of transition metals, which are strongly correlated and thus more prone to such inaccuracies.[84] An archetypal example of a qualitative error arising from overdelocalization is the case of Mott or charge-transfer insulators (e.g. FeO), which are mistakenly described as metallic by some functionals.[85]

While a hybrid functional would help correct for the electron correlation error, the computational cost of hybrids remains relatively high. For this reason, the Hubbard correction[84,85] has become a popular choice to address the issue of overdelocalization, though it does not always produce results in agreement with hybrid functionals.[86,87] The correction is straightforward to implement and has a negligible computational cost, allowing it to find use even in wide screening studies where computational efficiency must be highly prioritized.[88,89] While the Hubbard correction is not without its flaws, it can, for many purposes, produce a sufficiently accurate representation of the electronic structure. The correction was used in paper III to improve the description of the correlated electrons in ZrO_2.

The Hubbard correction in DFT arises from the Hubbard Hamiltonian

$$\hat{H}_{\text{Hub}} = t \sum_{\langle i,j \rangle,\sigma} (c^{\dagger}_{i,\sigma} c_{j,\sigma} + h.c.) + U \sum_i n_{i,\uparrow} n_{i,\downarrow}, \tag{21}$$

where $\langle i,j \rangle$ are the nearest-neighbor atomic sites, $c^{\dagger}_{i,\sigma}$, $c_{j,\sigma}$ and $n_{i,\sigma}$ are the electronic creation, annihilation and number operators for electrons of spin σ on site i, t is the hopping amplitude and U is the Coulomb repulsion between electrons on the same site; this last term is what is commonly referred to as the "Hubbard U". The idea behind the Hubbard correction is to describe the strongly correlated states in the system with the Hubbard Hamiltonian, which allows one to modify the on-site electron–electron interactions by adjusting the value of U.

In current computational codes, the rotationally invariant Dudarev formulation is typically implemented.[90] In this formulation, the Hubbard energy correction is computed as

$$E_U = \sum_a \frac{U}{2} \operatorname{Tr} (\rho^a - \rho^a \rho^a), \tag{22}$$

where U is taken as an "effective" U parameter corresponding to $U - J$ in the traditional notation, and ρ^a is the atomic orbital occupation matrix (AOOM) corresponding to the l states on atom a. From this equation, it can be seen how the Hubbard correction discourages fractional occupations: when the occupations are integral (i.e., each eigenvalue n_i of ρ^a is 0 or 1), the AOOM is idempotent ($\rho^a = \rho^{a2}$) and the correction vanishes.[91] Otherwise, evaluating the trace as the sum of eigenvalues $n_i \in [0,1]$, the energy correction is positive and scales linearly with U:

$$E^a_U = \frac{U}{2} \operatorname{Tr} (\rho^a - \rho^a \rho^a) = \frac{U}{2} \left(\sum_i n_i - \sum_i n_i^2 \right) > 0. \tag{23}$$

To appreciate the effect of the correction on the potential and band structure, it is also illustrative to consider the one-electron potential correction

$$V^a_U = \frac{\delta E^a_U}{\delta \rho^a_{ij}} = U \left(\frac{1}{2} \delta_{ij} - \rho^a_{ij} \right). \tag{24}$$

The energies of localized, filled orbitals are lowered by $-U/2$, while the energies of empty orbitals are correspondingly raised by $+U/2$, also reflecting the favorability of integer occupation.[91] The correction therefore introduces a potential discontinuity of magnitude U on the localized states. This discontinuity can,

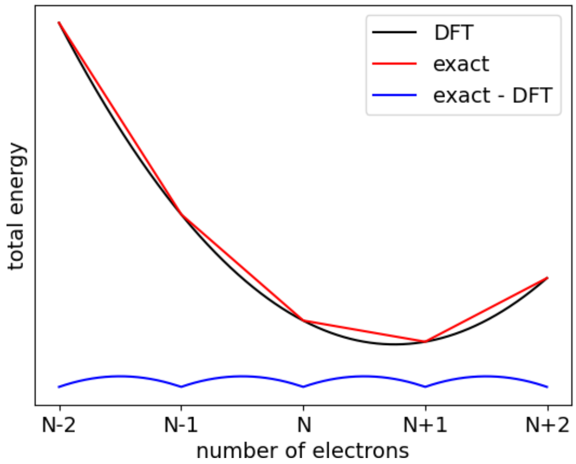

FIGURE 4 Schematic plot of the exact piecewise linear energy and the approximate DFT energy (drawn as parabolic).[84] The necessary correction (blue curve) is zero at integer occupations and piecewise parabolic, resembling the Hubbard correction in Eq. (22).

to some extent, recover the xc potential discontinuity of the exact DFT functional that is missing from most approximate functionals.[84,92] This feature also leads to the widening of the band gap typically associated with the Hubbard correction.[84]

The potential discontinuity corresponds to the derivative discontinuity in the exact Kohn–Sham energy as a function of electron number (Figure 4).[93] As typical DFT functionals do not reproduce the potential discontinuity, they predict a smooth energy variation instead of a piecewise linear relationship. If the spurious curvature corresponds to a constant second derivative $\mathrm{d}^2E/\mathrm{d}n^2$, the correction required to recover the piecewise linear relationship is piecewise parabolic with second derivative $-\mathrm{d}^2E/\mathrm{d}n^2$. From Eq. (22), such a correction is attained when $U = \mathrm{d}^2E/\mathrm{d}n^2$. While the situation is more complicated for realistic calculations, this correspondence provides a possible method to determine U from first principles, which will be discussed in section 2.1.3.1.

In practical terms, the occupation matrix ρ^a in GPAW is calculated using the atom-projected density matrix

$$D^a_{i_1 i_2} = \sum_n f_n P^{a*}_{ni_1} P^a_{ni_2} = \sum_n f_n \langle \tilde{\psi}_n | \tilde{p}^a_{i_1} \rangle \langle \tilde{p}^a_{i_2} | \tilde{\psi}_n \rangle, \tag{25}$$

where f_n are the occupation numbers, while the other terms have been defined in Section 2.1.2.[81] The atom-projected density matrix can further be projected onto the valence orbitals with the desired orbital quantum number l:

$$\rho^a_{mm'} = \sum_{n,n'} D^a_{nlm,n'lm'} \langle \phi^a_{nlm} | \phi^a_{n'lm'} \rangle, \tag{26}$$

where $n = 1$ is the bound state projector and $n = 2$ is the unbound state projector.

The integration in $\langle \phi^a_{nlm} | \phi^a_{n'lm'} \rangle$ is truncated at the augmentation sphere radius, resulting in a projection that is always less than 1. The Hubbard correction is most commonly applied for d and f orbitals, which are usually compact enough to mostly fit inside the augmentation spheres; however, this is not the case for the more diffuse s and p orbitals. For these orbitals, the truncation can considerably lower the orbital-projected density (i.e., occupation number). In GPAW, each orbital-projected density is, by default, normalized to the integral of the atomic orbital within the augmentation sphere:

$$\rho^a_{mm'} = \sum_{n,n'} D^a_{nlm,n'lm'} \frac{\langle \phi^a_{nlm} | \phi^a_{n'lm'} \rangle}{\langle \phi^a_{1lm} | \phi^a_{1lm'} \rangle}. \tag{27}$$

This choice has been demonstrated to better reproduce the expected p splitting in atomic nitrogen,[94] and has been consistently applied throughout this work.

The Hubbard U is essentially a free parameter, for which a good value must somehow be found. One popular method is to calculate some property (or properties) of the system for varying values of U, and choose the one that produces the closest agreement to a known reference.[95] Typical reference quantities include bandgaps and geometric parameters. While this "empirical fitting" approach can be viable, it has certain limitations. There is no guarantee that a U value optimized for one quantity provides good results for other properties of the system;[95] for instance, reproducing an experimental bandgap can require a fairly high U, which can have an undesirable impact on other properties of the system. Furthermore, sometimes good reference data is simply not available.

Although the value of the U parameter tends to receive most of the attention, the choice of orbitals to correct and the projectors used for them can also be considered adjustable parameters of the model. While the TM d or f orbitals are typically most in need of correction, it can be beneficial to also employ the correction for, e.g., oxygen p orbitals.[96] This is a modeling choice as much as the value of U, though it is often scantly addressed. Likewise, the projectors are usually atomic orbital functions taken directly from the pseudopotential/PAW setup, which may not be the best choice: depending on the chemical environment, the orbitals may have a very different shape.[97] At minimum, the values of U should be derived in accordance with the chosen orbitals to maintain consistency; to get the best results, the choice of orbitals and projectors can also be optimized.

Occasionally, the use of U values found in the literature is reported. This is a problematic practice, as the effect of the Hubbard correction depends on the details of the calculation. In particular, the set of localized orbital functions (Hubbard projectors) used to compute the occupations of the corrected states (Eq. (22)) is not unique, and affects the behavior of the correction.[97,98] This can practically manifest as a dependence on the chosen pseudopotential/PAW setup. Even technical details like the normalization procedure in Eq. (27) can alter the behavior. In addition to the projectors, the correction also depends on the chemical environment of the Hubbard states, and is therefore system-dependent.[99,100] Thus, U values are not transferable between computational implementations, and should ideally be derived using the same methods and systems as the production simulations.

It is possible to avoid many of the aforementioned issues by calculating the value of U ab initio using the computational setup intended for the production calculations. This way, the parameter comes with a clear justification, and can be found in an equivalent manner for any system. Various methods to accomplish this have been proposed, with the easy-to-implement linear response method[101,102] being one of the most popular. This method was implemented in GPAW and used to compute an ab initio U for the Zr d electrons in paper III. Recently, a constrained DFT variant has been reported as a more robust alternative,[103] and machine learning has also been applied to tackle the problem.[104]

2.1.3.1 Linear response method

As discussed above, the ideal value to recover the piecewise linear behavior of energy versus occupation would be $U = \mathrm{d}^2E/\mathrm{d}n^2$. In principle, the required curvature could be computed by evaluating

$$E[\{q_I\}] = \min_{\rho,\{\alpha_I\}} \{E[\rho] - \sum_I \alpha_I (n_I - q_I)\} \tag{28}$$

for various site occupations q_I, with α_I as Lagrange multipliers:[101,105]

$$\alpha_I = -\frac{\mathrm{d}E[\{q_I\}]}{\mathrm{d}q_I}. \tag{29}$$

However, manually modifying the occupations is typically not an easy task, so it is useful to instead consider the Legendre transformed representation

$$E[\{\alpha_I\}] = \min_{\rho} \{E[\rho] - \sum_I \alpha_I n_I\}, \tag{30}$$

where the energy shifts α_I are the independent variables. Now the curvature can instead be computed from

$$\frac{\mathrm{d}^2E}{\mathrm{d}n_I^2} = \frac{\mathrm{d}\alpha_I}{\mathrm{d}n_I} = \left(\frac{\mathrm{d}n_I}{\mathrm{d}\alpha_I}\right)^{-1} =: \chi_I, \tag{31}$$

which can be found by measuring the linear responses of the Hubbard orbital occupations n_I to small orbital energy perturbations α_I.[101,105] Plotting the occupations against a few different α_I values typically produces a line with a downward slope, and this slope χ_I is the eponymous linear response.

To compute U, two separate kinds of linear responses are considered: the "bare response" χ_0, which is measured immediately after the first SCF iteration for the perturbed system, and the "self-consistent response" χ, which is measured after SCF convergence.[101] This is because χ_0 corresponds to the rehybridization of

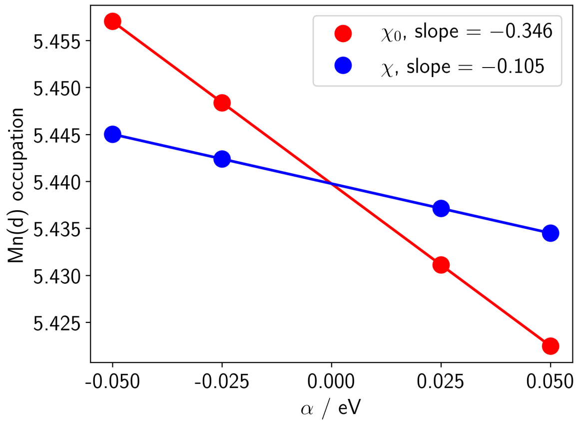

FIGURE 5 Bare (χ_0) and self-consistent (χ) occupations for Mn d orbitals in a MnO dimer when the orbital energies are perturbed by α.

the wavefunctions in response to the perturbation, which is not related to the electron-electron interactions, and must be subtracted out. For a single type of orbital, the Hubbard U is then computed simply as

$$U = \chi_0^{-1} - \chi^{-1}. \tag{32}$$

Usually both responses are negative (increasing occupation with lowering energy) and the bare response is more negative than the self-consistent response, resulting in a positive U, as expected. If the responses are very small, numerical noise in the inverted responses can make the results unreliable.[96]

When multiple Hubbard orbitals are considered, the responses are collected into response matrices, where $\chi_{IJ} = \mathrm{d}n_I/\mathrm{d}\alpha_J$ corresponds to the response of orbital I occupation to the perturbation of orbital J. In this case, the U values are found as the diagonal elements of the matrix:

$$U_I = (\chi_0^{-1} - \chi^{-1})_{II}. \tag{33}$$

With the matrix formulation, it is possible to apply a so-called "background correction" to speed up the convergence with regard to supercell size.[101] This is achieved by simply adding an extra row and column to the response matrices such that each row and column sums to zero. Such matrices are singular by construction, but this can be circumvented by adding a small number to each element of the matrix, which makes it invertible without affecting the final results.[105] Finally, it is worth noting that the off-diagonal elements of the matrix directly provide the so-called V parameters, which can be used to extend the Hubbard correction for intersite interactions.[106]

As a simple example inspired by Ref. 107, Figure 5 shows the bare and self-consistent responses for Mn d orbitals in a MnO dimer. As expected, both response slopes are negative and the bare response is stronger than the self-consistent one. The linear response U for Mn d orbitals can be computed from the slopes according to Eq. 32:

$$U = \chi_0^{-1} - \chi^{-1} = (-0.346\ \mathrm{eV}^{-1})^{-1} - (-0.105\ \mathrm{eV}^{-1})^{-1} = 6.63\ \mathrm{eV}. \tag{34}$$

2.1.4 Tkatchenko–Scheffler correction

To describe the long-distance dispersion interaction, the Tkatchenko–Scheffler (TS) correction was utilized in papers II and IV.[108–110] The method is nonempirical, fast and quite accurate for many systems, though some limitations have also been noted on, e.g., strongly ionic surfaces.[111] In the TS scheme, the R^{-6} dependence that is not captured by local xc functionals is explicitly added onto the DFT energy by the pairwise interatomic term

$$-\frac{1}{2}\sum_{A,B} f_{\mathrm{damp}}(R_{AB}, R_A^0, R_B^0)C_{6AB}R_{AB}^{-6}, \tag{35}$$

where f_{damp} is a short-range damping function, C_{6AB} and R_{AB} are the C_6 coefficient and distance between atoms A and B, and R_A^0 and R_B^0 are the vdW radii. The C_6 coefficient is derived from atomic polarizabilities and describes the asymptotic magnitude of the vdW energy. The damping function eliminates the correction at short range, where the R_{AB}^{-6} factor becomes singular.

In the TS method, C_6 parameters obtained from TDDFT-based atomic polarizabilities for free atoms[109] are refined by considering the effective volume of the atom in a molecule or a solid:

$$C_{6AA}^{\mathrm{eff}} = \frac{\eta_A^{\mathrm{eff}}}{\eta_A^{\mathrm{free}}}\left(\frac{\kappa_A^{\mathrm{free}}}{\kappa_A^{\mathrm{eff}}}\right)^2\left(\frac{V_A^{\mathrm{eff}}}{V_A^{\mathrm{free}}}\right)^2 C_{6AA}^{\mathrm{free}}, \tag{36}$$

where η are effective frequencies, κ are proportionality constants between volume and polarizability and V are volumes from the Hirshfeld partitioning[112] of the electron density:

$$\frac{V_A^{\mathrm{eff}}}{V_A^{\mathrm{free}}} = \frac{\int r^3 w_A(\vec{r})n(\vec{r})\mathrm{d}^3\vec{r}}{\int r^3 n_A^{\mathrm{free}}(\vec{r})\mathrm{d}^3\vec{r}}, \tag{37}$$

where r is the distance to the nucleus of atom A,

$$w_A(\vec{r}) = \frac{n_A^{\mathrm{free}}(\vec{r})}{\sum_B n_B^{\mathrm{free}}(\vec{r})} \tag{38}$$

is the Hirshfeld weight of atom A, $n(\vec{r})$ is the total electron density and $n_{\mathrm{free}}(\vec{r})$ are electron densities of free atoms. The $\frac{\eta_A^{\mathrm{eff}}}{\eta_A^{\mathrm{free}}}\left(\frac{\kappa_A^{\mathrm{free}}}{\kappa_A^{\mathrm{eff}}}\right)^2$ factor is assumed to be unity, reducing the scaling coefficient to a Hirshfeld volume ratio that can be efficiently computed from the DFT density.

The vdW radii for the damping function are likewise scaled from free-atom values according to

$$R_{\mathrm{eff}}^0 = \left(\frac{V^{\mathrm{eff}}}{V^{\mathrm{free}}}\right)^{1/3} R_{\mathrm{free}}^0. \tag{39}$$

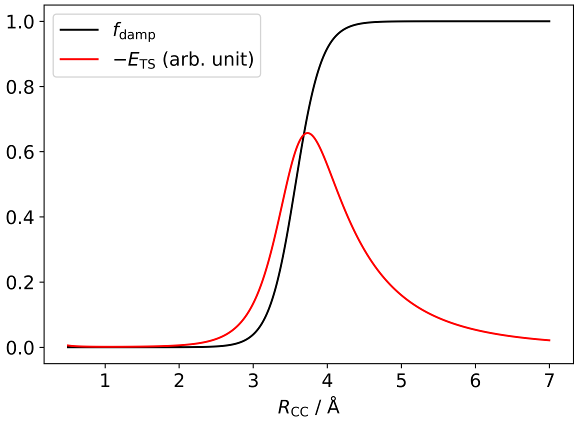

FIGURE 6 Damping function and TS correction for a C–C bond with $d = 20$, $s_R = 0.94$, $R^0_{CC} = 3.80$ Å. The TS correction is shown as negative and scaled for clarity.

The free-atom radius of each atom is set such that the electron density at distance R^0_{free} from the nucleus matches the density at the vdW radius of the noble gas atom in the same period.[113] Finally, the damping function is defined as

$$f_{\text{damp}}(R_{AB}, R^0_{AB}) = \frac{1}{1 + \exp[-d(\frac{R_{AB}}{s_R R^0_{AB}} - 1)]}, \tag{40}$$

where d and s_R determine the steepness and onset of the damping function. For d, a value of 20 has been found to give good results, while s_R is defined individually for each xc functional based on high-quality reference calculations. The damping function and shape of the TS correction are shown in Figure 6, highlighting the shape of the energy correction: small at the length scale of a chemical bond, large around the sum of the vdW radii.

In the context of surface calculations, the major effect of the TS correction is to stabilize the adsorbed species. Due to the damping function, the direct (chemisorbed) surface-adsorbate bonds are largely unaffected, but the weakly interacting "tail" of the adsorbate is brought closer to the surface. This tends to increase the favorability of flat-lying geometries, which can benefit most from the additional R^{-6} energy term. The effect is most apparent for large adsorbates, which can have a lot of atoms at a suitable vdW interaction distance from the surface.

2.1.5 Bader charge analysis

Bader charge analysis[114] was utilized in paper III to evaluate the localization and transfer of charge. The charges were computed with the algorithm due to Henkelman's group.[115–118] In the Bader method, the studied system is partitioned along so-called zero flux surfaces, i.e., surfaces on which the gradient of the electron density vanishes in the normal direction. This provides a purely electron density based method of partitioning a chemical system into components that typically correspond to individual atoms in a useful way. The Bader charge of an atom is then calculated by integrating the electron density over the corresponding region of space.

2.1.6 Charged slab calculations

In paper III, we ran charged slab simulations to compute redox energies. Charged systems with periodic boundary conditions are well known to be challenging with regard to their energetics; even when complete divergence is avoided by means of, e.g., compensating background charges, the energies of systems in different charge states are generally not on an even footing without additional corrections. Furthermore, the charged part of the system can interact with its periodic images, which is undesirable if one wishes to study an isolated charge.

This issue has most widely been studied in the context of charged bulk defects, where the system is periodic in three dimensions. For such systems, many corrections have been proposed, such as the Makov–Payne,[119] Lany–Zunger[120,121] and FNV[122] schemes. To get good energetics for defect formation, the energies must be corrected properly; the position of the associated defect level may also be adjusted to better match experiment.[123] In addition to traditional charged defects, periodic charged system calculations are used to determine deprotonation energies in solid acids such as zeolites, in which context the issue of energetics has also been discussed.[124]

The bulk methods are not directly applicable to two-dimensional systems, such as charged slabs, where the differing boundary conditions and presence of vacuum cause additional complications. Methods have been developed to deal with these,[125,126] but they can be tricky to utilize, requiring a good understanding of the electrostatics in the system. In particular, the image charge correction accounting for the interaction of the defect with its periodic images is nontrivial to realize due to the properties of the system. The potential alignment correction is simpler to compute, only needing the electrostatic potential maps from the neutral and charged systems.

In general, the potential alignment and image charge corrections should be included simultaneously to avoid errors.[120] In paper III, however, the image charge interaction was expected to be close to equal for the studied systems, and therefore unlikely to affect the trends of interest. Thus, only the potential alignment correction was applied according to

$$\Delta E = q(V_{\text{charged}} - V_{\text{pristine}}), \tag{41}$$

where q is the added charge and V are the potentials at an equivalent reference

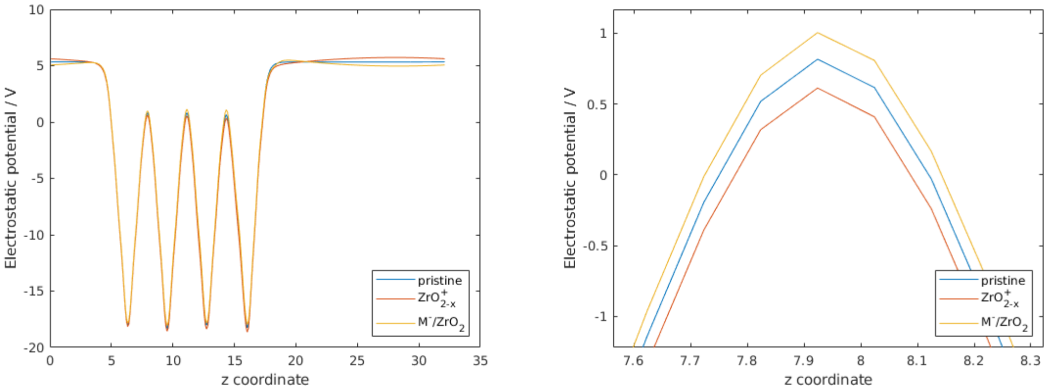

FIGURE 7 Left: planarly averaged electrostatic potentials from charged and neutral ZrO_2 slabs. Right: the same plot zoomed at the reference point (center plane of slab).

plane in the charged and neutral systems (Figure 7).

2.1.7 Hybridization analysis

In paper III, we employed a hybridization analysis method from Ref. 127 to help discuss the role of hybridization in metal–surface bonding. In this method, an index for the hybridization between the k and l orbitals of atoms I and J is computed as

$$H_{kl}^{IJ} = \sum_{i=1}^{N_e} \sum_{m,m'} w_{km,i}^{I} w_{lm',i'}^{J} \tag{42}$$

where m and m' are the magnetic quantum numbers corresponding to the angular quantum numbers k and l, and i runs over all N_e occupied bands. The $w_{km,i}^{I}$ terms are weight parameters representing the projections of the atomic orbitals ϕ_{km}^{I} to the DFT bands ψ_i; in practice, the weight was approximated using the PAW pseudoprojectors $\tilde{p}_{km}^{I}$:

$$w_{km,i}^{I} = \langle \phi_{km}^{I} | \psi_i \rangle \approx \langle \tilde{p}_{km}^{I} | \psi_i \rangle. \tag{43}$$

The index was applied for both intra- ($I \neq J$) and interatomic ($I = J$) hybridization using ASE/GPAW. In the intra-atomic case, the index sometimes indicates nonzero hybridization even when the atoms are too distant for their orbitals to realistically hybridize; this is due to highly delocalized bands ψ_i overlapping slightly with both ϕ_{km}^{I} and $\phi_{lm'}^{J}$ orbitals without really describing hybridization between them. This spurious contribution was minimized by only summing over bands with some minimum weight (typically $w > 0.1$) for one orbital of interest.

2.2 Nudged elastic band method

In order to compute the rates of chemical reactions with DFT, the shape of the relevant portion of the potential energy surface (PES) must be estimated. A typical way to do this is to locate the minimum energy path (MEP) between the initial and final states. On the MEP between two minima of the PES, the force on the atoms is parallel to the path, possible additional minima correspond to stable intermediates, and maxima are saddle points of the PES corresponding to transition states (TS). Once the MEP is known, the activation energy of a reaction can be computed as

$$E_{\mathrm{act}} = E_{\mathrm{TS}} - E_{\mathrm{init}}. \tag{44}$$

The difficulty of locating the MEP and corresponding TSs depends on the shape of the PES in the vicinity of the reaction path. For simple reactions, a constrained optimization algorithm can be sufficient to produce good transition states. In constrained optimization, the rest of the system is allowed to relax while a suitable coordinate (e.g., the length of a breaking bond) is fixed at different values to produce an approximate MEP. The energy maximum of the path corresponds to a transition state, or an approximation of one. The quality of the obtained TS candidate can be estimated by means of a vibrational analysis: if the TS candidate exhibits exactly one vibrational mode with an imaginary frequency, it is a saddle point of the PES, and if the mode geometrically corresponds to the reaction coordinate, the saddle point is the one relevant to the reaction. If the TS candidate does not exhibit these features, it does not correspond to the desired TS and needs to be further refined. Constrained optimization was used for some simple reactions in paper IV.

For more complicated reactions, it can be necessary to use more involved methods to find an accurate TS. One such technique is the nudged elastic band (NEB) method, the ASE implementation of which was used in papers I and IV.[128,129] Specifically, the initial guess for the pathway was constructed using an image-dependent pair potential interpolation,[130] and the transition state was typically finalized with a climbing image NEB (CI-NEB)[131] run. The maxima of the located pathways were verified to be the desired saddle points of the PES by vibrational analysis, as described above.

In the NEB method, the reaction pathway is modeled by a series of images corresponding to structures along the path (Figure 8). The images are connected with springs, such that the force acting on image i with atomic coordinates $\vec{R}_i$ is

$$\vec{F}_i^0 = -\nabla V(\vec{R}_i) - \nabla V(\vec{R}_i) \cdot \hat{\tau}_{\|}\hat{\tau}_{\|} + \vec{F}_i^s \cdot \hat{\tau}_{\|}\hat{\tau}_{\|}, \tag{45}$$

where $\nabla V(\vec{R}_i)$ is the true force acting on the image, $\hat{\tau}_{\|}$ is the unit tangent to the

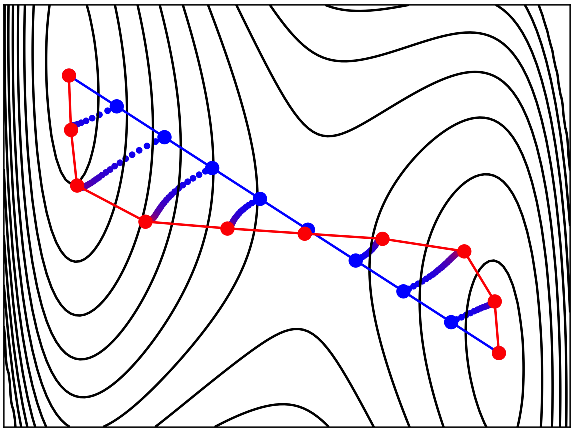

FIGURE 8 A simple example of a 10-image NEB on a model potential.[128,132] The intermediate pathways between the initial linear interpolation (big blue circles) to the converged MEP (big red circles) are shown with small circles.

path and

$$\vec{F}_i^s = k_{i+1}\left(\vec{R}_{i+1} - \vec{R}_i\right) - k_i\left(\vec{R}_i - \vec{R}_{i-1}\right), \tag{46}$$

where k_i is the spring constant corresponding to spring i. In Eq. (45), the path-parallel component of the true force $\nabla V(\vec{R}_i)$ and the path-perpendicular component of the spring force $\vec{F}_i^s$ are projected out. This eponymous "nudge" is carried out to keep the images on the minimum energy pathway (MEP): the parallel component of $\nabla V(\vec{R}_i)$ can cause images to slide off the MEP, while the perpendicular component of $\vec{F}_i^s$ can pull images away from the MEP ("corner-cutting") if the springs are too stiff.[128]

In CI-NEB, the highest-energy image from an initializing regular NEB run is identified and treated in a special way.[131] The force acting on this designated "climbing image" is defined as

$$\vec{F}_{i_{\max}} = -\nabla V\left(\vec{R}_{i_{\max}}\right) + 2\nabla V\left(\vec{R}_{i_{\max}}\right) \cdot \hat{\tau}_{\parallel}\hat{\tau}_{\parallel}, \tag{47}$$

where the spring force has been omitted entirely and the path-parallel component has been inverted. The inverted parallel component drives the climbing image upward along the band, guiding it toward the saddle point of the MEP. The removal of the spring force allows the image to climb unhindered by the neighboring images. For the method to be effective, the CI tangent $\hat{\tau}_{\parallel}$ should be parallel to the reaction coordinate, i.e., the neighboring images should approximate the MEP well. The density of images around the saddle point therefore has to be sufficient to provide a good description of the PES.

2.3 Generalized coordination number analysis

In paper I, we sought to rationalize the adsorption properties of M/ZrO_2 clusters by means of coordination number analysis. To account for the wide variety in local atomic environments, we used the strain-adjusted generalized coordination number (SGCN).[133] The SGCN is a refined version of the generalized coordination number (GCN),[134] which is itself an extension of the conventional coordination number (CN).

The conventional CN of cluster atom i is defined simply as

$$\mathrm{CN}(i) = \sum_{j}^{n_i} 1 = n_i, \tag{48}$$

where j runs over the n_i nearest neighbors of atom i. In the GCN, the nearest neighbors are instead weighted according to their coordination numbers:

$$\mathrm{GCN}(i) = \sum_{j}^{n_i} \frac{\mathrm{CN}(j)}{\mathrm{CN}_{\mathrm{max}}(j)}, \tag{49}$$

where $\mathrm{CN}(j)$ is the conventional CN of atom j, and $\mathrm{CN}_{\mathrm{max}}(j)$ is the corresponding bulk CN.[134] For the fcc metals Rh and Pt, $\mathrm{CN}_{\mathrm{max}} = 12$, while in m-ZrO_2, the bulk CNs are 7 for Zr and 3 or 4 for O, depending on the position of the anion.

In addition to cluster atoms, it is also possible to define GCNs for adsorption sites s on the clusters by summing over all nearest neighbors of the atoms that define the adsorption site and adjusting $\mathrm{CN}_{\mathrm{max}}$ accordingly:

$$\mathrm{GCN}(s) = \sum_{j} \frac{\mathrm{CN}(j)}{\mathrm{CN}_{\mathrm{max}}(s)}. \tag{50}$$

For top, bridge, 3-fold and 4-fold hollow sites the appropriate $\mathrm{CN}_{\mathrm{max}}(s)$ values are 12, 18, 22 and 26, respectively, and j runs over the nearest neighbors of the 1, 2, 3 or 4 atoms that define the adsorption site (only counting each neighbor once). For a top adsorption site, this reduces to the definition in Eq. (49), as such a site is defined by only one atom and $\mathrm{CN}_{\mathrm{max}}(\mathrm{s}) = 12$.

To account for the oxide support, the definition of the GCN was further extended to

$$\mathrm{GCN}(s) = \frac{\mathrm{CN}_{\mathrm{max}}(\mathrm{fcc})}{\mathrm{CN}_{\mathrm{max}}(s)} \sum_{j} \frac{\mathrm{CN}(j)}{\mathrm{CN}_{\mathrm{max}}(j)}, \tag{51}$$

where $\mathrm{CN}_{\mathrm{max}}(\mathrm{fcc}) = 12$. For systems with only fcc metal atoms, $\mathrm{CN}_{\mathrm{max}}(\mathrm{fcc}) = \mathrm{CN}_{\mathrm{max}}(j)\ \forall j$ and the definition reduces to Eq. (50). In the M/ZrO_2 systems, some

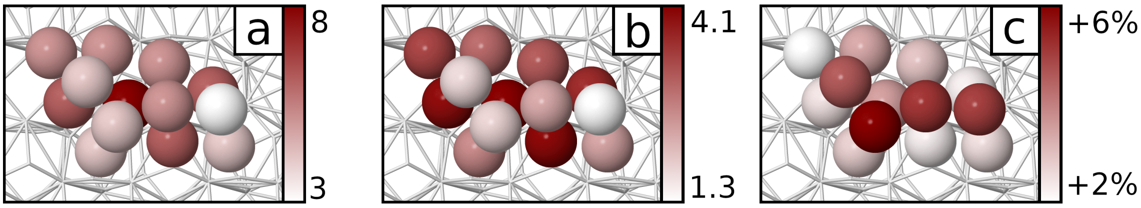

FIGURE 9 Comparison of various coordination numbers for a Pt_{13}/ZrO_2 cluster, color coded with gradients. Panel a: conventional CNs. Panel b: GCNs. Panel c: percentage change induced by the strain adjustment to the GCN. The change is presented in lieu of the actual SGCN, as the SGCN figure would be visually indistinguishable from panel b.

neighbors j can be Zr or O atoms, which have different maximum CNs. Finally, the strain adjustment was incorporated into the GCN as follows:

$$\mathrm{SGCN}(i) = \sum_j \frac{d_{\mathrm{bulk}}}{d(i,j)} \frac{\mathrm{CN}(j)}{\mathrm{CN}_{\mathrm{max}}(j)}, \tag{52}$$

where d_{bulk} is the optimal bulk bond length and $d(i,j)$ are the metal–metal bond lengths in the analyzed system. A corresponding adjustment was applied for the site GCNs defined by Eq. (51).

While the ordinary coordination number only accounts for the number of atomic neighbors, the GCN also includes the next-nearest neighbors, producing a more fine-grained measure of the local environment. In the SGCN, the description is further refined by also incorporating the interatomic distances, which allows strain-related properties to be described within the coordination number formalism. The different coordination numbers of a Pt_{13}/ZrO_2 cluster studied in paper I are visualized in Figure 9 in order to illustrate the differences between them. As expected based on Eq. 49, the GCNs are smaller than the CNs, as the neighbors of the undercoordinated cluster atoms are themselves undercoordinated. The strain adjustment (Figure 9c) has the largest effect on the top layer of the cluster, but is generally small in magnitude.

2.4 Molecular dynamics

Molecular dynamics (MD) simulations can be utilized, among other things, to evaluate the thermodynamic and transport properties of chemical systems and to study the time evolution of atomic-scale processes. In classical MD, the system is modeled with a force field consisting of potentials describing bonded interactions (intramolecular stretching, bending and torsion), electrostatic interactions and van der Waals interactions. The system is then allowed to evolve according to the laws of classical mechanics. While useful for many problems, classical MD is unable to describe phenomena such as bond breaking and formation. It is also dependent on the availability of good force field parameters.[135]

Instead of a classical force field, the forces required for the mechanics can be obtained from a quantum chemical calculation of the system.[135] This method has the obvious disadvantage of high computational cost, but provides a fully quantum description of the PES and avoids empirical fitting parameters. It can therefore be used to simulate chemical transformations and quantum interactions, such as hydrogen bonding,[136] in a realistic and consistent manner. In paper II, the time evolutions of a H_2O/Au system and a Pt cluster adsorbed on ZrO_2 were studied using DFT-MD.

2.4.1 Thermostats

In order to maintain the temperature of an MD simulation at a stable level, a thermostatting algorithm is often necessary. The simplest approach simply involves scaling the velocities of all the particles by a factor λ such that the post-scaling total kinetic energy corresponds to the target temperature of the simulation.[137] As the kinetic energy of an unconstrained particle with mass m and velocity v equals $\frac{1}{2}mv^2$, and a system of N unconstrained particles at temperature T should have a kinetic energy of $\frac{3N}{2}k_\mathrm{B}T$, the velocity scaling factor λ is found as

$$\lambda = \sqrt{\frac{\frac{3N}{2}k_\mathrm{B}T}{\sum_i \frac{1}{2}m_i{v_i}^2}}. \tag{53}$$

Scaling the velocity of each individual particle by λ scales the kinetic energy of the system by λ^2, bringing it to perfect agreement with the target temperature.

While the approach is straightforward and guarantees that the correct average temperature is maintained, it is known to produce anomalies in the distribution of the kinetic energy. A significant phenomenon is the "flying ice cube effect", in which the kinetic energy drains from high-frequency modes to low-frequency modes over the course of the simulation.[138,139] In an extreme case, the internal degrees of freedom could leak most of their kinetic energy to the center-of-mass motion of the system, causing the system to resemble a "flying ice cube". However, even if the COM is held fixed, the same phenomenon can be observed between internal degrees of freedom, where vibrations typically cool down at the expense of translations and rotations.[138,139]

The effect of a skewed KE distribution can become very apparent in the case of a heterogeneous or multi-component system. In such systems, each component includes different degrees of freedom, and a global thermostat can transfer KE between components. Thus, the component(s) with the highest-frequency degrees of freedom can cool down, while the others heat up, giving rise to interfacial temperature gradients.[139–141] Particular care is needed in these cases to make sure that the studied subsystem is at the proper temperature. In the case of DFT-MD, there is also the additional concern of convergence and force accuracy.[142,143] If the density is not sufficiently well converged, the forces derived from it can be too inaccurate to produce a correct trajectory. This effect can be exacerbated if the force errors are systematic,[144] causing direct overstimulation or damping of certain degrees of freedom. If the thermostat is already prone to artefacts in KE distribution, insufficient convergence can accelerate the skewing process.

The simple velocity rescaling thermostat is not the only one suffering from KE distribution issues; e.g. the Berendsen[145] and non-chained Nosé–Hoover[146] thermostats are also known to be susceptible. In spite of this, both thermostats have been extensively used in the literature to study a wide variety of systems.[147–150] This may be justified if the system only exhibits a weak flying ice cube effect, or if the effect is determined to be of lesser concern than the undesired effects possibly arising from alternative thermostats. Making these determinations requires careful benchmarking and monitoring of the simulation.

Thermostats that do not exhibit the flying ice cube effect are also available. For instance, the Langevin thermostat[151] avoids the issue by utilizing a stochastic friction term.[139] The thermostat is defined by the equations

$$m_i \dot{v}_i = F_i - m_i \gamma_i v_i + R_i(t) \tag{54}$$

$$\langle R_i(t) R_j(t+\tau) \rangle = 2 m_i \gamma_i k T_0 \delta(\tau) \delta_{ij} \tag{55}$$

$$\langle R_i(t) \rangle = 0, \tag{56}$$

where R_i is a Gaussian stochastic variable and γ_i are damping constants.[145,151] The R_i terms produce a random force corresponding to collisions with light particles at temperature T_0, while $-m_i \gamma_i v_i$ is a friction term. The damping constants γ_i control the coupling to the random force: if $\gamma_i = 0$, the thermostat is off and the dynamics are microcanonical, while for large γ_i, the simulation is dominated by the drag and random forces, destroying the dynamics of the studied system. The γ_i should therefore be set appropriately to maintain the temperature while minimizing the perturbation of the dynamics.[151,152]

The Berendsen thermostat is defined by the equations

$$m_i \dot{v}_i = F_i + m_i \gamma \left(\frac{T_0}{T} - 1 \right) v_i, \tag{57}$$

where the stochastic R_i component in the Langevin Eq. 54 has been replaced by a deterministic temperature scaling factor.[145] If $\gamma = 0$, the dynamics are microcanonical as in the Langevin case; if $\gamma = (\delta t)^{-1}$, the algorithm reduces to simple velocity rescaling.[139] Typically, in-between values are used, producing a weak coupling to the external bath and allowing the temperature to fluctuate around the target value. However, this method does not simulate a canonical ensemble and is susceptible to the flying ice cube effect.[139,152]

Finally, the Nosé–Hoover thermostat is defined by the equations[146]

$$\dot{q} = p/m \tag{58}$$

$$\dot{p} = F(q) - \zeta p \tag{59}$$

$$\dot{\zeta} = \left[\sum p^2/m - XkT_0\right]/Q, \tag{60}$$

where Q is a scaling parameter and X is the number of degrees of freedom in the system. Instead of directly scaling the velocities according to the instantaneous deviation from the target temperature as in the Berendsen method, the Nosé–Hoover thermostat utilizes a variable friction coefficient ζ, whose time evolution is controlled by the temperature deviation. This has the advantage of producing a canonical ensemble if the dynamics are ergodic; however, the method does not necessarily produce an ergodic trajectory, possibly resulting in flawed dynamics.[153] The issue can be mitigated by, e.g., the Nosé–Hoover chain approach, in which the thermostat variables are themselves thermostatted to improve phase space coverage.[153] The ASE implementation of the Nosé–Hoover thermostat used in paper II is based on Refs. 154 and 155.

2.4.2 Kinetic energy distribution

According to the equipartition theorem, the kinetic energy of an equilibrated system should, on average, be equally partitioned between all degrees of freedom. As discussed above, the flying ice cube effect or other anomalies can cause a simulated system to deviate from equipartition, resulting in unphysical behavior. It is therefore useful to monitor the distribution of kinetic energy over the course of the simulation, and verify that it is partitioned correctly.

The kinetic energy of a diatomic molecule is straightforward to partition into translational, rotational and vibrational components:[139]

$$E_{\mathrm{trans}} = \frac{1}{2}(m_1 + m_2)\left(v_{\mathrm{trans},x}^2 + v_{\mathrm{trans},y}^2 + v_{\mathrm{trans},z}^2\right) \tag{61}$$

$$E_{\mathrm{rot}} = \frac{1}{2}\mu\left((v_{2,x} - v_{1,x})^2 + (v_{2,y} - v_{1,y})^2\right) \tag{62}$$

$$E_{\mathrm{vib}} = \frac{1}{2}\mu(v_{2,z} - v_{1,z})^2, \tag{63}$$

where m_1 and m_2 are the masses of the atoms, μ is the reduced mass of the molecule, $v_{\mathrm{trans},j}$ is the center-of-mass velocity of the molecule in the j direction and $v_{i,j}$ is the velocity of atom i in the j direction. Here, the bond axis is assumed to align with the z axis.

More generally, the velocity of an atom j can be partitioned as[156]

$$v_j(t) = v_{j,\mathrm{tr}}(t) + v_{j,\mathrm{rot}}(t) + v_{j,\mathrm{vib}}(t). \tag{64}$$

The translational velocity $v_{j,\mathrm{tr}}(t)$ is the center of mass velocity of an atom or the molecule it belongs to. To compute the rotational velocity $v_{j,\mathrm{rot}}(t)$, the angular velocity $\vec{\omega}$ is first computed from the angular momentum $\vec{L}$ and inertia tensor $\mathbf{I}$ as

$$\vec{L} = \sum m_j(\vec{r}_j \times \vec{v}_j) = \mathbf{I}\vec{\omega}, \tag{65}$$

where the sum runs over the atoms in the molecule. The rotational velocity is then obtained as $\vec{v}_j = \vec{\omega} \times \vec{r}_j$, and the rest of the total velocity is assigned to vibrational motions according to Eq. (64). The translational and rotational velocities can be converted to kinetic energies using the standard formulae; the vibrational component of the energy can again be obtained by subtracting the other components from the total kinetic energy. This is the method used in the DoSPT code that was applied in paper II.[157]

3 RESULTS AND DISCUSSION

3.1 Water dissociation at the metal–ZrO_2 interface

The dissociation of water, a crucial elementary step in many industrially relevant catalytic reactions, was studied on the Pt/ZrO_2 and Rh/ZrO_2 interfaces. The interfaces were described using M_{13}/ZrO_2 and M_{19}/ZrO_2 cluster models whose structures were globally optimized in previous work, and thus readily available for further study.[44] In this size regime, the cluster is not organized into a bulklike structure, and features a wide variety of interfacial sites with different characteristics. Such small clusters are said to exhibit "non-scalable" behavior, meaning that their properties do not scale linearly with size. Furthermore, they can provide a way to buck the activity trends suggested by traditional linear energy scaling relations.[158]

While computational studies often focus on the most stable structures, a real catalytic system comprises a dynamic ensemble of cluster geometries. In combination with the variety inherent to each individual cluster, this results in a very broad array of possible reaction sites. To capture some of the ensemble effect, metastable near-global minimum (NGM) cluster geometries were considered in addition to the most stable global minimum (GM) structures. One NGM structure was considered in addition to the GM structure for each of Rh_{13}, Rh_{19}, Pt_{13} and Pt_{19}, resulting in eight total clusters. This necessarily produces a limited description of the true catalytic ensemble, which likely comprises a broader variety of structures and is also affected by the reaction environment; however, the model is sufficient to provide insight into the interfacial properties of clusters of varying shapes, sizes and stabilities. The geometries of the chosen clusters are shown in Figure 10.

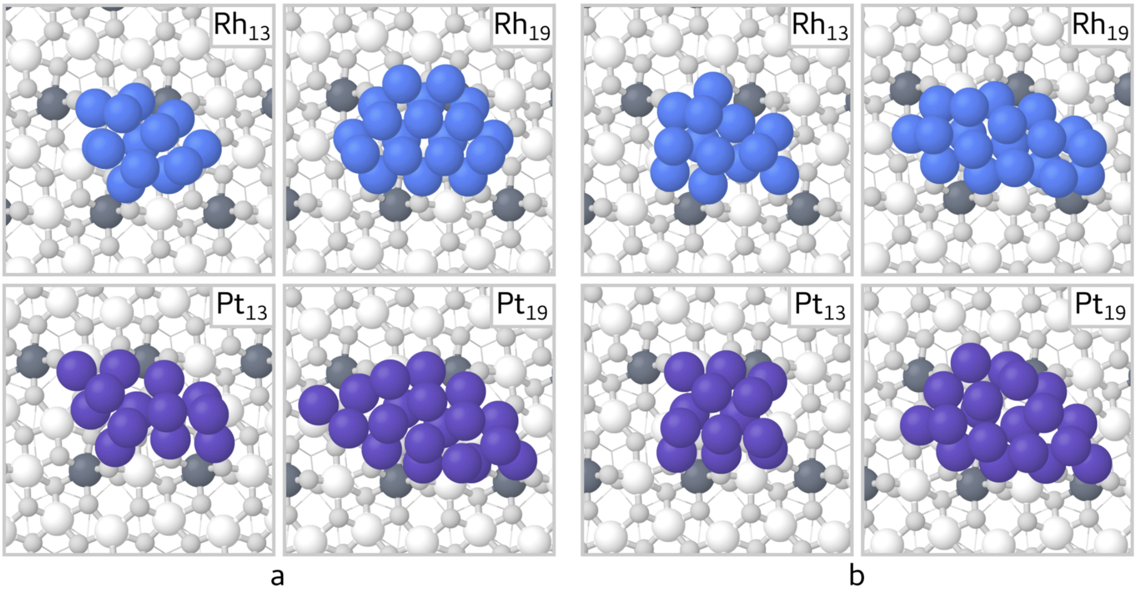

FIGURE 10 The (a) GM and (b) NGM cluster geometries considered for water dissociation. Color code: Rh in blue, Pt in purple, O in light grey, 6-coordinated Zr in white and 7-coordinated Zr in dark grey. Reprinted from Kauppinen, M. M.; Korpelin, V.; Verma, A. M.; Melander, M. M.; Honkala, K. *J. Chem. Phys.* **2019**, *151*, 164302, with the permission of AIP Publishing.

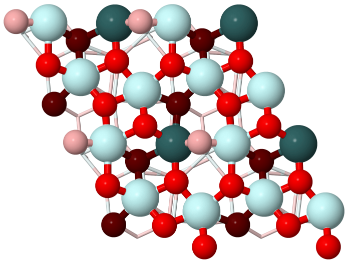

FIGURE 11 Coordination numbers of the m-ZrO$_2$($\bar{1}$11) surface ions. Light cyan: 6-coordinated Zr, dark cyan: 7-coordinated Zr, pink: 2-coordinated O, bright red: 3-coordinated O, dark red: 4-coordinated O.

Though the metal clusters themselves can already exhibit complicated features, the properties of the support and the specifics of the cluster–support interaction further complicate the picture. To begin with, the support in itself may already feature multiple different atoms and sites, immediately multiplying the complexity of the system. The cluster–support interaction can strongly modify the shape of the adsorbed cluster, while the cluster also deforms the surface to some extent. Likewise, the electronic structures of the cluster and support are influenced by each other. In the case of m-ZrO$_2$($\bar{1}$11), the bare surface features many inequivalent Zr and O ions with different coordinations and local environments (Figure 11). As an interfacial site consists of both metal and oxide components, both of which can exhibit different local environments and alter each other's properties, the structural and electronic complexity of the interface is very high. For small, irregular clusters, every site can be considered unique.

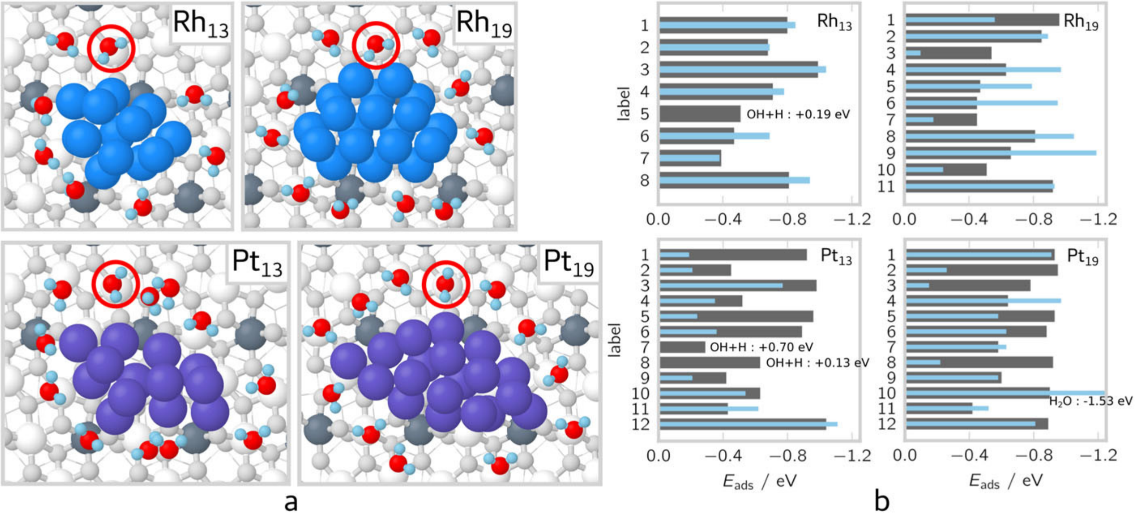

FIGURE 12 (a) H_2O adsorption geometries on the supported GM clusters. (b) The corresponding molecular (grey bars) and dissociative (thin blue bars) adsorption energies. On each cluster, the molecules have been labeled with a consecutive clockwise numbering, starting from the molecule marked with a red circle (molecule 1). While all H_2O geometries are shown in one figure for a concise representation, each molecule was adsorbed individually in the simulations. Reprinted from Kauppinen, M. M.; Korpelin, V.; Verma, A. M.; Melander, M. M.; Honkala, K. *J. Chem. Phys.* **2019**, *151*, 164302, with the permission of AIP Publishing.

This complexity is evident in Figure 12, showing H_2O adsorption geometries on the cluster–ZrO_2 interfaces. On the asymmetric Pt_{13} cluster, all interfacial Pt atoms have clearly different metal environments, and the variation is compounded by the surface geometry. Especially notable in this regard are the 7-coordinated Zr atoms, which are coordinatively saturated by surface O anions and therefore unable to bind H_2O molecules. Their presence reduces the number of available interfacial adsorption sites, and may block metal atoms that might otherwise be active for water dissociation. Unlike Pt_{13}, Rh_{19} is highly symmetric, but the differing oxide environment distinguishes the otherwise similar cluster sites, making each interfacial site unique. For instance, molecules 3 and 10 on opposite sides of Rh_{19} might be expected to exhibit similar behavior based on the cluster geometry, but the varying surface coordination breaks the symmetry.

The thermodynamics of molecular and dissociative water adsorption were compared between the GM and NGM clusters. The molecular adsorption energies on the interfacial oxide sites are largely similar between the two, indicating that the adsorption properties of the oxide are not strongly affected by the stability of the cluster. As shown in Figures 12 and 13, the interfacial H_2O molecules interact with the cluster mostly via weak H–M interactions, which are likely similar between the GM and NGM clusters. On the other hand, the dissociative adsorption energies are clearly more exothermic on the NGM clusters, resulting in more exothermic reaction energies for dissociation. Upon dissociation, the leaving H

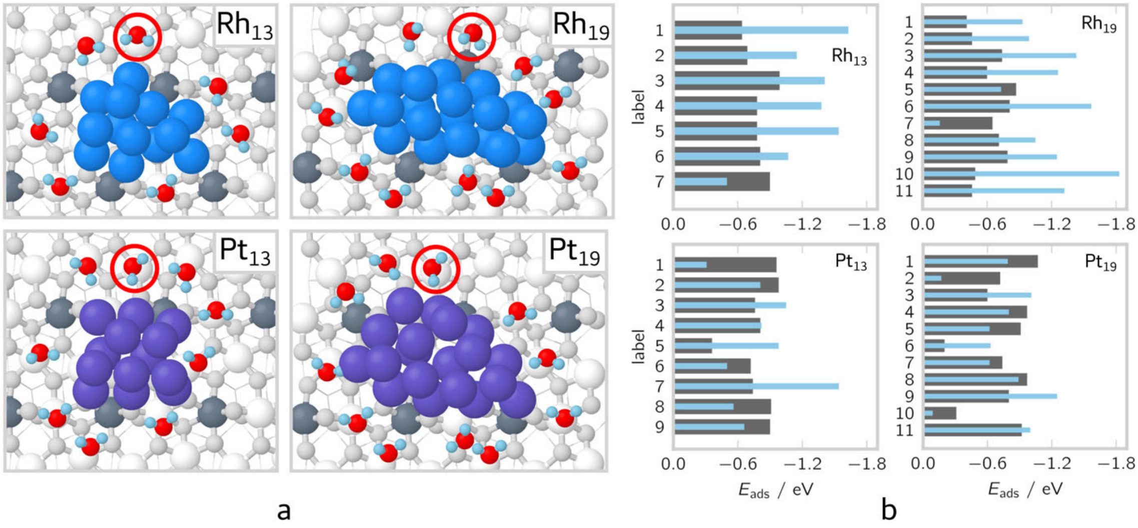

FIGURE 13 (a) H_2O adsorption geometries on the supported NGM clusters. (b) The corresponding molecular (grey bars) and dissociative (thin blue bars) adsorption energies. On each cluster, the molecules have been labeled with a consecutive clockwise numbering, starting from the molecule marked with a red circle (molecule 1). While all H_2O geometries are shown in one figure for a concise representation, each molecule was adsorbed individually in the simulations. Reprinted from Kauppinen, M. M.; Korpelin, V.; Verma, A. M.; Melander, M. M.; Honkala, K. *J. Chem. Phys.* **2019**, *151*, 164302, with the permission of AIP Publishing.

atom moves onto the cluster and the hydroxyl can also exhibit Pt–OH bonding. The less stable NGM clusters can bind these fragments more strongly than the GM clusters, explaining the difference in dissociative adsorption energies. The difference is larger for the Rh clusters than for the Pt clusters, which may be due to differences in the properties of the metals or the lower relative stability of the NGM Rh clusters chosen for the study; the instabilities relative to the corresponding GM clusters were 0.80 and 1.33 eV for the Rh_{13} and Rh_{19} NGM clusters, compared to 0.56 and 0.35 eV for Pt_{13} and Pt_{19}. In addition to the differences in energetics, the adsorption-induced geometric deformations are about 50% larger on average in the NGM clusters, as measured by mean cluster atom displacement. This indicates a greater degree of adsorption-induced fluxionality.

For each GM cluster, five H_2O adsorption geometries were selected for a study of dissociation kinetics. The site variation is again highlighted, as the activation energies for dissociation vary over a span of ca. 0.5 eV in each system. Due to the different properties of the reaction sites and transition state geometries, linear scaling relations between activation and reaction/adsorption energies do not hold for these interfacial dissociation reactions. This is to be expected, as the reactant, transition state and product structures are not very similar across different reaction sites. This variation in activity between sites highlights the catalytic relevance of the varied geometric and electronic landscape of metal–oxide interfaces.

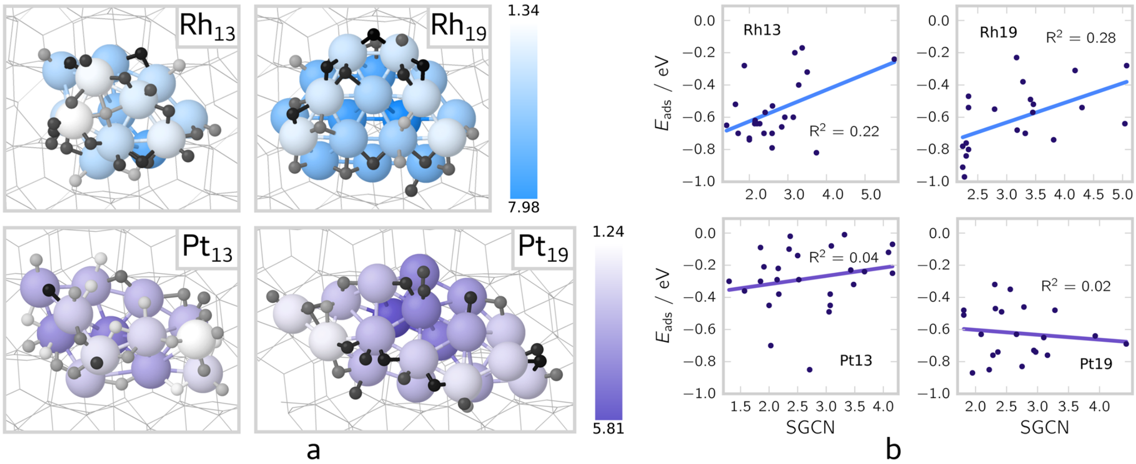

FIGURE 14 (a) Adsorption locations of H atoms on the GM clusters. The individually adsorbed H atoms have been added onto the optimal cluster structure for visual clarity. The metal atoms are colored according to their SGCNs (gradients in figure), while the H atoms are colored according to OH+H adsorption energies with OH far away from the cluster and H on the indicated site (white: −0.01 eV, black: −0.97 eV). (b) OH+H adsorption energies vs. SGCN. Reprinted from Kauppinen, M. M.; Korpelin, V.; Verma, A. M.; Melander, M. M.; Honkala, K. *J. Chem. Phys.* **2019**, *151*, 164302, with the permission of AIP Publishing.

In order to describe and understand the properties of the clusters, the SGCN descriptor[133] defined in Section 2.3 was utilized. SGCN provides a compact description of an individual atom's chemical environment, making it possible to quantify the geometric differences between the cluster atoms and adsorption sites. The SGCNs for the atoms in the GM clusters are shown in Figure 14a, highlighting the large variation in coordination. Interestingly, the SGCNs do not correlate with the H adsorption energies (Figure 14b), indicating that geometric reasons alone are not sufficient to predict H bonding. This conclusion was reinforced by also testing the SOAP descriptor,[159] which is another way to numerically describe the chemical environment of an atom. The SOAP similarities between the strongest-adsorbing site and the other sites on the M_{13} clusters were computed, also resulting in no correlation between H adsorption energy and site geometry.[1] To supplement the geometric analyses, various electronic descriptors were considered for Pt_{13}: the Bader charges[114,115] and projected d band centers of the cluster metal atoms,[11] the electrostatic potential surrounding the cluster[160] and the Fukui functions[161] of the cluster were studied, but found unable to clearly characterize the H binding at the cluster sites. The difficulty in predicting H adsorption energies via these geometric and electronic descriptors suggests that the properties of the adsorption sites are complicated functions of geometry and electronic structure.

---

[1] No machine learning was carried out; the analysis is purely based on the geometric similarity according to SOAP.

In this study, the wide variety of local chemical environments in cluster–oxide systems was highlighted. Even a single 13- or 19-atom cluster has about 10 unique interfacial sites of varying metal and oxide compositions, and this complexity is greatly multiplied in the complete cluster ensemble. The thermodynamics and kinetics of water dissociation at each site are different, and the activation energies do not scale with the initial or final state energies. In addition to the interfacial sites, the H adsorption sites on the cluster were also found to exhibit highly variable behavior that is difficult to predict with simple geometric or electronic descriptors. The intricate properties of small supported clusters are thus challenging to model and describe, but can enable chemical reactivity that is unreachable via catalysts in the scalable regime by breaking the trends that govern larger nanoparticles.

3.2 Temperature anomalies in DFT-MD

After considering the fluxionality and ensemble effects for supported clusters in paper I, a natural continuation would be to run molecular dynamics simulations in order to better understand how the clusters transform over time in different temperatures. These simulations could provide insight into, e.g., the temperature-induced fluxionality and isomerization rates of the clusters, elucidating the dynamics that are constantly ongoing within catalytic systems. However, in the course of testing such simulations for the supported clusters, anomalous temperature behavior was observed, with the metal cluster heating up by hundreds of K. This observation prompted a deeper investigation into the thermostatting and parametrization of AIMD calculations for heterogeneous systems, and how such anomalies could be avoided.

The main culprit behind the anomalous behavior is the “flying ice cube effect”, which causes the kinetic energy of a thermostatted system to disproportionately concentrate into low-frequency degrees of freedom, in violation of the equipartition theorem; this phenomenon is well known in classical MD.[138,139] In inhomogeneous systems, the closely related “hot-solvent/cold-solute” problem has also been identified.[140,162] Commonly used thermostatting algorithms that rely on rescaling the atomic velocities, such as Berendsen[145] and non-chained Nosé–Hoover,[146,163,164] are known to be susceptible to such anomalies.[139] As the supported clusters are inhomogeneous, two-component systems, thermostatting them with these algorithms is likely to result in an erroneous distribution of kinetic energy.

An example of such an anomaly is shown in Figure 15. In the left panel, the temperature of the cluster climbs to over 600 K, even though the thermostat was set

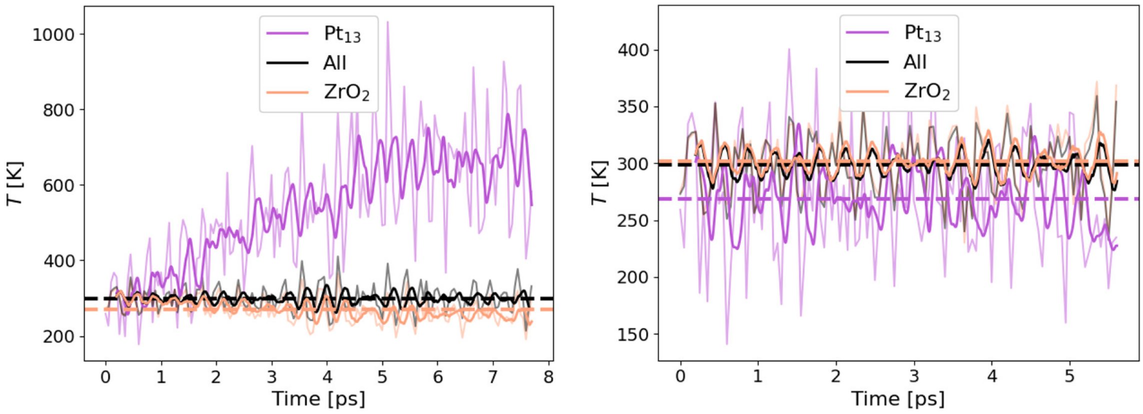

FIGURE 15 The Pt_{13} and ZrO_2 temperatures in a supported cluster system thermostatted with Nosé-Hoover. Left: energy convergence 10^{-7} eV, right: density convergence 10^{-6} e/v.e. (electrons per valence electron). The thick curves correspond to 200 fs moving averages. Reprinted under the CC BY 4.0 license from paper II, © 2022 Authors.

to maintain a constant target temperature of 300 K. While heating the cluster, the thermostat maintains the desired average temperature by correspondingly cooling the surface, resulting in a temperature gradient across the interface. In this fairly extreme case, the temperature anomaly is exacerbated by the insufficient SCF convergence; however, even when this is corrected, the distribution remains somewhat uneven (Figure 15, right panel). As the average temperature is always faithfully kept at 300 K, this type of anomaly may not be readily apparent from the simulation log files, where often only the average T is reported. This example therefore highlights the necessity of more fine-grained temperature monitoring during MD simulations.

The metal–water interface is another catalytically relevant system that could benefit from high-accuracy AIMD simulations. An accurate picture of the structure and dynamics of such interfaces is of key importance to the development and understanding of electrochemical systems, such as batteries, fuel cells and electrocatalysts. As shown in the right panel of Figure 16, our Au/H_2O model also suffers from an erroneous kinetic energy distribution brought on by the Nosé–Hoover thermostat. The average temperatures for each component are 360 K for translations, 329 K for rotations, and 284 K for vibrations, exhibiting the typical tendency to overheat low-frequency degrees of freedom. The kinetic energies also slowly drift around the average values. The left panel of Figure 16 shows the corresponding results for a Langevin[165] simulation, in which the drift is absent and all components correctly average at the target temperature of 330 K. The Langevin thermostat is therefore found to maintain equipartition, in agreement with previous work.[139]

These results demonstrate that both the thermostat and the convergence criteria need to be carefully selected in order to maintain a proper kinetic energy distribution. An SCF convergence criterion that is acceptable for geometry optimizations

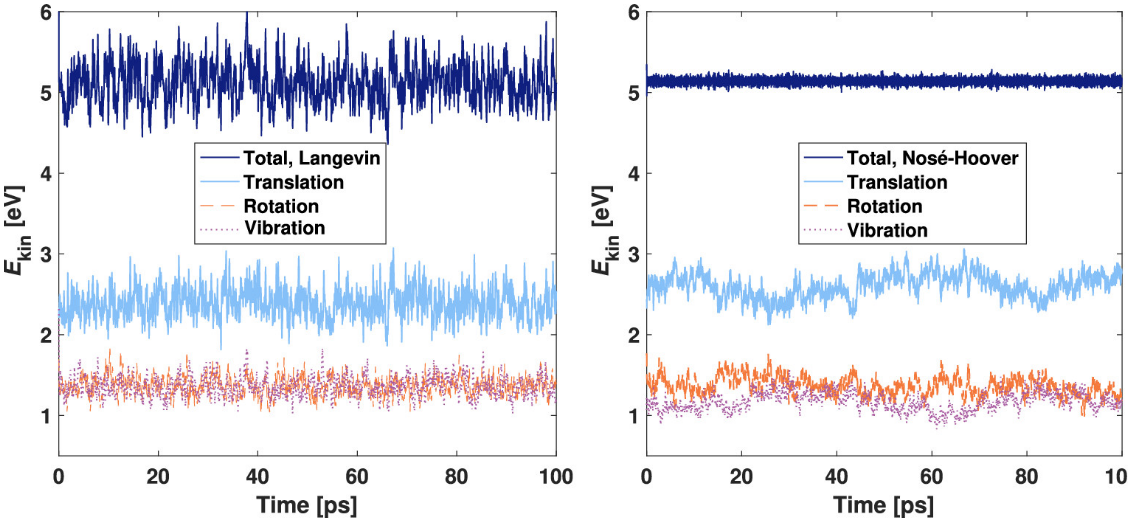

FIGURE 16 Kinetic energy distributions for VASP simulations of H_2O/Au thermostatted with Langevin (left) and Nosé–Hoover (right). Computed with the DoSPT code (see Section 2.4.2). Reprinted under the CC BY 4.0 license from paper II, © 2022 Authors.

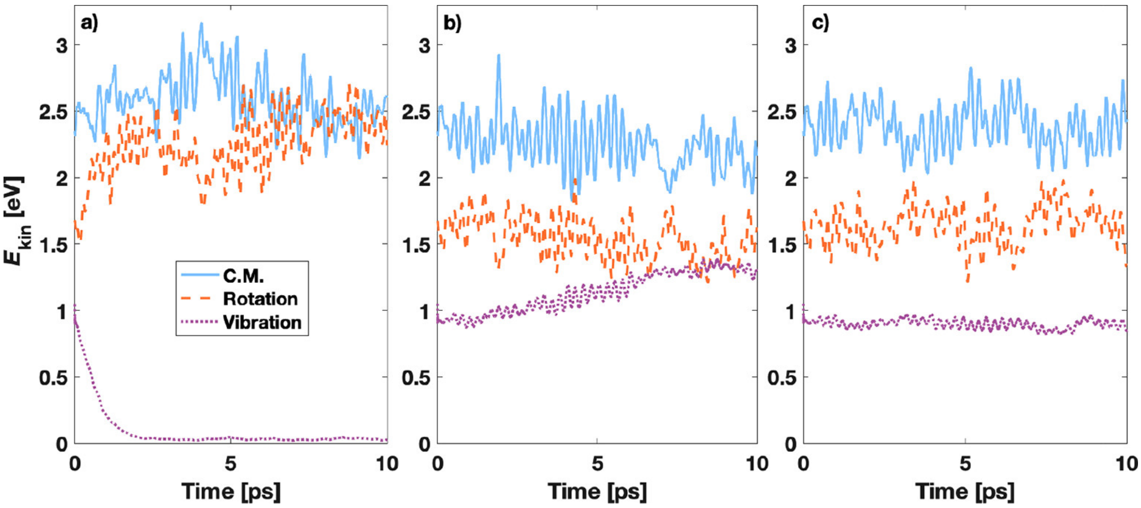

FIGURE 17 Kinetic energy distributions for ASE/GPAW Nosé–Hoover simulations of N_2 using various density convergence criteria. The applied criterion was a) 10^{-4} e/v.e., b) 10^{-5} e/v.e., c) 10^{-6} e/v.e. Using these criteria, the total energies were converged to at least a) 10^{-4} eV., b) 10^{-6} eV, c) 10^{-8} eV. Reprinted under the CC BY 4.0 license from paper II, © 2022 Authors.

is not necessarily strict enough to produce reliable AIMD trajectories. As a simple demonstration of the convergence effect, 64 N_2 molecules in a fully periodic, cubic 27 nm^3 box (a system inspired by similar ethane simulations[138,139]) were simulated with the Nosé–Hoover thermostat using different convergence criteria. The kinetic energy distributions are plotted in Figure 17. With the density convergence criterion of 10^{-4} e/v.e. (electrons per valence electron), the vibrational degrees of freedom are immediately quenched, while the rotations are accelerated. Note that this criterion is not especially loose; in fact, it is the GPAW default, and is perfectly suitable for many typical calculations. Tightening the criterion to 10^{-5} e/v.e. produces interesting behavior, as the vibrations are actually heated, in contrast with the typical flying ice cube effect. This is likely due to a systematic force error along the molecular axis driving the vibrations. At the tightest considered criterion of 10^{-6} e/v.e. (roughly corresponding to 10^{-8} eV in total energy), equipartition is finally maintained.

The errors in kinetic energy distribution are not just subtle technical issues, but can result in erroneous results and conclusions. In the case of a supported cluster, a temperature gradient may form between the two components of the system, causing the support and the cluster to deviate from the target temperature in opposite directions. If the cluster is too hot, it will appear more mobile and fluxional than it should, resulting in a flawed description of the structural dynamics. Even if the temperature (i.e., total kinetic energy) of a component is correctly maintained, the kinetic energy may not be equally partitioned between the degrees of freedom, resulting in errors. For instance, if the distribution is biased toward translational motions, diffusion and entropy may become overestimated. Careful parametrization, equilibration and thermostatting are therefore mandatory to run meaningful simulations yielding reliable results.

3.3 Metal-enhanced reducibility of ZrO_2

The properties of metal–zirconia systems were also investigated in paper III, in which the metal–oxide and metal–vacancy interactions were studied in detail to explain how the chemical identity of the adsorbed metal affects the reducibility of the oxide. Reducibility is a key property of the oxide support, with reducible and irreducible oxides exhibiting qualitatively different behavior in many catalytic reactions.[28] Tuning the reducibility of the support is therefore one possible avenue toward optimizing the reaction environment; especially if reducibility can be induced in typically irreducible oxides, they may find use in a wider range of reactions. Instead of the clusters studied in papers I and II, single metal atoms were used to probe the effect in paper III, maximizing the role of the metal–oxide interaction.

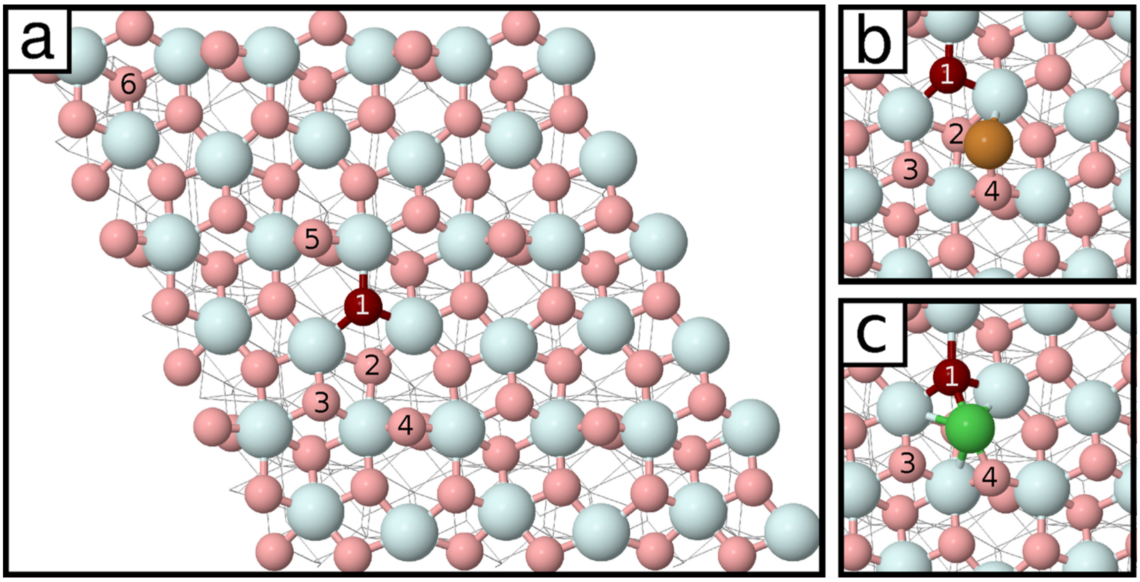

FIGURE 18 (a) Computational m-ZrO$_2$($\bar{1}$11) cell. Light blue: Zr, light red: O, dark red: the O atom that is removed to create the vacancy O1. The numbers on the O atoms are labels for ease of discussion. (b, c) Cu (brown) and Ni (green) as representative examples of metal–surface binding geometries. Reprinted under the CC BY 4.0 license from paper III, © 2022 Authors.

Building on earlier work on the Rh-enhanced reducibility of m-ZrO$_2$($\bar{1}$11),[166] the effect of 13 different single TM atoms (Fe, Co, Ni, Cu, Mo, Ru, Rh, Pd, Ag, Re, Ir, Pt and Au) on the reducibility of zirconia was investigated. The geometries for each atom were optimized on the intact surface and inside an oxygen vacancy, and the adsorption and reduction energies were defined as

$$E_{\mathrm{ads}} = E(\mathrm{M/ZrO_2}) - E(\mathrm{ZrO_2}) - E(\mathrm{M,g}), \tag{66}$$

where ZrO$_2$ can refer to either the ideal or the reduced surface, and

$$E_{\mathrm{R}} = E(\mathrm{M/ZrO}_{2-x}) + E(\mathrm{H_2O,g}) - E(\mathrm{M/ZrO_2}) - E(\mathrm{H_2,g}). \tag{67}$$

The computational cell is shown in Figure 18a. All atoms were initially placed atop the 3-coordinated oxygen atom O2 (Figure 18), as this was found to be the most favorable site for Rh adsorption.[166] While different TM atoms could preferentially adsorb on different sites, the same site was studied for all atoms to facilitate comparison of their properties. Even on the same site, the atoms exhibit different adsorption geometries: the Cu group atoms only bind to the 2-coordinated O4 atom (Figure 18b), Pd, Ir and Pt bind to O4 and another nearby anion, while the others bind to three oxide anions (Figure 18c).

Inside the vacancy, the TM atom adsorption geometries can also be divided into three categories: the Cu and Ni group metals, along with Co, stay in the middle of the vacancy (Figure 19b), the group 6–8 metals (Fe, Mo, Re, Ru) bind to the nearby 2-coordinated O5 anion (Figure 19c), with Rh and Ir being in-between cases that

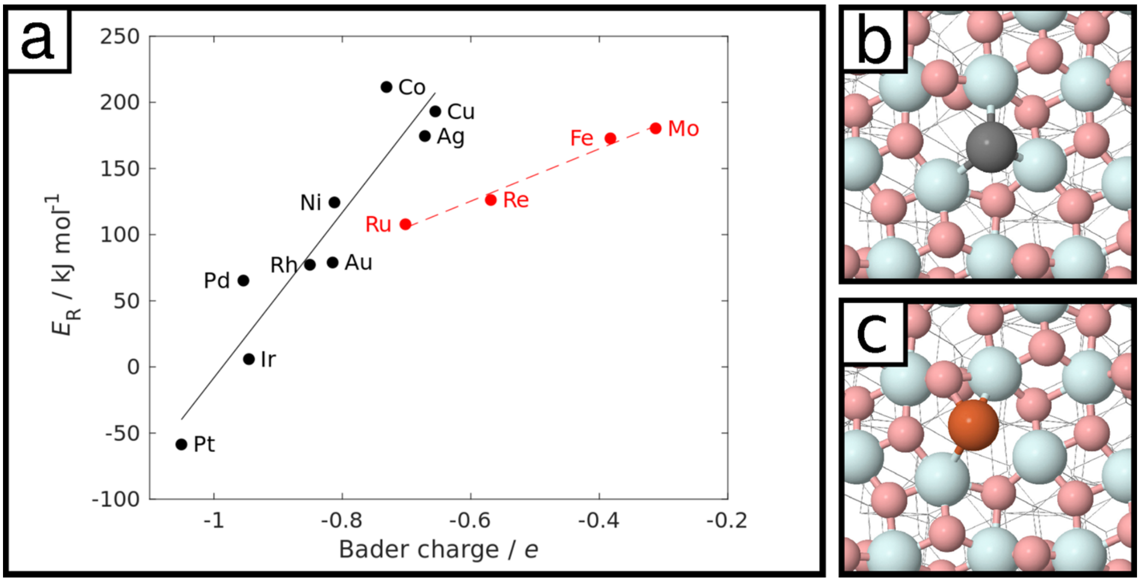

FIGURE 19 (a) Correlation between the reduction energy and the Bader charge of the vacancy-bound metal atom. Solid black line ($R^2 = 0.89$): metals that stay in the middle of the vacancy. Dashed red line ($R^2 = 0.98$): metals that bind to the 2-coordinated O5 anion. (b and c): Pt (grey) and Fe (brown) vacancy adsorption geometries as representative examples of the aforementioned categories. Reprinted under the CC BY 4.0 license from paper III, © 2022 Authors.

slightly approach O5. This variation is reflected in the reduction energy–Bader charge correlation (Figure 19a), in which the group 6–8 metals follow a separate trend from the other TMs. The direction of the trend is the same for all atoms, however: atoms with more negative Bader charges in the vacancy also feature more exothermic adsorption energies. The weaker correlation of the group 6–8 metals is likely due to their M–O5 bond leading to a weaker interaction with the vacancy electrons.

The charge correlation analysis was also run separately between the adsorption energies and charges on the ideal and reduced surfaces. On the reduced surface (Figure 20b), the adsorption energy correlations are qualitatively similar to the reduction energy correlation, although the slopes are considerably steeper. The distinct behavior of the group 6–8 metals is also observed here, reinforcing the conclusion that it is a feature of the vacancy adsorption geometry. On the ideal surface, a different trend is observed (Figure 20a): the group 6–8 metals are now in line with most others, while Cu, Ag, Au and Pd deviate. All of the deviating metals feature d^{10} electron structures, which causes their surface interaction to be qualitatively different than that of the other TM atoms. In particular, the strongly deviating Cu group metals have $d^{10}s^1$ electron structures, and the half-filled s orbital has been proposed to weaken adsorption by causing Pauli repulsion with the surface s orbitals.[167,168]

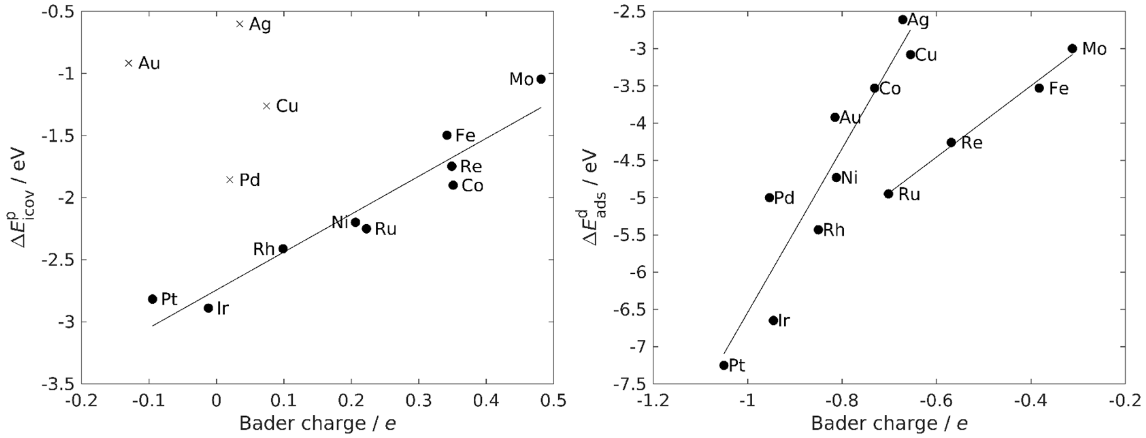

FIGURE 20 (a) Correlation between the adsorption energy and the Bader charge of the metal atom on the ideal surface. (b) Correlation between the adsorption energy and the Bader charge of the metal atom inside the vacancy. Reprinted under the CC BY 4.0 license from paper III, © 2022 Authors.

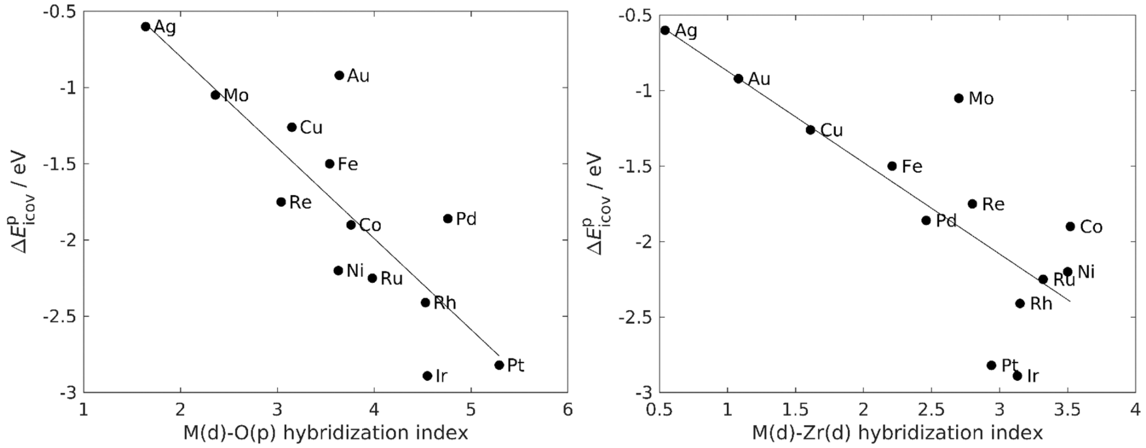

FIGURE 21 (a) Correlation of adsorption energy on the ideal surface and hybridization index between TM d and oxygen p orbitals. (b) Correlation of adsorption energy on the ideal surface and hybridization index between TM d and Zr d orbitals. Reprinted under the CC BY 4.0 license from paper III, © 2022 Authors.

The $d^{10}s^{1}$ metals also stand out in the hybridization index analysis, exhibiting markedly low d–d hybridization with the Zr d orbitals (Figure 21b); the same distinction is also observed in their adsorption heights, which are 0.3–0.6 Å higher than those of the other metals. For most metals, the adsorption energy on the ideal surface correlates with the metal d–oxide p hybridization index (Figure 21a), with Au being the clearest outlier. This result indicates that the covalent interaction between M and O is a key factor in determining the adsorption energetics, in agreement with earlier studies.[169,170]

The adsorption thermodynamics of selected metals (Fe, Cu, Rh, Pd, Ag, Ir, Pt, Au) were further dissected by means of the thermodynamic cycle presented in Fig-

$$\begin{tikzcd}
\mathrm{M(g)} + \mathrm{ZrO_2} + \mathrm{ZrO}_{2-x} \arrow[r, "\Delta E^{\mathrm{p}}_{\mathrm{icov}}"] \arrow[d, "\Delta E^{\mathrm{d}}_{\mathrm{ads}}"] & \mathrm{M/ZrO_2} + \mathrm{ZrO}_{2-x} \arrow[d, "\Delta E_{\mathrm{redox}}"'] \\
\mathrm{ZrO_2} + \mathrm{M^-/ZrO^+_{2-x}} & \mathrm{M^-/ZrO_2} + \mathrm{ZrO^+_{2-x}} \arrow[l, "\Delta E^{\mathrm{d}}_{\mathrm{icov}}"']
\end{tikzcd}$$

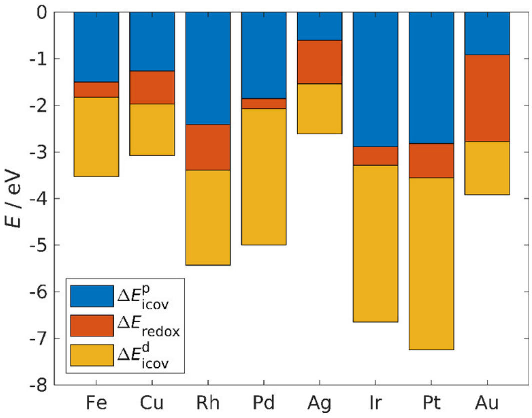

FIGURE 22 Left: definition of the thermodynamic cycle. Right: the magnitudes of the components as a stacked barplot. M(g) is the gas-phase metal atom, $\mathrm{ZrO_2}$ is the bare surface, ZrO_{2-x} is the bare surface with an oxygen vacancy, $\mathrm{M/ZrO_2}$ is the bare surface with an adsorbed M, and $\mathrm{M^-/ZrO^+_{2-x}}$ is ZrO_{2-x} with a metal in the vacancy. All of these systems were calculated as charge-neutral. The charged systems were $\mathrm{M^-/ZrO_2}$, where an M was adsorbed on an alternative site (see paper III) of the bare surface with an added electron, and $\mathrm{ZrO^+_{2-x}}$, where an electron was removed from ZrO_{2-x}. Reprinted under the CC BY 4.0 license from paper III, © 2022 Authors.

ure 22. The $\Delta E^{\mathrm{p}}_{\mathrm{icov}}$ component is simply the adsorption energy of the metal atom on the ideal surface. The $\Delta E_{\mathrm{redox}}$ term describing the metal–oxide charge-transfer is especially large for Au, which also has the largest electron affinity among the included metals; in general, the redox component does not perfectly correlate with the gas-phase electron affinities, likely because the surface interaction modulates the electronic structures of the metal atoms. Finally, $\Delta E^{\mathrm{d}}_{\mathrm{icov}}$ largely follows the same trend as $\Delta E^{\mathrm{p}}_{\mathrm{icov}}$, indicating that the ionocovalent interactions with the oxide and vacancy sites are similar to each other.

To summarize, the metal–oxide and metal–vacancy interactions in $\mathrm{M/ZrO_2}$ systems were analyzed with various electronic and thermodynamic analyses to elucidate the origin of metal-enhanced reducibility on zirconia. Pt and Ir were identified as especially potent reducibility enhancers. Here, the metal atom was assumed to fill the oxide vacancy, blocking it from being healed. This may be undesirable in practice, if facile O exchange with the oxide is necessary; on the other hand, the anchoring of metal atoms is relevant to the development of single atom catalysts. In future work, it would be interesting to study the dynamics of vacancy formation and the metal–vacancy interaction in order to understand in greater detail how they affect each other.

3.4 Acid-catalyzed glycerol dehydration

In paper IV, instead of studying small metal particles on oxides, a small oxide component (ReOH) on a metal surface (Rh(111)) was considered. Such systems have been explored for the hydrodeoxygenation of polyols, in which the metallic functionality is needed for hydrogen activation, while the oxide assists in removing hydroxyl from the reactant.[23,50] The role of the oxide component is not fully settled, with both Brønsted acidity and favorable reactant binding properties having been proposed.[23] In this work, the main focus is on the acid properties.

The dehydration of glycerol was studied on both bare and ReOH-modified Rh(111), focusing on the first dehydration step from glycerol to an enol intermediate. In this first step, either a primary or secondary OH is removed from glycerol, determining the selectivity toward 1,2- or 1,3-propanediol (PDO). The dehydration was assumed to occur via sequential C–H and C–OH cleavage steps (Figure 23). On bare Rh(111), the immediate C–OH cleavage was found kinetically very unfavorable, with activation energies of 1.8–1.9 eV (Figure 24). After an initial loss of H, the activation energies of the C–OH cleavage steps become considerably lower (1.1–1.3 eV). The reaction is therefore expected to proceed via an initial C–H cleavage step, followed by dehydroxylation. The results are in good agreement with prior work on the Rh(111) surface.[171]

ReOH was found to strongly catalyze the C–OH cleavage by protonating the leaving hydroxyl group: the activation energies for the initial glycerol dehydroxylation steps were lowered by 0.5–0.8 eV when the acid modifier was introduced (Figure 25). However, this was not sufficient to bring their barriers below those of the initial C–H cleavage steps, indicating that the initial step is C–H activation even on the acid-modified surface. The effect of the acid modifier on C–H cleav-

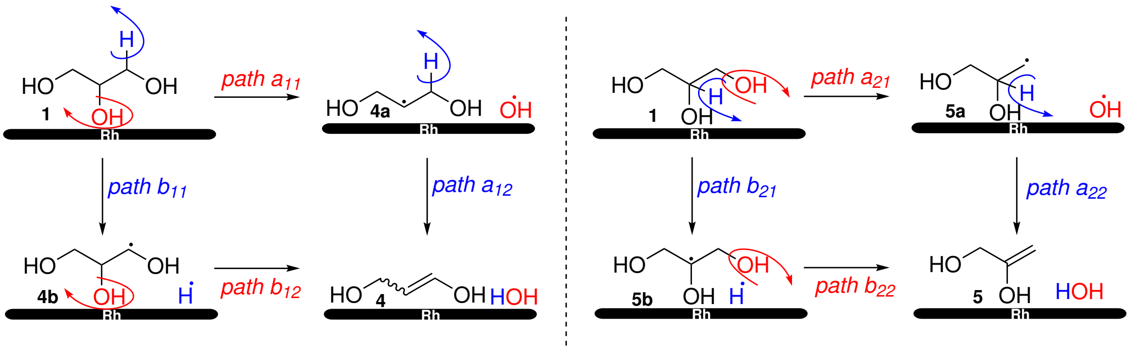

FIGURE 23 The pathways considered for glycerol dehydration. On the "a" paths, C–OH cleavage happens first, while on the "b" paths, C–H cleavage happens first. The same scheme applies for pure Rh and ReOH-modified Rh, except on the latter, the C–OH removal steps are catalyzed by the Brønsted acidic ReOH modifier instead of the metal.

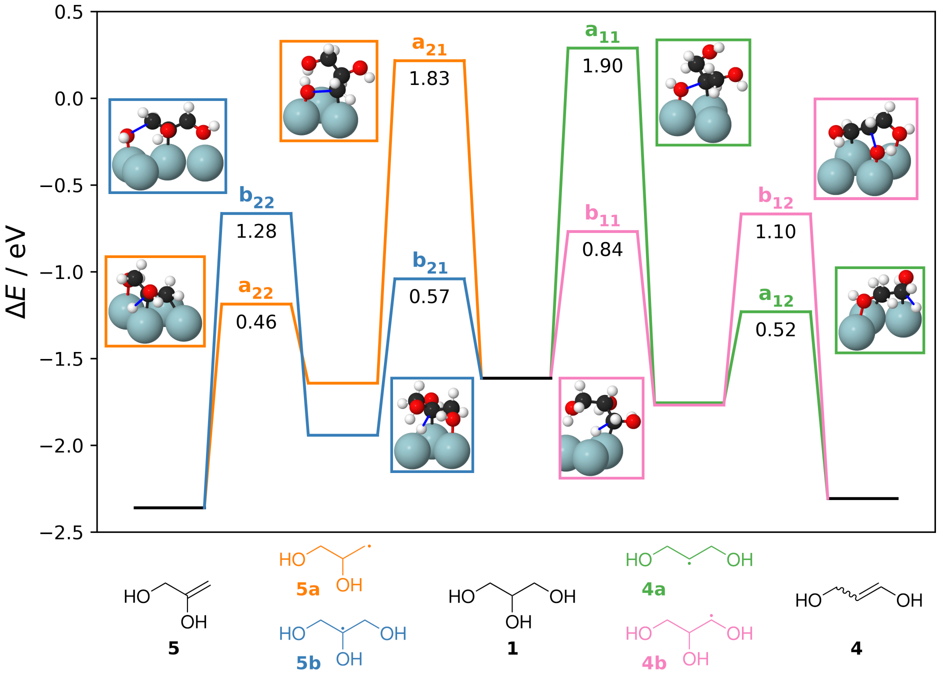

FIGURE 24 Potential energy surface and transition state geometries for glycerol on bare Rh(111). The paths labeled “a” start with a C–OH cleavage, while the paths labeled ”b” start with a C–H cleavage. The first number in the subscript is 1 for the 1,3-PDO pathways and 2 for the 1,2-PDO pathways. The second number in the subscript refers to the number of the step on a given pathway (first or second).

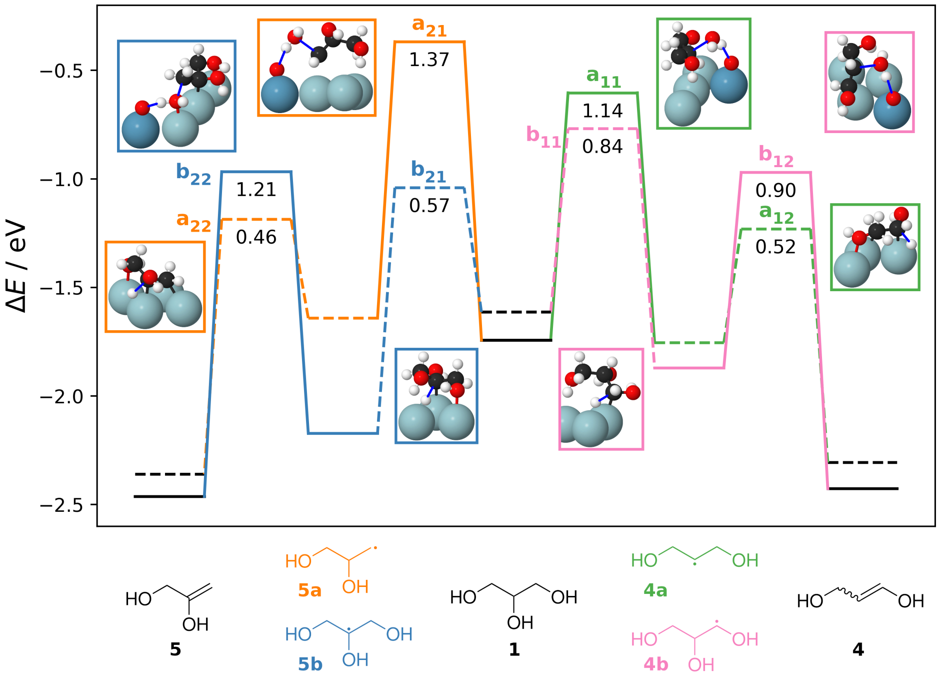

FIGURE 25 Potential energy surface and transition state geometries for glycerol on ReOH-modified Rh(111). The C–H cleavage steps drawn with dashed lines were computed on bare Rh(111) and are repeated from Figure 24, as the modifier was not found to substantially alter the C–H activation barriers. The step labels match those in Figure 24.

age was found minor. After C–H cleavage, the effect of the acid modifier becomes considerably weaker, as the second C–OH cleavage barriers were only lowered by 0.1–0.2 eV. This major difference between the first and second C–OH cleavages arises from the differences between their final states: the first dehydroxylation from glycerol produces a comparatively unstable surface radical intermediate, while the second dehydroxylation produces a stable enol molecule. As the reactions exhibit late transition states that resemble the products, the product stability determines the TS stability, i.e., the activation energy, by the BEP principle.[12]

The selectivity toward 1,3-PDO is improved on the acid-modified surface, but remains comparatively poor, in part due to the competition between C–H and C–OH cleavages. This observation is in agreement with experimental results.[172–174] Considerably better experimental selectivities toward 1,3-PDO have been reported on, e.g., ReOH–Ir catalysts, which are expected to feature more acidic protons capable of activating the C–OH cleavage even more effectively.[51,175–177] On the other hand, ReOH–Rh catalysts have been found highly selective toward α,ω-diols in various ring-opening reactions.[173,178–180] Inspired by these results, we simulated the ring-opening of glycidol, an epoxide derivative of glycerol whose role in the valorization of glycerol has been the subject of recent interest.[181] A selective ring opening mechanism could pave the way for a glycerol–glycidol–1,3-PDO process.

However, the ReOH modifier doesn't catalyze the ring opening reaction at all: the activation energies are unaffected, and the proton does not participate in the transition state. The selectivity of the metal-catalyzed ring opening is also quite poor (Figure 26). These observations are in stark contrast to previous results for tetrahydrofurfuryl alcohol (THFA), the ring opening of which has been computationally found both acid-catalyzed and highly selective (Figure 27).[51,173] This suggests that the size of the ring strongly affects the reaction pathway. A key difference between glycidol and THFA is the gas-phase protonation energy, which is 0.86 eV more endothermic for glycidol, indicating a much weaker affinity for protons. A very strong acid is thus likely required to activate the epoxide ring of glycidol by protonation. The three-membered glycidol ring also has a much higher ring strain than the five-membered ring in THFA, and the ring opening energy we find for glycidol on Rh(111) is more exothermic than that reported for THFA on the same surface.[182] Glycidol is thus inherently less stable than the larger rings, and a non-acid-catalyzed ring opening pathway can be competitive even if a very strong acid catalyst is used.

Apart from the ring opening, we also considered initial C–H cleavage steps for glycidol. For larger rings, the dehydrogenation is more likely to occur at the less substituted ether carbon (carbon 5 in Figure 27) due to steric reasons;[173,182] for glycidol, C–H cleavages from both ether carbons (2 and 3 in Figure 27) are roughly as facile. As glycidol is a fairly small molecule, steric effects likely play a smaller role in its reactions. The C–H cleavage at the more substituted ether

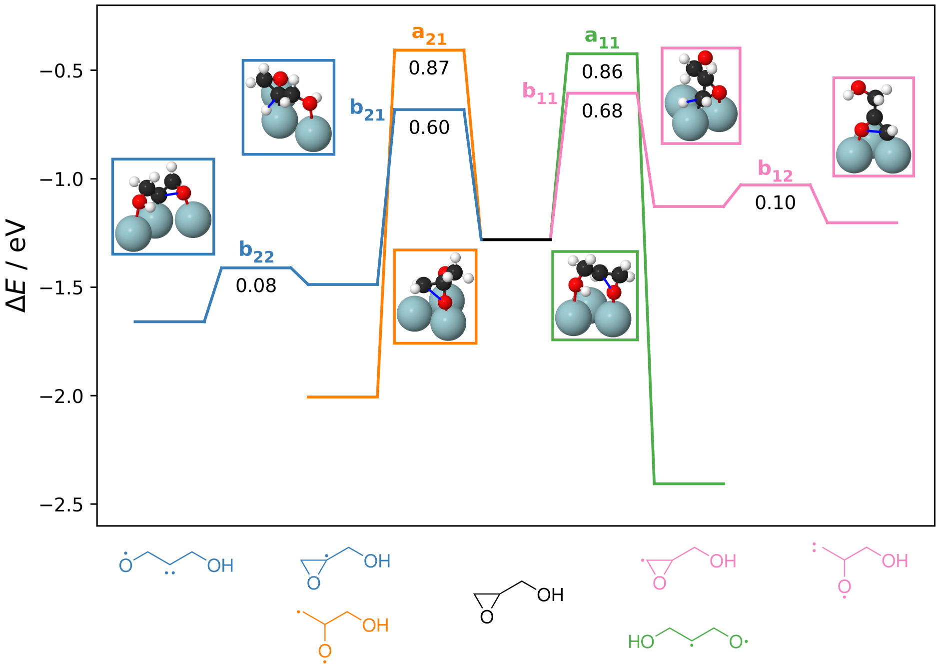

FIGURE 26 Potential energy surface and transition state geometries for glycidol on bare Rh(111).

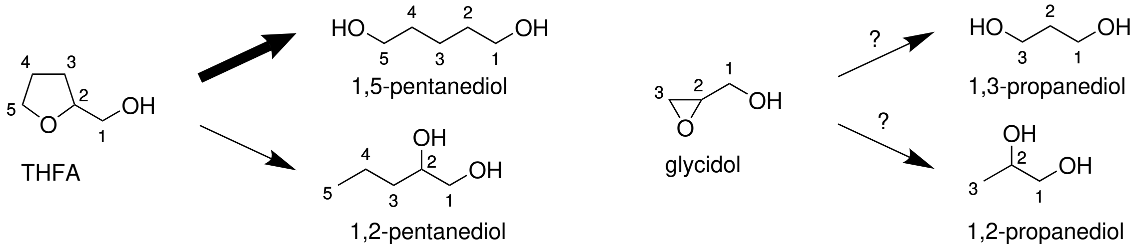

FIGURE 27 Possible ring-opening products of THFA and glycidol. Rh–ReO$_x$ selectively acid-catalyzes the ring opening of THFA into 1,5-propanediol,[51,173] but according to our results, does not acid-catalyze glycidol ring opening.

carbon 2 results in a more stable intermediate, which could be favored as the thermodynamic product. Interestingly, glycidol ring opening on late transition metal catalysts typically produces very little 1,3-PDO;[183–185] according to our simulations, the pathway toward 1,3-PDO should instead be mildly preferred. It is possible that the hydrogenation steps after ring opening are relevant for the product distribution. The simulations were also run with no H coverage, which is not the case under realistic hydrogenolysis conditions. The H coverage could be sufficiently high to inhibit C–H cleavage, and the metal-catalyzed ring opening may instead proceed through a hydride attack on an epoxide carbon. Such a reaction has been proposed to produce 1,2-PDO due to steric effects favoring hydride attack at the less substituted ring carbon 3.[180,186]

The role of an oxophilic metal modifier as a Brønsted acidic promoter in glycerol valorization was explored. Consistent with the literature, the selectivity toward

1,3-PDO was found to improve when ReOH was included, indicating that the acidic functionality is relevant in the catalytic mechanism. On the other hand, ReOH did not acid-catalyze the ring opening of glycidol, though it has been found to do so for larger ring structures. A similar computational study focusing on the alternative "hydride attack" mechanism would help further clarify the role of the modifier, which may also depend on the details of the structure and the reaction conditions. In particular, larger ReO_x models, possibly adsorbed rather than embedded, could facilitate different mechanisms by providing a wider variety of adsorption and acid sites.

4 CONCLUSIONS AND OUTLOOK

The work presented in this dissertation serves to improve the understanding of the properties of metal–oxide catalysts and the computational methods used to investigate them. The field has been investigated from many perspectives. In papers I and II, zirconia-supported metal clusters were studied with an eye toward the dynamic and ensemble properties. These studies are part of the ongoing effort to produce more realistic catalyst models in order to bridge the materials gap in catalysis. While valuable chemical insight can be obtained even from very simple model systems, understanding the features of real catalysts is crucial to enable rational catalyst design and fine-grained control over the stability, activity and selectivity. The dynamics and ensemble effects are key aspects that must be understood to account for the diverse chemical environment in a real catalytic system.

The cluster models studied in papers I and II were taken from global optimization calculations, which already represents a significant advance beyond simple models based on the Wulff[187] (or Winterbottom[188]) construction. Especially for small clusters on complex surfaces, the geometry can be heavily modulated by the surface interaction, diminishing the applicability of such models. In paper I, the description of the WGS reaction was refined by considering less stable cluster geometries in addition to the global minimum structures. Such clusters can be present in the system and catalytically relevant, especially at the elevated temperatures typical of realistic catalytic conditions. This way, some insight into the cluster ensemble could be obtained; the higher fluxionality and more exothermic water dissociation on NGM clusters were highlighted, indicating some ways in which the high-temperature ensemble can deviate from zero-Kelvin DFT models. Even on the GM clusters, the uniqueness of each interfacial reaction site was found to result in complicated and non-scaling adsorption and activity properties.

Of course, the ensemble is not a static collection of geometries, and the clusters can isomerize during the catalytic process. Paper II tackled some of the challenges in correctly describing the dynamics of catalytic systems using ab initio molecular dynamics. AIMD is well suited for studies of cluster dynamics, as the breaking and forming of metal–metal and metal–support bonds is central to the phenomenon and outside the capabilities of MD simulations based on conventional force fields. The method can also capture polarization effects and describe interfacial interactions without additional parametrization, making it useful for interfacial studies in general, though the high computational cost limits the attainable system size and time scale. More advanced force fields, such as reactive[189] and polarizable[190] ones, have been developed to describe these effects while avoiding expensive electronic structure calculations, though the parametrization is challenging for complex systems. Machine learning based force fields parameterized by ab initio calculations are being actively studied as a way to combine the accuracy of AIMD with the efficiency of classical MD.[191]

In addition to managing the computational cost, great care must be taken to obtain accurate, high-quality simulations and avoid anomalies such as temperature gradients or the flying ice cube effect, as shown in paper II. Especially in constant-temperature simulations, typical for studying catalytic conditions, maintaining the proper kinetic energy distribution is nontrivial, and the thermostatting and SCF convergence must be thoroughly tested and verified. As the issues may not be readily apparent from the log files or other condensed representations, they can only be reliably identified from the simulation trajectories themselves. This reinforces the importance of diligently analyzing the results, but also that of openly publishing full data sets, which is increasingly recognized as crucial for verification and reproduction purposes.[192]

The catalytic function of the metal–oxide interface can arise in various ways. In some systems, the interface can simply provide reaction sites in close proximity to two necessary functionalities; for instance, in paper IV, the Rh–ReOH active site studied for glycerol dehydration featured a metallic and an acidic component, with the metal accepting H from the reactant and the acid catalyzing the C–OH cleavage. The picture can also be more complicated, with the metal–oxide interaction altering the interfacial properties. One component can induce functionality in the other, such as in the case of the metal-enhanced oxide reducibility studied in paper III: the metal can provide its own function while also facilitating charge transfer or oxygen exchange with the oxide component. Such emergent multifunctionality can enable novel catalytic chemistry, but may not be easily predictable from the properties of the individual components. Understanding and rationally designing catalysts utilizing these concepts requires a thorough understanding of the detailed geometric and electronic structure at the interface.

From a computational standpoint, this understanding can be developed by improving the accuracy and widening the scope of interfacial simulations. Both approaches increase the usage of computational resources, and so the possibilities are partially determined by the technical progress made in computer science and engineering. Within DFT, the development of more accurate xc functionals is the most direct way toward higher accuracy, though the resource cost of "gold-standard" hybrid functionals remains high. Specific shortcomings of conventional DFT functionals can be addressed by various correction schemes, such as the Hubbard and Tkatchenko–Scheffler corrections discussed in this work. While these low-cost corrections can improve the description of the system when used judiciously, they are not universal solutions and can in some cases even make the results worse. Where applicable, such corrections can produce considerable resource savings, and correspondingly enable broader studies, by efficiently producing sufficiently accurate results.

Indeed, this concept of "sufficient accuracy" is key in computational work. If the methods or models are too simplified to describe the studied phenomenon, the results will be wrong or even completely meaningless. On the other hand, increasing the model or method complexity past a certain point will no longer produce accuracy gains commensurate to the incurred computational cost. Such "overoptimization" limits the possible scope of the study and wastes processor cycles. The necessary accuracy depends on the subject of the study, and has to be balanced between the model and the methods. For some purposes, a rough but wide screening is useful, while for others, the properties of a particular model must be calculated in great detail.

The breadth of computational studies can be extended in many dimensions. For catalysts with complicated structural features, large models are necessary to attain a good description of the system. In dynamics studies, long simulation times are required to sufficiently sample the phase space and produce accurate predictions of dynamic properties. Real catalysts feature a wide variety of structural features producing differing chemical environments, and sampling this structural space more thoroughly would provide a more complete picture of the catalytic system. In addition to the intrinsic variation in the catalyst geometry, the reactant and possible solvent can alter the properties of the active sites by simply blocking some of them or by inducing structural transformations.

Theoretical development is not only useful to improve the accuracy of computational methods. Equally valuable are conceptual advancements that facilitate the understanding of complicated systems and direct future work in fruitful directions. The activity volcano, d band model and BEP scaling relations are classic examples of successful predictive concepts in catalysis. Such models allow predictions and help reduce the conceptual complexity of catalytic systems, but also help identify interesting catalysts that deviate from the expected behavior. This area could prove challenging to develop using the emerging ML-based methods, which may produce good predictions for opaque reasons. On the other hand, by facilitating the production of large datasets, they can also expedite the discovery of relations and phenomena that can then be probed and explained by methods rooted in physics.

In summary, the work in this thesis has contributed in multiple ways to developing the description of the catalytic active sites on metal–oxide catalysts. Various metal–oxide models have been explored, and their properties, such as activity, selectivity, stability, reducibility and acidity, have been studied in detail using model reactions and analyses of the geometric and electronic structures of the active sites. To facilitate these investigations, many simulation and analysis methods were studied, implemented and developed, producing deeper methodological and technical understanding in addition to the attained chemical and catalytic knowledge. Further progress is required in all of these aspects in order to approach a realistic computational description of metal–oxide catalysts, which is crucial to understanding and predicting their properties.

BIBLIOGRAPHY

(1) Erisman, J. W.; Sutton, M. A.; Galloway, J.; Klimont, Z.; Winiwarter, W. How a century of ammonia synthesis changed the world. *Nat. Geosci.* **2008**, *1*, 636–639, DOI: 10.1038/ngeo325.

(2) Chorkendorff, I.; Niemantsverdriet, J. W., *Concepts of Modern Catalysis and Kinetics*, 3rd edition; Wiley-VCH: Weinheim, Germany, 2017.

(3) Nørskov, J. K.; Bligaard, T.; Rossmeisl, J.; Christensen, C. H. Towards the computational design of solid catalysts. *Nat. Chem.* **2009**, *1*, 37–46, DOI: 10.1038/nchem.121.

(4) Sabbe, M. K.; Reyniers, M.-F.; Reuter, K. First-principles kinetic modeling in heterogeneous catalysis: an industrial perspective on best-practice, gaps and needs. *Catal. Sci. Technol.* **2012**, *2*, 2010–2024, DOI: 10.1039/C2CY20261A.

(5) Hettel, M.; Wörner, M.; Deutschmann, O., Computational Fluid Dynamics of Catalytic Reactors In *Handbook of Materials Modeling – Applications: Current and Emerging Materials*, Andreoni, W., Ed., 2nd ed.; Springer International Publishing: 2018, pp 1–34, DOI: 10.1007/978-3-319-50257-1_6-1.

(6) Henkelman, G.; Jónsson, H. Long time scale kinetic Monte Carlo simulations without lattice approximation and predefined event table. *J. Chem. Phys.* **2001**, *115*, 9657–9666, DOI: 10.1063/1.1415500.

(7) Reuter, K., First-Principles Kinetic Monte Carlo Simulations for Heterogeneous Catalysis: Concepts, Status, and Frontiers In *Modeling and Simulation of Heterogeneous Catalytic Reactions*; John Wiley & Sons, Ltd: 2011; Chapter 3, pp 71–111, DOI: 10.1002/9783527639878.ch3.

(8) Motagamwala, A. H.; Dumesic, J. A. Microkinetic Modeling: A Tool for Rational Catalyst Design. *Chem. Rev.* **2021**, *121*, 1049–1076, DOI: 10.1021/acs.chemrev.0c00394.

(9) Chen, B. W. J.; Xu, L.; Mavrikakis, M. Computational Methods in Heterogeneous Catalysis. *Chem. Rev.* **2021**, *121*, 1007–1048, DOI: 10.1021/acs.chemrev.0c01060.

(10) Bruix, A.; Margraf, J. T.; Andersen, M.; Reuter, K. First-principles-based multiscale modelling of heterogeneous catalysis. *Nat. Catal.* **2019**, *2*, 659–670, DOI: 10.1038/s41929-019-0298-3.

(11) Hammer, B.; Nørskov, J. Electronic factors determining the reactivity of metal surfaces. *Surf. Sci.* **1995**, *343*, 211–220, DOI: 10.1016/0039-6028(96)80007-0.

(12) Van Santen, R. A.; Neurock, M.; Shetty, S. G. Reactivity Theory of Transition-Metal Surfaces: A Brønsted–Evans–Polanyi Linear Activation Energy–Free-Energy Analysis. *Chem. Rev.* **2010**, *110*, 2005–2048, DOI: 10.1021/cr9001808.

(13) Viñes, F.; Gomes, J. R. B.; Illas, F. Understanding the reactivity of metallic nanoparticles: beyond the extended surface model for catalysis. *Chem. Soc. Rev.* **2014**, *43*, 4922–4939, DOI: 10.1039/C3CS60421G.

(14) Pidko, E. A. Toward the Balance between the Reductionist and Systems Approaches in Computational Catalysis: Model versus Method Accuracy for the Description of Catalytic Systems. *ACS Catal.* **2017**, *7*, 4230–4234, DOI: 10.1021/acscatal.7b00290.

(15) Ro, I.; Resasco, J.; Christopher, P. Approaches for Understanding and Controlling Interfacial Effects in Oxide-Supported Metal Catalysts. *ACS Catal.* **2018**, *8*, 7368–7387, DOI: 10.1021/acscatal.8b02071.

(16) Bruix, A.; Rodriguez, J. A.; Ramírez, P. J.; Senanayake, S. D.; Evans, J.; Park, J. B.; Stacchiola, D.; Liu, P.; Hrbek, J.; Illas, F. A New Type of Strong Metal–Support Interaction and the Production of H_2 through the Transformation of Water on Pt/CeO_2(111) and Pt/CeO_x/TiO_2(110) Catalysts. *J. Am. Chem. Soc.* **2012**, *134*, 8968–8974, DOI: 10.1021/ja302070k.

(17) Heiz, U.; Sanchez, A.; Abbet, S.; Schneider, W.-D. Catalytic Oxidation of Carbon Monoxide on Monodispersed Platinum Clusters: Each Atom Counts. *J. Am. Chem. Soc.* **1999**, *121*, 3214–3217, DOI: 10.1021/ja983616l.

(18) Landman, U.; Yoon, B.; Zhang, C.; Heiz, U.; Arenz, M. Factors in gold nanocatalysis: oxidation of CO in the non-scalable size regime. *Top. Catal.* **2007**, *44*, 145–158, DOI: 10.1007/s11244-007-0288-6.

(19) Lykhach, Y.; Kozlov, S. M.; Skála, T.; Tovt, A.; Stetsovych, V.; Tsud, N.; Dvořák, F.; Johánek, V.; Neitzel, A.; Mysliveček, J.; Fabris, S.; Matolín, V.; Neyman, K. M.; Libuda, J. Counting electrons on supported nanoparticles. *Nat. Mater.* **2016**, *15*, 284–288, DOI: 10.1038/nmat4500.

(20) Li, Y.; Shen, W. Morphology-dependent nanocatalysts: Rod-shaped oxides. *Chem. Soc. Rev.* **2014**, *43*, 1543–1574, DOI: 10.1039/C3CS60296F.

(21) Sudarsanam, P.; Peeters, E.; Makshina, E. V.; Parvulescu, V. I.; Sels, B. F. Advances in porous and nanoscale catalysts for viable biomass conversion. *Chem. Soc. Rev.* **2019**, *48*, 2366–2421, DOI: 10.1039/C8CS00452H.

(22) Pacchioni, G. Role of Nanostructuring on the Properties of Oxide Materials: The Case of Zirconia Nanoparticles. *Eur. J. Inorg. Chem.* **2019**, *2019*, 751–761, DOI: 10.1002/ejic.201801314.

(23) Robinson, A. M.; Hensley, J. E.; Medlin, J. W. Bifunctional Catalysts for Upgrading of Biomass-Derived Oxygenates: A Review. *ACS Catal.* **2016**, *6*, 5026–5043, DOI: 10.1021/acscatal.6b00923.

(24) Liu, L.; Corma, A. Metal Catalysts for Heterogeneous Catalysis: From Single Atoms to Nanoclusters and Nanoparticles. *Chem. Rev.* **2018**, *118*, 4981–5079, DOI: 10.1021/acs.chemrev.7b00776.

(25) Green, I. X.; Tang, W.; Neurock, M.; Yates, J. T. Spectroscopic Observation of Dual Catalytic Sites During Oxidation of CO on a Au/TiO_2 Catalyst. *Science* **2011**, *333*, 736–739, DOI: 10.1126/science.1207272.

(26) Ishida, T.; Murayama, T.; Taketoshi, A.; Haruta, M. Importance of Size and Contact Structure of Gold Nanoparticles for the Genesis of Unique Catalytic Processes. *Chem. Rev.* **2020**, *120*, 464–525, DOI: 10.1021/acs.chemrev.9b00551.

(27) Bañares, M. A. Operando methodology: combination of in situ spectroscopy and simultaneous activity measurements under catalytic reaction conditions. *Catal. Today* **2005**, *100*, 71–77, DOI: 10.1016/j.cattod.2004.12.017.

(28) Ruiz Puigdollers, A.; Schlexer, P.; Tosoni, S.; Pacchioni, G. Increasing Oxide Reducibility: The Role of Metal/Oxide Interfaces in the Formation of Oxygen Vacancies. *ACS Catal.* **2017**, *7*, 6493–6513, DOI: 10.1021/acscatal.7b01913.

(29) Helali, Z.; Jedidi, A.; Syzgantseva, O. A.; Calatayud, M.; Minot, C. Scaling reducibility of metal oxides. *Theor. Chem. Acc.* **2017**, *136*, 100, DOI: 10.1007/s00214-017-2130-y.

(30) Paier, J.; Penschke, C.; Sauer, J. Oxygen Defects and Surface Chemistry of Ceria: Quantum Chemical Studies Compared to Experiment. *Chem. Rev.* **2013**, *113*, 3949–3985, DOI: 10.1021/cr3004949.

(31) Tauster, S. J.; Fung, S. C.; Garten, R. L. Strong metal-support interactions. Group 8 noble metals supported on titanium dioxide. *J. Am. Chem. Soc.* **1978**, *100*, 170–175, DOI: 10.1021/ja00469a029.

(32) Fu, Q.; Wagner, T. Interaction of nanostructured metal overlayers with oxide surfaces. *Surf. Sci. Rep.* **2007**, *62*, 431–498, DOI: 10.1016/j.surfrep.2007.07.001.

(33) Liu, X.; Liu, M.-H.; Luo, Y.-C.; Mou, C.-Y.; Lin, S. D.; Cheng, H.; Chen, J.-M.; Lee, J.-F.; Lin, T.-S. Strong Metal–Support Interactions between Gold Nanoparticles and ZnO Nanorods in CO Oxidation. *J. Am. Chem. Soc.* **2012**, *134*, 10251–10258, DOI: 10.1021/ja3033235.

(34) Metiu, H.; Chrétien, S.; Hu, Z.; Li, B.; Sun, X. Chemistry of Lewis Acid–Base Pairs on Oxide Surfaces. *J. Phys. Chem. C* **2012**, *116*, 10439–10450, DOI: 10.1021/jp301341t.

(35) Zhu, M.; Lai, J.-K.; Tumuluri, U.; Wu, Z.; Wachs, I. E. Nature of Active Sites and Surface Intermediates during SCR of NO with NH3 by Supported V2O5–WO3/TiO2 Catalysts. *J. Am. Chem. Soc.* **2017**, *139*, 15624–15627, DOI: 10.1021/jacs.7b09646.

(36) Baertsch, C. D.; Komala, K. T.; Chua, Y.-H.; Iglesia, E. Genesis of Brønsted Acid Sites during Dehydration of 2-Butanol on Tungsten Oxide Catalysts. *J. Catal.* **2002**, *205*, 44–57, DOI: 10.1006/jcat.2001.3426.

(37) Zhao, N.; Pan, D.; Nie, W.; Ji, X. Two-Phase Synthesis of Shape-Controlled Colloidal Zirconia Nanocrystals and Their Characterization. *J. Am. Chem. Soc.* **2006**, *128*, 10118–10124, DOI: 10.1021/ja0612145.

(38) Dastan, D. Effect of preparation methods on the properties of titania nanoparticles: solvothermal versus sol–gel. *Appl. Phys. A* **2017**, *123*, 699, DOI: 10.1007/s00339-017-1309-3.

(39) Xie, C.; Yan, D.; Li, H.; Du, S.; Chen, W.; Wang, Y.; Zou, Y.; Chen, R.; Wang, S. Defect Chemistry in Heterogeneous Catalysis: Recognition, Understanding, and Utilization. *ACS Catal.* **2020**, *10*, 11082–11098, DOI: 10.1021/acscatal.0c03034.

(40) Fernández-García, M.; Martínez-Arias, A.; Hanson, J. C.; Rodriguez, J. A. Nanostructured Oxides in Chemistry: Characterization and Properties. *Chem. Rev.* **2004**, *104*, 4063–4104, DOI: 10.1021/cr030032f.

(41) Ruiz Puigdollers, A.; Tosoni, S.; Pacchioni, G. Turning a Nonreducible into a Reducible Oxide via Nanostructuring: Opposite Behavior of Bulk ZrO2 and ZrO2 Nanoparticles Toward H2 Adsorption. *J. Phys. Chem. C* **2016**, *120*, 15329–15337, DOI: 10.1021/acs.jpcc.6b05984.

(42) Honkala, K.; Hellman, A.; Remediakis, I. N.; Logadottir, A.; Carlsson, A.; Dahl, S.; Christensen, C. H.; Nørskov, J. K. Ammonia Synthesis from First-Principles Calculations. *Science* **2005**, *307*, 555–558, DOI: 10.1126/science.1106435.

(43) Liu, J. Catalysis by Supported Single Metal Atoms. *ACS Catal.* **2017**, *7*, 34–59, DOI: 10.1021/acscatal.6b01534.

(44) Bazhenov, A. S.; Honkala, K. Globally Optimized Equilibrium Shapes of Zirconia-Supported Rh and Pt Nanoclusters: Insights into Site Assembly and Reactivity. *J. Phys. Chem. C* **2019**, *123*, 7209–7216, DOI: 10.1021/acs.jpcc.9b00272.

(45) Zhang, Z.; Zandkarimi, B.; Alexandrova, A. N. Ensembles of Metastable States Govern Heterogeneous Catalysis on Dynamic Interfaces. *Acc. Chem. Res.* **2020**, *53*, 447–458, DOI: 10.1021/acs.accounts.9b00531.

(46) Zhai, H.; Alexandrova, A. N. Fluxionality of Catalytic Clusters: When It Matters and How to Address It. *ACS Catal.* **2017**, *7*, 1905–1911, DOI: 10.1021/acscatal.6b03243.

(47) Hansen, T. W.; DeLaRiva, A. T.; Challa, S. R.; Datye, A. K. Sintering of Catalytic Nanoparticles: Particle Migration or Ostwald Ripening? *Acc. Chem. Res.* **2013**, *46*, 1720–1730, DOI: 10.1021/ar3002427.

(48) Wettergren, K.; Schweinberger, F. F.; Deiana, D.; Ridge, C. J.; Crampton, A. S.; Rötzer, M. D.; Hansen, T. W.; Zhdanov, V. P.; Heiz, U.; Langhammer, C. High Sintering Resistance of Size-Selected Platinum Cluster Catalysts by Suppressed Ostwald Ripening. *Nano Lett.* **2014**, *14*, 5803–5809, DOI: 10.1021/nl502686u.

(49) Farmer, J. A.; Campbell, C. T. Ceria Maintains Smaller Metal Catalyst Particles by Strong Metal-Support Bonding. *Science* **2010**, *329*, 933–936, DOI: 10.1126/science.1191778.

(50) Tomishige, K.; Nakagawa, Y.; Tamura, M. Selective hydrogenolysis and hydrogenation using metal catalysts directly modified with metal oxide species. *Green Chem.* **2017**, *19*, 2876–2924, DOI: 10.1039/C7GC00620A.

(51) Hibbitts, D.; Tan, Q.; Neurock, M. Acid strength and bifunctional catalytic behavior of alloys comprised of noble metals and oxophilic metal promoters. *J. Catal.* **2014**, *315*, 48–58, DOI: 10.1016/j.jcat.2014.03.016.

(52) Ten Dam, J.; Hanefeld, U. Renewable Chemicals: Dehydroxylation of Glycerol and Polyols. *ChemSusChem* **2011**, *4*, 1017–1034, DOI: doi.org/10.1002/cssc.201100162.

(53) Nakagawa, Y.; Tamura, M.; Tomishige, K. Catalytic materials for the hydrogenolysis of glycerol to 1,3-propanediol. *J. Mater. Chem. A* **2014**, *2*, 6688–6702, DOI: 10.1039/C3TA15384C.

(54) Besson, M.; Gallezot, P.; Pinel, C. Conversion of Biomass into Chemicals over Metal Catalysts. *Chem. Rev.* **2014**, *114*, 1827–1870, DOI: 10.1021/cr4002269.

(55) Reddy, B. M.; Patil, M. K. Organic Syntheses and Transformations Catalyzed by Sulfated Zirconia. *Chem. Rev.* **2009**, *109*, 2185–2208, DOI: 10.1021/cr900008m.

(56) Yan, G. X.; Wang, A.; Wachs, I. E.; Baltrusaitis, J. Critical review on the active site structure of sulfated zirconia catalysts and prospects in fuel production. *Appl. Catal., A* **2019**, *572*, 210–225, DOI: 10.1016/j.apcata.2018.12.012.

(57) Su, F.; Guo, Y. Advancements in solid acid catalysts for biodiesel production. *Green Chem.* **2014**, *16*, 2934–2957, DOI: 10.1039/C3GC42333F.

(58) Li, S.; Zheng, A.; Su, Y.; Zhang, H.; Chen, L.; Yang, J.; Ye, C.; Deng, F. Brønsted/Lewis Acid Synergy in Dealuminated HY Zeolite: A Combined Solid-State NMR and Theoretical Calculation Study. *J. Am. Chem. Soc.* **2007**, *129*, 11161–11171, DOI: 10.1021/ja072767y.

(59) Farrusseng, D.; Tuel, A. Perspectives on zeolite-encapsulated metal nanoparticles and their applications in catalysis. *New J. Chem.* **2016**, *40*, 3933–3949, DOI: 10.1039/C5NJ02608C.

(60) Wang, H.; Wang, L.; Xiao, F.-S. Metal@Zeolite Hybrid Materials for Catalysis. *ACS Cent. Sci.* **2020**, *6*, 1685–1697, DOI: 10.1021/acscentsci.0c01130.

(61) Hohenberg, P.; Kohn, W. Inhomogeneous Electron Gas. *Phys. Rev.* **1964**, *136*, B864–B871, DOI: 10.1103/PhysRev.136.B864.

(62) Kohn, W.; Sham, L. J. Self-Consistent Equations Including Exchange and Correlation Effects. *Phys. Rev.* **1965**, *140*, A1133–A1138, DOI: 10.1103/PhysRev.140.A1133.

(63) Perdew, J. P.; Yue, W. Accurate and simple density functional for the electronic exchange energy: Generalized gradient approximation. *Phys. Rev. B* **1986**, *33*, 8800–8802, DOI: 10.1103/PhysRevB.33.8800.

(64) Becke, A. D. Density-functional thermochemistry. III. The role of exact exchange. *J. Chem. Phys.* **1993**, *98*, 5648–5652, DOI: 10.1063/1.464913.

(65) Perdew, J. P.; Burke, K.; Ernzerhof, M. Generalized Gradient Approximation Made Simple. *Phys. Rev. Lett.* **1996**, *77*, 3865–3868, DOI: 10.1103/PhysRevLett.77.3865.

(66) Perdew, J. P.; Burke, K.; Ernzerhof, M. Generalized Gradient Approximation Made Simple [Phys. Rev. Lett. 77, 3865 (1996)]. *Phys. Rev. Lett.* **1997**, *78*, 1396–1396, DOI: 10.1103/PhysRevLett.78.1396.

(67) Perdew, J. P.; Chevary, J. A.; Vosko, S. H.; Jackson, K. A.; Pederson, M. R.; Singh, D. J.; Fiolhais, C. Atoms, molecules, solids, and surfaces: Applications of the generalized gradient approximation for exchange and correlation. *Phys. Rev. B* **1992**, *46*, 6671–6687, DOI: 10.1103/PhysRevB.46.6671.

(68) Becke, A. D. Density-functional exchange-energy approximation with correct asymptotic behavior. *Phys. Rev. A* **1988**, *38*, 3098–3100, DOI: 10.1103/PhysRevA.38.3098.

(69) Lee, C.; Yang, W.; Parr, R. G. Development of the Colle-Salvetti correlation-energy formula into a functional of the electron density. *Phys. Rev. B* **1988**, *37*, 785–789, DOI: 10.1103/PhysRevB.37.785.

(70) *A Primer in Density Functional Theory*; Fiolhais, C., Nogueira, F., Marques, M. A. L., Eds.; Lecture Notes in Physics; Springer Berlin: Heidelberg, Germany, 2003, DOI: 10.1007/3-540-37072-2.

(71) Kratzer, P.; Neugebauer, J. The Basics of Electronic Structure Theory for Periodic Systems. *Front. Chem.* **2019**, *7*, DOI: 10.3389/fchem.2019.00106.

(72) Monkhorst, H. J.; Pack, J. D. Special points for Brillouin-zone integrations. *Phys. Rev. B* **1976**, *13*, 5188–5192, DOI: 10.1103/PhysRevB.13.5188.

(73) Blöchl, P. E. Projector augmented-wave method. *Phys. Rev. B* **1994**, *50*, 17953–17979, DOI: 10.1103/PhysRevB.50.17953.

(74) Mortensen, J. J.; Hansen, L. B.; Jacobsen, K. W. Real-space grid implementation of the projector augmented wave method. *Phys. Rev. B* **2005**, *71*, 035109, DOI: 10.1103/PhysRevB.71.035109.

(75) Enkovaara, J. et al. Electronic structure calculations with GPAW: a real-space implementation of the projector augmented-wave method. *J. Phys.: Condens. Matter* **2010**, *22*, 253202, DOI: 10.1088/0953-8984/22/25/253202.

(76) Larsen, A. H. et al. The atomic simulation environment—a Python library for working with atoms. *J. Phys.: Condens. Matter* **2017**, *29*, 273002, DOI: 10.1088/1361-648x/aa680e.

(77) Hamann, D. R.; Schlüter, M.; Chiang, C. Norm-Conserving Pseudopotentials. *Phys. Rev. Lett.* **1979**, *43*, 1494–1497, DOI: 10.1103/PhysRevLett.43.1494.

(78) Vanderbilt, D. Soft self-consistent pseudopotentials in a generalized eigenvalue formalism. *Phys. Rev. B* **1990**, *41*, 7892–7895, DOI: 10.1103/PhysRevB.41.7892.

(79) Slater, J. C. Wave Functions in a Periodic Potential. *Phys. Rev.* **1937**, *51*, 846–851, DOI: 10.1103/PhysRev.51.846.

(80) Andersen, O. K. Linear methods in band theory. *Phys. Rev. B* **1975**, *12*, 3060–3083, DOI: 10.1103/PhysRevB.12.3060.

(81) Rostgaard, C. The Projector Augmented-wave Method, 2009, DOI: 10.48550/ARXIV.0910.1921.

(82) Mori-Sánchez, P.; Cohen, A. J.; Yang, W. Localization and Delocalization Errors in Density Functional Theory and Implications for Band-Gap Prediction. *Phys. Rev. Lett.* **2008**, *100*, 146401, DOI: 10.1103/PhysRevLett.100.146401.

(83) Perdew, J. P.; Zunger, A. Self-interaction correction to density-functional approximations for many-electron systems. *Phys. Rev. B* **1981**, *23*, 5048–5079, DOI: 10.1103/PhysRevB.23.5048.

(84) Himmetoglu, B.; Floris, A.; de Gironcoli, S.; Cococcioni, M. Hubbard-corrected DFT energy functionals: The LDA+U description of correlated systems. *Int. J. Quantum Chem.* **2014**, *114*, 14–49, DOI: 10.1002/qua.24521.

(85) Anisimov, V. I.; Zaanen, J.; Andersen, O. K. Band theory and Mott insulators: Hubbard U instead of Stoner I. *Phys. Rev. B* **1991**, *44*, 943–954, DOI: 10.1103/PhysRevB.44.943.

(86) Verma, P.; Truhlar, D. G. Does DFT+U mimic hybrid density functionals? *Theor. Chem. Acc.* **2016**, *135*, 182, DOI: 10.1007/s00214-016-1927-4.

(87) Zhao, Q.; Kulik, H. J. Where Does the Density Localize in the Solid State? Divergent Behavior for Hybrids and DFT+U. *J. Chem. Theory Comput.* **2018**, *14*, 670–683, DOI: 10.1021/acs.jctc.7b01061.

(88) Curtarolo, S.; Setyawan, W.; Hart, G. L.; Jahnatek, M.; Chepulskii, R. V.; Taylor, R. H.; Wang, S.; Xue, J.; Yang, K.; Levy, O.; Mehl, M. J.; Stokes, H. T.; Demchenko, D. O.; Morgan, D. AFLOW: An automatic framework for high-throughput materials discovery. *Comput. Mater. Sci.* **2012**, *58*, 218–226, DOI: 10.1016/j.commatsci.2012.02.005.

(89) Xu, Y.; Elcoro, L.; Song, Z.-D.; Wieder, B. J.; Vergniory, M. G.; Regnault, N.; Chen, Y.; Felser, C.; Bernevig, B. A. High-throughput calculations of magnetic topological materials. *Nature* **2020**, *586*, 702–707, DOI: 10.1038/s41586-020-2837-0.

(90) Dudarev, S. L.; Botton, G. A.; Savrasov, S. Y.; Humphreys, C. J.; Sutton, A. P. Electron-energy-loss spectra and the structural stability of nickel oxide: An LSDA+U study. *Phys. Rev. B* **1998**, *57*, 1505–1509, DOI: 10.1103/PhysRevB.57.1505.

(91) Rohrbach, A.; Hafner, J.; Kresse, G. Molecular adsorption on the surface of strongly correlated transition-metal oxides: A case study for CO/NiO(100). *Phys. Rev. B* **2004**, *69*, 075413, DOI: 10.1103/PhysRevB.69.075413.

(92) Perdew, J. P.; Levy, M. Physical Content of the Exact Kohn-Sham Orbital Energies: Band Gaps and Derivative Discontinuities. *Phys. Rev. Lett.* **1983**, *51*, 1884–1887, DOI: 10.1103/PhysRevLett.51.1884.

(93) Perdew, J. P.; Parr, R. G.; Levy, M.; Balduz, J. L. Density-Functional Theory for Fractional Particle Number: Derivative Discontinuities of the Energy. *Phys. Rev. Lett.* **1982**, *49*, 1691–1694, DOI: 10.1103/PhysRevLett.49.1691.

(94) DOI: https://wiki.fysik.dtu.dk/gpaw/tutorialsexercises/energetics/hubbardu/hubbardu.html#scaling-the-hubbard-correction.

(95) Capdevila-Cortada, M.; Łodziana, Z.; López, N. Performance of DFT+U Approaches in the Study of Catalytic Materials. *ACS Catal.* **2016**, *6*, 8370–8379, DOI: 10.1021/acscatal.6b01907.

(96) Kulik, H. J.; Marzari, N. Systematic study of first-row transition-metal diatomic molecules: A self-consistent DFT+U approach. *J. Chem. Phys.* **2010**, *133*, 114103, DOI: 10.1063/1.3489110.

(97) O'Regan, D. D.; Hine, N. D. M.; Payne, M. C.; Mostofi, A. A. Projector self-consistent DFT + U using nonorthogonal generalized Wannier functions. *Phys. Rev. B* **2010**, *82*, 081102, DOI: 10.1103/PhysRevB.82.081102.

(98) Pickett, W. E.; Erwin, S. C.; Ethridge, E. C. Reformulation of the LDA + U method for a local-orbital basis. *Phys. Rev. B* **1998**, *58*, 1201–1209, DOI: 10.1103/PhysRevB.58.1201.

(99) Hsu, H.; Umemoto, K.; Cococcioni, M.; Wentzcovitch, R. First-principles study for low-spin $LaCoO_3$ with a structurally consistent Hubbard U. *Phys. Rev. B* **2009**, *79*, 125124, DOI: 10.1103/PhysRevB.79.125124.

(100) Kulik, H. J.; Marzari, N. Accurate potential energy surfaces with a DFT+U(R) approach. *J. Chem. Phys.* **2011**, *135*, 194105, DOI: 10.1063/1.3660353.

(101) Cococcioni, M.; de Gironcoli, S. Linear response approach to the calculation of the effective interaction parameters in the LDA + U method. *Phys. Rev. B* **2005**, *71*, 035105, DOI: 10.1103/PhysRevB.71.035105.

(102) Kulik, H. J.; Cococcioni, M.; Scherlis, D. A.; Marzari, N. Density Functional Theory in Transition-Metal Chemistry: A Self-Consistent Hubbard U Approach. *Phys. Rev. Lett.* **2006**, *97*, 103001, DOI: 10.1103/PhysRevLett.97.103001.

(103) Timrov, I.; Marzari, N.; Cococcioni, M. Hubbard parameters from density-functional perturbation theory. *Phys. Rev. B* **2018**, *98*, 085127, DOI: 10.1103/PhysRevB.98.085127.

(104) Yu, M.; Yang, S.; Wu, C.; Marom, N. Machine learning the Hubbard U parameter in DFT+U using Bayesian optimization. *npj Comput. Mater.* **2020**, *6*, 180, DOI: 10.1038/s41524-020-00446-9.

(105) Cococcioni, M. A LDA+U study of selected iron compounds, Ph.D. Thesis, SISSA, Trieste, 2002, DOI: 20.500.11767/3939.

(106) Leiria Campo Jr, V.; Cococcioni, M. Extended DFT $+ U + V$ method with on-site and inter-site electronic interactions. *J. Phys.: Condens. Matter* **2010**, *22*, 055602, DOI: 10.1088/0953-8984/22/5/055602.

(107) DOI: http://hjkgrp.mit.edu/tutorials/2011-05-31-calculating-hubbard-u/.

(108) Tkatchenko, A.; Scheffler, M. Accurate Molecular Van Der Waals Interactions from Ground-State Electron Density and Free-Atom Reference Data. *Phys. Rev. Lett.* **2009**, *102*, 073005, DOI: 10.1103/PhysRevLett.102.073005.

(109) Chu, X.; Dalgarno, A. Linear response time-dependent density functional theory for van der Waals coefficients. *J. Chem. Phys.* **2004**, *121*, 4083–4088, DOI: 10.1063/1.1779576.

(110) Gould, T.; Bučko, T. C_6 Coefficients and Dipole Polarizabilities for All Atoms and Many Ions in Rows 1–6 of the Periodic Table. *J. Chem. Theory Comput.* **2016**, *12*, 3603–3613, DOI: 10.1021/acs.jctc.6b00361.

(111) Kebede, G. G.; Spångberg, D.; Mitev, P. D.; Broqvist, P.; Hermansson, K. Comparing van der Waals DFT methods for water on NaCl(001) and MgO(001). *J. Chem. Phys.* **2017**, *146*, 064703, DOI: 10.1063/1.4971790.

(112) Hirshfeld, F. L. Bonded-atom fragments for describing molecular charge densities. *Theor. Chim. Acta* **1977**, *44*, 129–138, DOI: 10.1007/BF00549096.

(113) Bondi, A. van der Waals Volumes and Radii. *J. Phys. Chem.* **1964**, *68*, 441–451, DOI: 10.1021/j100785a001.

(114) Bader, R. F. W., *Atoms in Molecules*; International Series of Monographs on Chemistry; Clarendon Press: Oxford, England, 1994.

(115) Henkelman, G.; Arnaldsson, A.; Jónsson, H. A fast and robust algorithm for Bader decomposition of charge density. *Comput. Mater. Sci.* **2006**, *36*, 354–360, DOI: 10.1016/j.commatsci.2005.04.010.

(116) Sanville, E.; Kenny, S. D.; Smith, R.; Henkelman, G. Improved grid-based algorithm for Bader charge allocation. *J. Comput. Chem.* **2007**, *28*, 899–908, DOI: 10.1002/jcc.20575.

(117) Tang, W.; Sanville, E.; Henkelman, G. A grid-based Bader analysis algorithm without lattice bias. *J. Phys.: Condens. Matter* **2009**, *21*, 084204, DOI: 10.1088/0953-8984/21/8/084204.

(118) Yu, M.; Trinkle, D. R. Accurate and efficient algorithm for Bader charge integration. *J. Chem. Phys.* **2011**, *134*, 064111, DOI: 10.1063/1.3553716.

(119) Makov, G.; Payne, M. C. Periodic boundary conditions in ab initio calculations. *Phys. Rev. B* **1995**, *51*, 4014–4022, DOI: 10.1103/PhysRevB.51.4014.

(120) Lany, S.; Zunger, A. Assessment of correction methods for the band-gap problem and for finite-size effects in supercell defect calculations: Case studies for ZnO and GaAs. *Phys. Rev. B* **2008**, *78*, 235104, DOI: 10.1103/PhysRevB.78.235104.

(121) Lany, S.; Zunger, A. Accurate prediction of defect properties in density functional supercell calculations. *Modell. Simul. Mater. Sci. Eng.* **2009**, *17*, 084002, DOI: 10.1088/0965-0393/17/8/084002.

(122) Freysoldt, C.; Neugebauer, J.; Van de Walle, C. G. Fully Ab Initio Finite-Size Corrections for Charged-Defect Supercell Calculations. *Phys. Rev. Lett.* **2009**, *102*, 016402, DOI: 10.1103/PhysRevLett.102.016402.

(123) Alkauskas, A.; Broqvist, P.; Pasquarello, A. Defect Energy Levels in Density Functional Calculations: Alignment and Band Gap Problem. *Phys. Rev. Lett.* **2008**, *101*, 046405, DOI: 10.1103/PhysRevLett.101.046405.

(124) Jones, A. J.; Iglesia, E. The Strength of Brønsted Acid Sites in Microporous Aluminosilicates. *ACS Catal.* **2015**, *5*, 5741–5755, DOI: 10.1021/acscatal.5b01133.

(125) Komsa, H.-P.; Pasquarello, A. Finite-Size Supercell Correction for Charged Defects at Surfaces and Interfaces. *Phys. Rev. Lett.* **2013**, *110*, 095505, DOI: 10.1103/PhysRevLett.110.095505.

(126) Freysoldt, C.; Neugebauer, J. First-principles calculations for charged defects at surfaces, interfaces, and two-dimensional materials in the presence of electric fields. *Phys. Rev. B* **2018**, *97*, 205425, DOI: 10.1103/PhysRevB.97.205425.

(127) Häkkinen, H.; Moseler, M.; Landman, U. Bonding in Cu, Ag, and Au Clusters: Relativistic Effects, Trends, and Surprises. *Phys. Rev. Lett.* **2002**, *89*, 033401, DOI: 10.1103/PhysRevLett.89.033401.

(128) Jónsson, H.; Mills, G.; Jacobsen, K. W., Nudged elastic band method for finding minimum energy paths of transitions In *Classical and Quantum Dynamics in Condensed Phase Simulations*, Berne, B. J., Ciccotti, G., Coker, D. F., Eds.; World Scientific: 1998, pp 385–404, DOI: 10.1142/9789812839664_0016.

(129) Kolsbjerg, E. L.; Groves, M. N.; Hammer, B. An automated nudged elastic band method. *J. Chem. Phys.* **2016**, *145*, 094107, DOI: 10.1063/1.4961868.

(130) Smidstrup, S.; Pedersen, A.; Stokbro, K.; Jónsson, H. Improved initial guess for minimum energy path calculations. *J. Chem. Phys.* **2014**, *140*, 214106, DOI: 10.1063/1.4878664.

(131) Henkelman, G.; Uberuaga, B. P.; Jónsson, H. A climbing image nudged elastic band method for finding saddle points and minimum energy paths. *J. Chem. Phys.* **2000**, *113*, 9901–9904, DOI: 10.1063/1.1329672.

(132) DOI: https://github.com/chc273/mep.

(133) Calle-Vallejo, F.; Bandarenka, A. S. Enabling Generalized Coordination Numbers to Describe Strain Effects. *ChemSusChem* **2018**, *11*, 1824–1828, DOI: 10.1002/cssc.201800569.

(134) Calle-Vallejo, F.; Martínez, J. I.; García-Lastra, J. M.; Sautet, P.; Loffreda, D. Fast Prediction of Adsorption Properties for Platinum Nanocatalysts with Generalized Coordination Numbers. *Angew. Chem., Int. Ed.* **2014**, *53*, 8316–8319, DOI: 10.1002/anie.201402958.

(135) Tuckerman, M. E. *Ab initio* molecular dynamics: basic concepts, current trends and novel applications. *J. Phys.: Condens. Matter* **2002**, *14*, R1297–R1355, DOI: 10.1088/0953-8984/14/50/202.

(136) Zhao, X.; Liu, Y. Unveiling the Active Structure of Single Nickel Atom Catalysis: Critical Roles of Charge Capacity and Hydrogen Bonding. *J. Am. Chem. Soc.* **2020**, *142*, 5773–5777, DOI: 10.1021/jacs.9b13872.

(137) Woodcock, L. Isothermal molecular dynamics calculations for liquid salts. *Chem. Phys. Lett.* **1971**, *10*, 257–261, DOI: 10.1016/0009-2614(71)80281-6.

(138) Harvey, S. C.; Tan, R. K.-Z.; Cheatham III, T. E. The flying ice cube: Velocity rescaling in molecular dynamics leads to violation of energy equipartition. *J. Comput. Chem.* **1998**, *19*, 726–740, DOI: 10.1002/(SICI)1096-987X(199805)19:7<726::AID-JCC4>3.0.CO;2-S.

(139) Braun, E.; Moosavi, S. M.; Smit, B. Anomalous Effects of Velocity Rescaling Algorithms: The Flying Ice Cube Effect Revisited. *J. Chem. Theory Comput.* **2018**, *14*, 5262–5272, DOI: 10.1021/acs.jctc.8b00446.

(140) Lingenheil, M.; Denschlag, R.; Reichold, R.; Tavan, P. The "Hot-Solvent/Cold-Solute" Problem Revisited. *J. Chem. Theory Comput.* **2008**, *4*, 1293–1306, DOI: 10.1021/ct8000365.

(141) Mor, A.; Ziv, G.; Levy, Y. Simulations of proteins with inhomogeneous degrees of freedom: The effect of thermostats. *J. Comput. Chem.* **2008**, *29*, 1992–1998, DOI: 10.1002/jcc.20951.

(142) Herbert, J. M.; Head-Gordon, M. Accelerated, energy-conserving Born–Oppenheimer molecular dynamics via Fock matrix extrapolation. *Phys. Chem. Chem. Phys.* **2005**, *7*, 3269–3275, DOI: 10.1039/B509494A.

(143) Martínez, E.; Cawkwell, M. J.; Voter, A. F.; Niklasson, A. M. N. Thermostating extended Lagrangian Born-Oppenheimer molecular dynamics. *J. Chem. Phys.* **2015**, *142*, 154120, DOI: 10.1063/1.4917546.

(144) Pulay, P.; Fogarasi, G. Fock matrix dynamics. *Chem. Phys. Lett.* **2004**, *386*, 272–278, DOI: 10.1016/j.cplett.2004.01.069.

(145) Berendsen, H. J. C.; Postma, J. P. M.; van Gunsteren, W. F.; DiNola, A.; Haak, J. R. Molecular dynamics with coupling to an external bath. *J. Chem. Phys.* **1984**, *81*, 3684–3690, DOI: 10.1063/1.448118.

(146) Hoover, W. G. Canonical dynamics: Equilibrium phase-space distributions. *Phys. Rev. A* **1985**, *31*, 1695–1697, DOI: 10.1103/PhysRevA.31.1695.

(147) Wang, D.; Liu, Z.-P.; Yang, W.-M. Revealing the Size Effect of Platinum Cocatalyst for Photocatalytic Hydrogen Evolution on TiO_2 Support: A DFT Study. *ACS Catal.* **2018**, *8*, 7270–7278, DOI: 10.1021/acscatal.8b01886.

(148) Wang, Y.-H.; Zheng, S.; Yang, W.-M.; Zhou, R.-Y.; He, Q.-F.; Radjenovic, P.; Dong, J.-C.; Li, S.; Zheng, J.; Yang, Z.-L.; Attard, G.; Pan, F.; Tian, Z.-Q.; Li, J.-F. In situ Raman spectroscopy reveals the structure and dissociation of interfacial water. *Nature* **2021**, *600*, 81–85, DOI: 10.1038/s41586-021-04068-z.

(149) Fazio, G.; Selli, D.; Ferraro, L.; Seifert, G.; Di Valentin, C. Curved TiO_2 Nanoparticles in Water: Short (Chemical) and Long (Physical) Range Interfacial Effects. *ACS Appl. Mater. Interfaces* **2018**, *10*, 29943–29953, DOI: 10.1021/acsami.8b08172.

(150) Bagger, A.; Arnarson, L.; Hansen, M. H.; Spohr, E.; Rossmeisl, J. Electrochemical CO Reduction: A Property of the Electrochemical Interface. *J. Am. Chem. Soc.* **2019**, *141*, 1506–1514, DOI: 10.1021/jacs.8b08839.

(151) Schneider, T.; Stoll, E. Molecular-dynamics study of a three-dimensional one-component model for distortive phase transitions. *Phys. Rev. B* **1978**, *17*, 1302–1322, DOI: 10.1103/PhysRevB.17.1302.

(152) Basconi, J. E.; Shirts, M. R. Effects of Temperature Control Algorithms on Transport Properties and Kinetics in Molecular Dynamics Simulations. *J. Chem. Theory Comput.* **2013**, *9*, 2887–2899, DOI: 10.1021/ct400109a.

(153) Martyna, G. J.; Klein, M. L.; Tuckerman, M. Nosé–Hoover chains: The canonical ensemble via continuous dynamics. *J. Chem. Phys.* **1992**, *97*, 2635–2643, DOI: 10.1063/1.463940.

(154) Melchionna, S.; Ciccotti, G.; Holian, B. L. Hoover NPT dynamics for systems varying in shape and size. *Mol. Phys.* **1993**, *78*, 533–544, DOI: 10.1080/00268979300100371.

(155) Melchionna, S. Constrained systems and statistical distribution. *Phys. Rev. E* **2000**, *61*, 6165–6170, DOI: 10.1103/PhysRevE.61.6165.

(156) Lin, S.-T.; Maiti, P. K.; Goddard, W. A. Two-Phase Thermodynamic Model for Efficient and Accurate Absolute Entropy of Water from Molecular Dynamics Simulations. *J. Phys. Chem. B* **2010**, *114*, 8191–8198, DOI: 10.1021/jp103120q.

(157) Caro, M. A.; Laurila, T.; Lopez-Acevedo, O. Accurate schemes for calculation of thermodynamic properties of liquid mixtures from molecular dynamics simulations. *J. Chem. Phys.* **2016**, *145*, 244504, DOI: 10.1063/1.4973001.

(158) Zandkarimi, B.; Alexandrova, A. N. Dynamics of Subnanometer Pt Clusters Can Break the Scaling Relationships in Catalysis. *J. Phys. Chem. Lett.* **2019**, *10*, 460–467, DOI: 10.1021/acs.jpclett.8b03680.

(159) Bartók, A. P.; Kondor, R.; Csányi, G. On representing chemical environments. *Phys. Rev. B* **2013**, *87*, 184115, DOI: 10.1103/PhysRevB.87.184115.

(160) Halldin Stenlid, J.; Johansson, A. J.; Brinck, T. The local electron attachment energy and the electrostatic potential as descriptors of surface–adsorbate interactions. *Phys. Chem. Chem. Phys.* **2019**, *21*, 17001–17009, DOI: 10.1039/C9CP03099A.

(161) Parr, R. G.; Yang, W. Density functional approach to the frontier-electron theory of chemical reactivity. *J. Am. Chem. Soc.* **1984**, *106*, 4049–4050, DOI: 10.1021/ja00326a036.

(162) Cheng, A.; Merz, K. M. Application of the Nosé–Hoover Chain Algorithm to the Study of Protein Dynamics. *J. Phys. Chem.* **1996**, *100*, 1927–1937, DOI: 10.1021/jp951968y.

(163) Nosé, S. A unified formulation of the constant temperature molecular dynamics methods. *J. Chem. Phys.* **1984**, *81*, 511–519, DOI: 10.1063/1.447334.

(164) Nosé, S. A molecular dynamics method for simulations in the canonical ensemble. *Mol. Phys.* **1984**, *52*, 255–268, DOI: 10.1080/00268978400101201.

(165) Tuckerman, M., *Statistical Mechanics: Theory and Molecular Simulation*; Oxford University Press: 2010.

(166) Bazhenov, A. S.; Kauppinen, M. M.; Honkala, K. DFT Prediction of Enhanced Reducibility of Monoclinic Zirconia upon Rhodium Deposition. *J. Phys. Chem. C* **2018**, *122*, 6774–6778, DOI: 10.1021/acs.jpcc.8b01046.

(167) Matveev, A. V.; Neyman, K. M.; Yudanov, I. V.; Rösch, N. Adsorption of transition metal atoms on oxygen vacancies and regular sites of the MgO(001) surface. *Surf. Sci.* **1999**, *426*, 123–139, DOI: 10.1016/S0039-6028(99)00327-1.

(168) Wang, Y.; Florez, E.; Mondragon, F.; Truong, T. N. Effects of metal–support interactions on the electronic structures of metal atoms adsorbed on the perfect and defective MgO(100) surfaces. *Surf. Sci.* **2006**, *600*, 1703–1713, DOI: 10.1016/j.susc.2005.12.062.

(169) Jung, C.; Ishimoto, R.; Tsuboi, H.; Koyama, M.; Endou, A.; Kubo, M.; Del Carpio, C. A.; Miyamoto, A. Interfacial properties of ZrO_2 supported precious metal catalysts: A density functional study. *Appl. Catal., A* **2006**, *305*, 102–109, DOI: 10.1016/j.apcata.2006.02.050.

(170) Grau-Crespo, R.; Hernández, N. C.; Sanz, J. F.; de Leeuw, N. H. Theoretical Investigation of the Deposition of Cu, Ag, and Au Atoms on the ZrO_2(111) Surface. *J. Phys. Chem. C* **2007**, *111*, 10448–10454, DOI: 10.1021/jp0704057.

(171) Auneau, F.; Michel, C.; Delbecq, F.; Pinel, C.; Sautet, P. Unravelling the Mechanism of Glycerol Hydrogenolysis over Rhodium Catalyst through Combined Experimental–Theoretical Investigations. *Chem. – Eur. J.* **2011**, *17*, 14288–14299, DOI: 10.1002/chem.201101318.

(172) Shinmi, Y.; Koso, S.; Kubota, T.; Nakagawa, Y.; Tomishige, K. Modification of Rh/SiO_2 catalyst for the hydrogenolysis of glycerol in water. *Appl. Catal., B* **2010**, *94*, 318–326, DOI: 10.1016/j.apcatb.2009.11.021.

(173) Chia, M.; Pagán-Torres, Y. J.; Hibbitts, D.; Tan, Q.; Pham, H. N.; Datye, A. K.; Neurock, M.; Davis, R. J.; Dumesic, J. A. Selective Hydrogenolysis of Polyols and Cyclic Ethers over Bifunctional Surface Sites on Rhodium–Rhenium Catalysts. *J. Am. Chem. Soc.* **2011**, *133*, 12675–12689, DOI: 10.1021/ja2038358.

(174) Koso, S.; Watanabe, H.; Okumura, K.; Nakagawa, Y.; Tomishige, K. Comparative study of Rh–MoO_x and Rh–ReO_x supported on SiO_2 for the hydrogenolysis of ethers and polyols. *Appl. Catal., B* **2012**, *111-112*, 27–37, DOI: 10.1016/j.apcatb.2011.09.015.

(175) Amada, Y.; Shinmi, Y.; Koso, S.; Kubota, T.; Nakagawa, Y.; Tomishige, K. Reaction mechanism of the glycerol hydrogenolysis to 1,3-propanediol over Ir–ReO_x/SiO_2 catalyst. *Appl. Catal., B* **2011**, *105*, 117–127, DOI: 10.1016/j.apcatb.2011.04.001.

(176) Varghese, J. J.; Cao, L.; Robertson, C.; Yang, Y.; Gladden, L. F.; Lapkin, A. A.; Mushrif, S. H. Synergistic Contribution of the Acidic Metal Oxide–Metal Couple and Solvent Environment in the Selective Hydrogenolysis of Glycerol: A Combined Experimental and Computational Study Using ReO_x–-Ir as the Catalyst. *ACS Catal.* **2019**, *9*, 485–503, DOI: 10.1021/acscatal.8b03079.

(177) Liu, L.; Asano, T.; Nakagawa, Y.; Tamura, M.; Okumura, K.; Tomishige, K. Selective Hydrogenolysis of Glycerol to 1,3-Propanediol over Rhenium-Oxide-Modified Iridium Nanoparticles Coating Rutile Titania Support. *ACS Catal.* **2019**, *9*, 10913–10930, DOI: 10.1021/acscatal.9b03824.

(178) Koso, S.; Furikado, I.; Shimao, A.; Miyazawa, T.; Kunimori, K.; Tomishige, K. Chemoselective hydrogenolysis of tetrahydrofurfuryl alcohol to 1,5-pentanediol. *Chem. Commun.* **2009**, 2035–2037, DOI: 10.1039/B822942B.

(179) Chen, K.; Koso, S.; Kubota, T.; Nakagawa, Y.; Tomishige, K. Chemoselective Hydrogenolysis of Tetrahydropyran-2-methanol to 1,6-Hexanediol over Rhenium-Modified Carbon-Supported Rhodium Catalysts. *ChemCatChem* **2010**, *2*, 547–555, DOI: 10.1002/cctc.201000018.

(180) Koso, S.; Nakagawa, Y.; Tomishige, K. Mechanism of the hydrogenolysis of ethers over silica-supported rhodium catalyst modified with rhenium oxide. *J. Catal.* **2011**, *280*, 221–229, DOI: 10.1016/j.jcat.2011.03.018.

(181) Prete, P.; Cespi, D.; Passarini, F.; Capacchione, C.; Proto, A.; Cucciniello, R. Glycidol syntheses and valorizations: Boosting the glycerol biorefinery. *Curr. Opin. Green Sustainable Chem.* **2022**, *35*, 100624, DOI: 10.1016/j.cogsc.2022.100624.

(182) Guan, J.; Li, J.; Yu, Y.; Mu, X.; Chen, A. DFT Studies of the Selective C–O Hydrogenolysis and Ring-Opening of Biomass-Derived Tetrahydrofurfuryl Alcohol over Rh(111) surfaces. *J. Phys. Chem. C* **2016**, *120*, 19124–19134, DOI: 10.1021/acs.jpcc.6b05026.

(183) Sajiki, H.; Hattori, K.; Hirota, K. Pd/C(en)-catalyzed regioselective hydrogenolysis of terminal epoxides to secondary alcohols. *Chem. Commun.* **1999**, 1041–1042, DOI: 10.1039/A902213I.

(184) Cucciniello, R.; Pironti, C.; Capacchione, C.; Proto, A.; Di Serio, M. Efficient and selective conversion of glycidol to 1,2-propanediol over Pd/C catalyst. *Catal. Commun.* **2016**, *77*, 98–102, DOI: 10.1016/j.catcom.2016.01.026.

(185) Sun, Y.; Cai, Z.; Li, X.; Chen, P.; Hou, Z. Selective synthesis of 1,3-propanediol from glycidol over a carbon film encapsulated Co catalyst. *Catal. Sci. Technol.* **2019**, *9*, 5022–5030, DOI: 10.1039/C9CY01162E.

(186) Gebretsadik, F.; Ruiz-Martinez, J.; Salagre, P.; Cesteros, Y. Glycidol hydrogenolysis on a cheap mesoporous acid saponite supported Ni catalyst as alternative approach to 1,3-propanediol synthesis. *Appl. Catal., A* **2017**, *538*, 91–98, DOI: 10.1016/j.apcata.2017.03.018.

(187) Herring, C. Some Theorems on the Free Energies of Crystal Surfaces. *Phys. Rev.* **1951**, *82*, 87–93, DOI: 10.1103/PhysRev.82.87.

(188) Winterbottom, W. Equilibrium shape of a small particle in contact with a foreign substrate. *Acta Metall.* **1967**, *15*, 303–310, DOI: 10.1016/0001-6160(67)90206-4.

(189) Senftle, T. P.; Hong, S.; Islam, M. M.; Kylasa, S. B.; Zheng, Y.; Shin, Y. K.; Junkermeier, C.; Engel-Herbert, R.; Janik, M. J.; Aktulga, H. M.; Verstraelen, T.; Grama, A.; van Duin, A. C. T. The ReaxFF reactive force-field: development, applications and future directions. *npj Comput. Mater.* **2016**, *2*, 15011, DOI: 10.1038/npjcompumats.2015.11.

(190) Warshel, A.; Kato, M.; Pisliakov, A. V. Polarizable Force Fields: History, Test Cases, and Prospects. *J. Chem. Theory Comput.* **2007**, *3*, 2034–2045, DOI: 10.1021/ct700127w.

(191) Behler, J. Perspective: Machine learning potentials for atomistic simulations. *J. Chem. Phys.* **2016**, *145*, 170901, DOI: 10.1063/1.4966192.

(192) Coudert, F.-X. Reproducible Research in Computational Chemistry of Materials. *Chem. Mater.* **2017**, *29*, 2615–2617, DOI: 10.1021/acs.chemmater.7b00799.

ORIGINAL PAPERS

I

ESCAPING SCALING RELATIONSHIPS FOR WATER DISSOCIATION AT INTERFACIAL SITES OF ZIRCONIA-SUPPORTED RH AND PT CLUSTERS

by

Minttu M. Kauppinen, Ville Korpelin, Anand Mohan Verma, Marko M. Melander, and Karoliina Honkala

The Journal of Chemical Physics **2019**, 151, 164302

DOI:10.1063/1.5126261

The Journal of Chemical Physics ARTICLE scitation.org/journal/jcp

Escaping scaling relationships for water dissociation at interfacial sites of zirconia-supported Rh and Pt clusters

Cite as: J. Chem. Phys. 151, 164302 (2019); doi: 10.1063/1.5126261
Submitted: 2 September 2019 • Accepted: 2 October 2019 •
Published Online: 22 October 2019

Minttu M. Kauppinen,[a] **Ville Korpelin,**[a] **Anand Mohan Verma,** **Marko M. Melander,**
and Karoliina Honkala[b]

AFFILIATIONS

Department of Chemistry, Nanoscience Center, University of Jyväskylä, P.O. Box 35 (YN), Jyväskylä FI-40014, Finland

Note: The paper is part of the JCP Special Topic Collection on Catalytic Properties of Model Supported Nanoparticles.
[a] **Contributions:** M. M. Kauppinen and V. Korpelin contributed equally to this work.
[b] karoliina.honkala@jyu.fi

ABSTRACT

Water dissociation is an important reaction involved in many industrial processes. In this computational study, the dissociation of water is used as a model reaction for probing the activity of interfacial sites of globally optimized ZrO_2 supported Pt and Rh clusters under the framework of density functional theory. Our findings demonstrate that the perimeter sites of these small clusters can activate water, but the dissociation behavior varies considerably between sites. It is shown that the studied clusters break scaling relationships for water dissociation, suggesting that these catalysts may achieve activities beyond the maximum imposed by such relations. Furthermore, we observed large differences in the thermodynamics of the water dissociation reaction between global minimum and near-global minimum isomers of the clusters. Overall, our results highlight the uniqueness of interfacial sites in catalytic reactions and the need for developing new concepts and tools to deal with the associated complexity.

I. INTRODUCTION

The dissociation of water into hydroxyl and hydrogen species plays a key role in many industrially relevant processes, such as the water-gas shift (WGS) reaction and steam reforming. The water dissociation reaction has been studied computationally over a number of different systems such as clean metal surfaces [e.g., Cu(111),[1] Au(111),[1] Pt(111),[1,2] Rh(111)[1,2]] and unsupported metal clusters (e.g., Cu,[3] Au,[3] Pt,[2] and Rh[2]). Varying activation energies are reported for ideal metal surfaces, ranging from as low as 0.67[4] to 0.96[1] eV on Ni(111), ~0.8 eV over Pt(111)[1,5] and Rh(111),[2,6] and even as high as ~2 eV over Au(111).[1,7] Numerous studies strongly advocate the vital role of support, and the metal-support interface, for the overall catalytic activity.[6,8–12] Therefore, both the metal and the support should be considered when investigating such systems computationally. The choice of the supported metal catalyst model is nontrivial; typical models employ either supported finite clusters or nanorods, and different metal-support combinations have been investigated (e.g., Au/MgO,[7] Cu/ZrO_2,[13] Rh/ZrO_2,[6] Ni/Al_2O_3,[9] and Pt/CeO_2[10]). In contrast to clean metal surfaces, on the metal-support interfaces such as Ni/Al_2O_3,[9] Rh/ZrO_2,[6] Cu/ZrO_2,[13] and Au/TiO_2,[14] the barriers are reported to be much lower than those on the corresponding pure metals.

In our current study, we use globally optimized supported clusters to model zirconia-supported rhodium and platinum catalysts. Both materials have been found to be active toward the WGS reaction,[15,16] and Rh/ZrO_2 is also active for H_2 oxidation[17] and the partial oxidation of methane.[18] Recent studies have highlighted the importance of considering the catalyst as an ensemble of clusters with similar energies rather than as the static minimum energy structure.[19–22] While the clusters may spend most of their time as the global minimum (GM) structure, at reaction conditions there is available energy for them to isomerize to one of the structures lying only slightly higher in energy. These near-global minimum (NGM) structures can be more reactive than the most stable isomer and may even dominate catalytic activity while being minority species.[20] With this in mind, we have investigated the GM as well as NGM structures of zirconia-supported rhodium and platinum clusters of different sizes.

Multiple ways to escape traditional scaling relations have been proposed for heterogeneous catalysts,[23] among which the fluxionality under reaction conditions[24] and the presence of multiple different adsorption sites[25] are highly relevant for small, supported clusters. The absence of scaling relations makes it difficult to predict activation energies; however, it also provides a way to improve catalyst performance beyond a previously proposed maximum.[26] The Brønsted–Evans–Polanyi (BEP) relation[27] between the reaction energy and barrier for water dissociation over extended transition metal surfaces has been established before, and oxygen atom adsorption energy was found to be a good descriptor for the reaction.[28] Over unsupported Rh and Pt nanoparticles, the transition state (TS) energies were found to correlate well with water adsorption energies across different sites.[2] The descriptors in this case were the projected d-band center and coordination number of the surface atoms forming the site, which also correlated linearly with the transition state energies.[2] However, the extended surfaces were observed to not fit in the same scaling relation as the nanoparticles.

In this study, we focus on the water dissociation reaction at the perimeter sites of GM and NGM isomers of supported Rh and Pt clusters. The activation energies are compared to the reaction energies in order to establish a BEP relation to predict the activity of interfacial sites toward water dissociation. Transition-state scaling between the initial (or final) state and the transition state energy is also evaluated. Next, we compare the thermodynamics of the water dissociation reaction on the GM and NGM structures. Finally, we screen hydrogen adsorption sites on the clusters, and the adsorption energies are compared to the strain-adjusted generalized coordination numbers (SGCN)[29] of the sites, as well as the smooth overlap of atomic position (SOAP)[30] descriptor. Our results further highlight the importance of thorough consideration of the interface sites of small fluxional clusters and the heterogeneity and catalytic behavior found at the perimeter of such clusters.

II. COMPUTATIONAL DETAILS

All density functional theory (DFT) calculations were carried out in the projector-augmented wave (PAW)[31] formalism of DFT as implemented in the GPAW 1.4.0 package.[32–34] The Perdew–Burke–Ernzerhof (PBE) functional[35,36] was used to describe the exchange and correlation effects under the generalized gradient approximation (GGA). The core electrons of all elements were described by PAW setups in the frozen-core approximation. Setups with 15 and 16 valence electrons were used for Rh and Pt, respectively. The maximum spacing for the real-space grid basis was 0.2 Å, a value our group has previously used successfully for related systems.[2,6,37–39] The reciprocal space was sampled at the Γ point.

The interface model was built using 13 and 19 metal atom clusters (Pt and Rh) dispersed over monoclinic zirconia, $m\text{-ZrO}_2(\bar{1}11)$, as support. The Rh_{13}, Rh_{19}, Pt_{13}, and Pt_{19} clusters supported on $m\text{-ZrO}_2(\bar{1}11)$ were modeled using the globally optimized geometries discovered in previous work by our group.[39] In that study, the global optimizations using a genetic algorithm (GA) were carried out for three sizes (13, 19, and 43 atoms) of Rh and Pt clusters over the $m\text{-ZrO}_2(\bar{1}11)$ support. For each M/ZrO_2 system, three optimization runs were performed starting from randomly generated populations. The offspring was created using cut-and-splice crossover (70% probability) and mutation (30% probability) operations. First, metal atoms were allowed to relax (f_{max} = 0.08 eV/Å) over a fixed 3 × 3 single layer ZrO_2 surface. The resulting structures from all GA runs were merged, and for the 60 lowest energy structures, the metal fragments were cut and adsorbed over a 2 layers thick (bottom layer fixed) 3 × 3 ZrO_2 support. Finally, the optimization runs were carried out until the maximum residual forces reached below 0.05 eV/Å. Overall, ~9900 M/ZrO_2 structures were screened. For further details, please see Ref. 39.

The $m\text{-ZrO}_2(\bar{1}11)$ support was selected because of its representation of the most stable polymorph at the considered WGS reaction conditions and $(\bar{1}11)$ being the most stable facet. The oxide support was described by a slab model consisting of 3 × 3 unit cells with a thickness of two stoichiometric layers. All global minimum (GM) Rh_{13}/ZrO_2, Rh_{19}/ZrO_2, Pt_{13}/ZrO_2, and Pt_{19}/ZrO_2 catalyst structures are depicted in Fig. 1. We also employed near-global minimum (NGM) isomers lying higher in energy studied by our research group[39] to compare the energetics with their respective global minimum catalytic systems (see Fig. 1). The NGM clusters were chosen based on geometrical as well as energetic considerations; we picked NGM geometries that were noticeably different from the GM clusters and whose energies were within roughly 1 eV of the global minima. The relative instabilities of the chosen NGM isomers of Rh_{13}, Rh_{19}, Pt_{13}, and Pt_{19} clusters compared to their respective GM clusters were calculated as 0.80, 1.33, 0.56, and 0.35 eV, respectively. The gas-phase reference for molecular water was computed in a nonperiodic cell of size 17.5 × 16.0 × 16.6 Å.

In the geometry optimizations, the bottom layer of the zirconia slab was kept frozen to its initial geometry, while the top zirconia layer, the metal cluster, and the adsorbed atoms were allowed to relax until the maximum residual force reached below 0.05 eV Å^{-1}. We consider this an acceptable criterion, considering the large sizes of our systems with about 2000 valence electrons; the choice is also consistent with our work on the global optimization of these clusters.[39] The transition state structures of water dissociation reactions at various interfacial sites were located using the climbing-image nudged elastic band (CI-NEB) method.[40–43] The obtained transition state structures were confirmed by harmonic vibrational analysis with the presence of an imaginary frequency mode corresponding to the reaction coordinate.

The adsorption energies of molecular and dissociated water were computed as

$$E_{\text{ads}} = E_{\text{total}} - E_{\text{M}_X/\text{ZrO}_2} - E_{\text{H}_2\text{O}(g)}, \qquad (1)$$

where E_{total} is the energy of the optimized supported cluster and the water molecule (or dissociated water). $E_{\text{M}_X/\text{ZrO}_2}$ is the energy of the supported metal cluster, where M corresponds to either Pt or Rh and X is either 13 or 19. $E_{\text{H}_2\text{O}(g)}$ is the computed energy of the gas-phase water molecule under nonperiodic boundary conditions. The reaction energy of water dissociation is defined as

$$\Delta E = E_{\text{ads}}(\text{OH} + \text{H}) - E_{\text{ads}}(\text{H}_2\text{O}). \qquad (2)$$

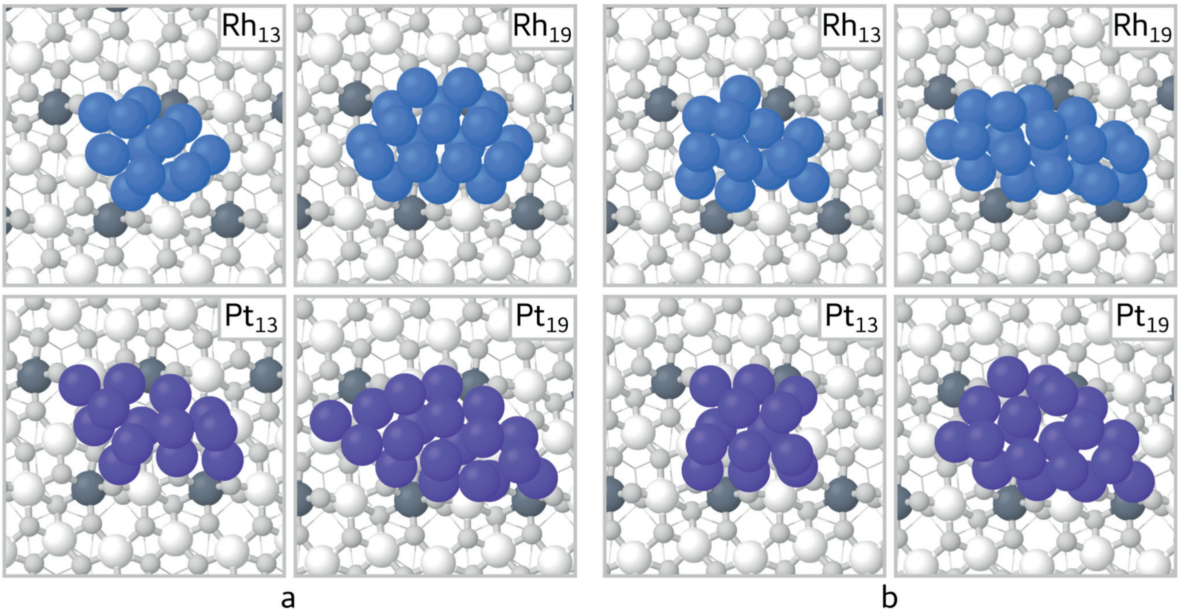

FIG. 1. Structure geometries of (a) global minimum and (b) near-global minimum zirconia-supported Rh_{13}, Rh_{19}, Pt_{13}, and Pt_{19} clusters. Rh, Pt, and O atoms are colored blue, purple, and light gray, respectively. High-coordinated Zr atoms are colored dark gray, while lower-coordinated Zr are colored white.

A. Generalized coordination numbers

Following Ref. 44, the generalized coordination number (GCN) of cluster atom i is defined as

$$\mathrm{GCN}(i) = \sum_{j}^{n_i} \frac{\mathrm{CN}(j)}{\mathrm{CN}_{\mathrm{max}}(j)}, \qquad (3)$$

where j runs over the nearest neighbors of atom i, n_i is the number of nearest neighbors for atom i, CN(j) is the conventional coordination number of atom j, and $\mathrm{CN}_{\mathrm{max}}(j)$ is the maximum coordination number of atom j (12 for an fcc metal; 7 for Zr; and 3 or 4 for O). To account for bridge and hollow sites s, the definition is extended as follows:

$$\mathrm{GCN}(s) = \frac{\mathrm{CN}_{\mathrm{max}}(\mathrm{fcc})}{\mathrm{CN}_{\mathrm{max}}(s)} \sum_{j} \frac{\mathrm{CN}(j)}{\mathrm{CN}_{\mathrm{max}}(j)}. \qquad (4)$$

Here, $\mathrm{CN}_{\mathrm{max}}(s) = 12$, 18, 22, or 26, for top, bridge, 3-fold, or 4-fold hollow sites, respectively, and $\mathrm{CN}_{\mathrm{max}}(\mathrm{fcc}) = 12$. The index j runs over the nearest neighbors of the atoms that define the adsorption site, without double-counting any atoms. This is a slightly generalized version of the definition in Ref. 44 to allow for the inclusion of atoms other than fcc metals.

The GCNs were refined by considering strain effects for the metal cluster atoms.[29] This is done by including a factor describing the ratio of the optimal bulk bond length d_{bulk} to the particular metal–metal bond length $d(i, j)$,

$$\mathrm{SGCN}(i) = \sum_{j} \frac{d_{\mathrm{bulk}}}{d(i,j)} \frac{\mathrm{CN}(j)}{\mathrm{CN}_{\mathrm{max}}(j)}, \qquad (5)$$

where SGCN denotes strain-adjusted GCN. A similar strain adjustment can be written for Eq. (4). In the site calculations, if a neighbor of the site was coordinated to multiple site-defining atoms, the average distance was used to determine the strain adjustment.

III. RESULTS

A. Water adsorption and dissociation at global minimum cluster-support interfaces

The molecular adsorption of water at interfacial sites of the zirconia-supported global minimum Rh_{13}, Rh_{19}, Pt_{13}, and Pt_{19} clusters was thoroughly screened. The starting geometries were chosen based on results from previous studies concerning water adsorption on Rh and Pt,[2] ZrO_2,[37] and the Rh–ZrO_2 interface,[6] which show that water should preferably adsorb on the oxide sites rather than on the metal. Therefore, we initially deposited molecular water on each of the Zr top sites in the immediate vicinity of the clusters, sitting almost horizontally with one hydrogen pointing toward the cluster. The optimized adsorption geometries are depicted in Fig. 2 along with their adsorption energies as bar charts. The data can also be found in the supplementary material in a tabular form (Table S1). Please note that the geometry optimizations were performed for one deposited water molecule at a time, and in Fig. 2, for brevity's sake, the molecules are shown in a single image with the cluster being in its optimized geometry.

Upon optimization, some water molecules moved far away from the cluster, while some moved to be adsorbed on a Rh/Pt top site instead of the Zr top site (labeled 5 and 7 for Rh_{13} and 7, 9, and 11

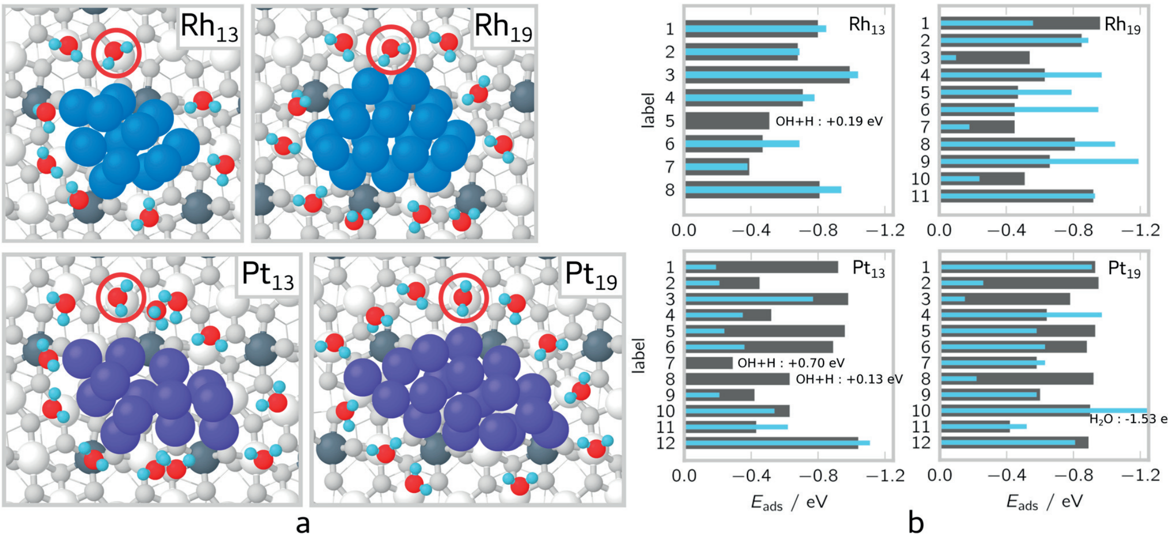

FIG. 2. (a) H_2O adsorption geometries and (b) molecular and dissociative adsorption energies on global minimum Rh_{13}, Rh_{19}, Pt_{13}, and Pt_{19} clusters. Oxygen atoms that are not part of the support are colored red, while hydrogen atoms are colored light blue. For the rest of the atom colors, please refer to Fig. 1. H_2O molecules are labeled clockwise starting from H_2O indicated in each case with a red circle (labeled "1"). The H_2O adsorption energies are indicated with gray bars, while OH + H adsorption energies are indicated with blue bars.

for Pt_{13} in Fig. 2). All such water molecules were initially deposited on high-coordinated Zr atoms (colored dark gray in Fig. 2). While most surface Zr atoms are bound to 6 lattice oxygens, the high-coordinated ones are bound to 7, rendering them unable to adsorb water at all. The molecules that moved far away from the cluster were omitted from Fig. 2 as well as further calculations since they were deemed to be too far from the interface to be activated by it.

The adsorption energies display significant variation along the perimeters of all clusters. For instance, over Rh_{13}/ZrO_2 and Rh_{19}/ZrO_2, the adsorption energies range from −0.99 to −0.32 eV and from −0.96 to −0.45 eV, respectively. This roughly spans the whole range of adsorption energies previously calculated for Rh(111) and $m\text{-}ZrO_2(\bar{1}11)$ surfaces, with the weakest adsorption energy being comparable to that of Rh(111) (−0.34 eV)[2] and the strongest to that of $m\text{-}ZrO_2(\bar{1}11)$ (−1.01 eV).[37]

Over Pt_{13}/ZrO_2 and Pt_{19}/ZrO_2, the adsorption energies range from −1.04 to −0.29 eV and from −0.95 to −0.42 eV, respectively. Like in the case of Rh clusters, the strongest adsorption energies are comparable to the adsorption energy found on bare zirconia, and the weakest are similar to the adsorption energy found on Pt(111).[2]

The bare $ZrO_2(\bar{1}11)$ presents four Zr atoms per unit cell, and water adsorption energies vary from one Zr top site to the next.[37] The weakest adsorption energy on the pristine zirconia corresponds to the high-coordinated Zr cation, and as discussed above, water cannot adsorb atop these Zr at the interface. Another factor is the formation of hydrogen bonds to the surface oxygen atoms, which is different from one site to the next.[37] However, the rest of the variance in adsorption strength cannot be explained only by comparing the Zr sites to those on pure zirconia. One possible explanation could be that the presence of the metal cluster changes the coordination of the Zr cations as well as the surface oxygen atoms; however, the irregular shape and size of the clusters means that the effect is unpredictable.

Dissociative adsorption geometries of water at the global minimum clusters were optimized for the same interface sites as the molecular adsorption. Starting geometries were constructed by moving one of the hydrogen atoms to the nearest promising adsorption site (e.g., nearest hollow) on the metal, with OH staying at the original water adsorption site. Geometries were allowed to fully relax, and in some cases, hydrogen diffused quite far away from the initial placement. In the case of the Pt_{13} cluster, three dissociated water structures (H_2O labeled 2, 3, and 12) preferably have the hydrogen sitting on an interfacial surface oxygen atom instead of the metal site. The OH species generally stayed near their initial positions, with some of them moving closer to the cluster to bind through the O atom to both Zr and Rh. This bridge-bonded geometry was previously also found for the nanorod model of the Rh–ZrO_2 interface.[6] On the Rh_{13} cluster, two structures (H_2O labeled 5 and 7) were found with OH preferably binding to a Rh top site, which was the original H_2O adsorption site. The same applies for Pt_{13} structures with H_2O labels 7, 9, and 11.

As in the case of molecular water, dissociative adsorption energies vary significantly from site to site (see Fig. 2 and Table S1 in the supplementary material for details). On average, the water dissociation reaction is mildly exothermic at the Rh cluster interfaces but slightly endothermic at the Pt cluster interfaces. On the extended Rh(111) surface, the reaction has been found to be weakly exothermic by ~0.1 eV,[2,6] while on the extended Pt(111) surface, the reaction is moderately endothermic by ca. 0.3 eV.[2,45] The difference in reaction energies between Rh and Pt has previously been shown to be less pronounced for gas-phase nanoclusters than for extended surfaces.[2] Here, although the average reaction energies between the clusters are comparable to each other, comparing reaction energies between roughly equivalent sites reveals how different the water dissociation energetics are between the clusters. For instance, H_2O label 1 occupies the same Zr top site on all systems, and while the molecular adsorption energies are very similar, the OH + H adsorption energies and therefore the reaction energies are different. One explanation may be that the hydrogen adsorption strength varies since it adsorbs on completely different sites on the clusters. Furthermore, the Zr sites are not exactly equivalent due to the presence of the clusters. In general, all of the clusters include some sites at their perimeter where water dissociation is thermodynamically more favorable than on the extended metal (111) and m-$ZrO_2(\bar{1}11)$ surfaces and some sites where water dissociation is unfeasible.

In order to supplement the results obtained from the adsorption energy calculations, we analyzed the scaling between molecular and dissociated water adsorption energies. The obtained scaling plots of OH + H vs H_2O adsorption energies show very poor R^2 values for all clusters (see Figs. S1–S4 of the supplementary material for details), except for Rh_{13}/ZrO_2 which has a slightly better value (R^2 = 0.80, slope = 0.71). Thus, the energies of the initial and final states of the dissociation reaction do not scale with each other at the Rh_{19}, Pt_{13}, and Pt_{19} cluster perimeters. For these clusters, a particular site may bind both molecular water and dissociated water equally well, or it might bind one weaker or stronger than the other. Note that only sites for which activation energies were determined are included in the scaling relationships and that sites where dissociation does not occur "across" the interface (H_2O adsorbs on metal/OH and H both adsorb on oxide or metal) were excluded from the analysis. The exclusion of outliers does not lead to any significant improvement of the R^2 values, except for Rh_{13}/ZrO_2 for which there is no scaling (R^2 = 0.18) between the initial and final state energies if all sites are included.

B. Activation energies

A thorough screening of transition state (TS) structures at the interfacial sites was carried out over the Pt_{13}/ZrO_2 and Rh_{13}/ZrO_2 clusters. To reduce the computational cost, five transition state calculations across the interface were performed over the Pt_{19}/ZrO_2 and Rh_{19}/ZrO_2 clusters. Over the M_{19} (M = Rh or Pt) clusters, we selected water molecules for TS calculations solely based on geometry so that each water is adsorbed on a Zr top site with one hydrogen pointing toward the cluster (see Tables S2 and S3 in the supplementary material). The transition state structures corresponding to the lowest barriers are depicted in Fig. 3. All activation energies pertaining to each cluster are supplied in Tables S2 and S3 of the supplementary material along with the corresponding imaginary frequencies, as well as O–H and M–H bond lengths.

Locating transition state structures at the asymmetric metal-oxide interfacial sites has its fair share of complications. We came across a few examples where the dissociation occurred at the nearby metal sites or over the zirconia surface instead of across the interface. Therefore, careful observation is mandatory while dealing with interfacial reactions over asymmetric cluster models. We note that the abovementioned TS cases were removed from our scaling relationships, but full data and further discussion are provided in Table S3 and Sec. I of the supplementary material.

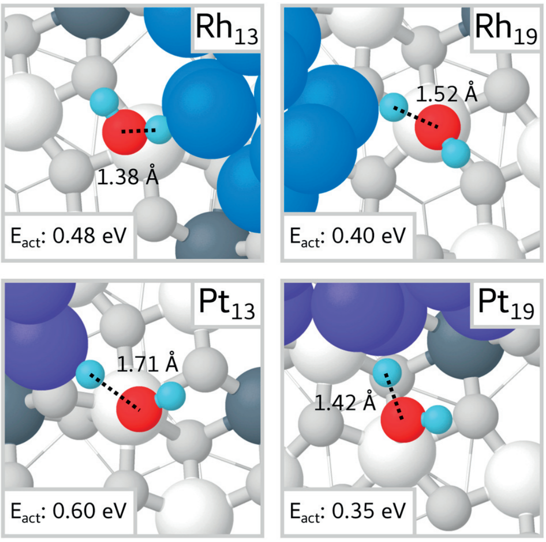

FIG. 3. Transition states corresponding to the lowest water dissociation barrier.

The forward activation energies over the Pt_{13} and Rh_{13} clusters range from 0.60 to 1.13 eV and from 0.48 to 0.81 eV, respectively. Over the Pt_{19} and Rh_{19} clusters, the forward activation energies range from 0.35 to 0.76 eV and from 0.40 to 0.88 eV, respectively. The varying nature of the activation energies, even between Zr sites that are equivalent on the bare surface, can partially be attributed to the different Zr coordinations due to cluster asymmetries. Therefore, similar to the adsorption strengths of H_2O and OH + H, there is no predictability between the type of Zr site and barrier height. The M_{19} and Rh_{13} clusters exhibit a similar range of barriers, whereas Pt_{13} has slightly higher barriers. Interestingly, over Rh clusters, lower barriers often correspond to lower water binding strengths, but Pt clusters show mixed behavior and there is no relation between adsorption energies and barriers.

The smallest calculated activation energies are lower compared to clean Rh(111) and Pt(111) surfaces and unsupported Rh_{147} and Pt_{147} metal nanoparticles (~0.72 eV).[1,2,6] The present metal-oxide interfaces also perform better in terms of activation energy compared to the Cu/ZrO_2[13] and Au/MgO interfaces[7] for the activation of water. Evidently, the results for Rh-based clusters are in good agreement with the Rh/ZrO_2 rod model interface (E_{act} = 0.35 eV) previously studied by our research group.[6] The lowest activation energies over the Rh_{19} and Rh_{13} clusters differ only by 0.05 eV and 0.13 eV from that on the rod model interface. The larger difference observed for Rh_{13} may be explained by its smaller size.

Although the barriers obtained for the activation of water over the present cluster interfaces are lower or similar compared to various metal-oxide catalysts, they are still higher compared to the pure zirconia surface. Our research group has previously found the activation of water over pure zirconia to be spontaneous and mildly exothermic.[6] Therefore, the water activation might occur over zirconia first, followed by hydrogen diffusion to the metal frame. The diffusion of a hydrogen atom on m-$ZrO_2(\bar{1}11)$ is likely a complex process, as there exist multiple possible pathways for diffusion. Under reaction conditions, the behavior is further complicated by the adsorbate (e.g., hydroxyl) coverage of the surface.[46] As an example, we have simulated the diffusion of H from a 2-coordinated lattice oxygen atom to the nearest lattice oxygen on the ideal m-$ZrO_2(\bar{1}11)$ surface and found the activation energy to be fairly high at about 1.3 eV. We emphasize that this value corresponds to one possible route out of many, and a thorough analysis of diffusion pathways is required to definitively describe the diffusion behavior.

The presence of hydrogen at the metal site is desired for further reaction with CO in the WGS process because, as previously observed, CO strongly prefers metal sites.[6,7,13] Interestingly, we found a few cases in our study where the water molecule preferably dissociated onto a ZrO_2 lattice oxygen next to the cluster. In these cases, H_2O is initially hydrogen bonded to a 2-coordinated surface oxygen atom, facilitating the dissociation onto it. The barriers for such dissociations range between 0.04 and 0.75 eV, meaning that the cluster can impede the ordinarily spontaneous dissociation on zirconia to varying degrees. With regard to the diffusion of H from oxide to metal, we found two paths on Pt_{13} with diffusion barriers of 0.60 and 1.10 eV. On a Rh/ZrO_2 rod model using similar computational methods as in the present work (please see Ref. 6 for details), the oxide-to-metal H diffusion barrier was found to be 0.62 eV. These barriers are of comparable magnitude to those of water dissociation across the cluster-oxide interface, suggesting that both pathways could supply H to the cluster.

The Brønsted–Evans–Polanyi (BEP) relationships based on forward activation energies and reaction energies were studied in order to further analyze the results obtained from the calculations. They demonstrated weak trends over Rh_{13}, Rh_{19}, and Pt_{13} clusters, as indicated by low R^2 values. Interestingly, the Pt_{19} cluster delivers an improved trend ($R^2 = 0.83$) compared to the other systems. We note that the M_{19} relationships contained only five data points, and therefore, a slight difference in correlation cannot be ruled out with a larger number of data. A BEP relation with an R^2 value of 0.54 has been reported earlier for dissociation over numerous clean metal surfaces.[28]

We also analyzed the transition state scaling (TSS) relationships based on the adsorption energies of TS and molecular water (initial state) or dissociated water (final state). The Pt_{19} cluster delivered a good linear trend based on the TS and final states of water with an R^2 value of 0.89. This correlation arises from the fact that the TS structures resemble the final states on the Pt_{19} cluster. Other systems expressed no dependencies between two considered parameters. In comparison with the present models, the unsupported Rh and Pt nanoparticles previously investigated by our research group exhibited R^2 values of 0.92 and 0.85, respectively.[2] Furthermore, we studied the bonding patterns in the TS structures in relation to their adsorption energies. There was no observed correlation between O–H bond lengths and E_{ads} of TS structures over any cluster. The trend between Rh–H bond lengths and E_{ads} (TS) over Rh_{19} showed a little improvement but not to a significant level. Moreover, no dependencies were found in between M–H bond lengths and E_{ads} of TS structures over other clusters.

C. Water adsorption over near-global minimum catalytic systems

Next, we address the thermodynamics of dissociative water adsorption over systems with near-global minimum (NGM) cluster isomers and compare the values to those obtained on the global minima. The initial geometries for both molecular and dissociated water were built in the same way as on the GM clusters, and the optimization behavior was similar. Figure 4(a) shows all the considered water molecules at various interfacial sites of NGM isomers of the Rh_{13}/ZrO_2, Rh_{19}/ZrO_2, Pt_{13}/ZrO_2, and Pt_{19}/ZrO_2 catalytic systems. The adsorption energies of water on the Rh_{13} and Rh_{19} clusters range from −0.99 to −0.64 eV and −0.87 to −0.41 eV, respectively. On the Pt_{13} and Pt_{19} clusters, the corresponding ranges are −0.98 to −0.36 eV and −1.07 to −0.20 eV. These ranges are comparable to those obtained on the GM clusters, which is to be expected, since molecular water usually adsorbs to the oxide Zr top sites in both cases. The adsorption energies are summarized in Fig. 4(b) and reported in detail in the supplementary material (Table S4).

In contrast to the molecular water adsorption energies, the dissociative adsorption energies on the NGM clusters differ from those on the global minima. The dissociative adsorption energies over the NGM isomers are considerably more exothermic; while only one water molecule with dissociative adsorption energy below −1.20 eV was found on the GM clusters, a total of 12 such cases were discovered on the NGM clusters, ranging from −1.83 eV to −1.25 eV. For instance, the most exothermic adsorption energy for dissociated water on GM Pt_{13} is −1.04 eV, while the corresponding figure on the NGM cluster is −1.54 eV (water label 7). To investigate this difference, the OH group of dissociated water label 7 on the NGM Pt_{13} cluster was moved to a Zr top site on a faraway corner of the cluster. As a consequence, the OH + H adsorption energy changed from −1.54 eV to −0.74 eV. This suggests that the stronger dissociative adsorption on NGM sites cannot be attributed (at least solely) to differences in H adsorption sites between the clusters, as similar OH + H adsorption energies were obtained for the global minima when the OH group was placed at the same corner (see Sec. III D).

The stronger OH + H binding on the NGM clusters seems to be related to the deformation of the clusters upon adsorption. Both molecular and dissociated water deform the NGM clusters more than the GM clusters, with the mean metal atom displacement for NGM clusters being roughly 50% higher averaged over all cases. This is evidence of the NGM clusters' higher fluxionality, which stands to reason considering their lower stability compared to the GM clusters. Since the less stable clusters are capable of relaxing to more favorable geometries upon adsorption, the OH + H binding is more exothermic on the NGM clusters than the GM clusters. This effect is not observed for H_2O binding because molecular adsorption causes considerably less cluster deformation than dissociative adsorption. We note that the clusters usually maintain their shapes fairly well even upon dissociative adsorption, however, and significant deformations only occur in a few cases.

Because of the stronger adsorption of dissociated water, the reaction energies for water dissociation on the NGM clusters are more exothermic than those on the global minima. In agreement with the results observed for the GM clusters, the reaction energies are more exothermic for Rh than Pt interfaces. A similar trend

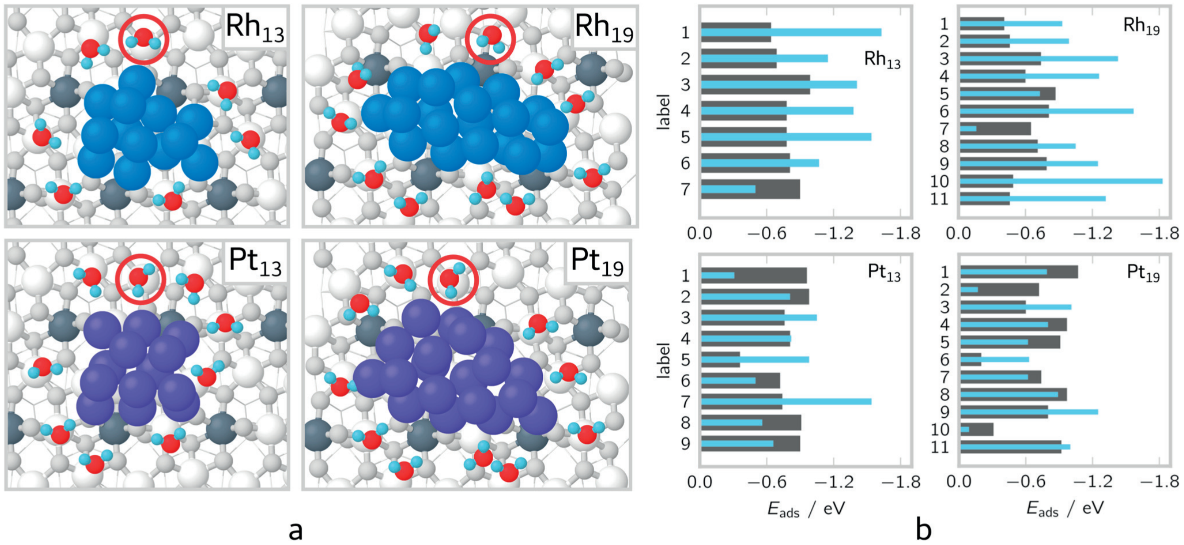

FIG. 4. (a) H_2O adsorption geometries and (b) molecular and dissociative adsorption energies on near-global minimum Rh_{13}, Rh_{19}, Pt_{13}, and Pt_{19} clusters. Oxygen atoms which are not part of the support are colored red, while hydrogen atoms are colored light blue. For the rest of the atom colors, please refer to Fig. 1. H_2O molecules are labeled clockwise starting from the H_2O indicated in each case with a red circle (labeled "1"). The H_2O adsorption energies are indicated with gray bars, while OH + H adsorption energies are indicated with blue bars.

has been observed earlier for Rh and Pt surfaces and nanoparticles, though in that investigation the difference became insignificant for small (M_{55}) nanoparticles.[2] Here, the average ΔE is roughly −0.5 eV for both NGM Rh clusters and 0.0 eV for both NGM Pt clusters. The variation in reaction energy is dominated by the variation in dissociative water adsorption energy, as the molecular adsorption energies are rather similar to one another by comparison. The linear scaling behavior between molecular and dissociated water adsorption energy remains similar to the GM case, with no notable correlation.

D. Hydrogen adsorption at various cluster sites

In order to estimate the significance of the H adsorption site to the water dissociation energy, we conducted a thorough screening of the available sites. This was carried out by computing the adsorption energy of dissociated water for various H adsorption sites with the OH group on a Zr top site at a faraway corner of the computational cell. The OH site was chosen to minimize the effect of cluster-OH and H–OH interaction and to eliminate the adsorption energy variation caused by changes in the OH adsorption site. These OH + H adsorption energies are used as a measure of the H binding strength. The optimized locations of the H atoms, color-coded according to the corresponding adsorption energies, are presented in Fig. 5(a). Each OH + H adsorption energy was calculated separately, but all H locations have been collected into the same figure for brevity. This is reasonable because the deformation of the cluster in response to H adsorption was fairly modest: the highest individual metal atom displacement observed was 0.62 Å, while the average displacement was on the order of 0.1 Å.

The OH + H adsorption energies exhibit considerable variation with differing H adsorption sites. For instance, on the Rh_{13} cluster, the adsorption energy ranges from −0.99 to −0.17 eV depending on the site. Notably, we find no obvious connection between the geometry of the H adsorption site and the adsorption energy on any of the clusters; both top and bridge sites can bind H strongly or weakly, depending on the specific position of the site. This is at least partially explained by the irregularity of the cluster geometries, which results in each adsorption site on the clusters having a unique chemical environment. Only few H atoms relaxed to hollow sites, though, and the binding is fairly weak in these cases. A preference for top and bridge sites has also been reported for both gas-phase and γ-Al_2O_3-supported Pt_{13} clusters with varying H coverages.[20,47]

Since the coordination number or location of the hydrogen atom on the cluster does not seem to explain the variation in adsorption energy, we turned our attention to more sophisticated descriptors. In earlier studies, the generalized coordination number (GCN) has been successfully used to explain differences in adsorbate binding between different adsorption sites on nanoparticles.[2,44] Due to the irregularity of the cluster geometries, we also incorporated the strain adjustment proposed in Ref. 29, resulting in the SGCN descriptor. The OH + H adsorption energies have been plotted against the SGCN values of the H adsorption sites in Fig. 5(b), from which it is evident that these quantities show no correlation with each other. Thus, the SGCN is unable to explain the adsorption behavior of hydrogen on these supported clusters.

Alternatively, the chemical environment can be characterized by the smooth overlap of atomic position (SOAP) descriptor, which we utilized as implemented in the DScribe 0.2.8 package.[30,48] SOAP

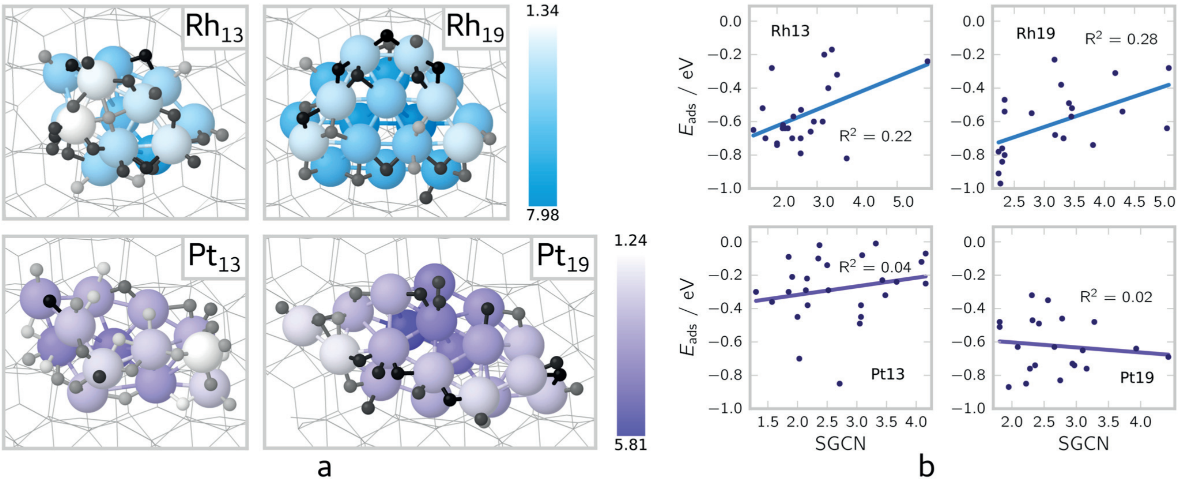

FIG. 5. (a) Adsorption geometries of all hydrogen atoms on supported global minimum Rh_{13} (upper-left), Rh_{19} (upper-right), Pt_{13} (lower-left), and Pt_{19} (lower-right) clusters, and (b) plots of OH + H adsorption energies vs SGCN. The colors of the metal atoms correspond to their SGCN values (gradients shown in the figure), while the color gradient of the H atoms corresponds to the adsorption energy of OH + H with OH far away and H at the pictured site (white: −0.01 eV and black: −0.97 eV).

vectors were computed for each H adsorption site on the M_{13} clusters, with the parameters $n_{\max} = 12$, $l_{\max} = 9$, and $r_{\text{cut}} = 12$ Å. For each cluster, the most strongly hydrogen-adsorbing site was used as the reference to which other sites were compared by SOAP similarity analysis. The dot product and the Euclidean 2-norm were used as similarity metrics. These metrics find no correlation between the OH + H adsorption energy and SOAP similarity to the strongest-adsorbing site. Other SOAP parameter combinations were also explored, but they resulted in the same conclusion. However, we cannot rule out the possibility that, e.g., machine learning could allow SOAP to explain the adsorption behavior.

Further analyses were carried out using the Pt_{13} cluster as a test case. Explanations for the H adsorption behavior were sought from the Bader charges[49] and projected d-band centers[50,51] of the cluster metal atoms, the electrostatic potential surrounding the cluster,[52] and the Fukui functions of the cluster.[53] These methods describe the electronic structure and response of the cluster, thus complementing the geometric descriptors discussed above; the d-band model is a simple approach to rationalize covalent bonding in terms of a Newns–Anderson Hamiltonian, the electrostatic potential map is a measure of Lewis acidity, while Fukui functions characterize the electron donor/acceptor properties. The analyses provided no clear relationship between the H adsorption site and binding strength, indicating that the electronic as well as geometric structures of the supported clusters are quite complicated. Finally, we note a connection between the geometric and electronic descriptors: the SGCN and projected d-band center exhibit a moderate correlation ($R^2 = 0.65$ for Pt_{13} and 0.45 for Rh_{13}).

IV. DISCUSSION

The elucidation of catalytic activities under the computational framework, while mimicking the experimental conditions, requires a careful analysis of the nature of catalytic active sites. The formation and understanding of these active sites at the interfaces of supported metal catalysts is complex to pursue due to the irregular shapes of the clusters. Deposition of asymmetric clusters over a catalyst support results in different coordinations of metal atoms throughout the cluster perimeter. Herein, the adsorption analyses at the perimeter of zirconia-supported Pt and Rh clusters report similar challenges. Every interfacial adsorption site over each cluster is found to be unique, and the differences in adsorption energies are notable. The molecular water preferably adsorbs on Zr top sites near the cluster, avoiding adsorption over high-coordinated zirconia atoms. Deformation of the clusters upon molecular adsorption is small, whereas with dissociated water, the clusters show comparatively larger changes in geometry. Overall, the binding of H_2O and OH + H is highly dependent on the adsorption sites over our clusters, making it difficult to predict the pattern.

In this work, all screening was done by manually constructing plausible initial guesses for geometry optimizations. This approach is good when the system is simple and only a moderate number of structures are required for screening. Manual screening in complicated systems, such as these clusters, is somewhat arduous and may cause a sampling bias: catalytically significant structures can be missed if the human building the initial structure does not realize their importance. This is highlighted especially when the behavior of the system at hand is difficult to predict. In the case of the H screening discussed in Sec. III D, for instance, a more complete description of hydrogen adsorption on the clusters could be obtained by conducting a thorough, automated scan of the adsorption energy as a function of H position.[54] Such an approach would avoid human sampling bias and also provide a larger quantity of data without an extensive manual setup. Of course, such a comprehensive scan would also require using more computational resources or lowering the level of theory.

Linear regressions using physics-based descriptors were found unable to rationalize the observed variations in adsorption, reaction, and transition state energies. In addition to linear regression, the data could be analyzed using more refined regression models which are rapidly gaining traction[55] as means to describe chemical systems. For instance, the physics-based descriptors used herein could be taken as input parameters (features) used for training a supervised regression or neural network algorithm. Such an approach can possibly describe the data as a nonlinear function of several physically meaningful features.[55] Alternatively, the data could be analyzed using automatized and more abstract featurization approaches such as SOAP used in this work. While abstract features may alleviate manual labor, they may also provide a qualitative understanding of the important features or descriptors. Whether physics-based or more abstract featurization is used, large data sets are needed to obtain a reliable machine learning model—obtaining this data from DFT may well become the bottleneck for the machine learning approaches.

Water adsorption strength over clean metal surfaces is often reported to be weak compared to that on pure zirconia;[1,2,6,7,37] therefore, the support is needed for overall catalytic activity. According to previous works, zirconia alone cannot catalyze the WGS reaction.[6,16] As the water activation behavior of Rh(111) and Pt(111) are quite similar,[2] the Pt(111) surface could be expected to perform similarly toward WGS. Therefore, even though the interfacial sites make up a minority of the whole system, they can play a key role in the catalytic activity. In line with previous results, molecular water binds at the present interface sites with moderate strengths and displays lower dissociation barriers than on the pure metal surfaces.[1,2,6] Our present study shows that water dissociation can take place across the interface, thereby supplying hydrogen to the metal cluster for further reaction with CO in the WGS process.

The presence of NGM isomers highlights the importance of considering the ensemble of structures instead of focusing only on the GM isomer.[19] Our study shows that molecular water adsorption is rather similar between GM and NGM structures, but a considerable difference is observed for OH + H adsorption, which may be partially attributed to the cluster deformations. Consequently, the results based on NGM isomers raise numerous questions: (i) at elevated temperatures, what is the extent of fluxionality during the reaction? (ii) how does cluster fluxionality affect the reaction mechanism and minimum energy pathways? (iii) how and to what extent do surface species modify the cluster geometry? Note that we exclude kinetics over NGM clusters, and the present comments are based on thermodynamic analysis. Moreover, only low-coverage cases were considered; higher adsorbate coverages may introduce larger structural deformations than those observed here, in particular, if the adsorbates are included in the global optimization.

Finally, the breaking of energy scaling relationships is an inherent way to overtake the maximum catalytic activities proposed based on volcano plots.[56] In our study, the linear scaling relationships between adsorption energies of H_2O and OH + H over all GM and NGM clusters show, at best, poor correlations. As meaningful BEP and TS scaling relationships were also not observed, we are unable to predict activation energies based on adsorption or reaction energies over these clusters. This is perhaps unsurprising given that scaling relations assume that the initial structures as well as the transition state and final structures are relatively similar across the studied sites. Our results demonstrate that simple scaling relationships do not hold for these zirconia-supported Rh and Pt clusters and, consequently, interfacial sites may display unexpected catalytic behavior. This calls for systematic computational and experimental studies on atomically well-defined clusters in order to better understand these systems and formulate new concepts for the prediction of catalytic properties.

V. CONCLUSIONS

We have investigated the dissociation of water over globally optimized Rh and Pt clusters on m-$ZrO_2(\bar{1}11)$. It was observed that the adsorption and reaction properties of the system are complex and cannot be easily predicted from simple geometric or electronic structure measures of the cluster or from scaling relations. Three main factors likely contribute to this complexity: (i) the irregular morphology of the clusters, (ii) the small size of the clusters, and (iii) the low symmetry of the support. Together these factors result in very intricate properties for the clusters and cause every adsorption site to be unique.

As the properties of a cluster are highly dependent on its exact geometry, and there exist multiple cluster isomers that are close in energy to the GM structures, focusing only on the most stable geometry provides a limited view of a catalytic system. Indeed, we found that NGM clusters can bind dissociated water more strongly than the GM clusters. This effect could stabilize cluster geometries that are less favorable on the bare surface, further increasing the number of thermodynamically feasible structures in the $H_2O/M/ZrO_2$ system.

The aspects mentioned above indicate that there is potential for rich catalytic chemistry on small, fluxional clusters. Our results reinforce the necessity of using an ensemble model comprising a variety of cluster geometries to gain a complete picture of the catalytic process.

SUPPLEMENTARY MATERIAL

See supplementary material for the complete water adsorption and dissociation data, including adsorption and reaction energies, activation energies, TS bond lengths, imaginary frequencies, and scaling relationship plots.

ACKNOWLEDGMENTS

The work was funded by the Academy of Finland, Project Nos. 307853 and 317739, and the University of Jyväskylä. The electronic structure calculations were made possible by the computational resources provided by the CSC—IT Center for Science, Espoo, Finland (https://www.csc.fi/en/). V.K. thanks Mr. Lauri Himanen from Aalto University for fruitful discussions on SOAP.

REFERENCES

[1] A. A. Phatak, W. N. Delgass, F. H. Ribeiro, and W. F. Schneider, J. Phys. Chem. C **113**, 7269 (2009).
[2] A. S. Bazhenov, L. Lefferts, and K. Honkala, J. Phys. Chem. C **121**, 4324 (2017).
[3] P. Liu and J. A. Rodriguez, J. Chem. Phys. **126**, 164705 (2007).
[4] A. Mohsenzadeh, T. Richards, and K. Bolton, Surf. Sci. **644**, 53 (2016).
[5] L. C. Grabow, A. A. Gokhale, S. T. Evans, J. A. Dumesic, and M. Mavrikakis, J. Phys. Chem. C **112**, 4608 (2008).

[6] M. M. Kauppinen, M. M. Melander, A. S. Bazhenov, and K. Honkala, ACS Catal. **8**, 11633 (2018).

[7] Z.-J. Zhao, Z. Li, Y. Cui, H. Zhu, W. F. Schneider, W. N. Delgass, F. Ribeiro, and J. Greeley, J. Catal. **345**, 157 (2017).

[8] T. K. Slot, D. Eisenberg, and G. Rothenberg, ChemCatChem **10**, 2119 (2018).

[9] L. Foppa, T. Margossian, S. M. Kim, C. Müller, C. Copéret, K. Larmier, and A. Comas-Vives, J. Am. Chem. Soc. **139**, 17128 (2017).

[10] A. Bruix, J. A. Rodriguez, P. J. Ramírez, S. D. Senanayake, J. Evans, J. B. Park, D. Stacchiola, P. Liu, J. Hrbek, and F. Illas, J. Am. Chem. Soc. **134**, 8968 (2012).

[11] G. R. Jenness and J. R. Schmidt, ACS Catal. **3**, 2881 (2013).

[12] S. Aranifard, S. C. Ammal, and A. Heyden, J. Catal. **309**, 314 (2014).

[13] Q.-L. Tang and Z.-P. Liu, J. Phys. Chem. C **114**, 8423 (2010).

[14] J. A. Rodríguez, J. Evans, J. Graciani, J.-B. Park, P. Liu, J. Hrbek, and J. F. Sanz, J. Phys. Chem. C **113**, 7364 (2009).

[15] O. Thinon, F. Diehl, P. Avenier, and Y. Schuurman, Catal. Today **137**, 29 (2008).

[16] P. Graf, D. J. M. de Vlieger, B. L. Mojet, and L. Lefferts, J. Catal. **262**, 181 (2009).

[17] Y. Suchorski, M. Datler, I. Bespalov, C. Freytag, J. Zeininger, and G. Rupprechter, Surf. Sci. **679**, 163 (2019).

[18] M. Campa, G. Ferraris, D. Gazzoli, I. Pettiti, and D. Pietrogiacomi, Appl. Catal., B **142–143**, 423 (2013).

[19] H. Zhai and A. N. Alexandrova, ACS Catal. **7**, 1905 (2017).

[20] G. Sun and P. Sautet, J. Am. Chem. Soc. **140**, 2812 (2018).

[21] E. T. Baxter, M. A. Ha, A. C. Cass, A. N. Alexandrova, and S. L. Anderson, ACS Catal. **7**, 3322 (2017).

[22] M.-A. Ha, E. T. Baxter, A. C. Cass, S. L. Anderson, and A. N. Alexandrova, J. Am. Chem. Soc. **139**, 11568 (2017).

[23] J. Greeley, Annu. Rev. Chem. Biomol. Eng. **7**, 605 (2016).

[24] B. Zandkarimi and A. N. Alexandrova, J. Phys. Chem. Lett. **10**, 460 (2019).

[25] M. Jørgensen and H. Grönbeck, ACS Catal. **9**, 8872 (2019).

[26] A. H. Motagamwala, M. R. Ball, and J. A. Dumesic, Annu. Rev. Chem. Biomol. Eng. **9**, 413 (2018).

[27] R. A. van Santen, M. Neurock, and S. G. Shetty, Chem. Rev. **110**, 2005 (2010).

[28] J. L. Fajín, M. N. D. Cordeiro, F. Illas, and J. R. Gomes, J. Catal. **276**, 92 (2010).

[29] F. Calle-Vallejo and A. S. Bandarenka, ChemSusChem **11**, 1824 (2018).

[30] A. P. Bartók, R. Kondor, and G. Csányi, Phys. Rev. B **87**, 184115 (2013).

[31] P. E. Blöchl, Phys. Rev. B **50**, 17953 (1994).

[32] J. Enkovaara, C. Rostgaard, J. J. Mortensen, J. Chen, M. Dułak, L. Ferrighi, J. Gavnholt, C. Glinsvad, V. Haikola, H. A. Hansen, H. H. Kristoffersen, M. Kuisma, A. H. Larsen, L. Lehtovaara, M. Ljungberg, O. Lopez-Acevedo, P. G. Moses, J. Ojanen, T. Olsen, V. Petzold, N. A. Romero, J. Stausholm-Møller, M. Strange, G. A. Tritsaris, M. Vanin, M. Walter, B. Hammer, H. Häkkinen, G. K. H. Madsen, R. M. Nieminen, J. K. Nørskov, M. Puska, T. T. Rantala, J. Schiøtz, K. S. Thygesen, and K. W. Jacobsen, J. Phys.: Condens. Matter **22**, 253202 (2010).

[33] J. J. Mortensen, L. B. Hansen, and K. W. Jacobsen, Phys. Rev. B **71**, 035109 (2005).

[34] A. H. Larsen, J. J. Mortensen, J. Blomqvist, I. E. Castelli, R. Christensen, M. Dułak, J. Friis, M. N. Groves, B. Hammer, C. Hargus, E. D. Hermes, P. C. Jennings, P. B. Jensen, J. Kermode, J. R. Kitchin, E. L. Kolsbjerg, J. Kubal, K. Kaasbjerg, S. Lysgaard, J. B. Maronsson, T. Maxson, T. Olsen, L. Pastewka, A. Peterson, C. Rostgaard, J. Schiøtz, O. Schütt, M. Strange, K. S. Thygesen, T. Vegge, L. Vilhelmsen, M. Walter, Z. Zeng, and K. W. Jacobsen, J. Phys.: Condens. Matter **29**, 273002 (2017).

[35] J. P. Perdew, K. Burke, and M. Ernzerhof, Phys. Rev. Lett. **77**, 3865 (1996).

[36] J. P. Perdew, K. Burke, and M. Ernzerhof, Phys. Rev. Lett. **78**, 1396 (1997).

[37] A. S. Bazhenov and K. Honkala, Top. Catal. **60**, 382 (2017).

[38] A. S. Bazhenov, M. M. Kauppinen, and K. Honkala, J. Phys. Chem. C **122**, 6774 (2018).

[39] A. S. Bazhenov and K. Honkala, J. Phys. Chem. C **123**, 7209 (2019).

[40] H. Jónsson, G. Mills, and K. W. Jacobsen, in *Classical and Quantum Dynamics in Condensed Phase Simulations*, edited by B. J. Berne, G. Ciccotti, and D. F. Coker (World Scientific, Singapore, 1998), p. 385.

[41] G. Henkelman and H. Jónsson, J. Chem. Phys. **113**, 9978 (2000).

[42] G. Henkelman, B. P. Uberuaga, and H. Jónsson, J. Chem. Phys. **113**, 9901 (2000).

[43] S. Smidstrup, A. Pedersen, K. Stokbro, and H. Jónsson, J. Chem. Phys. **140**, 214106 (2014).

[44] F. Calle-Vallejo, J. I. Martínez, J. M. García-Lastra, P. Sautet, and D. Loffreda, Angew. Chem., Int. Ed. **53**, 8316 (2014).

[45] J. P. Clay, J. P. Greeley, F. H. Ribeiro, W. N. Delgass, and W. F. Schneider, J. Catal. **320**, 106 (2014).

[46] K.-D. Jung and A. T. Bell, J. Catal. **193**, 207 (2000).

[47] C. Mager-Maury, G. Bonnard, C. Chizallet, P. Sautet, and P. Raybaud, ChemCatChem **3**, 200 (2011).

[48] L. Himanen, M. O. J. Jäger, E. V. Morooka, F. Federici Canova, Y. S. Ranawat, D. Z. Gao, P. Rinke, and A. S. Foster, Comput. Phys. Commun. (to be published); e-print arXiv:1904.08875 [cond-mat.mtrl-sci] (2019).

[49] G. Henkelman, A. Arnaldsson, and H. Jónsson, Comput. Mater. Sci. **36**, 354 (2006).

[50] B. Hammer and J. K. Nørskov, Surf. Sci. **343**, 211 (1995).

[51] D. M. Newns, Phys. Rev. **178**, 1123 (1969).

[52] J. Halldin Stenlid, A. J. Johansson, and T. Brinck, Phys. Chem. Chem. Phys. **21**, 17001 (2019).

[53] R. G. Parr and W. Yang, J. Am. Chem. Soc. **106**, 4049 (1984).

[54] M. O. J. Jäger, E. V. Morooka, F. Federici Canova, L. Himanen, and A. S. Foster, npj Comput. Mater. **4**, 37 (2018).

[55] P. Schlexer-Lamoureux, K. T. Winther, J. A. Garrido-Torres, V. Streibel, M. Zhao, M. Bajdich, F. Abild-Pedersen, and T. Bligaard, ChemCatChem **11**, 3581 (2019).

[56] A. Vojvodic and J. K. Nørskov, Natl. Sci. Rev. **2**, 140 (2015).

II

ADDRESSING DYNAMICS AT CATALYTIC HETEROGENEOUS INTERFACES WITH DFT-MD: ANOMALOUS TEMPERATURE DISTRIBUTIONS FROM COMMONLY USED THERMOSTATS

by

Ville Korpelin, Toni Kiljunen, Marko M. Melander, Miguel A. Caro, Henrik H. Kristoffersen, Nisha Mammen, Vesa Apaja, and Karoliina Honkala

The Journal of Physical Chemistry Letters **2022**, 13, 2644–2652

DOI:10.1021/acs.jpclett.2c00230

THE JOURNAL OF
PHYSICAL CHEMISTRY
LETTERS
A JOURNAL OF THE AMERICAN CHEMICAL SOCIETY

Addressing Dynamics at Catalytic Heterogeneous Interfaces with DFT-MD: Anomalous Temperature Distributions from Commonly Used Thermostats

Ville Korpelin,[‖] Toni Kiljunen,[‖] Marko M. Melander,[‖] Miguel A. Caro, Henrik H. Kristoffersen, Nisha Mammen, Vesa Apaja, and Karoliina Honkala[*]

Cite This: *J. Phys. Chem. Lett.* 2022, 13, 2644−2652 **Read Online**

ACCESS | Metrics & More | Article Recommendations | Supporting Information

ABSTRACT: Density functional theory-based molecular dynamics (DFT-MD) has been widely used for studying the chemistry of heterogeneous interfacial systems under operational conditions. We report frequently overlooked errors in thermostated or constant-temperature DFT-MD simulations applied to study (electro)catalytic chemistry. Our results demonstrate that commonly used thermostats such as Nosé−Hoover, Berendsen, and simple velocity-rescaling methods fail to provide a reliable temperature description for systems considered. Instead, nonconstant temperatures and large temperature gradients within the different parts of the system are observed. The errors are not a "feature" of any particular code but are present in several *ab initio* molecular dynamics implementations. This uneven temperature distribution, due to inadequate thermostatting, is well-known in the classical MD community, where it is ascribed to the failure in kinetic energy equipartition among different degrees of freedom in heterogeneous systems (Harvey *et al. J. Comput. Chem.* 1998, 726−740) and termed the flying ice cube effect. We provide tantamount evidence that interfacial systems are susceptible to substantial flying ice cube effects and demonstrate that the traditional Nosé−Hoover and Berendsen thermostats should be applied with care when simulating, for example, catalytic properties or structures of solvated interfaces and supported clusters. We conclude that the flying ice cube effect in these systems can be conveniently avoided using Langevin dynamics.

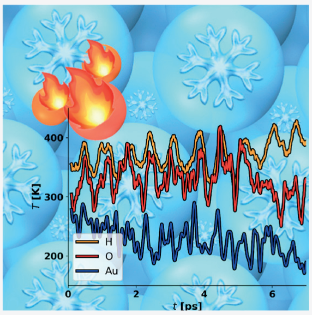

Molecular dynamics (MD) simulations in the canonical, fixed *NVT* ensemble are a powerful way to study thermodynamic properties of condensed phases. In past years, density functional theory (DFT) based MD simulations have been widely applied to study interfacial and heterogeneous systems such as metal−water interfaces and supported nanoclusters relevant for heterogeneous (electro)catalytic processes.[1,2] These studies require substantial computer resources for well-converged simulation results and are often considered to provide an unbiased benchmark-quality description of such complex interfaces with warranted accuracy.[3]

From a technical perspective, sampling the *NVT* ensemble requires the use of thermostats to achieve constant temperatures in simulations. A thermostat introduces an approximate, preferably nonintrusive, coupling of the system to a fictitious heat bath, and several types of thermostats have been developed[4] for this purpose over the years. However, the vast majority of existing DFT-MD studies of heterogeneous and interfacial systems have employed Nosé−Hoover thermostats,[3,5−27] the Berendsen[28−36] or even simple velocity-rescaling thermostats,[37] or Langevin dynamics.[38−42] All the referenced works have focused on either solvated interfaces in (electro)catalytic systems or on (supported) nanocluster catalysts which exemplify the wide adoption of simple, single-chain Nosé−Hoover,[43,44] Berendsen,[45] or simple velocity-rescaling thermostats by the catalysis community. Another common aspect is that these studies represent high-profile research, which has established the use of DFT-MD in providing crucial atomistic insight into (electro)catalytic processes.

While these methods used in the above-mentioned studies can faithfully reproduce the *average temperature* of the system correctly, we have observed that both the Nosé−Hoover and Berendsen thermostats fail to provide a *uniform temperature* throughout the simulation cell. Instead, substantial *temperature gradients* exist in the simulated systems, for example, between water and a metallic surface, or an active metal catalyst and an oxide support, and even within bulk water, where rotations, vibrations, and translations exhibit different thermal energies.[46]

Received: January 24, 2022
Accepted: March 11, 2022
Published: March 17, 2022

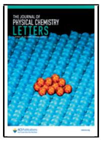

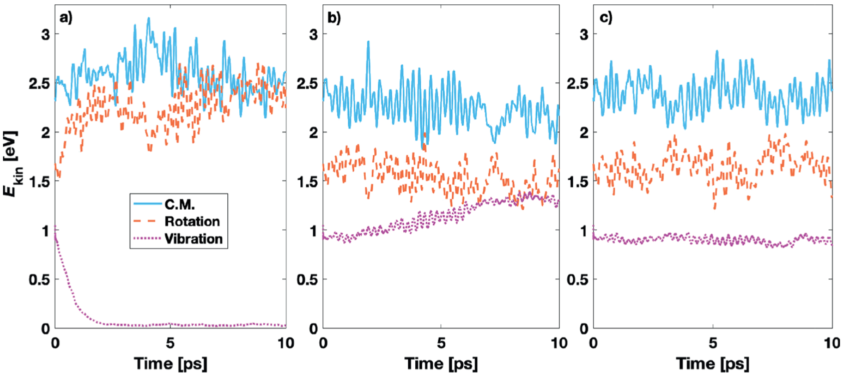

Figure 1. Kinetic energy partitioning for the 64 N_2 molecules thermostated by Nosé−Hoover at 300 K with density convergence criteria of (a) 10^{-4} e/v.e., (b) 10^{-5} e/v.e., and (c) 10^{-6} e/v.e. The DFT-MD trajectories were obtained using ASE/GPAW code. Moving averages of trailing 0.1 ps are plotted for C.M. translations, rotations, and vibrations.

Similar anomalies are likely present in several DFT-MD simulations of interfacial systems. Therefore, some previous results obtained with DFT-MD and the Berendsen or Nosé−Hoover thermostats should be approached cautiously and re-examined with other thermostats or Langevin dynamics.

Previously such anomalies have been demonstrated and thoroughly analyzed for classical MD simulations with weak velocity-rescaling thermostats such as the Berendsen thermostat. This led to the identification of the "flying ice cube" effect where the kinetic energy is incorrectly partitioned within the system and becomes transferred from high-frequency modes to low-frequency modes.[47−50] Another manifestation of similar issues is the "hot-solvent/cold-solute" problem,[51] which was resolved by using separate Nosé−Hoover chains for the solute and the solvent.[52] The flying ice cube effect can be reduced, for example, by increasing the system size, decreasing the time step, or adjusting the thermostat,[47] but these measures would further increase the already high cost of DFT-MD simulations. The presence of temperature gradients and incorrect temperature partitioning has most often been observed and discussed for the Berendsen thermostat, but in principle it is possible to have similar issues also with other thermostats, such as Nosé−Hoover.[51,53−55] The issue is not only theoretical but also affects the observed thermodynamics, sampling and ergodicity, temporal dynamics, and computed expectation values.[47,52,56] As highlighted in a recent study,[57] accurate modeling of both the average temperature and its fluctuations is important to reconcile computed and measured adsorption energies.

The present Letter aims to illustrate, to our knowledge for the first time, that the widely used single-chain Nosé−Hoover and Berendsen thermostats can show extreme features of the flying ice cube effect in heterogeneous (electro)catalysis DFT-MD simulations, even when tight convergence criteria are used for self-consistency. We show that temperatures or kinetic energy partitioning from these thermostats do not follow their expected average values even with improved convergence and that the deviations escalate with typical convergence criteria. We demonstrate that extremely well-converged calculations are needed to obtain the correct kinetic energy partitioning even in a simple diatomic condensed phase system (N_2); otherwise, the energy is incorrectly partitioned between vibrations, rotations, and translations. For more complex systems, we show that temperature gradients persist even when the energies are converged to 10^{-5}−10^{-7} eV accuracy for an electrochemical interface (a water−Au(111) interface) and for a heterogeneous catalyst model (a zirconia-supported Pt cluster). Furthermore, we demonstrate that using typical energy convergence criteria of 10^{-3}−10^{-4} eV can lead to incorrect temperature/kinetic energy distributions between different kinds of atoms even in the same phase.

Several different DFT softwares, including GPAW[58,59] with ASE,[60] VASP,[61] CP2K,[62] and Quantum ESPRESSO (QE),[63] were used to carry out DFT-MD simulations for the considered interfacial model systems shown in Figures S1 and S2. Depending on the availability of different thermostats in these codes, we examined the performance of single-chain Nosé−Hoover[64−66] and Berendsen[45] thermostats and the Langevin dynamics.[4] Various energy and density convergence criteria were tested to address the coupling between accurate energies (forces) and the performance of the temperature controls as detailed in the Supporting Information.

The time step of 1 fs was considered a valid starting point for typical DFT-MD simulations. The thermostat parameters were chosen as representative values to illustrate the flying ice cube effects. The influence of temperature gradients on dynamical and thermodynamics values was probed by computing entropies for the simulated trajectories using velocity−velocity correlation functions within the 2PT formalism[67] as implemented in the DoSPT code.[46] The DoSPT program distinguishes between translational, rotational, and vibrational degrees of freedom (DoF) in the kinetic energy partitioning. For extracting dynamic quantities, such as correlation functions, from Langevin dynamics, the selection of a friction parameter is important to achieve efficient thermalization without disturbing the system dynamics too much.[56] Therefore, a rather small friction coefficient was applied and we expect that the accuracy of the computed velocity autocorrelation functions is not substantially affected by this choice. A more comprehensive overview on the computational methods is provided in the Supporting Information.

We start with presenting the results for 64 N_2 molecules in a fully periodic cubic 27 nm^3 simulation cell corresponding to supercritical fluid conditions. This homogeneous system allows the evaluation of thermostat performance in a simple case where the kinetic energy partitioning is easy to define. The

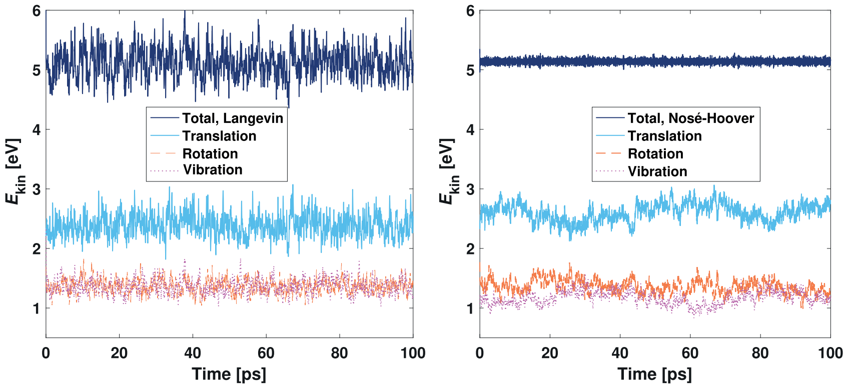

Figure 2. Kinetic energy partitioning into translational, rotational, and vibrational degrees of freedom in VASP simulations of the Au(111)−H_2O system with Langevin dynamics (left) or Nosé−Hoover thermostat (right) targeted at 330 K. For clarity, the moving averages of trailing 0.1 ps periods are plotted.

choice of the test system was motivated by refs 47 and 48, in which the kinetic energy partitioning in ethane was considered in a similar manner.

The DFT-MD simulations were started with the 18.5 ps Langevin dynamics run to equilibrate the N_2 system at 300 K. Density of states analysis shows (Table S1) that the dynamics maintains the correct equipartition between center-of-mass (C.M.) translations (192 degrees of freedom), rotations (128), and vibrations (64) within acceptable limits. This demonstrates that Langevin dynamics performs well even with the loose GPAW-default density convergence criterion of 10^{-4} electrons per valence electron (e/v.e.), which amounts to 0.064 electrons in the present system. After equilibration, we switched on the Nosé−Hoover thermostat with a coupling time constant of 50 fs and followed the time evolution of the kinetic energy partitioning for 10 ps. Panels in Figure 1 show this evolution for three distinct values of the density convergence criterion given in the figure caption that converge the total energies at least to 10^{-4}, 10^{-6}, and 10^{-8} eV.

From Figure 1 it is clear that insufficient convergence together with the Nosé−Hoover thermostat leads to unwanted kinetic energy partitioning in the N_2 system. Using the loosest criterion of 10^{-4} e/v.e., the vibrational motions almost completely freeze after 2 ps, while the rotational and translational energies become roughly equal with each other. The same anomaly occurs by using the Berendsen thermostat (shown in Figure S3). The distribution can be somewhat improved by tightening the density convergence by an order of magnitude to 10^{-5} e/v.e, but now the vibrational component gains too much energy. Note that the average temperature is always correct and around the wanted 300 K, but the kinetic energy is incorrectly distributed. The proper equipartition for the diatomic system is maintained only by tightening the density convergence by yet another order of magnitude, down to 10^{-6} e/v.e. (shown in Figure 1 c). This density convergence reduces the energy change between electronic iterations below 10^{-8} eV, which is an unusually tight energy convergence criterion rarely achieved in large-scale DFT-MD simulations. The resulting energy partitioning compares to that of the Langevin dynamics reasonably well, as shown in Figure S4. In addition, we employed the CP2K software to verify that with tight, 10^{-6} Ha convergence, the quality of energy partitioning is similar between the Langevin and the Nosé−Hoover simulations (please see Figure S5). We also compared the Berendsen thermostat to the simple velocity rescaling using the QE code (Figure S6). In these simulations, the loose convergence manifests itself in energy anomalies despite the strict control over the total kinetic energy and temperature. Here, the energy distribution is very different from the above ASE/GPAW Nosé−Hoover and Berendsen cases.

All these examples demonstrate that the force inaccuracy, originating from insufficient energy convergence, intensifies the tendency to exhibit the flying ice cube effect even when the convergence criteria are tighter than the default values. We note that in systems with frequent collisions, the dynamical energy redistribution may level out the energy partitioning and counteract the flying ice cube effect. However, the present N_2 test system is relatively sparse and thus serves as an example to highlight the role of the molecule−thermostat coupling.

Metal−water interfaces are ubiquitous and of great significance in the field of (electro)catalysis. Atomic level knowledge of the dynamical properties of these interfaces is essential for fundamental understanding of (electro)catalytic reaction mechanisms and design of advanced (electro)catalysts for efficient conversion of energy and molecules. Before considering the performance of different thermostats and software on probing the dynamic evolution of the metal−water interface, bulk water was studied. It is homogeneous but denser and more complex than the model N_2 system. The bulk water model consists of 64 molecules in a $(1.242 \text{ nm})^3$ cube. The simulations were carried out with the ASE/GPAW software and the Nosé−Hoover thermostat, Langevin dynamics, or *NVE* dynamics using 10^{-4} e/v.e. density convergence and 2 u for hydrogen mass to ensure the same 1 fs time step as for N_2. The instantaneous temperature given in Figure S7 and the density of state plot in Figure S8 show that Langevin dynamics clearly outperforms the Nosé−Hoover thermostat. Furthermore, the *NVE* dynamics runs revealed the necessity to tighten the convergence to 10^{-6} e/v.e. (below 10^{-8} eV) to obtain energy conservation and proper partitioning (see Figure S9). The DoS plot (Figure S8) illustrates the flying ice cube effect by showing a thermostat-dependent misproportion of high-frequency vibrational modes and low-frequency translations and rotations.

The presence of metal surface modifies the water degrees of freedom and the entropy reflecting the mobility constraint due to the surface, and collisions with surface atoms introduce an energy-exchange mechanism, both dependent on the accuracy of the kinetic energy partitioning. We performed DFT-MD simulations for a solvated Au(111) surface having 32 water molecules and 24 mobile Au atoms and employing different software. The most extensive, over 100 ps, simulations were carried out with the VASP code using an energy convergence criterion of 10^{-4} eV. Figure 2 illustrates the kinetic energy partitioning and allows a comparison between the Langevin and Nosé–Hoover runs. The plotted curves again represent center of mass, rotational, and vibrational motions, as well as the total sum of the energy components. For Langevin dynamics, rotations and vibrations fully overlap at the energy of ~1.4 eV as expected, and translations are offset by approximately 1.0 eV because of the mobile surface Au atoms. The total kinetic energy is 5.12 eV, and all its components faithfully average to the target temperature of 330 K. With the Nosé–Hoover thermostat, the oscillations of total energy efficiently level out with the 0.1 ps smoothing. However, the inability of the thermostat to work properly is demonstrated by the kinetic energy components which average to 360 K (2.61 eV) for translations, 329 K (1.36 eV) for rotations, and 284 K (1.17 eV) for vibrations. In contrast to Langevin dynamics, the thermostated energies also exhibit drifting from the average values.

As the VASP DFT-MD simulations for the Au(111)–H_2O were long enough, they allow reliable evaluation of thermodynamic properties like entropy (S) and the impact of incorrect temperature partitioning on a thermodynamic observable. The number of degrees of freedom provides a convenient measure for the accuracy of kinetic energy partitioning. The 24 mobile gold atoms should exhibit 72 (3 × 24) DoF in the translational mode, while the total number of 288 DoF of the 32 water molecules should be evenly distributed in 96 translations, 96 rotations, and 96 vibrations. These numbers display as areas under the density of states (DoS) curves obtained from the DoSPT program. Figure 3 shows the separate DoS plots for the water molecules and surface gold atoms. The most notable difference between the Langevin and Nosé–Hoover results is seen in the Au translations, for which Nosé–Hoover gives a peaked structure while Langevin shows a smooth curve. A similar excess in density is also present at the translational frequencies of water. The difference in other water modes appears almost indistinguishable. On closer inspection, comparing Langevin DoS curves to Nosé–Hoover DoS curves shows slight decrease in density of the high-frequency vibrational mode and accordingly slight increase in the low-frequency vibrational mode in the Nosé–Hoover DoS curve. The observed energy transfer is in line with the description of the flying ice cube effect.[48]

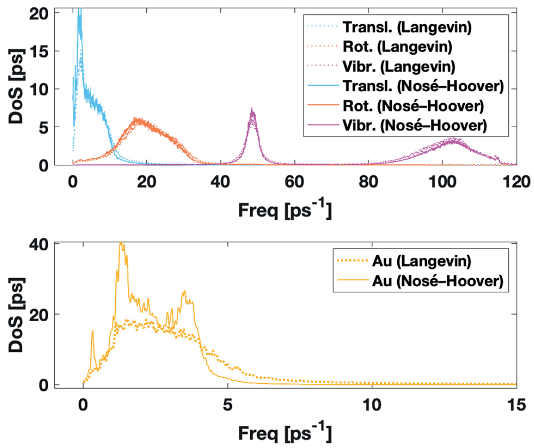

Figure 3. Density of states plot for the H_2O–Au(111) system presenting translational, rotational, and vibrational degrees of freedom of water molecules (upper) and of Au atoms (lower).

The DoF numbers deviate more clearly. While Langevin produces them correctly, giving 72 translation DoF to the Au slab and 96 DoF to each water mode, Nosé–Hoover produces 82 Au translations, and the water modes are 101, 96, and 83 DoF for translations, rotations, and vibrations, respectively. The entropy value computed from the Langevin dynamics is S = 50 J K^{-1} mol^{-1} for H_2O, whereas the Nosé–Hoover gives 61 J K^{-1} mol^{-1}. The 20% entropy difference principally reflects the varying number of translational DoF and thus entropies for the translational Au part expectedly differ, being 48 J K^{-1} mol^{-1} and 63 J K^{-1} mol^{-1}, respectively.

Next, we compared the performance of different DFT codes and analyzed the instantaneous temperatures for solvated Au(111) from the Langevin dynamics and the Nosé–Hoover thermostat simulations. The DFT packages VASP, GPAW, and CP2K were used. Table 1 summarizes the instantaneous temperatures and shows that Langevin dynamics produces the correct average temperature (330 K for VASP and CP2K, 300 K for ASE/GPAW) in the entire system and also all the atoms are reasonably close to the average temperature. Whereas the Nosé–Hoover thermostat satisfactorily keeps the expected average temperature (350 K ASE/GPAW, 330 K others), the different atoms show large temperature variations. We observed up to 100 K differences between water and surface temperatures, although the DFT-MD calculations were tightly converged (see Figures S10–S12). Interestingly, depending on the code, the water molecules may be either hotter (CP2K) or colder (VASP) than the Au surface despite the very similar computational setups. The CP2K Nosé–Hoover data has, for example, high-temperature hydrogen atoms, which are accompanied by a marked increase in the vibrational stretching mode intensity (see Figures S14 and S15), whereas other DoF are reduced with respect to the CP2K Langevin data, pointing toward the opposite[68] or “inverted flying ice cube effect”. In the VASP Nosé–Hoover simulations, the Au atoms, in turn, appear overheated, which indicates energy transfer from high-frequency vibrational modes to translational modes due to the conventional flying ice cube effect. Figure 2 reveals that the inverted flying ice cube may change to the conventional one and vice versa on a time scale of tens of picoseconds. Altogether, these results highlight the fact that the kinetic energy partitioning for Nosé–Hoover trajectories depends sensitively on the DFT-MD software, making it challenging to identify the underlying reason for the incorrect kinetic energy distribution between the two subsystems of a metal–water interface.

The spurious temperature distribution from Nosé–Hoover dynamics was aggravated when the convergence criteria were left looser, as shown in Figure S10 for ASE/GPAW trajectories. Despite strayed atomic constituents, the average temperature is correct, which hides the erroneous performance. The thermostat time scale may also have an effect on the temperature

Table 1. Comparison of Atom-Specific Instantaneous Temperatures for the Solvated Au(111) Surface Obtained Using Langevin Dynamics and Nosé–Hoover Thermostat with Different DFT-MD Codes[a]

Code	Langevin	Nosé–Hoover
VASP	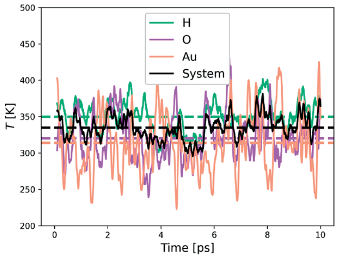	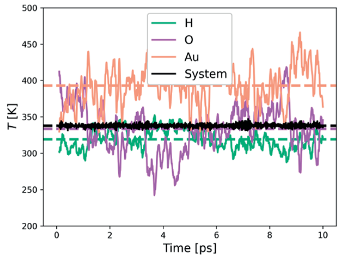
ASE/GPAW	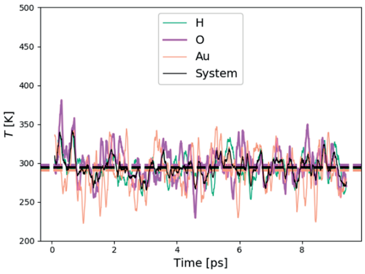	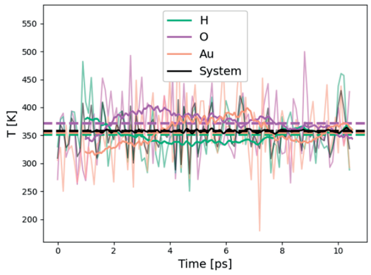
CP2K	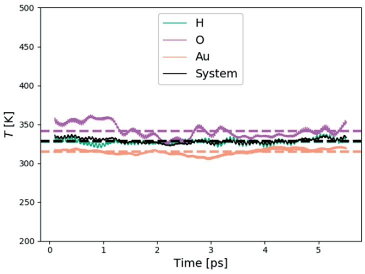	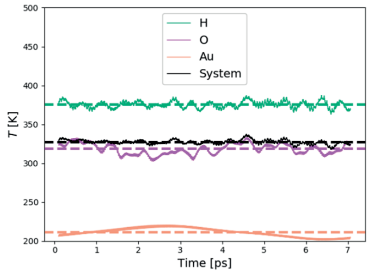

[a] The inserted figures show 0.1 ps moving averages along with the full averages from the presented time slice.

distribution, and in Figure S11 we show that with a tighter coupling, that is, using a smaller time scale parameter, the system achieved thermalization faster and more correctly. It should, however, be noted that too aggressive thermostatting can disturb the system dynamics and, for example, impact the calculation of correlation functions.

In addition to our own data, we also analyzed temperature distributions from two examples of recently published electrochemical interface studies, where computational data were freely available. In the first example, solvated Cu surfaces with and without adsorbed hydrogen atoms were simulated using the Berendsen thermostat.[36] The temperature analysis is presented in Figure S17, and it reveals that the temperature distributions of the hydrogen and oxygen atoms in the water solvent depend strongly on the surface structure. However, it is the adsorbed H atoms which suffer from a more striking temperature variation and appear up to 500 K hotter than other species. If a H diffusion constant were computed from these results, the atom would appear anomalously mobile. In the second example, a solvated Au surface was studied in the presence of Li^+ ions with and without an adsorbed CO_2, using the Nosé–Hoover thermostat.[26] The temperature analysis given in Figure S18 demonstrates significant temperature gradients and differences. In particular, the temperature of both the Li^+ ions and the CO_2 molecule are, for the major part of the 2 ps production run, far from the target temperature of 300 K and thermodynamic equilibrium.

Finally, we discuss a metal–oxide interfacial system. Oxide-supported metals are typical examples of heterogeneous catalysts, and the metal–oxide interface can provide a rich variety of possible reaction sites. An accurate picture of the interfacial structure and dynamics is necessary to understand the nature of these sites. Here, we use Pt_{13} on m-$ZrO_2(\bar{1}11)$ as our model system. The globally optimized geometry determined previously in the group was taken as an initial structure for the DFT-MD simulation.[69] The isomerization and diffusion of supported clusters are highly relevant phenomena in determining the structure and activity of a heterogeneous catalyst, and DFT-MD can be used to study these in atomic detail.[2] To attain reliable results that properly

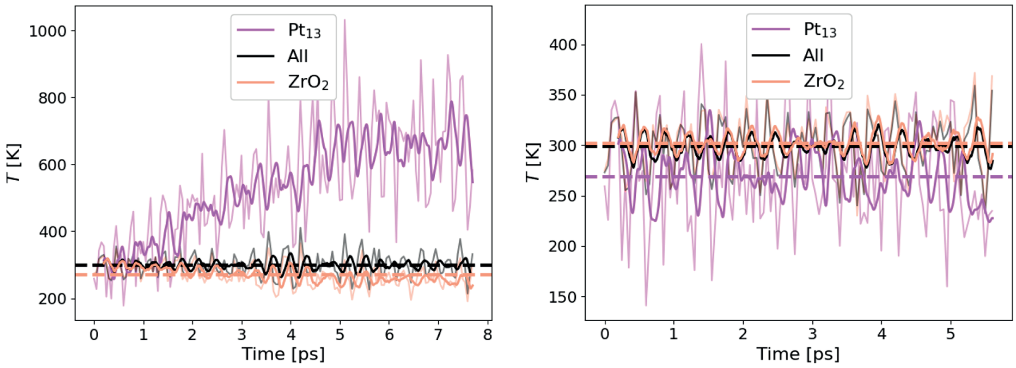

Figure 4. Surface and cluster temperatures for the Pt_{13}/ZrO_2 system obtained with Nosé−Hoover thermostat in GPAW. Left: energy convergence set at 10^{-7} eV/v.e. Right: density convergence set at 10^{-6} e/v.e. Thick curves correspond to 200 fs moving averages.

describe the system under *NVT* conditions, the correct kinetic energy distribution between the cluster and the oxide is crucial. If the effective temperature of the cluster is too low/high, this leads to too low/high isomerization and diffusion rates and the biased distribution of the cluster isomer structures skewing the observed cluster ensemble. The importance of knowing properties of the entire cluster ensemble, rather than just the most stable structure, has been increasingly recognized recently,[2] and a biased view of the ensemble could lead to misrepresented catalytic properties.

We started an ASE/GPAW Nosé−Hoover run from a Langevin-equilibrated structure, using the default GPAW eigenstate and density convergence criteria with a tightened energy criterion of 10^{-7} eV/v.e. (in absolute terms, ca. 2×10^{-4} eV for this system). The left panel in Figure 4 shows that the smoothed average temperature of the Pt cluster increases almost linearly at the rate of ∼60 K/ps, reaching over 700 K after 7 ps had passed. Correspondingly, the zirconia surface cools to maintain the average temperature at 300 K. The temperature distribution is uneven also within the ZrO_2 surface, where the Zr cations heat to ∼350 K while the O anions cool to ∼200 K. This unphysical temperature behavior clearly demonstrates that tighter-than-usual SCF convergence should be enforced when running DFT-MD.

Therefore, we further tightened the convergence by setting the density criterion to 10^{-6} e/v.e. (ca. 10^{-8} eV in practice), which produced a correct kinetic energy partitioning in the N_2 system and improves the description of Pt_{13}/ZrO_2 system as well, as seen in the right panel of Figure 4. In comparison to the previous, loosely converged run, the Pt cluster now cools compared to the ZrO_2 surface, which instead heats up. The cooling effect is much smaller in magnitude, however, and the smoothed average of the cluster temperature hovered around 270 K during the 5 ps run. Still, the results show that even an unusually tight convergence criterion does not guarantee a uniform temperature throughout the system; we presume the flying ice cube effect is likely behind the observed violation of equipartition.

In conclusion, we have shown that combining DFT-MD with widely applied thermostats cannot provide a uniformly constant temperature description of interfacial systems relevant to heterogeneous catalysis and electrocatalysis. Using the DoSPT analysis, we observed that even very tightly converged DFT calculations combined with Nosé−Hoover or Berendsen thermostats lead to temperature gradients between metal and water or between a support and a catalyst. The incorrect temperature description of common thermostats is due to the incorrect kinetic energy distribution between different subsystems present in the simulation—a physical anomaly known as the “flying ice cube” effect. It is present even when we use extremely tight convergence criteria and is further exacerbated if the atomic forces are inaccurate as a result of poor energy convergence.

Our study conclusively demonstrates that current gold standard methods combining DFT-MD and Nosé−Hoover/Berendsen thermostats yield an erroneous thermodynamic description of heterogeneous systems and that previous benchmark simulations are likely subject to significant inaccuracies due to the presence of unphysical temperature gradients. Langevin dynamics instead provides a uniform constant temperature throughout the system, but the friction coefficient needs to be carefully chosen to balance between correct kinetic energy partitioning and minimal disturbance to the system dynamics. Also advanced methods such as the Bussi−Donadio−Parrinello[70] or Nosé−Hoover chain[71] thermostats are known[47] to alleviate the flying ice cube effect, but they are not widely available in common DFT-MD codes such as VASP and QuantumEspresso or through the ASE interface. Overall, the results and analysis presented herein serve as a reminder that accurate and thermodynamically consistent DFT-MD simulations of heterogeneous interfaces require careful testing and validation of both the DFT and MD parts of the method.

■ ASSOCIATED CONTENT

Supporting Information

The Supporting Information is available free of charge at https://pubs.acs.org/doi/10.1021/acs.jpclett.2c00230.

More details on different simulation methods, additional computational results to complement the analysis data provided in the Letter, and the analysis of recent literature data on solvated copper and gold interfaces (PDF)

Transparent Peer Review report available (PDF)

■ AUTHOR INFORMATION

Corresponding Author

Karoliina Honkala − *Department of Chemistry, Nanoscience Center, University of Jyväskylä, FI-40014 Jyväskylä, Finland;*

orcid.org/0000-0002-3166-1077;
Email: karoliina.honkala@jyu.fi

Authors

Ville Korpelin − *Department of Chemistry, Nanoscience Center, University of Jyväskylä, FI-40014 Jyväskylä, Finland;* orcid.org/0000-0002-5947-402X
Toni Kiljunen − *Department of Chemistry, Nanoscience Center, University of Jyväskylä, FI-40014 Jyväskylä, Finland*
Marko M. Melander − *Department of Chemistry, Nanoscience Center, University of Jyväskylä, FI-40014 Jyväskylä, Finland;* orcid.org/0000-0001-7111-1603
Miguel A. Caro − *Department of Electrical Engineering and Automation, Aalto University, FIN-02150 Espoo, Finland;* orcid.org/0000-0001-9304-4261
Henrik H. Kristoffersen − *Department of Chemistry, University of Copenhagen, 2100 Copenhagen Ø, Denmark;* orcid.org/0000-0001-6943-0752
Nisha Mammen − *Department of Physics,Nanoscience Center, University of Jyväskylä, FI-40014 Jyväskylä, Finland;* orcid.org/0000-0002-1550-6333
Vesa Apaja − *Department of Physics,Nanoscience Center, University of Jyväskylä, FI-40014 Jyväskylä, Finland;* orcid.org/0000-0002-3808-4735

Complete contact information is available at:
https://pubs.acs.org/10.1021/acs.jpclett.2c00230

Author Contributions

[‖]V.K., T.K., and M.M.M. contributed equally. V.K. performed the N_2 and supported Pt cluster simulations with GPAW/ASE. M.M.M. performed the GPAW/ASE Au−H_2O calculations and all the CP2K simulations. H.H.K. performed the VASP simulations. N.M. performed the QuantumEspresso calculations. T.K. performed the DoSPT analyses and ran the GPAW/ASE water simulations. M.A.C. extended the DoSPT method for simulation of 2D periodic systems. V.K., M.M.M., T.K., N.M., V.A., and K.H. contributed to analyzing the results and to writing the manuscript.

Notes

The authors declare no competing financial interest.

Most analyzed and presented data and used scripts are available through the Etsin fairdata service at 10.23729/00d5f9e0-a188-4512-ac95-2069a5aaf6ef. The VASP data was not uploaded because of its extremely large size but can be obtained from the authors.

■ ACKNOWLEDGMENTS

The project was funded by the Academy of Finland projects 307853 (M.M.M.), 338228 (M.M.M.), 310574 (M.A.C.), 330488 (M.A.C.), 317739 (M.M.M., N.M., and K.H.), and 332290 (N.M.). M.M.M. and K.H. also acknowledge Jane and Aatos Erkko Foundation for funding to the LACOR project. The computational resources were provided by CSC-IT Center for Science Ltd through the pilot project initiatives (H2OINTE and FLUXMD). We also thank Professor Jakob Schiøtz for helpful discussions related to the thermostats implemented in ASE. Prof. Gerrit Groenhof and Dr. Dimitry Morozov are acknowledged for careful reading of the work and their fruitful comments.

■ REFERENCES

(1) Magnussen, O. M.; Gross, A. Toward an Atomic-Scale Understanding of Electrochemical Interface Structure and Dynamics. *J. Am. Chem. Soc.* **2019**, *141*, 4777−4790.

(2) Zhang, Z.; Zandkarimi, B.; Alexandrova, A. N. Ensembles of Metastable States Govern Heterogeneous Catalysis on Dynamic Interfaces. *Acc. Chem. Res.* **2020**, *53*, 447−458.

(3) Heenen, H. H.; Gauthier, J. A.; Kristoffersen, H. H.; Ludwig, T.; Chan, K. Solvation at metal/water interfaces: An ab initio molecular dynamics benchmark of common computational approaches. *J. Chem. Phys.* **2020**, *152*, 144703.

(4) Tuckerman, M. *Statistical Mechanics: Theory and Molecular Simulations*; Oxford University Press, 2010.

(5) Zhang, Z.; Cui, Z.-H.; Jimenez-Izal, E.; Sautet, P.; Alexandrova, A. N. Hydrogen Evolution on Restructured B-Rich WB: Metastable Surface States and Isolated Active Sites. *ACS Catal.* **2020**, *10*, 13867−13877.

(6) Le, J.; Iannuzzi, M.; Cuesta, A.; Cheng, J. Determining Potentials of Zero Charge of Metal Electrodes versus the Standard Hydrogen Electrode from Density-Functional-Theory-Based Molecular Dynamics. *Phys. Rev. Lett.* **2017**, *119*, 016801.

(7) Le, J.; Cuesta, A.; Cheng, J. The structure of metal-water interface at the potential of zero charge from density functional theory-based molecular dynamics. *J. Electroanal. Chem.* **2018**, *819*, 87−94.

(8) Kristoffersen, H. H.; Chan, K.; Vegge, T.; Hansen, H. A. Energy-entropy competition in cation-hydroxyl interactions at the liquid water-Pt(111) interface. *Commun. Chem.* **2020**, *56*, 427−430.

(9) Kristoffersen, H. H.; Vegge, T.; Hansen, H. A. OH formation and H2 adsorption at the liquid water−Pt(111) interface. *Chem. Sci.* **2018**, *9*, 6912−6921.

(10) Li, C.-Y.; Le, J.-B.; Wang, Y.-H.; Chen, S.; Yang, Z.-L.; Li, J.-F.; Cheng, J.; Tian, Z.-Q. In situ probing electrified interfacial water structures at atomically flat surfaces. *Nat. Mater.* **2019**, *18*, 697−701.

(11) Clabaut, P.; Fleurat-Lessard, P.; Michel, C.; Steinmann, S. N. Ten Facets, One Force Field: The GAL19 Force Field for Water−Noble Metal Interfaces. *J. Chem. Theory Comput.* **2020**, *16*, 4565−4578.

(12) Zhai, H.; Alexandrova, A. N. Local Fluxionality of Surface-Deposited Cluster Catalysts: The Case of Pt7 on Al2O3. *J. Phys. Chem. Lett.* **2018**, *9*, 1696−1702.

(13) Li, Y.; Li, S.; Bäumer, M.; Ivanova-Shor, E. A.; Moskaleva, L. V. What Changes on the Inverse Catalyst? Insights from CO Oxidation on Au-Supported Ceria Nanoparticles Using Ab Initio Molecular Dynamics. *ACS Catal.* **2020**, *10*, 3164−3174.

(14) Ha, M.-A.; Baxter, E. T.; Cass, A. C.; Anderson, S. L.; Alexandrova, A. N. Boron Switch for Selectivity of Catalytic Dehydrogenation on Size-Selected Pt Clusters on Al_2O_3. *J. Am. Chem. Soc.* **2017**, *139*, 11568−11575.

(15) Wang, D.; Liu, Z.-P.; Yang, W.-M. Revealing the Size Effect of Platinum Cocatalyst for Photocatalytic Hydrogen Evolution on TiO_2 Support: A DFT Study. *ACS Catal.* **2018**, *8*, 7270−7278.

(16) Wang, D.; Liu, Z.-P.; Yang, W.-M. Proton-Promoted Electron Transfer in Photocatalysis: Key Step for Photocatalytic Hydrogen Evolution on Metal/Titania Composites. *ACS Catal.* **2017**, *7*, 2744−2752.

(17) Li, M.-R.; Song, Y.-Y.; Wang, G.-C. The Mechanism of Steam-Ethanol Reforming on Co_{13}/CeO2−x: A DFT Study. *ACS Catal.* **2019**, *9*, 2355−2367.

(18) Singh, N.; Lee, M.-S.; Akhade, S. A.; Cheng, G.; Camaioni, D. M.; Gutiérrez, O. Y.; Glezakou, V.-A.; Rousseau, R.; Lercher, J. A.; Campbell, C. T. Impact of pH on Aqueous-Phase Phenol Hydrogenation Catalyzed by Carbon-Supported Pt and Rh. *ACS Catal.* **2019**, *9*, 1120−1128.

(19) Gorey, T. J.; Zandkarimi, B.; Li, G.; Baxter, E. T.; Alexandrova, A. N.; Anderson, S. L. Coking-Resistant Sub-Nano Dehydrogenation Catalysts: Pt_nSn_x/SiO_2 (n = 4, 7). *ACS Catal.* **2020**, *10*, 4543−4558.

(20) Xiong, Y.; et al. Single-atom Rh/N-doped carbon electrocatalyst for formic acid oxidation. *Nat. Nanotechnol.* **2020**, *15*, 390−397.

(21) Bellarosa, L.; García-Muelas, R.; Revilla-López, G.; López, N. Diversity at the Water−Metal Interface: Metal, Water Thickness, and Confinement Effects. *ACS Cent. Sci.* **2016**, *2*, 109−116.

(22) Vorobyeva, E.; Fako, E.; Chen, Z.; Collins, S. M.; Johnstone, D.; Midgley, P. A.; Hauert, R.; Safonova, O. V.; Vilé, G.; López, N.; Mitchell, S.; Pérez-Ramírez, J. Atom-by-Atom Resolution of Structure−Function Relations over Low-Nuclearity Metal Catalysts. *Angew. Chem., Int. Ed.* **2019**, *58*, 8724−8729.

(23) Daelman, N.; Capdevila-Cortada, M.; López, N. Dynamic charge and oxidation state of Pt/CeO_2 single-atom catalysts. *Nat. Mater.* **2019**, *18*, 1215−1221.

(24) Li, M.; Hua, B.; Wang, L.-C.; Sugar, J. D.; Wu, W.; Ding, Y.; Li, J.; Ding, D. Switching of metal−oxygen hybridization for selective CO2 electrohydrogenation under mild temperature and pressure. *Nat. Catal.* **2021**, *4*, 274−283.

(25) Wang, Y.-H.; Zheng, S.; Yang, W.-M.; Zhou, R.-Y.; He, Q.-F.; Radjenovic, P.; Dong, J.-C.; Li, S.; Zheng, J.; Yang, Z.-L.; Attard, G.; Pan, F.; Tian, Z.-Q.; Li, J.-F. In situ Raman spectroscopy reveals the structure and dissociation of interfacial water. *Nature* **2021**, *600*, 81−85.

(26) Monteiro, M. C. O.; Dattila, F.; López, N.; Koper, M. T. M. The Role of Cation Acidity on the Competition between Hydrogen Evolution and CO_2 Reduction on Gold Electrodes. *J. Am. Chem. Soc.* **2022**, *144*, 1589.

(27) Monteiro, M. C. O.; Dattila, F.; Hagedoorn, B.; García-Muelas, R.; López, N.; Koper, M. T. M. Absence of CO2 electroreduction on copper, gold and silver electrodes without metal cations in solution. *Nat. Catal.* **2021**, *4*, 654−662.

(28) Bagger, A.; Arnarson, L.; Hansen, M. H.; Spohr, E.; Rossmeisl, J. Electrochemical CO Reduction: A Property of the Electrochemical Interface. *J. Am. Chem. Soc.* **2019**, *141*, 1506−1514.

(29) Hansen, M. H.; Nilsson, A.; Rossmeisl, J. Modelling pH and potential in dynamic structures of the water/Pt(111) interface on the atomic scale. *Phys. Chem. Chem. Phys.* **2017**, *19*, 23505−23514.

(30) Nong, H. N.; et al. Key role of chemistry versus bias in electrocatalytic oxygen evolution. *Nature* **2020**, *587*, 408−413.

(31) Zare, M.; Saleheen, M.; Kundu, S. K.; Heyden, A. Dependency of solvation effects on metal identity in surface reactions. *Commun. Chem.* **2020**, *3*, 187.

(32) Bagger, A.; Arán-Ais, R. M.; Halldin Stenlid, J.; Campos dos Santos, E.; Arnarson, L.; Degn Jensen, K.; Escudero-Escribano, M.; Roldan Cuenya, B.; Rossmeisl, J. Ab Initio Cyclic Voltammetry on Cu(111), Cu(100) and Cu(110) in Acidic, Neutral and Alkaline Solutions. *ChemPhysChem* **2019**, *20*, 3096−3105.

(33) Rossmeisl, J.; Jensen, K. D.; Petersen, A. S.; Arnarson, L.; Bagger, A.; Escudero-Escribano, M. Realistic Cyclic Voltammograms from Ab Initio Simulations in Alkaline and Acidic Electrolytes. *J. Phys. Chem. C* **2020**, *124*, 20055−20065.

(34) Naserifar, S.; Chen, Y.; Kwon, S.; Xiao, H.; Goddard, W. A. Artificial Intelligence and QM/MM with a Polarizable Reactive Force Field for Next-Generation Electrocatalysts. *Matter* **2021**, *4*, 195−216.

(35) Fazio, G.; Selli, D.; Ferraro, L.; Seifert, G.; Di Valentin, C. Curved TiO_2 Nanoparticles in Water: Short (Chemical) and Long (Physical) Range Interfacial Effects. *ACS Appl. Mater. Interfaces* **2018**, *10*, 29943−29953.

(36) Sebastián-Pascual, P.; Petersen, A. S.; Bagger, A.; Rossmeisl, J.; Escudero-Escribano, M. pH and Anion Effects on Cu−Phosphate Interfaces for CO Electroreduction. *ACS Catal.* **2021**, *11*, 1128−1135.

(37) Goldsmith, Z. K.; Calegari Andrade, M. F.; Selloni, A. Effects of applied voltage on water at a gold electrode interface from ab initio molecular dynamics. *Chem. Sci.* **2021**, *12*, 5865−5873.

(38) Sakong, S.; Forster-Tonigold, K.; Gross, A. The structure of water at a Pt(111) electrode and the potential of zero charge studied from first principles. *J. Chem. Phys.* **2016**, *144*, 194701.

(39) Sakong, S.; Gross, A. Water structures on a Pt(111) electrode from ab initio molecular dynamic simulations for a variety of electrochemical conditions. *Phys. Chem. Chem. Phys.* **2020**, *22*, 10431−10437.

(40) Le, J.-B.; Fan, Q.-Y.; Li, J.-Q.; Cheng, J. Molecular origin of negative component of Helmholtz capacitance at electrified Pt(111)/water interface. *Sci. Adv.* **2020**, *6*, eabb1219.

(41) Fan, Q.-Y.; Sun, J.-J.; Wang, F.; Cheng, J. Adsorption-Induced Liquid-to-Solid Phase Transition of Cu Clusters in Catalytic Dissociation of CO_2. *J. Phys. Chem. Lett.* **2020**, *11*, 7954−7959.

(42) Surendralal, S.; Todorova, M.; Neugebauer, J. Impact of Water Coadsorption on the Electrode Potential of H-Pt(111)-Liquid Water Interfaces. *Phys. Rev. Lett.* **2021**, *126*, 166802.

(43) Nosé, S. A unified formulation of the constant temperature molecular dynamics methods. *J. Chem. Phys.* **1984**, *81*, 511−519.

(44) Hoover, W. G. Canonical dynamics: Equilibrium phase-space distributions. *Phys. Rev. A* **1985**, *31*, 1695−1697.

(45) Berendsen, H. J. C.; Postma, J. P. M.; van Gunsteren, W. F.; DiNola, A.; Haak, J. R. Molecular dynamics with coupling to an external bath. *J. Chem. Phys.* **1984**, *81*, 3684−3690.

(46) Caro, M. A.; Laurila, T.; Lopez-Acevedo, O. Accurate schemes for calculation of thermodynamic properties of liquid mixtures from molecular dynamics simulations. *J. Chem. Phys.* **2016**, *145*, 244504.

(47) Braun, E.; Moosavi, S. M.; Smit, B. Anomalous Effects of Velocity Rescaling Algorithms: The Flying Ice Cube Effect Revisited. *J. Chem. Theory Comput.* **2018**, *14*, 5262−5272.

(48) Harvey, S. C.; Tan, R. K.-Z.; Cheatham, T. E., III The flying ice cube: Velocity rescaling in molecular dynamics leads to violation of energy equipartition. *J. Comput. Chem.* **1998**, *19*, 726−740.

(49) Lemak, A. S.; Balabaev, N. K. On The Berendsen Thermostat. *Mol. Simul.* **1994**, *13*, 177−187.

(50) Mor, A.; Ziv, G.; Levy, Y. Simulations of proteins with inhomogeneous degrees of freedom: The effect of thermostats. *J. Comput. Chem.* **2008**, *29*, 1992−1998.

(51) Lingenheil, M.; Denschlag, R.; Reichold, R.; Tavan, P. The "Hot-Solvent/Cold-Solute" Problem Revisited. *J. Chem. Theory Comput.* **2008**, *4*, 1293−1306.

(52) Cheng, A.; Merz, K. M. Application of the Nosé-Hoover Chain Algorithm to the Study of Protein Dynamics. *J. Phys. Chem.* **1996**, *100*, 1927−1937.

(53) Wong-ekkabut, J.; Karttunen, M. The good, the bad and the user in soft matter simulations. *Biochim. Biophys. Acta (BBA) - Biomembranes* **2016**, *1858*, 2529−2538. Biosimulations of lipid membranes coupled to experiments.

(54) Watanabe, H. Failure of Deterministic and Stochastic Thermostats to Control Temperature of Molecular Systems. *J. Phys. Soc. Jpn.* **2017**, *86*, 075004.

(55) Li, Z.; Xiong, S.; Sievers, C.; Hu, Y.; Fan, Z.; Wei, N.; Bao, H.; Chen, S.; Donadio, D.; Ala-Nissila, T. Influence of thermostatting on nonequilibrium molecular dynamics simulations of heat conduction in solids. *J. Chem. Phys.* **2019**, *151*, 234105.

(56) Basconi, J. E.; Shirts, M. R. Effects of Temperature Control Algorithms on Transport Properties and Kinetics in Molecular Dynamics Simulations. *J. Chem. Theory Comput.* **2013**, *9*, 2887−2899.

(57) Li, W.-L.; Lininger, C. N.; Chen, K.; Vaissier Welborn, V.; Rossomme, E.; Bell, A. T.; Head-Gordon, M.; Head-Gordon, T. Critical Role of Thermal Fluctuations for CO Binding on Electrocatalytic Metal Surfaces. *JACS Au* **2021**, *1*, 1708−1718.

(58) Mortensen, J. J.; Hansen, L. B.; Jacobsen, K. W. Real-space grid implementation of the projector augmented wave method. *Phys. Rev. B* **2005**, *71*, 035109.

(59) Enkovaara, J.; et al. Electronic structure calculations with GPAW: a real-space implementation of the projector augmented-wave method. *J. Condens. Matter Phys.* **2010**, *22*, 253202.

(60) Hjorth Larsen, A.; et al. The atomic simulation environment—a Python library for working with atoms. *J. Condens. Matter Phys.* **2017**, *29*, 273002.

(61) Kresse, G.; Furthmüller, J. Efficient iterative schemes for ab initio total-energy calculations using a plane-wave basis set. *Phys. Rev. B* **1996**, *54*, 11169−11186.

(62) Kühne, T. D.; et al. CP2K: An electronic structure and molecular dynamics software package - Quickstep: Efficient and accurate electronic structure calculations. *J. Chem. Phys.* **2020**, *152*, 194103.

(63) Giannozzi, P.; Baseggio, O.; Bonfà, P.; Brunato, D.; Car, R.; Carnimeo, I.; Cavazzoni, C.; de Gironcoli, S.; Delugas, P.; Ferrari Ruffino, F.; Ferretti, A.; Marzari, N.; Timrov, I.; Urru, A.; Baroni, S. Quantum ESPRESSO toward the exascale. *J. Chem. Phys.* **2020**, *152*, 154105.

(64) Nosé, S. A unified formulation of the constant temperature molecular dynamics methods. *J. Chem. Phys.* **1984**, *81*, 511−519.

(65) Hoover, W. G. Canonical dynamics: Equilibrium phase-space distributions. *Phys. Rev. A* **1985**, *31*, 1695−1697.

(66) Nosé, S. A molecular dynamics method for simulations in the canonical ensemble. *Mol. Phys.* **1984**, *52*, 255−268.

(67) Lin, S.-T.; Blanco, M.; Goddard, W. A. The two-phase model for calculating thermodynamic properties of liquids from molecular dynamics: Validation for the phase diagram of Lennard-Jones fluids. *J. Chem. Phys.* **2003**, *119*, 11792−11805.

(68) Yan, L.-M.; Sun, C.; Liu, H.-T. Opposite phenomenon to the flying ice cube in molecular dynamics simulations of flexible TIP3P water. *Adv. Manuf.* **2013**, *1*, 160−165.

(69) Bazhenov, A. S.; Honkala, K. Globally Optimized Equilibrium Shapes of Zirconia-Supported Rh and Pt Nanoclusters: Insights into Site Assembly and Reactivity. *J. Phys. Chem. C* **2019**, *123*, 7209−7216.

(70) Bussi, G.; Donadio, D.; Parrinello, M. Canonical sampling through velocity rescaling. *J. Chem. Phys.* **2007**, *126*, 014101.

(71) Martyna, G. J.; Klein, M. L.; Tuckerman, M. Nosé−Hoover chains: The canonical ensemble via continuous dynamics. *J. Chem. Phys.* **1992**, *97*, 2635−2643.

III

REDUCING THE IRREDUCIBLE: DISPERSED METAL ATOMS FACILITATE REDUCTION OF IRREDUCIBLE OXIDES

by

Ville Korpelin, Marko M. Melander, and Karoliina Honkala

The Journal of Physical Chemistry C **2022**, 126, 933–945

DOI:10.1021/acs.jpcc.1c08979

THE JOURNAL OF PHYSICAL CHEMISTRY C
A JOURNAL OF THE AMERICAN CHEMICAL SOCIETY

pubs.acs.org/JPCC Article

Reducing the Irreducible: Dispersed Metal Atoms Facilitate Reduction of Irreducible Oxides

Ville Korpelin, Marko M. Melander, and Karoliina Honkala*

Cite This: *J. Phys. Chem. C* 2022, 126, 933−945 Read Online

ACCESS | Metrics & More | Article Recommendations | Supporting Information

ABSTRACT: Oxide reducibility is a central concept quantifying the role of the support in catalysis. While reducible oxides are often considered catalytically active, irreducible oxides are seen as inert supports. Enhancing the reducibility of irreducible oxides has, however, emerged as an effective way to increase their catalytic activity while retaining their inherent thermal stability. In this work, we focus on the prospect of using single metal atoms to increase the reducibility of a prototypical irreducible oxide, zirconia. Based on extensive self-consistent DFT+*U* calculations, we demonstrate that single metal atoms significantly improve and tune the surface reducibility of zirconia. Detailed analysis of the observed single atom induced reducibility allows us to attribute the enhanced reducibility to strong interactions between the metal atom and the electrons trapped in the vacancy and d−p orbital interactions between the metal atom and oxygen. This analysis enables transferring the obtained theoretical understanding to other irreducible oxides as well. The detailed understanding of how oxide reducibility can be tuned offers precise control over the catalytic properties of metal oxides.

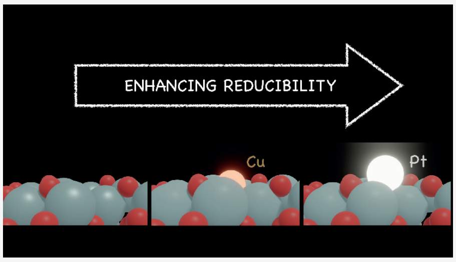

1. INTRODUCTION

Metal oxides play a crucial role in heterogeneous catalysis, where they are considered as both catalysts and support materials,[1] but this division is artificial, as oxides often play multiple roles.[1] In particular, the catalyst−oxide interfaces may be more active than the catalyst and oxide phases alone[2−5] with some elementary steps taking place on the support oxide and others on the metal catalyst.[6] The oxide may also play an integral role in stabilizing the catalyst and in preventing catalyst sintering.[3,7] Given such diverse roles of metal oxides in catalysis, utilizing, modifying, and understanding their chemistry offers a powerful tool to tailor the performance of heterogeneous catalysts.

Structural defects are known to have a substantial influence on the physical and chemical properties of oxides. In particular, the ability to form oxygen vacancies, that is, the oxide reducibility, is central to the catalytic properties of metal oxides.[6,8] The reducibility determines the oxide's propensity to catalyze, for example, Mars-van Krevelen-type elementary steps, dehydrogenation, and redox reactions.[9] Metal oxides can be roughly divided into reducible and irreducible oxides where the former are characterized by facile oxygen vacancy formation, small band gaps, and the active redox properties of metal cations, which can adopt electrons remaining on the oxide surface.[6,8] Irreducible oxides, on the other hand, have large band gaps, and the electrons cannot localize on the cations, which leads to high vacancy formation energies.[6] From these perspectives, irreducible oxides are often considered as inert supports, while reducible oxides are thought to be more catalytically active.[6,8]

An attractive venue to modify or tailor metal oxide catalysis is to activate surfaces of irreducible oxides while retaining their bulk stability to realize thermally stable oxide supports with enhanced catalytic activity. Thus far, three approaches to enhance the reducibility of irreducible oxides have been identified: nanostructuring, bulk doping, and metal-oxide interfaces.[6] The first two affect both the surface and the bulk properties of the oxide, which may decrease their bulk stability. The last one modifies only the surface properties, which is beneficial in retaining the bulk stability while simultaneously enhancing surface reducibility to activate the oxide toward catalytic applications.

Recently, the above strategies have been successfully applied in the activation of a typical irreducible oxide, zirconia (ZrO_2), for nonoxidative dehydrogenation of hydrocarbons by creating oxygen vacancies on the surface of monoclinic zirconia.[10] From a mechanistic perspective, the introduction of oxygen vacancies leads to the formation of coordinatively unsaturated Zr cations, which are active sites for the dehydrogenation reaction.[10−12] Crucially, the catalytic activity of ZrO_2 has been directly correlated with its ability to release oxygen, that is, zirconia's reducibility.[10,13] The reducibility and catalytic activity toward

Received: October 14, 2021
Revised: December 10, 2021
Published: January 10, 2022

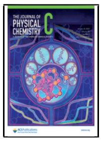

hydrocarbon dehydrogenation have successfully been increased by reducing the ZrO_2 particle size.[11,12] Doping ZrO_2 with Ca^{2+}, Mg^{2+}, and Li^{+} decreases the activity below that of pristine zirconia, whereas introducing La^{3+}, Y^{3+}, and Sm^{3+} dopants promotes reducibility and activity;[14,15] Cr-promoted ZrO_2 was even found to outperform the commercial CrO_x-K/Al_2O_3 catalyst for propane dehydrogenation.[13] In general, tuning the reducibility of zirconia through size-control or doping are envisioned as means to develop eco-friendly and cost-efficient hydrocarbon dehydrogenation catalysts.[13] However, while the oxygen vacancies are crucial for enhancing the activity of ZrO_2, it remains poorly understood how and why different dopants or variations in crystal size enhance the reducibility.

In addition to structuring and doping, adsorbed metal clusters have been found to enhance zirconia's reducibility. The effects of an adsorbed Ru_{10} cluster[6] and an Au nanorod[16] on the reducibility of t-ZrO_2 have been computationally investigated, and both were found to significantly stabilize nearby oxygen vacancies. One of the present authors has shown that small Rh clusters and single Rh atoms on zirconia increase the reducibility more than large metal-oxide interfaces.[17] Guided by these results, we now consider a new approach to enhance the surface reducibility of ZrO_2 with individual dispersed metal atoms. Using single atoms (SA) maximizes metal utilization and greatly facilitates the surface reducibility as shown herein. SAs themselves exhibit catalytic properties distinct from clusters and nanoparticles, but are often unstable and sinter easily.[18] SAs are, however, significantly stabilized when anchored in oxygen vacancies.[7,19] This way the SA-enhanced reducibility can be used for dynamically introducing vacancies to stabilize the SAs for catalytic applications. Besides modifying the reducibility of a specific oxide using SAs, it is crucial to understand to what extent and why certain metal atoms impact oxygen vacancy formation. The atomic level understanding gained for SA-enhanced reducibility on one specific oxide can be transferred to other oxides.

In this work, we have addressed the ability of several different metal SAs to modify the reducibility of zirconia (ZrO_2), a widely utilized and highly irreducible metal oxide support. The $(\bar{1}11)$ facet of monoclinic ZrO_2 was chosen as the model surface based on its catalytic relevance and high stability, which makes it a robust system for probing reducibility enhancement. Making use of extensive Hubbard-corrected density functional theory (DFT+U) calculations we show how different metal SAs affect the reducibility and analyze in detail the reasons behind this behavior. To obtain a reliable DFT description of the electronic structure, we implemented and utilized the self-consistent Hubbard-corrected DFT approach and developed several electronic structure, charge transfer, and covalent bond analyses to explain and understand the SA-induced reducibility. We demonstrate that the detailed understanding obtained for zirconia can be transferred to other irreducible oxides, such as MgO, but not to reducible oxides, such as TiO_2. In general, the work herein establishes the possibility of rationally enhancing and tuning the reducibility of irreducible oxide surfaces through the use of deposited single metal atoms.

2. METHODS

2.1. DFT Calculations.

Spin-polarized density functional theory (DFT) calculations were performed using GPAW 1.1.0[20−23] together with the Perdew−Burke−Ernzerhof (PBE) exchange-correlation functional.[24,25] As discussed in section 2.2, a Hubbard+U correction was also applied on the Zr d electrons. The core electrons of each element were represented by PAW[26] setups in the frozen-core approximation. The reciprocal space of the bulk m-ZrO_2 unit cell was sampled by a (6 × 6 × 6) Monkhorst−Pack k-point mesh, while for the m-$ZrO_2(\bar{1}11)$ surface, modeled with a four-layer thick 3 × 3 cell, only the Γ point was sampled; both choices have been validated in previous studies.[17,27] The slab calculations were performed with periodic boundary conditions in three dimensions with ∼2 nm vacuum between slabs in the vertical direction. The wave functions and the electron density were described on a real-space grid with maximum spacing 0.20 Å, and atomic structures were allowed to relax until the maximum residual force fell below 0.05 eV $Å^{-1}$. To validate this choice, selected systems were converged to 0.025 eV $Å^{-1}$, but the effect on energy and geometry was minor. The lattice parameters and adsorption geometries were reoptimized for each different value of U.

The reference energies for gas-phase metal atoms were computed in a 12.00 Å × 12.01 Å × 12.02 Å cell with the atom shifted 0.1 Å from the center to improve convergence. The magnetic moments were fixed to their known experimental values, and a Fermi−Dirac smearing temperature of 232 K was applied. Most atoms converged to their experimental electronic structures, with the exception of Co and Ir, for which we found the configuration d^8s^1 instead of d^7s^2. For Ni, which is known to have very close-lying d^8s^2 and d^9s^1 configurations,[28] we obtained the latter one. More details are presented in the Supporting Information (SI), section S1. When the metals were adsorbed on the surface, their magnetic moments were allowed to relax freely.

2.2. Computation of the U Parameter.

The Hubbard+U correction to DFT exchange-correlation functionals reduces the electron self-interaction error present in all current DFT functionals.[29] In transition oxide materials, the +U correction accounts for the strong correlation within localized d and f states, reduces the delocalization error of electrons in these states and improves the electronic structure description. Therefore, the Hubbard correction is usually only applied to the metal atoms in transition metal oxides. This approach has been commonly used for ZrO_2 to improve electron localization while also widening the band gap.[9,16,30,31] We chose to follow this approach as well, but decided to take a closer look at the choice of the U parameter.

The U parameter is usually determined semiempirically by varying its value until the obtained result matches some experimental parameter, such as a band gap, as discussed in section S3.1 in the Supporting Information. While this approach can be well-justified, care must be taken, as improving the value of one parameter by changing a U value might worsen the others.[32] Furthermore, a given U value is not generally transferable between different DFT implementations, as the value is sensitive to the underlying basis set, pseudopotential, and so on (see SI). To reduce the empiricism and code-dependency of the DFT+U method, several schemes have been introduced to self-consistently compute the U parameter (see SI). The benefit of such ab initio methods is that they avoid any parameter transferability issues that might arise between codes or systems and allow direct computation of the U value for the system of interest.

To reliably estimate the U values, we implemented the self-consistent linear response method (LR-DFT+U)[33,34] into the

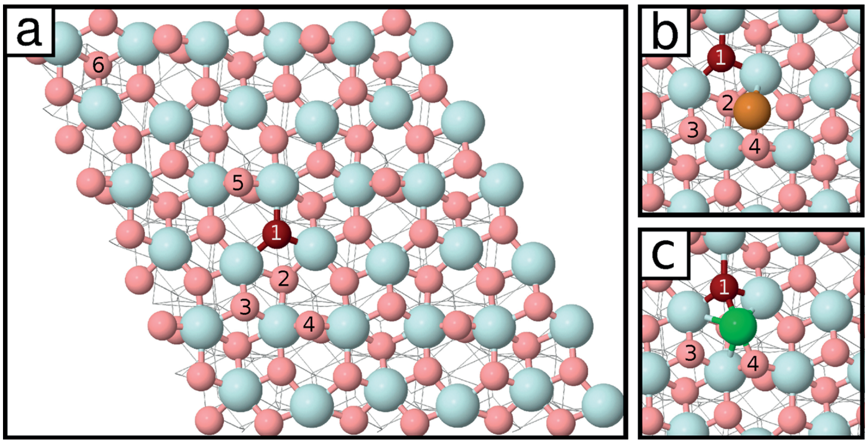

Figure 1. (a) Computational m-ZrO$_2$($\bar{1}$11) cell. Light blue: Zr, light red: O, dark red: the O atom that is removed to create the vacancy O1. The O atoms important for our discussion have been numbered for clarity. (b, c) Cu (brown) and Ni (green) as representative examples of metal−surface binding geometries.

GPAW software (see SI, section S3 for details) within the simplified, rotationally invariant DFT+U method by Dudarev et al.[35] This implementation was used to compute the U value for the Zr d electrons. While an oxygen p correction has been found to improve the description of, for example, bond lengths and electronic structures in some cases,[36−39] no such correction was employed herein.

For bulk m-ZrO$_2$, we computed the Hubbard U parameter in a 2 × 2 × 2 supercell (96 atoms). The background correction[33] had only a negligible effect on the result, indicating that the size of the supercell is sufficient. The obtained U_d value is 1.9 eV, giving the following the cell parameters (without U): a = 5.197 (5.161) Å, b = 5.263 (5.231) Å, c = 5.365 (5.340) Å, and β = 99.6 (99.6) degrees. The changes are minor and as such it was not considered necessary to do a structurally self-consistent U determination.[40]

The appropriate U parameter for a given orbital can depend on its local chemical environment, and therefore, we also calculated the Hubbard U parameter for the m-ZrO$_2$($\bar{1}$11) surface using a four-layer thick 2 × 2 × 1 supercell (in total 192 atoms). For the top-layer Zr atoms, we obtained U_d = 1.9 eV, while for the second-layer Zr atoms, the corresponding value was 1.8 eV. This demonstrates that the effect of the local environment is minor, as the values are similar to the one computed for the bulk. This small variation was neglected, and we employed U_d = 2.0 eV for all Zr atoms in the slab.

We also considered U_d(Zr) = 4.0 eV, which is a fairly common choice in the literature,[9,16,30,31] to elucidate the effect of the Hubbard correction on our results. In general, due to the possible transferability issues, U values taken from the literature should be validated using the specific computational method and system one is studying. In this case, the difference in TM adsorption energies between the U = 2.0 eV and U = 4.0 eV calculations was found to be modest; a detailed comparison is presented in the SI, section S6. The insensitivity of adsorption energy to metal U in early TM oxides has been noted before in a study highlighting the divergent surface energetics between DFT+U and hybrid functionals.[41]

As it is well-known that GGA functionals underestimate the band gaps of semiconductors and insulators[42] and the Hubbard correction can, at least partially, correct this, we examined the impact of the Hubbard U parameter on the band gaps of the m-ZrO$_2$ bulk and surface via a density of states (DOS) analysis. Note that since freezing the bottom two layers of the slab introduces spurious constraint-induced gap states,[43] only the electronic states originating from the unconstrained surface layers are analyzed (see SI, section S2). Comparison with experiment is complicated by the fact that various experimental band gap values for m-ZrO$_2$ have been reported in the 4.2−5.8 eV range, depending on the method.[44−47] The reason behind this wide variation between measurements has not been conclusively addressed, though at least the presence of defect states[46] and resolution issues[48] have been suggested as explanations. At any rate, we find that our uncorrected (U = 0) bulk band gap value of 3.7 eV lies below the experimental range as expected, and the gap widens with increasing U, bringing it closer to the measured values. Our LR value U_d(Zr) = 2.0 eV produces a bulk band gap of 4.1 eV, and increasing the correction to 4.0 eV widens the gap to 4.5 eV. The m-ZrO$_2$($\bar{1}$11) surface band gap was computed to be 3.6 eV for both U_d(Zr) = 2.0 eV and U_d(Zr) = 4.0 eV. Introducing the oxygen vacancy into the surface leads to the formation of a gap state ~2.8 eV above the valence band (VB) edge. Our findings agree with a previous PBE+U study, which reported a band gap of 3.2 eV and the appearance of a gap state 2.6 eV above the VB.[30]

2.3. Analyzing Reduction Energies.

The adsorption energy of a transition metal atom M on ZrO$_2$ is defined as follows:

$$E_{\mathrm{ads}} = E(\mathrm{M/ZrO_2}) - E(\mathrm{ZrO_2}) - E(\mathrm{M,\ g}) \tag{1}$$

where E(M/ZrO$_2$) is the total energy of a ZrO$_2$ slab with an adsorbed metal atom M, E(ZrO$_2$) stands for the energy of the slab without any adsorbate, and E(M,g) corresponds to the energy of a gas-phase metal atom M. Here, ZrO$_2$ can be either the ideal or reduced surface.

The reduction energy of a system is computed as

$$E_{\mathrm{R}} = E_{\mathrm{red}} + E(\mathrm{H_2O,\ g}) - E_{\mathrm{stoich}} - E(\mathrm{H_2,\ g}) \tag{2}$$

where E_{red} and E_{stoich} are the respective energies of the reduced and stoichiometric systems, whereas E(H$_2$O,g) and E(H$_2$,g) are the energies of gas-phase water and molecular hydrogen, respectively. Water was selected as a reference instead of molecular oxygen, since the energy of O_2 is not accurately described by DFT.[49,50]

We applied several analyses to understand the transition metal (TM) adsorption energies and their effect on the reducibility of m-$ZrO_2(\bar{1}11)$. The atomic charges were computed using the Bader partition scheme and the algorithm by Henkelman et al.[51]

To quantify orbital hybridization and covalent bonding, we employed a modified version of the hybridization index H_{kl} proposed in ref 52. The hybridization index is defined as

$$H_{kl}^{IJ} = \sum_{i=1}^{N_e} \sum_{m,m'} w_{km,i}^{I} w_{lm',i}^{J} \tag{3}$$

where k and l are the angular quantum numbers of interest for atoms I and J, m and m' are the corresponding magnetic quantum numbers and i runs over all N_e occupied bands. The weight parameter $w_{km,i}^{I} = \langle \phi_{km}^{I} | \psi_i \rangle$ represents the projection of the km atomic orbital ϕ of atom I on band ψ_i obtained from the DFT+U calculations. The PAW[26] pseudoprojector $\tilde{p}_{km}^{I}$ is utilized when approximating the weight as $w_{km,i}^{I} \approx \langle \tilde{p}_{km}^{I} | \psi_i \rangle$.[21] In practice, summing over all the bands introduces spurious hybridization contributions from bands that are close to each other in energy but spatially distant. To avoid this, we only sum over the bands that have large weight on one of the orbitals of interest, typically $w > 0.1$ for metal orbitals M_d. Note that the hybridization index is a qualitative measure, but it can nonetheless be useful for characterizing the metal−surface bonding as we show herein.

3. RESULTS AND DISCUSSION

3.1. Deposition of Single Transition Metal Atoms on ZrO_2.

The studied m-$ZrO_2(\bar{1}11)$ surface is rather complex and exhibits a variety of differently coordinated surface anion and cation sites for adsorption, as shown in Figure 1. The majority of the exposed Zr atoms are 6-coordinated, but there are some 7-coordinated cations as in the m-ZrO_2 bulk. The surface anions have coordination numbers 2, 3, and 4, and the least endothermic oxygen vacancy formation energy (i.e., reduction energy), ∼3.2 eV, is obtained for a four-coordinated oxygen atom (O6 in Figure 1a).[17]

We explored the influence of an adsorbed metal atom on the reduction energy by depositing single transition metal (TM) atoms one by one on both ideal and O-deficient m-$ZrO_2(\bar{1}11)$. Owing to the relatively large computational cell, shown in Figure 1a, the TM atom coverage is low (ca. 1 atom/4 nm^2) and the TM atoms can be considered nearly isolated. Previously, we have found a Rh atom to favor binding atop the four-coordinated O2 anion (Figure 1a) on the pristine ZrO_2 surface[17] and, therefore, selected the same site for the present systematic screening study. As the focus of this study is in the comparison of the reducibility-enhancing properties of different single metal atoms rather than in identifying the most favorable adsorption site for each metal atom on m-$ZrO_2(\bar{1}11)$, the other sites are only considered in selected cases. Excluding site variation by focusing on a single adsorption site facilitates the direct comparison of metal properties. With the Rh atom on the O2 site (see Figure 1), the reduction energy was found to vary from one surface anion to the other, highlighting the different coordinations of lattice oxygen anions. The lowest vacancy formation energy, 0.70 eV, was computed for the O1 anion nearest to the O2 anion, with Rh shown in Figure 1a.[17] Below, the vacancy formation energies, that is, reduction energies, are always computed for the O1 vacancy to ensure comparability between different adsorbed metals.

When an O1 vacancy is formed by removing the corresponding oxygen atom from the pristine m-$ZrO_2(\bar{1}11)$, two electrons are trapped inside the vacancy, which is usual for irreducible oxides. Bader analysis does not locate a charge maximum at the vacancy site and the surrounding three Zr^{4+} cations instead gain 1.17 electrons in total. This observation is in agreement with previous results,[17,30] and the additional charge on the cations is close to the negative Bader charge residing on a surface O^{2-} anion. This does not imply that the surface cations are reduced; the resulting state is a singlet, and a PDOS analysis (Figure S4 in the SI, section 7.3) reveals no net magnetic moment on any of the nearby cations. We conclude that the added charge on the cations is simply a feature of the charge partitioning scheme.

To explore the TM-induced reducibility of m-$ZrO_2(\bar{1}11)$, we consider the following 13 transition metals: Fe, Co, Ni, Cu, Mo, Ru, Rh, Pd, Ag, Re, Ir, Pt, and Au. The set consists of the nine naturally occurring elements from groups 9−11 and four elements (Fe, Mo, Ru, Re) from groups 6−8. These metals were selected based on their importance in catalysis and their different chemical properties to gain a broad understanding of their influence on zirconia reducibility without having to compute through the entire d block.

On the O2 site of the ideal ZrO_2 surface, each metal atom forms a bond with O4, a nearby two-coordinated oxygen anion (bond distances 1.9−2.4 Å). This interaction gives rise to a unique property of the O2 site: the deposited metal atom does not readily accept charge from a distant vacancy, preventing reducibility enhancement when the metal atom does not enter the vacancy. This effect will be discussed in more detail later on in Section 3.3. The copper group metals (Cu, Ag, Au) only bind to the O4 anion, while TMs from other groups interact to some extent also with the other three nearby oxygen anions O1−O3. Comparison of the computed M−O bond lengths indicates that Pd, Ir, and Pt bind to two out of the four available O anions, while the rest bind to three of them. Here we consider two atoms bound if their distance is less than the sum of the covalent radius of the TM atom[53] and the radius of the oxide anion[54] (1.26 Å). The varying adsorption behavior arises from the relatively diverse surface structure and atom coordination of m-$ZrO_2(\bar{1}11)$, as described earlier. The exact metal−oxide distances are provided in Table S3.

On the defected surface created by removing O1, most metal atoms migrated to this vacancy during structure optimization, while the group 6−8 metals Fe, Mo, Ru, and Re remained in the original O2 site. Manually placing these atoms into the O1 vacancy enhances the adsorption energies by up to 2.0 eV, which means that adsorption in the vacancy site is also thermodynamically more favorable for these atoms as well. The structural characteristics of the adsorbed metals inside the vacancy exhibit some clear differences: while the copper and nickel group metals and Co remain essentially in the center of the vacancy with their distances to the surrounding Zr atoms being 2.6−3.1 Å, the others migrate toward a nearby Zr bridge site due to interaction with the two-coordinated O5. This phenomenon is particularly notable for the group 6−8 metals forming a bond with the O5 atom (bond distance ca. 2 Å).

3.2. Adsorption and Reduction Energies.

In this subsection, we address the thermodynamics of TM adsorption on the pristine m-$ZrO_2(\bar{1}11)$ and inside the O1 vacancy. This is followed by a comparison with the literature on MgO and TiO_2 and a discussion on the reduction energies of m-$ZrO_2(\bar{1}11)$. Finally, the feasibility of further reduction and the distance dependence of the reducibility enhancement are briefly considered.

The TM adsorption energies on the pristine surface range from −2.89 to −0.60 eV (see Table 1) and mostly follow a clear periodic trend: E_{ads} becomes more exothermic when moving from left to right and from top to bottom in the periodic table. The Cu group metals are an exception, as their adsorption is fairly weak (− 1.26 to −0.60 eV) even though in the periodic table they are located to the right of all other studied TMs. Pd also binds weaker than Ni and Rh, the elements directly above and to the left of it. We propose that the closed d shell electronic structure of the Cu group metals and Pd is behind the divergent behavior of these elements, which is also observed in other analyses and discussed in detail in Sections 3.3.1 and 3.3.2.

Table 1. Adsorption (E_{ads}) and Reduction (E_R) Energies (eV), Bader Charges, and Atomic Spin Moments for Each Adsorbed Metal Atom[a]

	on pristine			in vacancy			
metal	E^p_{ads}	charge	spin	E^d_{ads}	charge	spin	E_R
Fe	−1.50	+0.34	3.78	−3.53	−0.38	2.48	1.79
Co	−1.90	+0.35	1.17	−3.53	−0.73	0.13	2.19
Ni	−2.20	+0.21	0.00	−4.73	−0.81	0.00	1.29
Cu	−1.26	+0.07	0.56	−3.08	−0.66	0.00	2.00
Mo	−1.05	+0.48	3.72	−3.00	−0.31	2.05	1.87
Ru	−2.25	+0.22	1.92	−4.95	−0.70	0.00	1.12
Rh	−2.41	+0.10	0.91	−5.43	−0.85	0.82	0.80
Pd	−1.86	+0.02	0.00	−5.00	−0.95	0.00	0.68
Ag	−0.60	+0.03	0.52	−2.61	−0.67	0.07	1.81
Re	−1.75	+0.35	2.85	−4.26	−0.57	1.05	1.31
Ir	−2.89	−0.01	0.90	−6.65	−0.95	0.86	0.06
Pt	−2.82	−0.09	0.00	−7.25	−1.05	0.00	−0.61
Au	−0.92	−0.13	0.58	−3.92	−0.82	0.00	0.82

[a] E_R for the O1 vacancy on the ideal surface without an adsorbed metal atom is 3.82 eV.

The results in Table 1 show that TM adsorption in the O1 vacancy is significantly more exothermic than on the pristine surface. The in-vacancy adsorption energies also present a wider range of values, varying from −7.25 eV for Pt to −2.61 eV for Ag. The vacancy adsorption energies follow the same trend that was observed for the ideal surface. In general, the adsorption energy of a TM atom in the O1 vacancy is at least 1.6 eV more exothermic than on the O2 site of the defect-free surface. Particularly exothermic vacancy adsorption energies are found for Ir (−6.65 eV) and Pt (−7.25 eV). Figure 2 displays that the adsorption energies on the pristine surface (E^p_{ads}) and inside the vacancy (E^d_{ads}) are strongly linked to each other, which we briefly discuss later in Section 3.3.2.

Next, we compare our results with previous studies on irreducible (MgO,[55−59] ZrO_2[60]) and reducible (TiO_2[61,62]) oxides. Computational studies of single TM atom adsorption on ZrO_2 at the DFT-GGA level of theory have focused on Pt, Pd, and Rh[60] and the Cu group on the ideal c-$ZrO_2(111)$ surface.[63] In line with our findings, these results for ZrO_2 highlight that Pd adsorbs less strongly than Rh and Pt,[60] while the comparison between Rh and Pt adsorption energies is less clear due to the strong site-dependency. Our adsorption energy trend also agrees with that observed for the Cu group (Cu < Au < Ag) on the cubic surface.[63]

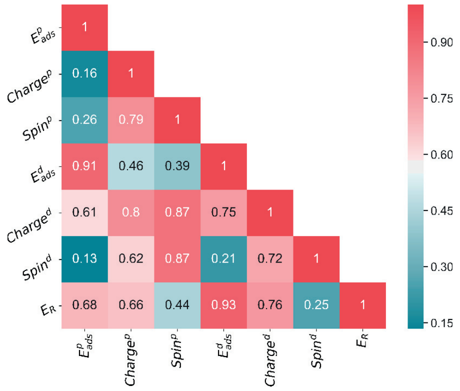

Figure 2. Pearson correlations between the values presented in Table 1. “p” and “d” stand for pristine and defected, respectively.

MgO is an irreducible oxide like ZrO_2, though it is more ionic in character and has an even higher vacancy formation energy.[64] In terms of the surface structure, MgO(001) is highly symmetric: all top-layer Mg and O atoms are equivalent to each other. m-$ZrO_2(\bar{1}11)$, on the other hand, is a relatively complex surface, as discussed earlier. The adsorption behavior on both ideal and defected m-$ZrO_2(\bar{1}11)$ is broadly similar to what has been reported for the corresponding MgO(001) surfaces. On both surfaces, the adsorption energies exhibit similar trends, and the predicted spin states of the metals largely agree.[58,59] This is in accordance with the qualitatively similar properties of the oxides, and also their defects; on both MgO and ZrO_2, the vacancy electrons are trapped inside the vacancy, as they are not able to reduce the surface cations. Thus, the trends observed in the present work can likely be generalized for other irreducible oxides as well. There are some exceptions to the trends between MgO and ZrO_2, but they can be rationalized based on the differing geometries of the two oxide surfaces. A more comprehensive comparison in presented in the SI, section S4.

In contrast to MgO and ZrO_2, TiO_2 is reducible. The adsorption of the first TM row metals, as well as Pd, Ir, Pt and Au, has been studied using GGA-DFT on both pristine and defected rutile $TiO_2(110)$ surfaces.[61,62] Contrary to the results obtained for ZrO_2 and MgO, the adsorption energies of the studied metal atoms in the TiO_2 vacancy are typically more endothermic than or roughly equal to the corresponding energies on the ideal surface.[62] Only Au and, when the Hubbard correction was introduced, Pt bound more strongly inside a surface vacancy than on the ideal surface, though Pd and Ir were also noted as borderline cases. This comparatively weaker metal−vacancy interaction in reducible oxides is caused by the ability of the vacancy electrons to reduce the oxide cations instead of staying in the vacancy to interact with the adsorbed TM atom. These results suggest that the metal-induced reducibility enhancement is weaker on reducible oxides, and only some TM atoms are able to overcome the tendency of the vacancy electrons to localize on the oxide cations.

After TM adsorption on the pristine surface and in the O1 vacancy, we focus on the enhanced reducibility induced by the

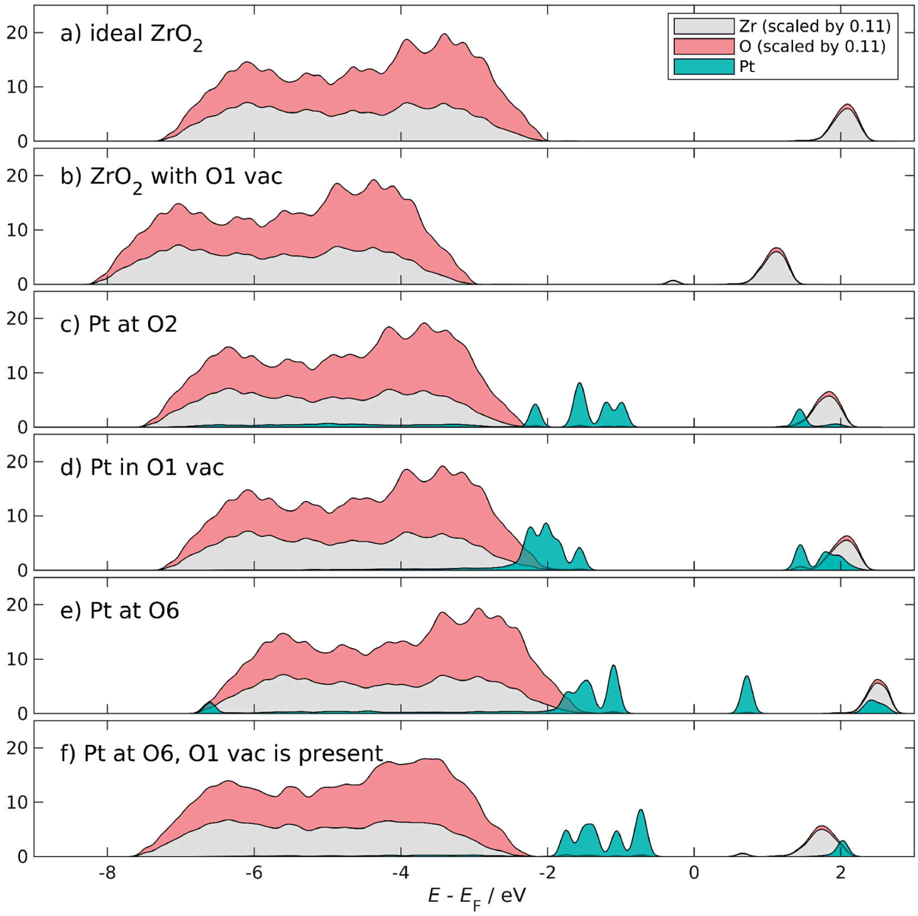

Figure 3. Atom-projected densities of states of ZrO_2 and Pt/ZrO_2 in various cases. The calculations were spin-polarized, but in these cases, the plots are visually identical for both spin directions and only one is shown. Only the states from the top two layers of the slab are pictured here, since the bottom layers have spurious constraint-induced gap states (see SI, section S2 for details). The DOS's of Zr and O have been scaled by 1/9 for visual clarity; 1/9 of the top two layers corresponds to one unit cell of monoclinic ZrO_2.

TM adsorption. The reduction energies computed according to eq 2 using the adsorption energies discussed above are reported in Table 1. In some cases the metal atom resides in the vacancy, whereas as in other cases it is initially more distant from the vacancy, as discussed earlier in Section 3.1. As the adsorption energies on the pristine and defected surfaces correlate strongly with each other (Figure 2), and because the reduction energies are computed as their differences (plus a constant), the trends of E_R follow those of the adsorption energies discussed above.

The reduction energy of the ideal m-$ZrO_2(\bar{1}11)$ surface without any adsorbed TMs is found to be 3.82 eV when the O1 vacancy is formed. Table 1 shows that all of the considered metals lower E_R considerably. Even though Co causes the weakest effect, E_R is still lowered by 1.6 eV. On the other hand, the strongest reducibility-enhancing effect is observed for Pt, which actually makes E_R exothermic, a very unusual observation for an irreducible oxide. Ir also provides a strong enhancement, with an E_R of 0.06 eV.

To investigate whether an adsorbed TM atom can enhance a second reduction of the surface, we placed a Pt atom on O6 and formed the O1 and O1′ vacancies. Pt was chosen for this test, since it produced the most favorable first reduction. However, we find that the adsorbed Pt atom has essentially no effect on the second reduction energy. Thus, one Pt atom can only facilitate the removal of one oxygen atom as Pt's initially empty electronic states become populated upon vacancy formation. Motivated by an earlier investigation, where the adsorption of Rh on m-$ZrO_2(\bar{1}11)$ was suggested to induce an "enhanced reducibility zone" of about 4 Å around the adsorbed Rh atom,[17] we also addressed the spatial effect of the TM-induced reducibility. In this work, we find three distinct classes of reducibility-altering effects depending on the adsorption site of the metal atom. The enhancement is strongest when the adsorbed metal atom is near the removed oxygen atom and fills the vacancy. A weaker, essentially distance-independent (within our computational cell) enhancement is observed for most adsorption sites when the metal stays out of the vacancy. Finally, on a distant O2 site, the adsorbed TM does not enhance the reducibility at all.

3.3. Analyzing the Adsorption.

Upon the adsorption of a metal atom onto oxide surfaces, multiple interdependent

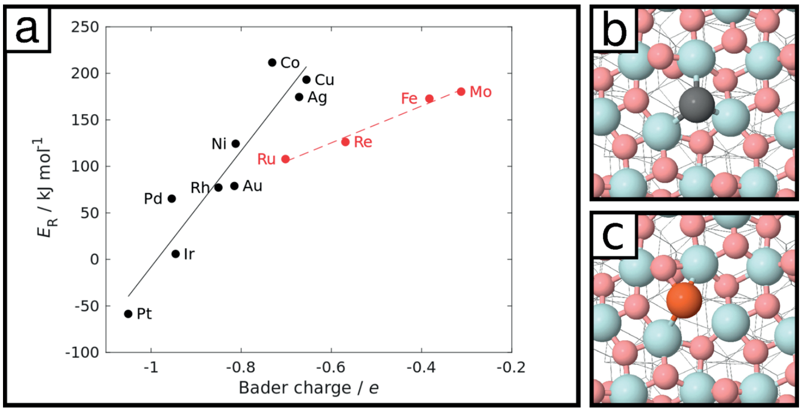

Figure 4. (a) The correlation of the reduction energy and the Bader charge of the metal in the vacancy. Solid line (R^2 = 0.89): metals that stay in the center of the vacancy. Dashed red line (R^2 = 0.98): metals that bond strongly to a nearby two-coordinated O atom. (b) Pt vacancy binding geometry as a representative example of the metals that stay in the center of the vacancy. (c) Fe vacancy binding geometry as a representative example of the metals that bind to the two-coordinated O atom.

phenomena can take place, including charge transfer, metal—surface hybridization, and polarization. In order to understand how these different factors contribute to the TM adsorption and TM-induced reducibility discussed above, we carried out an extensive analysis of the electronic structure, charge transfer, magnetism, energy partitioning, and hybridization. To this end, we have analyzed the density of states (DOS) plots, Bader charges, and magnetic moments of the M/ZrO_2 systems. We also note that various electronic and thermodynamic properties are strongly correlated, as shown in Figure 2.

3.3.1. Electronic Properties of Adsorbed TM Atoms. The electronic effects are analyzed in terms of the density of states (DOS). Here we focus on platinum, which exhibits the strongest impact on the reducibility, while DOSs for the other elements are shown in SI, section S7. Figure 3 displays the DOS plots for various bare and Pt-adsorbed ZrO_2 surfaces as examples of typical M/ZrO_2 electronic structures (see SI, section S5 for U = 0 comparison). As Figure 3a shows, the VB edge of bare ZrO_2 mainly consists of O 2p states, while the conduction band (CB) is dominated by Zr states. In the presence of an O1 vacancy, a gap state appears just below the Fermi level, see Figure 3b). The majority of the Pt states are located in the band gap near the VB edge, while some states overlap with the CB. Comparison of Figure 3c and d, corresponding to the ideal and defected Pt/ZrO_2 surfaces, shows that when Pt is in the vacancy its electronic states cluster together and overlap more with the oxide states than on the ideal surface. This suggests that the Pt orbitals hybridize with each other when Pt binds inside the vacancy. This kind of hybridization turns out to be important for vacancy adsorption and will be discussed in detail in Section 3.3.2.

Figure 3c,e demonstrate the difference between the "charge-rejecting" adsorption site, O2, and the "charge-accepting" adsorption site, O6, respectively. A Pt atom at site O6, even when further away from the vacancy, can accept ~1 electron from the vacancy and enhance the reducibility of ZrO_2 by 1.1 eV, whereas Pt at an O2 site far away from the vacancy gains no charge and has no effect on the reducibility. In the case of the O2 site, the DOS analysis (panel c) shows that most available Pt states are already filled, likely due to the Pt—O4 interaction, whereas in the case of the O6 site (panel e), there are unoccupied Pt states. These can accept electrons from the vacancy, stabilize the vacancy formation, and lead to a more exothermic reduction energy. The unoccupied states become populated even when the vacancy is formed further away, as shown in Figure 3f. The population of these originally unpopulated Pt states leads to a formation of a small peak above the Fermi level (panel f) that is due to the depopulation of the vacancy state, which is occupied when no Pt is present on the surface (Figure 3b). Note that this charge-transfer interaction is mediated by the zirconia atoms, as no direct orbital interaction between the Pt atom and the vacancy is visible in Figure 3f.

To further investigate the charge transfer between the oxide (or vacancy) and the adsorbed TM atom, the Bader charges of the metal atoms were computed and collected into Table 1). Metal atoms are, in general, neutral or slightly positive on the ideal surface, and the largest positive charges were found for the group 6—8 metals for which we obtained values from +0.22 to +0.48e. Similar values were calculated also for Co and Ni. Ir, Pt, and Au have slightly negative Bader charges, which, however, are small and do not necessarily indicate reduction of the metals. The Bader charges broadly follow the trends in atomic electronegativities and electron affinities, which are presented in detail in the SI (Figure S5). Care should be taken when interpreting computed Bader charges, because the analysis does not solely describe charge transfer and, for example, polarization effects may also have a contribution for an adsorbed metal atom.[65]

The Bader charges of vacancy-bound metal atoms range from −1.05 to −0.31e and the observed trends are largely similar to those on the nondefected surface, with a strong correlation (0.91, Figure 2) between the in-vacancy and on-surface atoms. A similar correlation is also visible for the adsorption energies on the pristine surface and in the O1 vacancy, which further reinforces the conclusion that the two types of adsorption configurations share similar properties. Based on the Bader analysis, the studied TMs can be grouped into two main categories: Fe, Mo, and the Cu group metals are ~0.7e more negatively charged in the vacancy, while for the other metals, the corresponding value is ~1.0e. This categorization is also reflected in the thermodynamic proper-

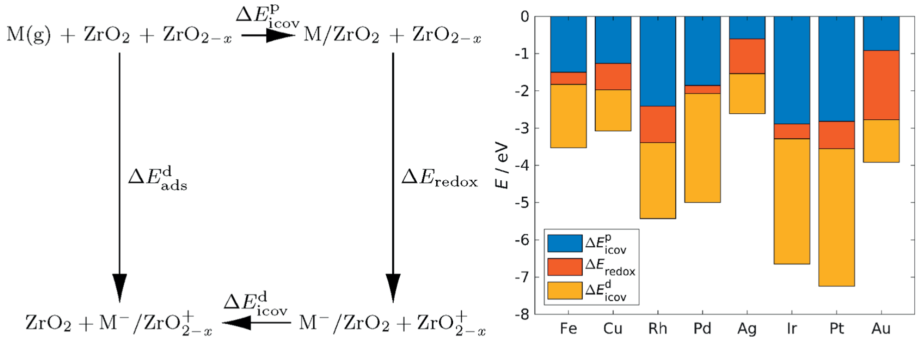

Figure 5. Left: The thermodynamic cycle used to divide the vacancy adsorption energy into components, following the idea in ref 68. Here, M(g) is the gas-phase metal atom, $\mathrm{ZrO_2}$ is the bare ideal surface, ZrO_{2-x} is the bare surface with the O1 vacancy, $\mathrm{M/ZrO_2}$ is the ideal surface with M on site O2, $\mathrm{M^-/ZrO_2}$ is the ideal surface with M on site O6 and 1 e of negative charge, ZrO^+_{2-x} is ZrO_{2-x} with 1 e of positive charge, and $\mathrm{M^-/ZrO}^+_2$ is the (noncharged) surface with M in the O1 vacancy. Right: The contributions of each component to the total vacancy adsorption energies. The total length of the bar corresponds to $\Delta E^{\mathrm{d}}_{\mathrm{ads}}$. The values have been tabulated in section S11 of the Supporting Information.

ties as atoms in the first category bind weaker than atoms in the second category both on the pristine surface and inside the vacancy. The sole exception is Co binding more weakly than Au in the vacancy, which may be related to the large changes in Co's electronic structure when moving from the pristine surface to vacancy (SI, section S7) and the known difficulties in describing the spin state of Co with DFT.[66,67]

The TM charges correlate strongly also with the reduction energies as shown by Figure 4 for the E_{R} and the Bader charge of the vacancy-adsorbed metal atom. While the majority of the studied elements fall on the same line in Figure 4, Fe, Mo, and Re and Ru deviate from the general trend as they bind to the O5 oxygen and reside asymmetrically in the vacancy. We note that a similar correlation between E_{R} and the Bader charge is also seen in Figure 2.

To characterize the electronic properties of the adsorbed metal atoms, we computed their magnetic moments upon surface deposition. On ideal $\mathrm{ZrO_2}$, the gas-phase moments are retained for Fe and the d^{10} metals, whereas for the other metals, the magnetic moments are quenched by 2 μ_{B}. This could be due to surface-induced d-level splitting favoring lower-spin configurations or by hybridization between the metal s and d states and oxygen p states. The vacancy enhances the quenching effect since the vacancy and metal atom orbitals may be mixing with each other. The effect is largest for Mo, Ru and Re, whose magnetic moments are quenched by 4 μ_{B} compared to their gas-phase values.

Comparison of the magnetic moments on the ideal surface versus those in the vacancy reveals a periodic trend. The group 6−8 metals (Fe, Mo, Ru, Re) undergo a quenching of 2 μ_{B} and bind closely (∼2.0 Å) to the O5 atom. Of the group 9 metals, Rh and Ir retain their doublet configurations and bind somewhat closely (∼2.4 Å) to O5, while Co has its moment quenched by 1 μ_{B} and remains at the center of the vacancy. Again, the divergent behavior of Co may originate from the intricacies of its spin state description. The group 10 metals (Ni, Pd, Pt) adsorb in the center of the vacancy and are already singlets on the ideal surface, preventing further magnetic quenching. Finally, of the group 11 metals, all of which also adsorb in the center of the vacancy, Cu and Au undergo a quenching by 1 μ_{B}, while Ag remains as a doublet even in the vacancy. This is likely explained by its high s−d excitation energy, which inhibits s−d hybridization, as discussed later in more detail.

3.3.2. Metal−Vacancy Interaction: Thermodynamic Cycle.

For further analysis of metal−vacancy interaction, we devised the thermodynamic cycle shown in Figure 5. Similar approaches have been previously employed to understand the factors governing Au binding on a doped CaO surface,[68] the adsorption of catalytic intermediates on metal−oxide interfaces,[69] and terephthalic acid monolayer self-assembly.[70] In the cycle, the metal−vacancy interaction is broken down into three components: iono-covalent on the ideal surface, redox, and iono-covalent inside the vacancy.

The E_{redox} and $E^{\mathrm{d}}_{\mathrm{icov}}$ components are computed using charged slab calculations in three-dimensional periodic boundary conditions, utilizing a homogeneous compensating background charge to neutralize the cell. To correct for the inconsistency in average electrostatic potential between calculations of different charge states, we have applied a Lany−Zunger-type potential alignment correction (see section S11 in the Supporting Information).[71] The planarly averaged electrostatic potentials were aligned at the midpoint of the frozen part of the slab, resulting in energy corrections of −0.21 eV for the positively charged vacancy and −0.18 eV for the negatively charged metal systems. The identity of the metal was found to have a negligible effect on the electrostatic potential profile, and thus on the alignment correction. In total, this correction results in a −0.39 eV uniform shift to the E_{redox} components (and a corresponding +0.39 eV shift to $E^{\mathrm{d}}_{\mathrm{icov}}$). The image charge interaction in charged slab calculations is challenging to treat correctly, and we neglect it here; however, it is not expected to depend strongly on the identity of the metal, so the observed E_{redox} trends should be unaffected.

ΔE^{p}_{icov} Component. The first component, $\Delta E^{\mathrm{p}}_{\mathrm{icov}}$, corresponds to the direct interaction between an adsorbing metal atom and the surface ions. It quantifies the hybridization of metal states with nearby surface orbitals and some charge transfer. The energy change related to this process varies from one metal to another between −0.6 and −2.9 eV, as shown in Figure 5.

The ionic and covalent contributions to $\Delta E^{\mathrm{p}}_{\mathrm{icov}}$ were studied by correlating the TM Bader charges on the ideal surface against $\Delta E^{\mathrm{p}}_{\mathrm{icov}}$ and $\Delta E^{\mathrm{d}}_{\mathrm{ads}}$. Note that a positive Bader charge does not indicate a reduction of the (irreducible) zirconia, but

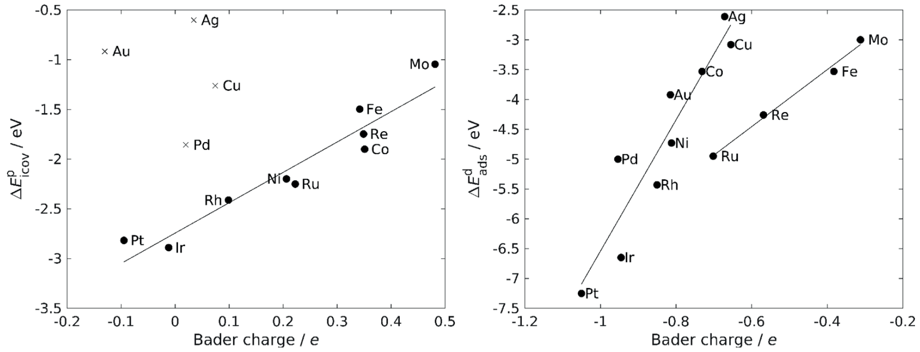

Figure 6. Left: the correlation of ΔE^{p}_{icov} and the Bader charge of the metal, $R^2 = 0.91$. The d^{10} metals (marked with crosses) have been excluded from the fit. Right: the correlation of ΔE^{d}_{ads} and the Bader charge of the metal, $R^2 = 0.87$ (Fe, Mo, Re, Ru excluded) and $R^2 = 0.99$ (the Fe, Mo, Re, Ru line).

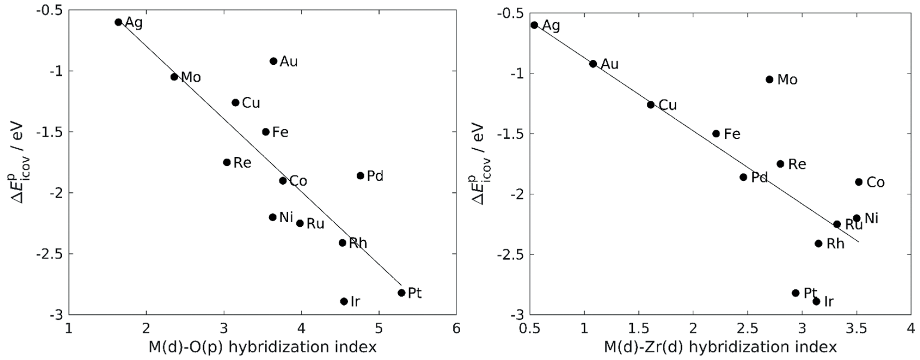

Figure 7. Correlations of ΔE^{p}_{icov} with $H_{M(d), O(p)}$ ($R^2 = 0.69$) and $H_{M(d), Zr(d)}$ ($R^2 = 0.63$). The hybridization indices have been summed over the nearest four atoms of each type.

the variation in Bader charges is considered to arise from the sharing of electrons along metal–surface bonds of partly covalent character. Figure 6 shows that a good correlation between ΔE^{p}_{icov} and the Bader charge is found when the d^{10} metals Cu, Ag, Au, and Pd are excluded. This exclusion is also chemically motivated as these TM atom have a filled d-shell, which cannot accept electrons.

The deviation observed for the d^{10} metals on the ideal surface suggests that they exhibit qualitatively different adsorption behavior from the others. We note that the deviation is largest for the Cu group $d^{10}s^{1}$ metals and somewhat smaller for Pd, which has a d^{10} structure and lacks a valence s electron. In studies on MgO(001), the comparatively weak binding of Cu group metals has been ascribed to Pauli repulsion brought on by the mandatory half-occupation of the valence s state.[56,72] While, for example, Pt also has a half-occupied vacancy s orbital in the gas phase ($d^{9}s^{1}$), it can (and does) reach a stable closed-shell structure upon adsorption due to the available space on the nonfilled d orbital. This is not possible for the $d^{10}s^{1}$ metals in the Cu group.

Good correlations are also found between ΔE^{d}_{ads} and the Bader charges of the vacancy-bound metal atoms (Figure 6). Here, as with E_R, the correlation is computed separately for Fe, Mo, Re, and Ru. These four atoms bind in a qualitatively different geometry than the others, as discussed earlier in Section 3.3.1. Notably, unlike with ΔE^{p}_{icov} on the ideal surface, the d^{10} metals follow the main correlation. This indicates that the d^{10} metals hybridize in the vacancy and can accept some electrons into these hybrid orbitals.

This deviation of the d^{10} metals was also investigated by considering the degree of hybridization between the metal and surface orbitals, which measures the covalent character of the metal–surface bonding. Our method of choice is the hybridization index H_{kl} (eq 3), which provides a measure of the overlap between atomic orbitals in DFT bands, and has been successfully applied for transition metal clusters.[52,73] This index was computed between the metal d orbitals and surface O_p and Zr_d orbitals. To describe the total effect from metal–surface hybridization on the ideal surface, the index is summed over the four oxide (or zirconium) ions nearest to the binding site.

The metal–oxygen hybridization index, M_d–O_p, correlates rather strongly with ΔE^{p}_{icov} ($R^2 = 0.69$), as shown in Figure 7. This implies that metal–oxygen covalent bonding has an important role in determining the M–ZrO_2 binding strength, which agrees with prior work on the subject.[60,63] We stress again that the m-$ZrO_2(\bar{1}11)$ surface allows multiple different metal–oxygen bonds to form, as opposed to simpler surfaces such as MgO(001), where each metal preferentially binds on top of a single O anion. In light of this, the observed correlation is remarkably good.

The d^{10} deviation discussed above can also be rationalized to some extent with the M_d–Zr_d hybridization index. The results

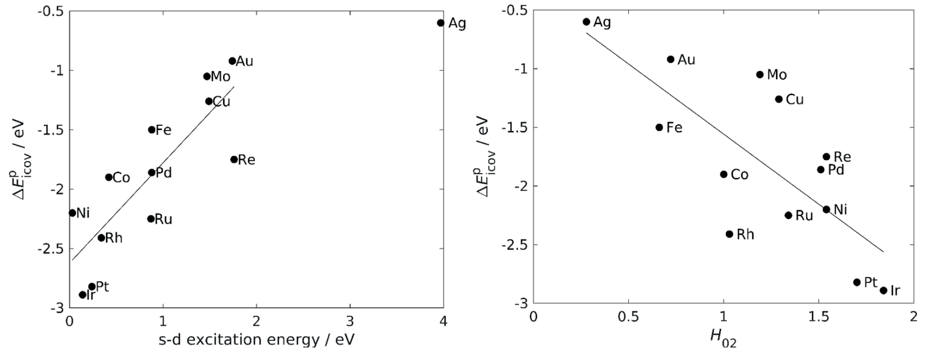

Figure 8. Left: ΔE^{p}_{icov} plotted against the s−d excitation energy of the metal from ref 74. $R^2 = 0.69$ (Ag excluded from fit). Right: ΔE^{p}_{icov} vs H_{02}, $R^2 = 0.57$.

in Figure 7 show that the $d^{10}s^{1}$ metals are weakly hybridized with Zr, indicating that the d−d interaction is less favorable for them. This is also supported by the adsorption heights of the metals, as the Cu group metals adsorb 0.2−0.5 Å further from the surface plane than the next-highest-adsorbing metal atom (Pd). In fact, the adsorption height correlates well ($R^2 = 0.91$) with the M_d−Zr_d hybridization index, while the correlation with the M_d−O_p hybridization index is nonexistent ($R^2 = 0.24$). The correlation plots are shown in Figure S6.

We also considered the s−d hybridization in the adsorbed TMs, as this has been previously noted as a contributor to the adsorption strength.[55,63,72] To assess the degree of s−d hybridization, we used two measures. The gas-phase s−d excitation energy corresponds with the energy difference between the s and d levels and thus is expected to correlate with the propensity for s−d hybridization. In addition, using the H_{kl} index with $k = 0$ and $l = 2$, we can directly estimate the degree of s−d hybridization in our computational system. The index also accounts for the adsorption-induced changes in the electronic structure of the metal atom, while the gas-phase s−d excitation energy lacks this effect.

Both measures were correlated against ΔE^{p}_{icov}. The gas-phase s−d excitation energy produces a reasonable correlation when the Ag outlier is excluded (Figure 8, left). The exclusion of Ag is justified by its very large s−d excitation energy, as even a somewhat smaller value could already preclude any possibility of s−d hybridization. The correlation between ΔE^{p}_{icov} and H_{02} turns out to be slightly weaker than the one obtained with the s−d excitation energy, though the extremes still match expectations: Ag has a low degree of hybridization, while Pt and Ir have a high one (Figure 8, right). The decent correlation between ΔE^{p}_{icov} and the gas-phase s−d excitation energy indicates that the surface adsorption does not dramatically alter the relative energies of the s and d orbitals, while the comparatively poorer correlation obtained with H_{02} reflects the qualitative nature of the hybridization index.

ΔE_{redox} Component. The ΔE_{redox} component describes the redox process where the initial state involves metal atom adsorption on the pristine surface far away from the vacancy. The final state is obtained by adding an electron to M/ZrO_2 and removing it from the ZrO_{2-x} system. Note that in the final state, a metal atom is placed on the O6 site, as it is unable to accept charge in the O2 position, as discussed earlier. This choice was justified by verifying that the adsorption energies of Au and Pt atoms on both sites are similar (within 0.25 eV). In the charged system, the TM atom gains 0.1−1.0e of Bader charge, depending on the metal, and sometimes shifts slightly from the position on the corresponding neutral system. In general, the redox contribution has a small negative value of 0 to −1 eV, except for Au which presents a more substantial redox energy of −1.86 eV. For Ag, the redox component also makes up a considerable part of the vacancy adsorption energy. For the other metals, the low values indicate that charge transfer is not a dominant contributor to the adsorption energy even in the case of vacancy adsorption, and the stabilization instead occurs primarily via metal−vacancy orbital hybridization.

We expect the redox component to depend on the electron affinity of the metal atom, as this contribution highlights the metal's ability to accept charge. Figure 9 shows that Pd, Rh, Cu, Ag, and Au exhibit a decent correlation, whereas Fe, Ir, and Pt deviate. In the case of Fe, the deviation may be explained by the different vacancy binding geometry involving Fe−O bonding. For Ir and Pt, the geometry is similar to the well-correlated metals and the explanation has to be sought from elsewhere. We note that Ir and Pt exhibit the most exothermic reduction energies, which could be related to the deviation. The redox and ΔE^{d}_{icov} components are not necessarily cleanly separated, as the charge of the metal atom may be different on

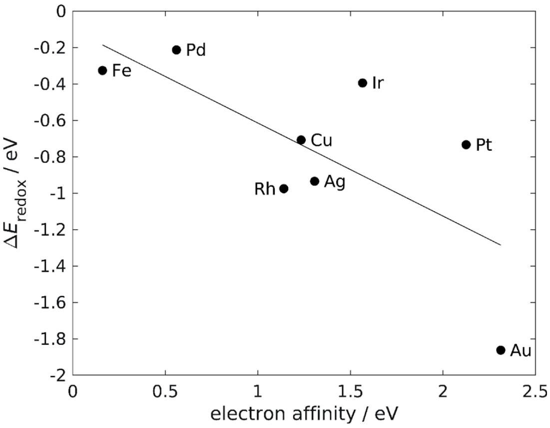

Figure 9. Correlation between ΔE_{redox} and electron affinity ($R^2 = 0.49$).

the charged surface versus in the vacancy. As such, $\Delta E^{\mathrm{d}}_{\mathrm{icov}}$ may also include some redox energy. Since the redox component is typically the smallest of the three components, these are relatively minor concerns.

ΔE^{d}_{icov} Component. In the last term of the cycle, $\Delta E^{\mathrm{d}}_{\mathrm{icov}}$, the interaction between the charged metal atom and the oxygen vacancy is considered. The term includes iono-covalent M−Zr and M−O interactions as well as hybridization between the metal and vacancy orbitals. While the redox term is comparatively small for all the studied metal atoms, with Ag and Au being the exceptions, $\Delta E^{\mathrm{d}}_{\mathrm{icov}}$ obtains large negative values, which vary from one metal to another with Pt and Ir being most exothermic. From Figure 5, we can conclude that the redox term has only a minor role in the adsorption of a metal atom into an oxygen vacancy of ZrO_2, while the ΔE_{icov} contributions dominate the adsorption.

It is also notable that $\Delta E^{\mathrm{p}}_{\mathrm{icov}}$ exhibits a correlation with both $\Delta E^{\mathrm{d}}_{\mathrm{ads}}$ ($R^2 = 0.82$) and $\Delta E^{\mathrm{d}}_{\mathrm{icov}}$ ($R^2 = 0.87$). This indicates that the metal−vacancy interaction is qualitatively similar to the metal−oxygen interaction. The similar (low) electron affinity of the surface oxygen and vacancy orbitals has been suggested as a reason for the similarity.[56]

In addition to the thermodynamic considerations discussed above, we considered the orbital interactions between the adsorbed metal atom and the (pristine or defected) surface. As the vacancy orbital is of s symmetry, the s orbitals of the adsorbed metal atoms are likely relevant in the vacancy bonding. For instance, Pd has an empty s orbital and as such there should be no Pauli repulsion between Pd and the vacancy, facilitating a strong metal−vacancy bond. The Cu group metals have $\mathrm{d}^{10}\mathrm{s}^{1}$ occupancies, meaning that the metal atoms are repulsed by the two s electrons of the vacancy. In spite of this, Au binds relatively strongly, which may be ascribed to relativistic effects enhancing the s−d hybridization.[59]

In summary, our results and detailed analysis show that $\Delta E^{\mathrm{p}}_{\mathrm{icov}}$ and $\Delta E^{\mathrm{d}}_{\mathrm{ads}}$ exhibit correlations with Bader charges and each other, with $\Delta E^{\mathrm{p}}_{\mathrm{icov}}$ also correlating with the $\mathrm{M_d}$−$\mathrm{O_p}$ hybridization index. Thus, surface oxygen/vacancy orbital interactions may be considered as the most important contributors to the binding energies, and the trends across metals are similar for the pristine surface and vacancy sites.

4. CONCLUSIONS

We have systematically considered the adsorption of 13 different single transition metal atoms on the pristine and defected m-$ZrO_2(\bar{1}11)$ surface, and shown that each metal makes the reduction energy of the surface more exothermic. The reducibility enhancement when the atom enters the vacancy ranges from −1.6 to −4.4 eV. The magnitude of the effect depends on the electronic properties of the metal atom, the metal adsorption site and, to a limited extent, on the metal−vacancy distance. In particular, we found that binding to a two-coordinated surface oxygen completely prevents the reducibility enhancement. It was also shown that a single metal atom can only facilitate the removal of one oxygen atom from the surface.

The reduction energies as well as the metal adsorption energies correlate with the Bader charges on the transition metal atoms, which we ascribe to the TM atoms withdrawing some electron density from surface oxides via covalent bonding, and to variations in the interaction with the vacancy electrons. Applying a hybridization index, originally developed for clusters, in our solid metal−oxide system, we show that the hybridization of the metal d and oxygen p, and to some extent zirconium d, orbitals is a main contributor to the metal−surface bonding. The metal−surface interaction correlates with the s−d excitation energy of the metal, as previously found for MgO(001), another irreducible oxide, making the obtained results more widely applicable to enhancing the reducibility of irreducible oxides besides ZrO_2. In addition, a thermodynamic cycle was constructed to describe the various metal−surface and metal−vacancy interactions, and especially to analyze the role of charge transfer.

To conclude, our results show that the irreducible zirconia can be made reducible by adsorbed single transition metal atoms, with Ir and Pt being especially effective reducibility enhancers. The main results are expected to generalize over other irreducible oxides as well, and this has been explicitly discussed in the case of MgO. In addition, the variable behavior of different TM adsorbates allows a broad range of reducibilities to be accessed, making it possible to rationally tune the properties of the oxide surface. Such enhanced surface reducibility retains the bulk stability while making the catalyst more active for oxidation reactions (e.g., Mars−von Krevelen-type elementary steps) and nonoxidative dehydrogenation of hydrocarbons and also stabilizing single atom catalyst adsorption. By elucidating the effects of adsorbed TM atoms on oxide reducibility, our results help pave the way for activating irreducible oxides in heterogeneous catalyst design.

■ ASSOCIATED CONTENT

Supporting Information

The Supporting Information is available free of charge at https://pubs.acs.org/doi/10.1021/acs.jpcc.1c08979.

> Gas-phase reference data, constraint-induced gap states, technical details for the linear-response DFT+U implementation in GPAW, effects of varying U on adsorbed TM properties, projected density of states plots, and analysis between the correlations (PDF)

■ AUTHOR INFORMATION

Corresponding Author

Karoliina Honkala − *Department of Chemistry, Nanoscience Center, University of Jyväskylä, FI-40014 Jyväskylä, Finland;* orcid.org/0000-0002-3166-1077;
Email: karoliina.honkala@jyu.fi

Authors

Ville Korpelin − *Department of Chemistry, Nanoscience Center, University of Jyväskylä, FI-40014 Jyväskylä, Finland*
Marko M. Melander − *Department of Chemistry, Nanoscience Center, University of Jyväskylä, FI-40014 Jyväskylä, Finland;* orcid.org/0000-0001-7111-1603

Complete contact information is available at: https://pubs.acs.org/10.1021/acs.jpcc.1c08979

Notes

The authors declare no competing financial interest.

■ ACKNOWLEDGMENTS

The work was supported by the Academy of Finland through Projects 277222 (V.K. and K.H.), 307853 (M.M.M.), and 317739 (M.M.M. and K.H.). The computational resources

were provided by the CSC-IT Center for Science, Espoo, Finland (https://www.csc.fi/en/).

■ REFERENCES

(1) Liu, L.; Corma, A. Metal Catalysts for Heterogeneous Catalysis: From Single Atoms to Nanoclusters and Nanoparticles. *Chem. Rev.* **2018**, *118*, 4981−5079.

(2) Kauppinen, M. M.; Melander, M. M.; Bazhenov, A. S.; Honkala, K. Unraveling the Role of the Rh−ZrO_2 Interface in the Water−Gas-Shift Reaction via a First-Principles Microkinetic Study. *ACS Catal.* **2018**, *8*, 11633−11647.

(3) Campbell, C. T. The Energetics of Supported Metal Nanoparticles: Relationships to Sintering Rates and Catalytic Activity. *Acc. Chem. Res.* **2013**, *46*, 1712−1719.

(4) Kauppinen, M. M.; Korpelin, V.; Verma, A. M.; Melander, M. M.; Honkala, K. Escaping scaling relationships for water dissociation at interfacial sites of zirconia-supported Rh and Pt clusters. *J. Chem. Phys.* **2019**, *151*, 164302.

(5) Green, I. X.; Tang, W.; Neurock, M.; Yates, J. T., Jr. Spectroscopic Observation of Dual Catalytic Sites During Oxidation of CO on a Au/TiO_2 Catalyst. *Science* **2011**, *333*, 736−739.

(6) Ruiz Puigdollers, A.; Schlexer, P.; Tosoni, S.; Pacchioni, G. Increasing Oxide Reducibility: The Role of Metal/Oxide Interfaces in the Formation of Oxygen Vacancies. *ACS Catal.* **2017**, *7*, 6493−6513.

(7) Kauppinen, M. M.; Melander, M. M.; Honkala, K. First-principles insight into CO hindered agglomeration of Rh and Pt single atoms on *m*-ZrO_2. *Catal. Sci. Technol.* **2020**, *10*, 5847−5855.

(8) Daelman, N.; Hegner, F. S.; Rellan-Pineiro, M.; Capdevila-Cortada, M.; Garcia-Muelas, R.; Lopez, N. Quasi-degenerate states and their dynamics in oxygen deficient reducible metal oxides. *J. Chem. Phys.* **2020**, *152*, 050901.

(9) Schlexer, P.; Ruiz Puigdollers, A.; Pacchioni, G. Role of Metal/Oxide Interfaces in Enhancing the Local Oxide Reducibility. *Top. Catal.* **2019**, *62*, 1192−1201.

(10) Otroshchenko, T.; Jiang, G.; Kondratenko, V. A.; Rodemerck, U.; Kondratenko, E. V. Current status and perspectives in oxidative, non-oxidative and CO_2-mediated dehydrogenation of propane and isobutane over metal oxide catalysts. *Chem. Soc. Rev.* **2021**, *50*, 473−527.

(11) Zhang, Y.; Zhao, Y.; Otroshchenko, T.; Han, S.; Lund, H.; Rodemerck, U.; Linke, D.; Jiao, H.; Jiang, G.; Kondratenko, E. V. The effect of phase composition and crystallite size on activity and selectivity of ZrO_2 in non-oxidative propane dehydrogenation. *J. Catal.* **2019**, *371*, 313−324.

(12) Zhang, Y.; Zhao, Y.; Otroshchenko, T.; Lund, H.; Pohl, M.-M.; Rodemerck, U.; Linke, D.; Jiao, H.; Jiang, G.; Kondratenko, E. V. Control of coordinatively unsaturated Zr sites in ZrO_2 for efficient C−H bond activation. *Nat. Commun.* **2018**, *9*, 3794.

(13) Zhang, Y.; Zhao, Y.; Otroshchenko, T.; Perechodjuk, A.; Kondratenko, V. A.; Bartling, S.; Rodemerck, U.; Linke, D.; Jiao, H.; Jiang, G.; et al. Structure−Activity−Selectivity Relationships in Propane Dehydrogenation over Rh/ZrO_2 Catalysts. *ACS Catal.* **2020**, *10*, 6377−6388.

(14) Otroshchenko, T.; Sokolov, S.; Stoyanova, M.; Kondratenko, V. A.; Rodemerck, U.; Linke, D.; Kondratenko, E. V. ZrO_2-Based Alternatives to Conventional Propane Dehydrogenation Catalysts: Active Sites, Design, and Performance. *Angew. Chem., Int. Ed.* **2015**, *54*, 15880−15883.

(15) Otroshchenko, T. P.; Kondratenko, V. A.; Rodemerck, U.; Linke, D.; Kondratenko, E. V. Non-oxidative dehydrogenation of propane, *n*-butane, and isobutane over bulk ZrO_2-based catalysts: effect of dopant on the active site and pathways of product formation. *Catal. Sci. Technol.* **2017**, *7*, 4499−4510.

(16) Puigdollers, A. R.; Pacchioni, G. CO Oxidation on Au Nanoparticles Supported on ZrO_2: Role of Metal/Oxide Interface and Oxide Reducibility. *ChemCatChem.* **2017**, *9*, 1119−1127.

(17) Bazhenov, A. S.; Kauppinen, M. M.; Honkala, K. DFT Prediction of Enhanced Reducibility of Monoclinic Zirconia upon Rhodium Deposition. *J. Phys. Chem. C* **2018**, *122*, 6774−6778.

(18) Qin, R.; Liu, P.; Fu, G.; Zheng, N. Strategies for Stabilizing Atomically Dispersed Metal Catalysts. *Small Methods* **2018**, *2*, 1700286.

(19) Liu, J. Catalysis by Supported Single Metal Atoms. *ACS Catal.* **2017**, *7*, 34−59.

(20) Mortensen, J. J.; Hansen, L. B.; Jacobsen, K. W. Real-space grid implementation of the projector augmented wave method. *Phys. Rev. B* **2005**, *71*, 035109.

(21) Enkovaara, J.; Rostgaard, C.; Mortensen, J. J.; Chen, J.; Dułak, M.; Ferrighi, L.; Gavnholt, J.; Glinsvad, C.; Haikola, V.; Hansen, H. A.; et al. Electronic structure calculations with GPAW: a real-space implementation of the projector augmented-wave method. *J. Phys.: Condens. Matter* **2010**, *22*, 253202.

(22) Larsen, A. H.; Mortensen, J. J.; Blomqvist, J.; Castelli, I. E.; Christensen, R.; Dułak, M.; Friis, J.; Groves, M. N.; Hammer, B.; Hargus, C.; et al. The atomic simulation environment—a Python library for working with atoms. *J. Phys.: Condens. Matter* **2017**, *29*, 273002.

(23) Bahn, S. R.; Jacobsen, K. W. An object-oriented scripting interface to a legacy electronic structure code. *Comput. Sci. Eng.* **2002**, *4*, 56−66.

(24) Perdew, J. P.; Burke, K.; Ernzerhof, M. Generalized Gradient Approximation Made Simple. *Phys. Rev. Lett.* **1996**, *77*, 3865−3868.

(25) Perdew, J. P.; Burke, K.; Ernzerhof, M. Generalized Gradient Approximation Made Simple [Phys. Rev. Lett. 77, 3865 (1996)]. *Phys. Rev. Lett.* **1997**, *78*, 1396−1396.

(26) Blöchl, P. E. Projector augmented-wave method. *Phys. Rev. B* **1994**, *50*, 17953−17979.

(27) Bazhenov, A. S.; Honkala, K. Understanding Structure and Stability of Monoclinic Zirconia Surfaces from First-Principles Calculations. *Top. Catal.* **2017**, *60*, 382−391.

(28) Sansonetti, J.; Martin, W.; Young, S. *Handbook of Basic Atomic Spectroscopic Data (version 1.1.2)*; National Institute of Standards and Technology: Gaithersburg, MD, 2005; [Online] Available: http://physics.nist.gov/Handbook [2021, August 17].

(29) Himmetoglu, B.; Floris, A.; de Gironcoli, S.; Cococcioni, M. Hubbard-corrected DFT energy functionals: The LDA+U description of correlated systems. *Int. J. Quantum Chem.* **2014**, *114*, 14−49.

(30) Syzgantseva, O. A.; Calatayud, M.; Minot, C. Revealing the Surface Reactivity of Zirconia by Periodic DFT Calculations. *J. Phys. Chem. C* **2012**, *116*, 6636−6644.

(31) Chen, H.-Y. T.; Tosoni, S.; Pacchioni, G. Hydrogen Adsorption, Dissociation, and Spillover on Ru_{10} Clusters Supported on Anatase TiO_2 and Tetragonal ZrO_2 (101) Surfaces. *ACS Catal.* **2015**, *5*, 5486−5495.

(32) Lutfalla, S.; Shapovalov, V.; Bell, A. T. Calibration of the DFT/GGA+U Method for Determination of Reduction Energies for Transition and Rare Earth Metal Oxides of Ti, V, Mo, and Ce. *J. Chem. Theory Comput.* **2011**, *7*, 2218−2223.

(33) Cococcioni, M.; de Gironcoli, S. Linear response approach to the calculation of the effective interaction parameters in the LDA + U method. *Phys. Rev. B* **2005**, *71*, 035105.

(34) Kulik, H. J.; Cococcioni, M.; Scherlis, D. A.; Marzari, N. Density Functional Theory in Transition-Metal Chemistry: A Self-Consistent Hubbard *U* Approach. *Phys. Rev. Lett.* **2006**, *97*, 103001.

(35) Dudarev, S. L.; Botton, G. A.; Savrasov, S. Y.; Humphreys, C. J.; Sutton, A. P. Electron-energy-loss spectra and the structural stability of nickel oxide: An LSDA+U study. *Phys. Rev. B* **1998**, *57*, 1505−1509.

(36) Park, S.-G.; Magyari-Köpe, B.; Nishi, Y. Electronic correlation effects in reduced rutile TiO_2 within the LDA + *U* method. *Phys. Rev. B* **2010**, *82*, 115109.

(37) Plata, J. J.; Márquez, A. M.; Sanz, J. F. Communication: Improving the density functional theory+*U* description of CeO_2 by including the contribution of the O 2*p* electrons. *J. Chem. Phys.* **2012**, *136*, 041101.

(38) Huang, X.; Ramadugu, S. K.; Mason, S. E. Surface-Specific DFT + *U* Approach Applied to α-Fe_2O_3(0001). *J. Phys. Chem. C* **2016**, *120*, 4919−4930.

(39) Brown, J. J.; Page, A. J. The Hubbard-U correction and optical properties of d0 metal oxide photocatalysts. *J. Chem. Phys.* **2020**, *153*, 224116.

(40) Hsu, H.; Umemoto, K.; Cococcioni, M.; Wentzcovitch, R. First-principles study for low-spin $LaCoO_3$ with a structurally consistent Hubbard *U. Phys. Rev. B* **2009**, *79*, 125124.

(41) Zhao, Q.; Kulik, H. J. Stable Surfaces That Bind Too Tightly: Can Range-Separated Hybrids or DFT+U Improve Paradoxical Descriptions of Surface Chemistry? *J. Phys. Chem. Lett.* **2019**, *10*, 5090−5098.

(42) Perdew, J. P.; Levy, M. Physical Content of the Exact Kohn-Sham Orbital Energies: Band Gaps and Derivative Discontinuities. *Phys. Rev. Lett.* **1983**, *51*, 1884−1887.

(43) Çakır, D.; Gülseren, O. Adsorption of Pt and Bimetallic PtAu Clusters on the Partially Reduced Rutile (110) TiO_2 Surface: A First-Principles Study. *J. Phys. Chem. C* **2012**, *116*, 5735−5746.

(44) French, R. H.; Glass, S. J.; Ohuchi, F. S.; Xu, Y. N.; Ching, W. Y. Experimental and theoretical determination of the electronic structure and optical properties of three phases of ZrO_2. *Phys. Rev. B* **1994**, *49*, 5133−5142.

(45) McComb, D. W. Bonding and electronic structure in zirconia pseudopolymorphs investigated by electron energy-loss spectroscopy. *Phys. Rev. B* **1996**, *54*, 7094−7102.

(46) Dash, L. K.; Vast, N.; Baranek, P.; Cheynet, M.-C.; Reining, L. Electronic structure and electron energy-loss spectroscopy of ZrO_2 zirconia. *Phys. Rev. B* **2004**, *70*, 245116.

(47) Teeparthi, S.; Awin, E.; Kumar, R. Dominating role of crystal structure over defect chemistry in black and white zirconia on visible light photocatalytic activity. *Sci. Rep.* **2018**, *8*, 5541.

(48) Jiang, N.; Spence, J. C. Valence electron energy-loss spectroscopy study of $ZrSiO_4$ and ZrO_2. *Ultramicroscopy* **2013**, *134*, 68−76.

(49) Hammer, B.; Hansen, L. B.; Nørskov, J. K. Improved adsorption energetics within density-functional theory using revised Perdew-Burke-Ernzerhof functionals. *Phys. Rev. B* **1999**, *59*, 7413−7421.

(50) Klüpfel, S.; Klüpfel, P.; Jónsson, H. The effect of the Perdew-Zunger self-interaction correction to density functionals on the energetics of small molecules. *J. Chem. Phys.* **2012**, *137*, 124102.

(51) Tang, W.; Sanville, E.; Henkelman, G. A grid-based Bader analysis algorithm without lattice bias. *J. Phys.: Condens. Matter* **2009**, *21*, 084204.

(52) Häkkinen, H.; Moseler, M.; Landman, U. Bonding in Cu, Ag, and Au Clusters: Relativistic Effects, Trends, and Surprises. *Phys. Rev. Lett.* **2002**, *89*, 033401.

(53) Cordero, B.; Gómez, V.; Platero-Prats, A. E.; Revés, M.; Echeverría, J.; Cremades, E.; Barragán, F.; Alvarez, S. Covalent radii revisited. *Dalton Trans* **2008**, 2832−2838.

(54) Shannon, R. D. Revised effective ionic radii and systematic studies of interatomic distances in halides and chalcogenides. *Acta Crystallogr. A* **1976**, *32*, 751−767.

(55) Yudanov, I.; Pacchioni, G.; Neyman, K.; Rösch, N. Systematic Density Functional Study of the Adsorption of Transition Metal Atoms on the MgO(001) Surface. *J. Phys. Chem. B* **1997**, *101*, 2786−2792.

(56) Matveev, A. V.; Neyman, K. M.; Yudanov, I. V.; Rösch, N. Adsorption of transition metal atoms on oxygen vacancies and regular sites of the MgO(001) surface. *Surf. Sci.* **1999**, *426*, 123−139.

(57) Markovits, A.; Paniagua, J. C.; López, N.; Minot, C.; Illas, F. Adsorption energy and spin state of first-row transition metals adsorbed on MgO(100). *Phys. Rev. B* **2003**, *67*, 115417.

(58) Neyman, K.; Inntam, C.; Nasluzov, V.; Kosarev, R.; Rösch, N. Adsorption of d-metal atoms on the regular MgO(001) surface: Density functional study of cluster models embedded in an elastic polarizable environment. *Appl. Phys. A: Mater. Sci. Process.* **2004**, *78*, 823−828.

(59) Neyman, K. M.; Inntam, C.; Matveev, A. V.; Nasluzov, V. A.; Rösch, N. Single d-Metal Atoms on F_s and F_s^+ Defects of MgO(001): A Theoretical Study across the Periodic Table. *J. Am. Chem. Soc.* **2005**, *127*, 11652−11660.

(60) Jung, C.; Ishimoto, R.; Tsuboi, H.; Koyama, M.; Endou, A.; Kubo, M.; Del Carpio, C. A.; Miyamoto, A. Interfacial properties of ZrO_2 supported precious metal catalysts: A density functional study. *Appl. Catal., A* **2006**, *305*, 102−109.

(61) Helali, Z.; Markovits, A.; Minot, C.; Abderrabba, M. First-row transition metal atoms adsorption on rutile TiO_2(110) surface. *Struct. Chem.* **2012**, *23*, 1309−1321.

(62) Helali, Z.; Markovits, A.; Minot, C.; Abderrabba, M. Metal atom adsorption on a defective TiO_{2--x} support. *Chem. Phys. Lett.* **2014**, *594*, 23−29.

(63) Grau-Crespo, R.; Hernández, N. C.; Sanz, J. F.; de Leeuw, N. H. Theoretical Investigation of the Deposition of Cu, Ag, and Au Atoms on the ZrO_2(111) Surface. *J. Phys. Chem. C* **2007**, *111*, 10448−10454.

(64) Ganduglia-Pirovano, M. V.; Hofmann, A.; Sauer, J. Oxygen vacancies in transition metal and rare earth oxides: Current state of understanding and remaining challenges. *Surf. Sci. Rep.* **2007**, *62*, 219−270.

(65) Pacchioni, G. Electronic interactions and charge transfers of metal atoms and clusters on oxide surfaces. *Phys. Chem. Chem. Phys.* **2013**, *15*, 1737−1757.

(66) Dalverny, A.-L.; Filhol, J.-S.; Lemoigno, F.; Doublet, M.-L. Interplay between Magnetic and Orbital Ordering in the Strongly Correlated Cobalt Oxide: A DFT + *U* Study. *J. Phys. Chem. C* **2010**, *114*, 21750−21756.

(67) Singh, V.; Kosa, M.; Majhi, K.; Major, D. T. Putting DFT to the Test: A First-Principles Study of Electronic, Magnetic, and Optical Properties of Co_3O_4. *J. Chem. Theory Comput.* **2015**, *11*, 64−72.

(68) Andersin, J.; Nevalaita, J.; Honkala, K.; Häkkinen, H. The Redox Chemistry of Gold with High-Valence Doped Calcium Oxide. *Angew. Chem., Int. Ed.* **2013**, *52*, 1424−1427.

(69) Mehta, P.; Greeley, J.; Delgass, W. N.; Schneider, W. F. Adsorption Energy Correlations at the Metal−Support Boundary. *ACS Catal.* **2017**, *7*, 4707−4715.

(70) Song, W.; Martsinovich, N.; Heckl, W. M.; Lackinger, M. Born−Haber Cycle for Monolayer Self-Assembly at the Liquid−Solid Interface: Assessing the Enthalpic Driving Force. *J. Am. Chem. Soc.* **2013**, *135*, 14854−14862.

(71) Lany, S.; Zunger, A. Accurate prediction of defect properties in density functional supercell calculations. *Modell. Simul. Mater. Sci. Eng.* **2009**, *17*, 084002.

(72) Wang, Y.; Florez, E.; Mondragon, F.; Truong, T. N. Effects of metal−support interactions on the electronic structures of metal atoms adsorbed on the perfect and defective MgO(100) surfaces. *Surf. Sci.* **2006**, *600*, 1703−1713.

(73) Chaves, A. S.; Rondina, G. G.; Piotrowski, M. J.; Tereshchuk, P.; Da Silva, J. L. F. The Role of Charge States in the Atomic Structure of Cu_n and Pt_n ($n = 2−14$ atoms) Clusters: A DFT Investigation. *J. Phys. Chem. A* **2014**, *118*, 10813−10821.

(74) Raab, J.; Roos, B. O. Excitation Energies for Transition Metal Atoms − A Comparison between Coupled Cluster Methods and Second-Order Perturbation Theory. In *Adv. Quantum Chem.*; Academic Press: New York, 2005; Vol. *48*, pp 421−433.

IV

REO$_X$ AS A BRØNSTED ACIDIC MODIFIER IN GLYCEROL HYDRODEOXYGENATION: COMPUTATIONAL INSIGHT INTO THE BALANCE BETWEEN ACID AND METAL CATALYSIS

by

Ville Korpelin, Gokarneswar Sahoo, Rasmus Ikonen, and Karoliina Honkala

Submitted, **2022**

Request a copy from the author.

DEPARTMENT OF CHEMISTRY, UNIVERSITY OF JYVÄSKYLÄ
RESEARCH REPORT SERIES

1. Vuolle, Mikko: Electron paramagnetic resonance and molecular orbital study of radical ions generated from (2.2)metacyclophane, pyrene and its hydrogenated compounds by alkali metal reduction and by thallium(III)trifluoroacetate oxidation. (99 pp.) 1976
2. Pasanen, Kaija: Electron paramagnetic resonance study of cation radical generated from various chlorinated biphenyls. (66 pp.) 1977
3. Carbon-13 Workshop, September 6-8, 1977. (91 pp.) 1977
4. Laihia, Katri: On the structure determination of norbornane polyols by NMR spectroscopy. (111 pp.) 1979
5. Nyrönen, Timo: On the EPR, ENDOR and visible absorption spectra of some nitrogen containing heterocyclic compounds in liquid ammonia. (76 pp.) 1978
6. Talvitie, Antti: Structure determination of some sesquiterpenoids by shift reagent NMR. (54 pp.) 1979
7. Häkli, Harri: Structure analysis and molecular dynamics of cyclic compounds by shift reagent NMR. (48 pp.) 1979
8. Pitkänen, Ilkka: Thermodynamics of complexation of 1,2,4-triazole with divalent manganese, cobalt, nickel, copper, zinc, cadmium and lead ions in aqueous sodium perchlorate solutions. (89 pp.) 1980
9. Asunta, Tuula: Preparation and characterization of new organometallic compounds synthesized by using metal vapours. (91 pp.) 1980
10. Sattar, Mohammad Abdus: Analyses of MCPA and its metabolites in soil. (57 pp.) 1980
11. Bibliography 1980. (31 pp.) 1981
12. Knuuttila, Pekka: X-Ray structural studies on some divalent 3d metal compounds of picolinic and isonicotinic acid N-oxides. (77 pp.) 1981
13. Bibliography 1981. (33 pp.) 1982
14. 6th National NMR Symposium, September 9-10, 1982, Abstracts. (49 pp.) 1982
15. Bibliography 1982. (38 pp.) 1983
16. Knuuttila, Hilkka: X-Ray structural studies on some Cu(II), Co(II) and Ni(II) complexes with nicotinic and isonicotinic acid N-oxides. (54 pp.) 1983
17. Symposium on inorganic and analytical chemistry May 18, 1984, Program and Abstracts. (100 pp.) 1984
18. Knuutinen, Juha: On the synthesis, structure verification and gas chromatographic determination of chlorinated catechols and guaiacols occuring in spent bleach liquors of kraft pulp mill. (30 pp.) 1984
19. Bibliography 1983. (47 pp.) 1984
20. Pitkänen, Maija: Addition of BrCl, B_2 and Cl_2 to methyl esters of propenoic and 2-butenoic acid derivatives and ^{13}C NMR studies on methyl esters of saturated aliphatic mono- and dichlorocarboxylic acids. (56 pp.) 1985
21. Bibliography 1984. (39 pp.) 1985
22. Salo, Esa: EPR, ENDOR and TRIPLE spectroscopy of some nitrogen heteroaromatics in liquid ammonia. (111 pp.) 1985

DEPARTMENT OF CHEMISTRY, UNIVERSITY OF JYVÄSKYLÄ
RESEARCH REPORT SERIES

23. Humppi, Tarmo: Synthesis, identification and analysis of dimeric impurities of chlorophenols. (39 pp.) 1985
24. Aho, Martti: The ion exchange and adsorption properties of sphagnum peat under acid conditions. (90 pp.) 1985
25. Bibliography 1985 (61 pp.) 1986
26. Bibliography 1986. (23 pp.) 1987
27. Bibliography 1987. (26 pp.) 1988
28. Paasivirta, Jaakko (Ed.): Structures of organic environmental chemicals. (67 pp.) 1988
29. Paasivirta, Jaakko (Ed.): Chemistry and ecology of organo-element compounds. (93 pp.) 1989
30. Sinkkonen, Seija: Determination of crude oil alkylated dibenzothiophenes in environment. (35 pp.) 1989
31. Kolehmainen, Erkki (Ed.): XII National NMR Symposium Program and Abstracts. (75 pp.) 1989
32. Kuokkanen, Tauno: Chlorocymenes and Chlorocymenenes: Persistent chlorocompounds in spent bleach liquors of kraft pulp mills. (40 pp.) 1989
33. Mäkelä, Reijo: ESR, ENDOR and TRIPLE resonance study on substituted 9,10-anthraquinone radicals in solution. (35 pp.) 1990
34. Veijanen, Anja: An integrated sensory and analytical method for identification of off-flavour compounds. (70 pp.) 1990
35. Kasa, Seppo: EPR, ENDOR and TRIPLE resonance and molecular orbital studies on a substitution reaction of anthracene induced by thallium(III) in two fluorinated carboxylic acids. (114 pp.) 1990
36. Herve, Sirpa: Mussel incubation method for monitoring organochlorine compounds in freshwater recipients of pulp and paper industry. (145 pp.) 1991
37. Pohjola, Pekka: The electron paramagnetic resonance method for characterization of Finnish peat types and iron (III) complexes in the process of peat decomposition. (77 pp.) 1991
38. Paasivirta, Jaakko (Ed.): Organochlorines from pulp mills and other sources. Research methodology studies 1988-91. (120 pp.) 1992
39. Veijanen, Anja (Ed.): VI National Symposium on Mass Spectrometry, May 13-15, 1992, Abstracts. (55 pp.) 1992
40. Rissanen, Kari (Ed.): The 7. National Symposium on Inorganic and Analytical Chemistry, May 22, 1992, Abstracts and Program. (153 pp.) 1992
41. Paasivirta, Jaakko (Ed.): CEOEC'92, Second Finnish-Russian Seminar: Chemistry and Ecology of Organo-Element Compounds. (93 pp.) 1992
42. Koistinen, Jaana: Persistent polychloroaromatic compounds in the environment: structure-specific analyses. (50 pp.) 1993
43. Virkki, Liisa: Structural characterization of chlorolignins by spectroscopic and liquid chromatographic methods and a comparison with humic substances. (62 pp.) 1993
44. Helenius, Vesa: Electronic and vibrational excitations in some

biologically relevant molecules. (30 pp.) 1993

45. Leppä-aho, Jaakko: Thermal behaviour, infrared spectra and x-ray structures of some new rare earth chromates(VI). (64 pp.) 1994
46. Kotila, Sirpa: Synthesis, structure and thermal behavior of solid copper(II) complexes of 2-amino-2- hydroxymethyl-1,3-propanediol. (111 pp.) 1994
47. Mikkonen, Anneli: Retention of molybdenum(VI), vanadium(V) and tungsten(VI) by kaolin and three Finnish mineral soils. (90 pp.) 1995
48. Suontamo, Reijo: Molecular orbital studies of small molecules containing sulfur and selenium. (42 pp.) 1995
49. Hämäläinen, Jouni: Effect of fuel composition on the conversion of fuel-N to nitrogen oxides in the combustion of small single particles. (50 pp.) 1995
50. Nevalainen, Tapio: Polychlorinated diphenyl ethers: synthesis, NMR spectroscopy, structural properties, and estimated toxicity. (76 pp.) 1995
51. Aittola, Jussi-Pekka: Organochloro compounds in the stack emission. (35 pp.) 1995
52. Harju, Timo: Ultrafast polar molecular photophysics of (dibenzylmethine)borondifluoride and 4-aminophthalimide in solution. (61 pp.) 1995
53. Maatela, Paula: Determination of organically bound chlorine in industrial and environmental samples. (83 pp.) 1995
54. Paasivirta, Jaakko (Ed.): CEOEC'95, Third Finnish-Russian Seminar: Chemistry and Ecology of Organo-Element Compounds. (109 pp.) 1995
55. Huuskonen, Juhani: Synthesis and structural studies of some supramolecular compounds. (54 pp.) 1995
56. Palm, Helena: Fate of chlorophenols and their derivatives in sawmill soil and pulp mill recipient environments. (52 pp.) 1995
57. Rantio, Tiina: Chlorohydrocarbons in pulp mill effluents and their fate in the environment. (89 pp.) 1997
58. Ratilainen, Jari: Covalent and non-covalent interactions in molecular recognition. (37 pp.) 1997
59. Kolehmainen, Erkki (Ed.): XIX National NMR Symposium, June 4-6, 1997, Abstracts. (89 pp.) 1997
60. Matilainen, Rose: Development of methods for fertilizer analysis by inductively coupled plasma atomic emission spectrometry. (41 pp.) 1997
61. Koistinen, Jari (Ed.): Spring Meeting on the Division of Synthetic Chemistry, May 15-16, 1997, Program and Abstracts. (36 pp.) 1997
62. Lappalainen, Kari: Monomeric and cyclic bile acid derivatives: syntheses, NMR spectroscopy and molecular recognition properties. (50 pp.) 1997
63. Laitinen, Eira: Molecular dynamics of cyanine dyes and phthalimides in solution: picosecond laser studies. (62 pp.) 1997
64. Eloranta, Jussi: Experimental and theoretical studies on some

quinone and quinol radicals. (40 pp.) 1997

65. Oksanen, Jari: Spectroscopic characterization of some monomeric and aggregated chlorophylls. (43 pp.) 1998
66. Häkkänen, Heikki: Development of a method based on laser-induced plasma spectrometry for rapid spatial analysis of material distributions in paper coatings. (60 pp.) 1998
67. Virtapohja, Janne: Fate of chelating agents used in the pulp and paper industries. (58 pp.) 1998
68. Airola, Karri: X-ray structural studies of supramolecular and organic compounds. (39 pp.) 1998
69. Hyötyläinen, Juha: Transport of lignin–type compounds in the receiving waters of pulp mills. (40 pp.) 1999
70. Ristolainen, Matti: Analysis of the organic material dissolved during totally chlorine-free bleaching. (40 pp.) 1999
71. Eklin, Tero: Development of analytical procedures with industrial samples for atomic emission and atomic absorption spectrometry. (43 pp.) 1999
72. Välisaari, Jouni: Hygiene properties of resol-type phenolic resin laminates. (129 pp.) 1999
73. Hu, Jiwei: Persistent polyhalogenated diphenyl ethers: model compounds syntheses, characterization and molecular orbital studies. (59 pp.) 1999
74. Malkavaara, Petteri: Chemometric adaptations in wood processing chemistry. (56 pp.) 2000
75. Kujala Elena, Laihia Katri, Nieminen Kari (Eds.): NBC 2000, Symposium on Nuclear, Biological and Chemical Threats in the 21st Century. (299 pp.) 2000
76. Rantalainen, Anna-Lea: Semipermeable membrane devices in monitoring persistent organic pollutants in the environment. (58 pp.) 2000
77. Lahtinen, Manu: *In situ* X-ray powder diffraction studies of Pt/C, CuCl/C and Cu_2O/C catalysts at elevated temperatures in various reaction conditions. (92 pp.) 2000
78. Tamminen, Jari: Syntheses, empirical and theoretical characterization, and metal cation complexation of bile acid-based monomers and open/closed dimers. (54 pp.) 2000
79. Vatanen, Virpi: Experimental studies by EPR and theoretical studies by DFT calculations of α-amino-9,10-anthraquinone radical anions and cations in solution. (37 pp.) 2000
80. Kotilainen, Risto: Chemical changes in wood during heating at 150-260 °C. (57 pp.) 2000
81. Nissinen, Maija: X-ray structural studies on weak, non-covalent interactions in supramolecular compounds. (69 pp.) 2001
82. Wegelius, Elina: X-ray structural studies on self-assembled hydrogen-bonded networks and metallosupramolecular complexes. (84 pp.) 2001
83. Paasivirta, Jaakko (Ed.): CEOEC’2001, Fifth Finnish-Russian Seminar: Chemistry and Ecology of Organo-Element Compounds. (163 pp.) 2001
84. Kiljunen, Toni: Theoretical studies on spectroscopy and

atomic dynamics in rare gas solids. (56 pp.) 2001

85. Du, Jin: Derivatives of dextran: synthesis and applications in oncology. (48 pp.) 2001
86. Koivisto, Jari: Structural analysis of selected polychlorinated persistent organic pollutants (POPs) and related compounds. (88 pp.) 2001
87. Feng, Zhinan: Alkaline pulping of non-wood feedstocks and characterization of black liquors. (54 pp.) 2001
88. Halonen, Markku: Lahon havupuun käyttö sulfaattiprosessin raaka-aineena sekä havupuun lahontorjunta. (90 pp.) 2002
89. Falábu, Dezsö: Synthesis, conformational analysis and complexation studies of resorcarene derivatives. (212 pp.) 2001
90. Lehtovuori, Pekka: EMR spectroscopic studies on radicals of ubiquinones Q-*n*, vitamin K_3 and vitamine E in liquid solution. (40 pp.) 2002
91. Perkkalainen, Paula: Polymorphism of sugar alcohols and effect of grinding on thermal behavior on binary sugar alcohol mixtures. (53 pp.) 2002
92. Ihalainen, Janne: Spectroscopic studies on light-harvesting complexes of green plants and purple bacteria. (42 pp.) 2002
93. Kunttu, Henrik, Kiljunen, Toni (Eds.): 4th International Conference on Low Temperature Chemistry. (159 pp.) 2002
94. Väisänen, Ari: Development of methods for toxic element analysis in samples with environmental concern by ICP-AES and ETAAS. (54 pp.) 2002
95. Luostarinen, Minna: Synthesis and characterisation of novel resorcarene derivatives. (200 pp.) 2002
96. Louhelainen, Jarmo: Changes in the chemical composition and physical properties of wood and nonwood black liquors during heating. (68 pp.) 2003
97. Lahtinen, Tanja: Concave hydrocarbon cyclophane π-prismands. (65 pp.) 2003
98. Laihia, Katri (Ed.): NBC 2003, Symposium on Nuclear, Biological and Chemical Threats – A Crisis Management Challenge. (245 pp.) 2003
99. Oasmaa, Anja: Fuel oil quality properties of wood-based pyrolysis liquids. (32 pp.) 2003
100. Virtanen, Elina: Syntheses, structural characterisation, and cation/anion recognition properties of nano-sized bile acid-based host molecules and their precursors. (123 pp.) 2003
101. Nättinen, Kalle: Synthesis and X-ray structural studies of organic and metallo-organic supramolecular systems. (79 pp.) 2003
102. Lampiselkä, Jarkko: Demonstraatio lukion kemian opetuksessa. (285 pp.) 2003
103. Kallioinen, Jani: Photoinduced dynamics of $Ru(dcbpy)_2(NCS)_2$ – in solution and on nanocrystalline titanium dioxide thin films. (47 pp.) 2004
104. Valkonen, Arto (Ed.): VII Synthetic Chemistry Meeting and XXVI Finnish NMR Symposium. (103 pp.) 2004

DEPARTMENT OF CHEMISTRY, UNIVERSITY OF JYVÄSKYLÄ
RESEARCH REPORT SERIES

105. Vaskonen, Kari: Spectroscopic studies on atoms and small molecules isolated in low temperature rare gas matrices. (65 pp.) 2004
106. Lehtovuori, Viivi: Ultrafast light induced dissociation of Ru(dcbpy)$(CO)_2I_2$ in solution. (49 pp.) 2004
107. Saarenketo, Pauli: Structural studies of metal complexing Schiff bases, Schiff base derived *N*-glycosides and cyclophane π-prismands. (95 pp.) 2004
108. Paasivirta, Jaakko (Ed.): CEOEC’2004, Sixth Finnish-Russian Seminar: Chemistry and Ecology of Organo-Element Compounds. (147 pp.) 2004
109. Suontamo, Tuula: Development of a test method for evaluating the cleaning efficiency of hard-surface cleaning agents. (96 pp.) 2004
110. Güneş, Minna: Studies of thiocyanates of silver for nonlinear optics. (48 pp.) 2004
111. Ropponen, Jarmo: Aliphatic polyester dendrimers and dendrons. (81 pp.) 2004
112. Vu, Mân Thi Hong: Alkaline pulping and the subsequent elemental chlorine-free bleaching of bamboo (*Bambusa procera*). (69 pp.) 2004
113. Mansikkamäki, Heidi: Self-assembly of resorcinarenes. (77 pp.) 2006
114. Tuononen, Heikki M.: EPR spectroscopic and quantum chemical studies of some inorganic main group radicals. (79 pp.) 2005
115. Kaski, Saara: Development of methods and applications of laser-induced plasma spectroscopy in vacuum ultraviolet. (44 pp.) 2005
116. Mäkinen, Riika-Mari: Synthesis, crystal structure and thermal decomposition of certain metal thiocyanates and organic thiocyanates. (119 pp.) 2006
117. Ahokas, Jussi: Spectroscopic studies of atoms and small molecules isolated in rare gas solids: photodissociation and thermal reactions. (53 pp.) 2006
118. Busi, Sara: Synthesis, characterization and thermal properties of new quaternary ammonium compounds: new materials for electrolytes, ionic liquids and complexation studies. (102 pp.) 2006
119. Mäntykoski, Keijo: PCBs in processes, products and environment of paper mills using wastepaper as their raw material. (73 pp.) 2006
120. Laamanen, Pirkko-Leena: Simultaneous determination of industrially and environmentally relevant aminopolycarboxylic and hydroxycarboxylic acids by capillary zone electrophoresis. (54 pp.) 2007
121. Salmela, Maria: Description of oxygen-alkali delignification of kraft pulp using analysis of dissolved material. (71 pp.) 2007
122. Lehtovaara, Lauri: Theoretical studies of atomic scale impurities in superfluid ^{4}He. (87 pp.) 2007
123. Rautiainen, J. Mikko: Quantum chemical calculations of structures, bonding, and spectroscopic properties of some sulphur and selenium iodine cations. (71 pp.) 2007
124. Nummelin, Sami: Synthesis, characterization, structural and

retrostructural analysis of self-assembling pore forming dendrimers. (286 pp.) 2008

125. Sopo, Harri: Uranyl(VI) ion complexes of some organic aminobisphenolate ligands: syntheses, structures and extraction studies. (57 pp.) 2008
126. Valkonen, Arto: Structural characteristics and properties of substituted cholanoates and *N*-substituted cholanamides. (80 pp.) 2008
127. Lähde, Anna: Production and surface modification of pharmaceutical nano- and microparticles with the aerosol flow reactor. (43 pp.) 2008
128. Beyeh, Ngong Kodiah: Resorcinarenes and their derivatives: synthesis, characterization and complexation in gas phase and in solution. (75 pp.) 2008
129. Välisaari, Jouni, Lundell, Jan (Eds.): Kemian opetuksen päivät 2008: uusia oppimisympäristöjä ja ongelmalähtöistä opetusta. (118 pp.) 2008
130. Myllyperkiö, Pasi: Ultrafast electron transfer from potential organic and metal containing solar cell sensitizers. (69 pp.) 2009
131. Käkölä, Jaana: Fast chromatographic methods for determining aliphatic carboxylic acids in black liquors. (82 pp.) 2009
132. Koivukorpi, Juha: Bile acid-arene conjugates: from photoswitchability to cancer cell detection. (67 pp.) 2009
133. Tuuttila, Tero: Functional dendritic polyester compounds: synthesis and characterization of small bifunctional dendrimers and dyes. (74 pp.) 2009
134. Salorinne, Kirsi: Tetramethoxy resorcinarene based cation and anion receptors: synthesis, characterization and binding properties. (79 pp.) 2009
135. Rautiainen, Riikka: The use of first-thinning Scots pine (*Pinus sylvestris*) as fiber raw material for the kraft pulp and paper industry. (73 pp.) 2010
136. Ilander, Laura: Uranyl salophens: synthesis and use as ditopic receptors. (199 pp.) 2010
137. Kiviniemi, Tiina: Vibrational dynamics of iodine molecule and its complexes in solid krypton - Towards coherent control of bimolecular reactions? (73 pp.) 2010
138. Ikonen, Satu: Synthesis, characterization and structural properties of various covalent and non-covalent bile acid derivatives of N/O-heterocycles and their precursors. (105 pp.) 2010
139. Siitonen, Anni: Spectroscopic studies of semiconducting single-walled carbon nanotubes. (56 pp.) 2010
140. Raatikainen, Kari: Synthesis and structural studies of piperazine cyclophanes – Supramolecular systems through Halogen and Hydrogen bonding and metal ion coordination. (69 pp.) 2010
141. Leivo, Kimmo: Gelation and gel properties of two- and three-component Pyrene based low molecular weight organogelators. (116 pp.) 2011
142. Martiskainen, Jari: Electronic energy transfer in light-harvesting complexes isolated from *Spinacia oleracea* and from three

photosynthetic green bacteria *Chloroflexus aurantiacus, Chlorobium tepidum*, and *Prosthecochloris aestuarii*. (55 pp.) 2011

143. Wichmann, Oula: Syntheses, characterization and structural properties of [O,N,O,X´] aminobisphenolate metal complexes. (101 pp.) 2011
144. Ilander, Aki: Development of ultrasound-assisted digestion methods for the determination of toxic element concentrations in ash samples by ICP-OES. (58 pp.) 2011
145. The Combined XII Spring Meeting of the Division of Synthetic Chemistry and XXXIII Finnish NMR Symposium. Book of Abstracts. (90 pp.) 2011
146. Valto, Piia: Development of fast analysis methods for extractives in papermaking process waters. (73 pp.) 2011
147. Andersin, Jenni: Catalytic activity of palladium-based nanostructures in the conversion of simple olefinic hydro- and chlorohydrocarbons from first principles. (78 pp.) 2011
148. Aumanen, Jukka: Photophysical properties of dansylated poly(propylene amine) dendrimers. (55 pp.) 2011
149. Kärnä, Minna: Ether-functionalized quaternary ammonium ionic liquids – synthesis, characterization and physicochemical properties. (76 pp.) 2011
150. Jurček, Ondřej: Steroid conjugates for applications in pharmacology and biology. (57 pp.) 2011
151. Nauha, Elisa: Crystalline forms of selected Agrochemical actives: design and synthesis of cocrystals. (77 pp.) 2012
152. Ahkola, Heidi: Passive sampling in monitoring of nonylphenol ethoxylates and nonylphenol in aquatic environments. (92 pp.) 2012
153. Helttunen, Kaisa: Exploring the self-assembly of resorcinarenes: from molecular level interactions to mesoscopic structures. (78 pp.) 2012
154. Linnanto, Juha: Light excitation transfer in photosynthesis revealed by quantum chemical calculations and exiton theory. (179 pp.) 2012
155. Roiko-Jokela, Veikko: Digital imaging and infrared measurements of soil adhesion and cleanability of semihard and hard surfaces. (122 pp.) 2012
156. Noponen, Virpi: Amides of bile acids and biologically important small molecules: properties and applications. (85 pp.) 2012
157. Hulkko, Eero: Spectroscopic signatures as a probe of structure and dynamics in condensed-phase systems – studies of iodine and gold ranging from isolated molecules to nanoclusters. (69 pp.) 2012
158. Lappi, Hanna: Production of Hydrocarbon-rich biofuels from extractives-derived materials. (95 pp.) 2012
159. Nykänen, Lauri: Computational studies of Carbon chemistry on transition metal surfaces. (76 pp.) 2012
160. Ahonen, Kari: Solid state studies of pharmaceutically important molecules and their derivatives. (65 pp.) 2012

DEPARTMENT OF CHEMISTRY, UNIVERSITY OF JYVÄSKYLÄ
RESEARCH REPORT SERIES

161. Pakkanen, Hannu: Characterization of organic material dissolved during alkaline pulping of wood and non-wood feedstocks. (76 pp.) 2012
162. Moilanen, Jani: Theoretical and experimental studies of some main group compounds: from closed shell interactions to singlet diradicals and stable radicals. (80 pp.) 2012
163. Himanen, Jatta: Stereoselective synthesis of Oligosaccharides by *De Novo* Saccharide welding. (133 pp.) 2012
164. Bunzen, Hana: Steroidal derivatives of nitrogen containing compounds as potential gelators. (76 pp.) 2013
165. Seppälä, Petri: Structural diversity of copper(II) amino alcohol complexes. Syntheses, structural and magnetic properties of bidentate amino alcohol copper(II) complexes. (67 pp.) 2013
166. Lindgren, Johan: Computational investigations on rotational and vibrational spectroscopies of some diatomics in solid environment. (77 pp.) 2013
167. Giri, Chandan: Sub-component self-assembly of linear and non-linear diamines and diacylhydrazines, formulpyridine and transition metal cations. (145 pp.) 2013
168. Riisiö, Antti: Synthesis, Characterization and Properties of Cu(II)-, Mo(VI)- and U(VI) Complexes With Diaminotetraphenolate Ligands. (51 pp.) 2013
169. Kiljunen, Toni (Ed.): Chemistry and Physics at Low Temperatures. Book of Abstracts. (103 pp.) 2013
170. Hänninen, Mikko: Experimental and Computational Studies of Transition Metal Complexes with Polydentate Amino- and Aminophenolate Ligands: Synthesis, Structure, Reactivity and Magnetic Properties. (66 pp.) 2013
171. Antila, Liisa: Spectroscopic studies of electron transfer reactions at the photoactive electrode of dye-sensitized solar cells. (53 pp.) 2013
172. Kemppainen, Eeva: Mukaiyama-Michael reactions with α-substituted acroleins – a useful tool for the synthesis of the pectenotoxins and other natural product targets. (190 pp.) 2013
173. Virtanen, Suvi: Structural Studies of Dielectric Polymer Nanocomposites. (49 pp.) 2013
174. Yliniemelä-Sipari, Sanna: Understanding The Structural Requirements for Optimal Hydrogen Bond Catalyzed Enolization – A Biomimetic Approach.(160 pp.) 2013
175. Leskinen, Mikko V: Remote β-functionalization of β'-keto esters. (105 pp.) 2014
176. 12th European Conference on Research in Chemistry Education (ECRICE2014). Book of Abstracts. (166 pp.) 2014
177. Peuronen, Anssi: N-Monoalkylated DABCO-Based N-Donors as Versatile Building Blocks in Crystal Engineering and Supramolecular Chemistry. (54 pp.) 2014
178. Perämäki, Siiri: Method development for determination and recovery of rare earth elements from industrial fly ash. (88 pp.) 2014

DEPARTMENT OF CHEMISTRY, UNIVERSITY OF JYVÄSKYLÄ
RESEARCH REPORT SERIES

179. Chernyshev, Alexander, N.: Nitrogen-containing ligands and their platinum(IV) and gold(III) complexes: investigation and basicity and nucleophilicity, luminescence, and aurophilic interactions. (64 pp.) 2014
180. Lehto, Joni: Advanced Biorefinery Concepts Integrated to Chemical Pulping. (142 pp.) 2015
181. Tero, Tiia-Riikka: Tetramethoxy resorcinarenes as platforms for fluorescent and halogen bonding systems. (61 pp.) 2015
182. Löfman, Miika: Bile acid amides as components of microcrystalline organogels. (62 pp.) 2015
183. Selin, Jukka: Adsorption of softwood-derived organic material onto various fillers during papermaking. (169 pp.) 2015
184. Piisola, Antti: Challenges in the stereoselective synthesis of allylic alcohols. (210 pp.) 2015
185. Bonakdarzadeh, Pia: Supramolecular coordination polyhedra based on achiral and chiral pyridyl ligands: design, preparation, and characterization. (65 pp.) 2015
186. Vasko, Petra: Synthesis, characterization, and reactivity of heavier group 13 and 14 metallylenes and metalloid clusters: small molecule activation and more. (66 pp.) 2015
187. Topić, Filip: Structural Studies of Nano-sized Supramolecular Assemblies. (79 pp.) 2015
188. Mustalahti, Satu: Photodynamics Studies of Ligand-Protected Gold Nanoclusters by using Ultrafast Transient Infrared Spectroscopy. (58 pp.) 2015
189. Koivisto, Jaakko: Electronic and vibrational spectroscopic studies of gold-nanoclusters. (63 pp.) 2015
190. Suhonen, Aku: Solid state conformational behavior and interactions of series of aromatis oligoamide foldamers. (68 pp.) 2016
191. Soikkeli, Ville: Hydrometallurgical recovery and leaching studies for selected valuable metals from fly ash samples by ultrasound-assisted extraction followed by ICP-OES determination. (107 pp.) 2016
192. XXXVIII Finnish NMR Symposium. Book of Abstracts. (51 pp.) 2016
193. Mäkelä, Toni: Ion Pair Recognition by Ditopic Crown Ether Based bis-Urea and Uranyl Salophen Receptors. (75 pp.) 2016
194. Lindholm-Lehto, Petra: Occurrence of pharmaceuticals in municipal wastewater treatment plants and receiving surface waters in Central and Southern Finland. (98 pp.) 2016
195. Härkönen, Ville: Computational and Theoretical studies on Lattice Thermal conductivity and Thermal properties of Silicon Clathrates. (89 pp.) 2016
196. Tuokko, Sakari: Understanding selective reduction reactions with heterogeneous Pd and Pt: climbing out of the black box. (85 pp.) 2016
197. Nuora, Piia: Monitapaustutkimus LUMA-Toimintaan liittyvissä oppimisympäristöissä tapahtuvista kemian oppimiskokemuksista. (171 pp.) 2016

DEPARTMENT OF CHEMISTRY, UNIVERSITY OF JYVÄSKYLÄ RESEARCH REPORT SERIES

198. Kumar, Hemanathan: Novel Concepts on The Recovery of By-Products from Alkaline Pulping. (61 pp.) 2016
199. Arnedo-Sánchez, Leticia: Lanthanide and Transition Metal Complexes as Building Blocks for Supramolecular Functional Materials. (227 pp.) 2016
200. Gell, Lars: Theoretical Investigations of Ligand Protected Silver Nanoclusters. (134 pp.) 2016
201. Vaskuri, Juhani: Oppiennätyksistä opetussuunnitelman perusteisiin - lukion kemian kansallisen opetussuunnitelman kehittyminen Suomessa vuosina 1918-2016. (314 pp.) 2017
202. Lundell Jan, Kiljunen Toni (Eds.): 22nd Horizons in Hydrogen Bond Research. Book of Abstracts. 2017
203. Turunen, Lotta: Design and construction of halogen-bonded capsules and cages. (61 pp.) 2017
204. Hurmalainen, Juha: Experimental and computational studies of unconventional main group compounds: stable radicals and reactive intermediates. (88 pp.) 2017
205. Koivistoinen Juha: Non-linear interactions of femtosecond laser pulses with graphene: photo-oxidation, imaging and photodynamics. (68 pp.) 2017
206. Chen, Chengcong: Combustion behavior of black liquors: droplet swelling and influence of liquor composition. (39 pp.) 2017
207. Mansikkamäki, Akseli: Theoretical and Computational Studies of Magnetic Anisotropy and Exchange Coupling in Molecular Systems. (190 p. + included articles) 2018.
208. Tatikonda, Rajendhraprasad: Multivalent N-donor ligands for the construction of coordination polymers and coordination polymer gels. (62 pp.) 2018
209. Budhathoki, Roshan: Beneficiation, desilication and selective precipitation techniques for phosphorus refining from biomass derived fly ash. (64 pp.) 2018
210. Siitonen, Juha: Synthetic Studies on 1-azabicyclo[5.3.0]decane Alkaloids. (140 pp.) 2018
211. Ullah, Saleem: Advanced Biorefinery Concepts Related to Non-wood Feedstocks. (57 pp.) 2018
212. Ghalibaf, Maryam: Analytical Pyrolysis of Wood and Non-Wood Materials from Integrated Biorefinery Concepts. (106 pp.) 2018

DEPARTMENT OF CHEMISTRY, UNIVERSITY OF JYVÄSKYLÄ
DISSERTATIONS PUBLISHED IN THE JYU DISSERTATIONS RESEARCH SERIES

1. Bulatov, Evgeny: Synthetic and structural studies of covalent and non-covalent interactions of ligands and metal center in platinum(II) complexes containing 2,2′-dipyridylamine or oxime ligands. (58 pp.) 2019. JYU Dissertations 70.
2. Annala, Riia: Conformational Properties and Anion Complexes of Aromatic Oligoamide Foldamers. (80 pp.) 2019. JYU Dissertations 84.
3. Isoaho, Jukka Pekka: Dithionite Bleaching of Thermomechanical Pulp - Chemistry and Optimal Conditions. (73 pp.) 2019. JYU Dissertations 85.
4. Nygrén, Enni: Recovery of rubidium from power plant fly ash. (98 pp.) 2019. JYU Dissertations 136.
5. Kiesilä, Anniina: Supramolecular chemistry of anion-binding receptors based on concave macromolecules. (68 pp.) 2019. JYU Dissertations 137.
6. Sokolowska, Karolina: Study of water-soluble p-MBA-protected gold nanoclusters and their superstructures. (60 pp.) 2019. JYU Dissertations 167.
7. Lahtinen, Elmeri: Chemically Functional 3D Printing: Selective Laser Sintering of Customizable Metal Scavengers. (71 pp.) 2019. JYU Dissertations 175.
8. Larijani, Amir: Oxidative reactions of cellulose under alkaline conditions. (102 pp.) 2020. JYU Dissertations 217.
9. Kolari, Kalle: Metal-metal contacts in late transition metal polymers. (60 pp.) 2020. JYU Dissertations 220.
10. Kauppinen, Minttu: Multiscale computational investigation of catalytic properties of zirconia supported noble metals. (87 pp.) 2020. JYU Dissertations 231.
11. Ding, Xin: Halogen Bond in Crystal Engineering: Structural Studies on Crystals with Ruthenium Centered Complexes and 1-(4-Pyridyl)-4-thiopyridine Zwitterion as Halogen Bond Acceptors. (59 pp.) 2020. JYU Dissertations 323.
12. Neuvonen, Antti: Toward an Understanding of Hydrogen-Bonding Bifunctional Organocatalyst Conformations and Their Activity in Asymmetric Mannich Reactions. (77 pp.) 2020. JYU Dissertations 336.
13. Kortet, Sami: 2,5-Diarylpyrrolidines and Pyroglutamic-Acid-Derived 2-Diarylmethyl-5-Aryl-Pyrrolidines: Their Synthesis and Use in Asymmetric Synthesis. (221 pp.) 2020. JYU Dissertations 337.
14. Saarnio, Ville: Fluorescent probes, noble metal nanoparticles and their nanocomposites: detection of nucleic acids and other biological targets. (80 pp.) 2021. JYU Dissertations 361.
15. Chernysheva, Maria: σ-hole interactions: the effect of the donors and acceptors nature in selenoureas, thioureas, halogenated species, substituted benzenes, and their adducts. (72 pp.) 2021. JYU Dissertations 370.
16. Bulatova, Margarita: Noncovalent interactions as a tool for supramolecular self-assembly of metallopolymers. (62 pp.) 2021. JYU Dissertations 377.

DEPARTMENT OF CHEMISTRY, UNIVERSITY OF JYVÄSKYLÄ
DISSERTATIONS PUBLISHED IN THE JYU DISSERTATIONS RESEARCH SERIES

17. Romppanen, Sari: Laser-spectroscopic studies of rare earth element- and lithium-bearing minerals and rocks. (66 pp.) 2021. JYU Dissertations 393.
18. Kukkonen, Esa: Nonlinear optical materials through weak interactions and their application in 3D printing. (58 pp.) 2021. JYU Dissertations 441.
19. Kuosmanen, Riikka: The Effect of Structure on the Gel Formation Ability and the Properties of Bile Acid Based Supramolecular Organogels. (68 pp.) 2021. JYU Dissertations 465.
20. Reuna, Sini: Development of a Method for Phosphorus Recovery from Wastewaters. (67 pp.) 2022. JYU Dissertations 486.
21. Taipale, Essi: Synthetic and Structural Studies on the Effect of Non-Covalent Interactions on N(*sp2*)-Heterocyclic Molecules. (67 pp.) 2022. JYU Dissertations 496.
22. Järvinen, Teemu: Molecular Dynamics View on Matrix Isolation. (143 pp.) 2022. JYU Dissertations 544.
23. Kumar, Parveen: Synthesis and Structural Studies on Halogen(I) Complexes. (160 pp.) 2022. JYU Dissertations 549.
24. Forsblom, Samu: Design and Construction of Metal-Organic Polyhedra. (212 pp.) 2022. JYU Dissertations 569.